

Utah State University

DigitalCommons@USU

All Graduate Theses and Dissertations

Graduate Studies

12-2021

Estimation of High-Resolution Evapotranspiration in Heterogeneous Environments Using Drone-Based Remote Sensing

Ayman M. M. Nassar
Utah State University

Follow this and additional works at: <https://digitalcommons.usu.edu/etd>



Part of the [Civil and Environmental Engineering Commons](#)

Recommended Citation

Nassar, Ayman M. M., "Estimation of High-Resolution Evapotranspiration in Heterogeneous Environments Using Drone-Based Remote Sensing" (2021). *All Graduate Theses and Dissertations*. 8329.
<https://digitalcommons.usu.edu/etd/8329>

This Dissertation is brought to you for free and open access by the Graduate Studies at DigitalCommons@USU. It has been accepted for inclusion in All Graduate Theses and Dissertations by an authorized administrator of DigitalCommons@USU. For more information, please contact digitalcommons@usu.edu.



ESTIMATION OF HIGH-RESOLUTION EVAPOTRANSPIRATION IN
HETEROGENEOUS ENVIRONMENTS USING DRONE-BASED
REMOTE SENSING

by

Ayman M. M. Nassar

A dissertation submitted in partial fulfillment
of the requirements for the degree

of

DOCTOR OF PHILOSOPHY

in

Civil and Environmental Engineering

Approved:

Alfonso Torres-Rua, Ph.D.
Major Professor

Mac McKee, Ph.D.
Committee Member

David K. Stevens, Ph.D.
Committee Member

William P. Kustas, Ph.D.
Committee Member

Lawrence Hipps, Ph.D.
Committee Member

D. Richard Cutler, Ph.D.
Interim Vice Provost of Graduate
Studies

UTAH STATE UNIVERSITY
Logan, Utah

2021

Copyrights © Ayman M. M. Nassar 2021
All Rights Reserved

ABSTRACT

Estimation of High-Resolution Evapotranspiration in Heterogeneous Environments Using
Drone-Based Remote Sensing

by

Ayman M. M. Nassar, Doctor of Philosophy

Utah State University, 2021

Major Professor: Dr. Alfonso Torres-Rua

Department: Civil and Environmental Engineering

An accurate estimation of evapotranspiration (*ET*) is prerequisite to the water management practices for mitigating water overutilization and environmental degradation. Although many studies have investigated *ET* in agricultural settings, still there is limited understanding in quantifying *ET* in heterogeneous environments. Taking advantage of the wide range of data available from different remote sensing platforms, spatial *ET* maps can be generated at different scales using several algorithms. Nowadays, the advent of advanced small unmanned aerial systems (*sUAS*) technology with light sensors allows the capture of high-resolution data more quickly than traditional methods, described as “flexible in timing”.

The major focus of this study is to provide an improved understanding of remote sensing-based *ET* in heterogeneous areas, particularly in vineyards and natural environments. First, the influence of model grid size/spatial resolution on the estimation of surface energy fluxes/*ET* was investigated in vineyards using the Two Source Energy Balance (*TSEB*) model and *sUAS* imagery. Different spatial resolutions were considered

including 3.6 m, 7.2 m, 14.4 m, and 30 m. *ET* maps obtained from the *TSEB-2T* model at different contextual spatial domains were compared and validated against the ground measurements from eddy covariance (*EC*). Results indicated that the *TSEB-2T* model is slightly affected in the estimation of the net radiation (R_n) and the soil heat flux (G) at different resolutions, while the sensible and latent heat fluxes (H and LE , respectively) are significantly affected by coarse grid sizes. Moreover, agricultural water management practices require daily crop water estimates for irrigation scheduling. To achieve that, five different methods were used and tested to upscale/extrapolate the instantaneous evapotranspiration to daily values including (1) evaporative fraction (EF), (2) solar radiation (R_s), (3) ratio of net radiation to solar radiation (R_n/R_s), (4) Sine, and (5) Gaussian (GA). The *ET* from *EC* observations and *sUAS* information was used to assess those approaches. Overall, the analysis using *EC* and *TSEB* indicated that the R_s , EF , and GA approaches presented the best goodness-of-fit statistics in the time window between 1030 and 1330 PST, with the R_s approach yielding better agreement with the *EC* measurements. The promising results obtained from the *TSEB* model for *ET* estimates over a heterogeneous agricultural environment in vineyards encourage the implementation of that model in more heterogeneous natural area. *TSEB* was tested over the San Rafael River corridor, dominated by a wide range of vegetation density and diversity. The discrete wavelet transform (*DWT*) technique was used to identify adequate spatial resolution to represent the study area. Results indicated that spatial resolutions between 6 m and 15 m are suitable for representing energy fluxes with small differences in LE values between the two resolutions (6 m and 15 m).

PUBLIC ABSTRACT

Estimation of High-Resolution Evapotranspiration in Heterogeneous Environments Using
Drone-Based Remote Sensing

Ayman M. M. Nassar

Evapotranspiration (*ET*) is a key element of hydrological cycle analysis, irrigation demand, and for better allocation of water resources in the ecosystem. For successful water resources management activities, precise estimate of *ET* is necessary. Although several attempts have been made to achieve that, variation in temporal and spatial scales constitutes a major challenge, particularly in heterogeneous canopy environments such as vineyards, orchards, and natural areas. The advent of remote sensing information from different platforms, particularly the small unmanned aerial systems (*sUAS*) technology with lightweight sensors allows users to capture high-resolution data faster than traditional methods, described as “flexible in timing”. In this study, the Two Source Energy Balance Model (*TSEB*) along with high-resolution data from *sUAS* were used to bridge the gap in *ET* issues related to spatial and temporal scales. Over homogeneous vegetation surfaces, relatively low spatial resolution information derived from Landsat (e.g., 30 m) might be appropriate for *ET* estimate, which can capture differences between fields. However, in agricultural landscapes with presence of vegetation rows and interrows, the homogeneity is less likely to be met and the ideal conditions may be difficult to identify. For most agricultural settings, row spacing can vary within a field (vineyards and orchards), making the agricultural landscape less homogenous. This leads to a key question related to how the

contextual spatial domain/model grid size could influence the estimation of surface fluxes in canopy environments such as vineyards. Furthermore, temporal upscaling of instantaneous ET at daily or longer time scales is of great practical importance in managing water resources. While remote sensing-based ET models are promising tools to estimate instantaneous ET , additional models are needed to scale up the estimated or modeled instantaneous ET to daily values. Reliable and precise daily ET (ET_d) estimation is essential for growers and water resources managers to understand the diurnal and seasonal variation in ET . In response to this issue, different existing extrapolation/upscaling daily ET (ET_d) models were assessed using eddy covariance (EC) and $sUAS$ measurements. On the other hand, ET estimation over semi-arid naturally vegetated regions becomes an issue due to high heterogeneity in such environments where vegetation tends to be randomly distributed over the land surface. This reflects the conditions of natural vegetation in river corridors. While significant efforts were made to estimate ET at agricultural landscapes, accurate spatial information of ET over riparian ecosystems is still challenging due to various species associated with variable amounts of bare soil and surface water. To achieve this, the $TSEB$ model with high-resolution remote sensing data from $sUAS$ were used to characterize the spatial heterogeneity and calculate the ET over a natural environment that features arid climate and various vegetation types at the San Rafael River corridor.

DEDICATION

To my Parents, Mahmoud, and Rasmia,

To my wife Israa

To my extended family, uncles, aunts, cousins

To my teachers, mentors and fellow students

To my friends

To the generous donors who supported my scholarships and awards

ACKNOWLEDGMENTS

With pleasure and deep sense of gratitude, I would like to express my sense of indebtedness to my advisor Dr. Alfonso Torres-Rua for his kindness, mentorship, motivation, and encouragement to complete my PhD. His guidance helped me throughout my research and write-up phase of my dissertation.

I am also very grateful to my dissertation committee members: Drs. Mac McKee, David Stevens, William Kustas, and Lawrence Hipps, for their insightful comments and encouragement. They all provided significant feedback and advice that brought my work to a higher level. I would like to thank the members of the USDA-ARS Hydrology and Remote Sensing Laboratory, Beltsville, Maryland, especially Dr. Joseph Alfieri, Dr. William White, and Lynn McKee. Thanks to Dr. Héctor Nieto at Complutum Tecnologías de la Información Geográfica S.L. (COMPLUTIG), Madrid, Spain, who has provided important advice to my dissertation.

My sincere thanks also go to the Aggieair Service Center team (Dr. Calvin Coopmans, Ian Gowing and Shannon Syrstad) for their extraordinary support in this research, whose cooperation greatly improved the data collection and data processing, and the staff of Viticulture, Chemistry and Enology Division of E&J Gallo Winery, especially Drs. Maria Mar Alsina, Luis Sanchez, and Nick Dokoozlian for the assistance in the collection and processing of field data. I would also like to thank my research team for the stimulating discussions, for the sleepless nights we worked together before deadlines, and for making my time at USU an enjoyable experience.

This dissertation would not have been possible without the financial support from Utah Water Research Laboratory, NASA Applied Sciences-Water Resources Program

[NNX17AF51G], and the USDA Non-Assistance Cooperative Agreement 58-8042-5-092 funding. I would like to acknowledge and express my gratitude to Utah Division of Wildlife Resources [Grant No. 202421], which provided the funding for my third research project on the San Rafael River corridor.

Last but not the least; I would like to thank my family: my parents and my wife for their support and encouragement throughout writing this dissertation and my life in general.

Ayman M. M. Nassar

CONTENTS

	Page
Abstract	iii
Public Abstract.....	v
Dedication	vii
Acknowledgments.....	viii
List of Tables	xiii
List of Figures	xiv
Chapter 1	1
1.1 Background	1
1.2 Research Objectives	6
1.3 Dissertation Organization.....	8
References	10
Chapter 2.....	13
Abstract	13
2.1 Introduction	15
2.1.1 <i>TSEB-2T</i> Model	19
2.1.2 <i>TSEB-2T</i> Main Inputs	24
2.2 Materials and Methods	27
2.2.1 Study Area and Data Sources	28
2.2.2 Data Processing	32
2.2.3 Energy Balance Closure Adjustment Methods for <i>EC</i>	32
2.2.4 Contextual Spatial Domain.....	33
2.2.5 <i>TSEB-2T</i> Inputs.....	34
2.2.6 Goodness-of-Fit Statistics.....	35
2.3 Results and Discussion.....	37

2.3.1 <i>TSEB-2T</i> Contextual Spatial Domains Validation.....	37
2.3.2 Contextual Spatial Domain Aggregations Effects.....	42
2.4 Conclusion.....	57
References	60
Chapter 3.....	67
Abstract	67
3.1 Introduction	69
3.1.1 Daily <i>ET</i> Upscaling Approaches	72
3.1.2 Two Source Energy Balance (<i>TSEB</i>) Model	77
3.2 Methodology	81
3.2.1 Study Area	81
3.2.2 Procedure	83
3.2.3 Goodness-of-Fit Statistics.....	89
3.3 Results and Discussion.....	90
3.3.1 Diurnal Variation of Energy Fluxes from <i>EC</i> Measurements	90
3.3.2 Comparison between Different <i>ET_d</i> Extrapolation Approaches Using the <i>EC</i> Measurements.....	96
3.3.3 Assessing the Instantaneous <i>TSEB ET</i> Versus <i>EC</i> Measurements	99
3.3.4 Assessment of the Daily <i>ET</i> Extrapolation Approaches Using <i>TSEB sUAS</i> Results	102
3.4 Conclusion.....	108
References	110
Chapter 4.....	116
Abstract	116
4.1 Introduction	118
4.2 Methodology	122
4.2.1 Site Description	123
4.2.2 Characterizing the Spatial Heterogeneity Using Wavelet Analysis	126

4.2.3 Image Classification	129
4.2.4 <i>ET</i> Estimation Using the Two Source Energy Balance (<i>TSEB</i>) Model.....	130
4.3 Results and Discussion.....	134
4.3.1 Land Cover/Land Use Classification.....	134
4.3.2 Spatial Heterogeneity Using Wavelet Analysis.....	137
4.3.3 Retrieving the Biophysical Parameters.....	141
4.3.4 Spatial Scale Implications on <i>LE</i>	146
4.3.5 Daily <i>ET</i> Calculation for Vegetation Types	150
4.4 Conclusion.....	154
References	156
Chapter 5	160
5.1 Summary and Conclusions.....	160
5.2 Recommendations	163
Appendices.....	166

LIST OF TABLES

	Page
Table 2.1 Dates and times of <i>AggieAir GRAPEX</i> flights used in this study.....	30
Table 2.2 Description of in-situ micrometeorological measurements in this study.	31
Table 2.3 Goodness-of-fit statistics between the eddy covariance and the <i>TSEB-2T</i> fluxes at different spatial scales (3.6 m, 7.2 m, 14 m, and 30 m).	40
Table 2.4 Spatial domain effect on <i>LAI</i> estimation.....	47
Table 3.1 Dates and times of <i>AggieAir sUAS</i> flights used in this study.	86
Table 3.2 Description of <i>EC</i> towers in vineyards that were part of this study.	88
Table 3.3 Goodness-of-fit statistics of daily <i>ET</i> extrapolation methods at two different time windows (1030–1330 and 1430–1630 PST) using only <i>EC</i> tower information in California.	98
Table 3.4 Goodness-of-fit statistics between the eddy covariance (<i>EC</i>) and the instantaneous <i>TSEB sUAS</i> fluxes at the different vineyard sites of this project.	102
Table 3.5 Goodness-of-fit statistics comparing multiple daily <i>ET</i> methods at two different time windows (1030–1330 and 1430–1630).....	107
Table 4.1 Dates and times (launch and landing) of <i>AggieAir</i> flights at the San Rafael River corridor.....	126
Table 4.2 The technical specifications of the weather station used for this study.....	126
Table 4.3 Spatial resolution effect on <i>LE</i> estimation.....	147
Table 4.4 Average daily <i>ET</i> estimation for different vegetation types on different dates for the study area.....	151

LIST OF FIGURES

	Page
Figure 2.1 Schematic representation of <i>TSEB-2T</i> model.....	21
Figure 2.2 Schematic diagram for canopy w_c/h_c ratio.	26
Figure 2.3 Study methodology for assessing the impact of the <i>TSEB-2T</i> contextual spatial domain.	27
Figure 2.4 Layout of study area in Lodi, California, locations of <i>EC</i> towers and example of 90% of <i>EC</i> footprint at afternoon for June 02, 2015.....	29
Figure 2.5 Layout of 90% <i>EC</i> footprints for two towers at different times considered by this study.	38
Figure 2.6 Scatterplot of observed versus estimated surface fluxes using different model grid sizes/resolution with the <i>TSEB-2T</i> model; (a) 3.6 m, (b) 7.2 m, (c) 14.4 m, and (d) 30 m.	41
Figure 2.7 The <i>LST-NDVI</i> relationship used for finding T_c and T_s as proposed by the <i>TSEB-2T</i> model at different spatial domains (August 09, 2014). (a) 3.6 m, (b) 7.2 m, (c) 14.4 m, (d) 30 m.....	43
Figure 2.8 Example of (a) canopy temperature (T_c) and (b) soil temperature (T_s) in Kelvin (K) at different spatial domains for August 09, 2014.	44
Figure 2.9 Example of modeled LAI (unitless) across different spatial domains for August 09, 2014.....	46
Figure 2.10 Frequency curve of <i>LAI</i> at different times from 3.6 m and 7.2 m, 14.4 m and 30 m.....	48
Figure 2.11 <i>LE</i> (W/m^2) aggregation at 3.6 m, 7.2 m, 14.4 m and 30 m for August 09, 2014.....	49
Figure 2.12 Spatial domain effect on the mean of <i>LE</i> spatial data at different times.....	50
Figure 2.13 Spatial domain effect on the coefficient of variation (<i>CV</i>) of <i>LE</i> spatial data at different times.....	51
Figure 2.14 Frequency curve (left) and cumulative frequency distribution (right) plots of instantaneous <i>LE</i> for all <i>sUAS</i> flights at 3.6 m, 7.2 m, 14.4 m, and 30 m.....	53
Figure 2.15 Variation of the relative spatial mean of R_A for different flights.....	54

Figure 2.16 Relative error (E_r) at different spatial resolutions for LE with the triangle symbols indicating mean and light lines indicating the 25 th and 75 th percentiles for the coarse grid sizes.	86
Figure 3.1 Schematic representation of the Two Source Energy Balance ($TSEB$) model.	79
Figure 3.2 Layout of study vineyards in Central Valley, California with estimated typical flux footprint/source area for the EC towers.....	83
Figure 3.3 Study methodology for assessing different upscaling daily ET methods in $sUAS$	84
Figure 3.4 Diurnal variations of energy fluxes at Sierra Loma Sites 1 and 2 for the years 2014 to 2018, from the April to October irrigation season. (a) Net radiation (R_n), (b) sensible heat flux (H), (c) latent heat flux (LE), (d) soil heat flux (G).	92
Figure 3.5 Diurnal variations of LE for each EC included in this study for the years 2014 to 2018, from the April to October irrigation season.....	94
Figure 3.6 An example of the diurnal variations of (a) and $ET_h/ET_{h(max)}$ and (b) ET_h/ET_d at different phenological vine stages for Sierra Loma Sites 1 and 2 between 2014 and 2018.	96
Figure 3.7 Comparison of instantaneous $TSEB$ $sUAS$ energy fluxes against EC measurements (without flux closure). The presented subplots include the available $sUAS$ imagery, as described in Table 3.1.....	101
Figure 3.8 Comparison between daily ET from $TSEB$ $sUAS$ and EC at two different time windows (1030–1330 and 1430–1630).....	106
Figure 4.1 Flowchart of the methodology followed in this study.....	123
Figure 4.2 Layout of a section of the San Rafael River corridor area of study.	124
Figure 4.3 Schematic diagram of DWT for 2D image.....	128
Figure 4.4 Example of in-situ LAI measurements taken in the San Rafael River.....	134
Figure 4.5 Vegetation classification map of the San Rafael River Corridor.	136
Figure 4.6 Layout of river corridor and non-river corridor area for wavelet analysis....	139
Figure 4.7 Wavelet energy at multiple spatial domains for different flights.	141
Figure 4.8 Example of the spatial maps for biophysical parameters at 6-m and 15-m resolutions for FL1 (July 22, 2019).	145

Figure 4.9 Example of DEM and hc profiles in the study site.....	145
Figure 4.10 Example of modeled instantaneous LE (W/m^2) at 6-m and 15-m resolutions for July 22, 2019 at 10:05 am.	148
Figure 4.11 Frequency curves of instantaneous LE (W/m^2) for all sUAS flights at 6 m and 15 m. Note: Blue dashed line represents the spatial mean of LE at 6-m resolution, the red represents the 15-m resolution.	149
Figure 4.12 Daily ET estimation for each vegetation type on different sUAS flight dates in the study area.	152
Figure 4.13 Example of modeled daily ET for July 22, 2019.....	153
Figure 4.14 Example of RGB sUAS image from each flight date (June, July, and October).	154

CHAPTER 1

INTRODUCTION

1.1 Background

Evapotranspiration (*ET*) is a key element of the hydrological cycle, analysis of irrigation demand, and allocation of water resources [1]. Among the components of the hydrological cycle, *ET* could be one of the most difficult to estimate due to variability of vegetation types and densities, hydrological characteristics of soil and the wide temporal and spatial variation of climate [2]. For successful water resources management activities, accurate estimation of *ET* is needed. Although several attempts have been made to achieve this, the variation in temporal and spatial scales constitute a major challenge [3], particularly in complex canopy environments such as vineyards, orchards, and heterogeneous natural areas. The spatial scale could span from micro to macro scales [4], while the temporal scale could vary from an hour to a year depending on the application.

Surface energy balance (*SEB*) models are very important to understand the land-surface energy exchange. In recent years, many *SEB* models have been developed to estimate *ET* that vary in complexity from simple schemes to detailed representation of energy fluxes [5]. Generally, the *SEB* models can be categorized into two types: (semi-) empirical methods and analytical methods. (Semi-) empirical models are usually accomplished by creating generic relationships, while the analytical approach relies on an understanding of physical processes at the scale of interest that varies in complexity and may require direct and indirect measurements from ground observations and remote sensing data [6]. Technical advancement in ground-based instrumentation and the advent of remote sensing with a wide range of data [7] allows models to estimate the main energy

fluxes including the net radiation (R_n), sensible heat flux (H), latent heat flux (LE), and soil heat flux (G). While these four components (R_n , H , LE and G) are considered in the simplified form of the energy balance ($R_n = H + LE + G$), there are other energy fluxes used for photosynthesis or storage of energy by vegetation ignored due to their small magnitude [4]. R_n is the balance of shortwave radiation and longwave radiation. H is the turbulent heat flux exchange between surface and air due to temperature difference. LE is the flux of the heat from surface to the atmosphere associated with evaporation of water and used to represent ET in SEB models. G represents the heat flux that moves in/out the soil medium due to temperature changes between surface and subsurface.

The estimation of surface energy fluxes, particularly LE , depends on the land surface type, which requires information about the Earth's features at appropriate spatial and temporal scales. Traditional in-situ measurements used to estimate ET , such as pan evaporation and eddy covariance (EC), provide information at a local scale [8,9] making these methods inapplicable for large scale due to the heterogeneity of land surfaces and complex environment of the heat transfer process governing the ET [10]. The availability of remote sensing information from different platforms, including satellite, manned aircraft and small unmanned aerial system ($sUAS$), allows the collection of multi-spectral data in various spatial and temporal resolutions for estimation of ET . For example, Landsat can provide spatial information of 30 m every 16 days, while the Moderate Resolution Imaging Spectroradiometer ($MODIS$) data are available at 250-m to 1-km pixel resolution at 2 – 3 days. A major limitation of using data from these satellites is related to their coarse spatial and temporal resolution, as well as the presence of clouds at overpass time [11]. Imagery from manned aircraft is another remote sensing data source that can provide high-

resolution information for estimating ET and operate on demand. However, they are usually cost-prohibitive and, therefore, unlikely to be used to conduct multiple flights over an area of interest [12]. Nowadays, the advent of advanced $sUAS$ technology with light sensors allows users to capture high-resolution data more quickly than traditional methods, described as “flexible in timing”. According to previous studies, $sUAS$ is recognized as a more precise and cost-effective technology compared with satellites and manned aircrafts [13].

Taking advantage of the wide range of data available from different remote sensing platforms, spatial ET can be calculated using different algorithms if the required inputs are available. These inputs are related to the land surface features and their characteristics involving the land surface temperature (LST), vegetation fractional cover (f_c), leaf area index (LAI), and canopy height (h_c). To achieve precise and reliable ET estimation, a high level of accuracy is required for the input data [14]. Over homogeneous vegetation surfaces, relatively low spatial resolution information derived from Landsat (e.g., 30 m) might be appropriate for ET estimate, which can capture differences between fields [15]. However, in agricultural landscapes with presence of vegetation rows and interrows, the homogeneity is less likely to be met and the ideal conditions may be difficult to identify. Meanwhile, for most agricultural settings, the row spacing could vary within the field, such as in vineyards and orchards, making the agricultural landscape less homogeneous. For example, in vineyards, the row space varies between 6 ft and 12 ft [16], while in orchards, the row spacing varies between 8 ft and 18 ft [17]. On the other hand, in the early growing stage of vegetation, completely closed canopies are rarely available [18], which increases the degree of heterogeneity. *This leads to a key question related to how the contextual*

spatial domain/model grid size could influence the estimation of surface fluxes in complex canopy environments, such as vineyards.

Temporal upscaling of instantaneous *ET* at daily or longer time scale is of great practical importance in managing water resources [19,20]. While remote sensing-based *ET* models are promising tools to estimate instantaneous *ET*, additional models are needed to scale up the instantaneous *ET* to daily values. Reliable and precise daily *ET* (*ET_d*) estimation is essential for growers and water resources managers to understand the variation in *ET* [21], particularly in drought-stricken regions, such as California. To achieve that, accuracy in both the instantaneous *ET* estimation and the upscaling methods is necessary. On the other hand, the time window selected to extrapolate the instantaneous *ET* to the daily value might be an issue due to the diurnal variation of solar radiation and other micrometeorological data. For example, Landsat-based *ET* models can provide information to estimate daily *ET* at the satellite overpass time; however, images could be jeopardized by intermittent clouds resulting in unsatisfying results for daily *ET* to quantify the agricultural water demand. To overcome that, the advent of advanced *sUAS* technology with high-resolution data allows on-demand acquisition of detailed images to assure the consideration of a reasonable temporal coverage. *In response to this issue, two research questions are raised related to “Which daily ET extrapolation approach at grapevine row scales can provide reliable values under a variety of vegetation and environmental conditions and thermal-based ET models like TSEB?” and “What time window for acquiring a remotely sensed ET provides the most reliable daily ET using an extrapolation approach?”*

Besides the evaporative losses from irrigated lands, *ET* assessment over arid/semi-arid naturally vegetated regions becomes an issue due to high heterogeneity in such environments where vegetation tends to be distributed in complex ways over the land surface [4]. In arid areas, *ET* is more crucial, returning up to 90% or more of the annual precipitation to the atmosphere [22]. This reflects the surface conditions that are typically dominated by the natural vegetation, such as river corridors. Precise estimate of *ET* over riparian areas is essential to properly allocate river water for human and ecosystem needs [23]. In the western U.S., many river corridors are now prevailed by tamarisk replacing the native vegetation such as willow and cottonwood [23]. Previous studies indicated that tamarisk has higher *ET* rate than other native vegetation with high potential to increase the water used by the vegetation dominating the river corridor [24]. While multiple efforts have been made to estimate *ET* at different agricultural landscapes, accurate spatial information of *ET* over riparian ecosystems is still a challenging issue due to spatial variability in the land surface (vegetation, bare soil, and water) and narrow size of the riparian corridors [23]. In such a heterogeneous natural environment, a relatively high-resolution imagery (e.g., <30 m) is highly recommended [25] to detect the different types of vegetative species on the ground and accurately estimate the land surface properties, such as fractional cover and the land surface temperature, which are key inputs for remote sensing-based *ET* models. *To achieve this, a physically-based SEB model, namely TSEB, associated with high-resolution remote sensing data from sUAS was used to characterize the spatial variability and calculate the ET over a natural environment described by arid climate and various types of vegetation at the San Rafael River corridor.*

1.2 Research Objectives

The overall objective of this dissertation is to provide an improved understanding of a remote sensing-based *ET* model, namely the Two Source Energy Balance (*TSEB*) model, in vineyards and natural environments using high-resolution information derived from *sUAS* imagery. An accurate estimation of *ET* is prerequisite to the water management practices for mitigating the water overutilization and environmental degradation. *TSEB* is a soil-canopy-atmosphere scheme, which uses radiometric surface temperature as a key boundary condition to estimate energy fluxes. This model proved to be better for handling a wide range of heterogeneous surfaces. However, spatial and temporal scales for *ET* estimation still constitutes challenging issues, particularly in heterogeneous environments such as vineyards and natural areas. The structure of vineyard canopy is very heterogeneous due to variation of lateral vine growth, along with other complications from within-field variations in soil texture and elevation. In addition, interrows are usually occupied by a cover crop, which increases the complexity of the vineyard structure. Therefore, identifying a suitable spatial domain/model grid size to represent the vineyard is necessary for accurate *ET* estimates. In this study, different spatial domains/model grid sizes have been considered, including 3.6 m, 7.2 m, 14.4 m, and 30 m, to investigate the influence of domain size on the *TSEB* estimates. These selected values correspond to multiple vine rows spacing of 3.6 m (one row), 7.2 m (two rows), 14.4 m (four rows), and 30 m (Landsat scale—nine rows). Energy flux maps obtained from the *TSEB* model at different contextual spatial domains were compared and validated against the ground measurements from *EC* towers installed in the field. Moreover, for practical irrigation water requirements, daily or weekly crop water use estimates to schedule irrigations are

needed, which require an accurate crop *ET* calculation. To achieve that, five different methods were used and tested to upscale/extrapolate the instantaneous evapotranspiration (ET_i) to daily values including (1) evaporative fraction (EF), (2) solar radiation (R_s), (3) ratio of net radiation to solar radiation (R_n/R_s), (4) Sine approach, and (5) Gaussian (GA) model. The accuracy of daily *ET* estimation has been tested by (a) assessing the performance of daily *ET* scaling approaches using *EC* observations and *sUAS* information, and (b) determining an optimal time window for *ET* upscaling from one-time-of-day measurement. The promising results obtained from the *TSEB* model for *ET* estimates over a heterogeneous agricultural environment in vineyards encouraged the implementation of that model in more heterogeneous natural areas with a wide range of vegetation types and different features. *TSEB* was used over the highly heterogeneous area at the San Rafael River corridor in east central Utah, dominated by a wide range of vegetation types, including treated tamarisk, cottonwood, willow, grass and others. The study area is also characterized with arid conditions, different soil moisture status, various types of soil and various tree heights. To capture the spatial heterogeneity in the study area, the discrete wavelet transform (*DWT*) technique was used by decomposing the *sUAS NDVI* (Normalized Difference Vegetation Index) image into different scales to identify adequate spatial resolution to represent the San Rafael River corridor domain for *ET* estimation. Then the selected spatial scales were used to derive the *TSEB* inputs to evaluate their effects on *ET* estimation.

To accomplish the previously mentioned objectives, several questions are addressed as follows:

- (1) How can “validity” of T_c vs. T_s at coarse scales/model grid sizes be quantified?

- (2) How do changes in spatial resolution/model grid size affect *LE*?
- (3) Which spatial resolution/model grid size is appropriate? Why?
- (4) Which daily *ET* extrapolation approach at grapevine row scales can provide reliable values under a variety of vegetation and environmental conditions and thermal-based *ET* models like *TSEB*?
- (5) What time window for acquiring a remotely sensed *ET* provides the most reliable daily *ET* using an extrapolation approach?
- (6) What is the dominant spatial resolution/model grid size to represent a heterogeneous natural environment/San Rafael River corridor with a wide range of vegetation?
- (7) Which spatial resolution/model grid size is most appropriate for the river corridor and surrounding arid vegetation to estimate *LE*?
- (8) What is the daily *ET* estimation for each of the two ecosystems (river corridor and surrounding arid vegetation) in a heterogeneous natural environment/San Rafael River corridor?

1.3 Dissertation Organization

The dissertation is prepared in five chapters, three of which are in paper format addressing the different objectives mentioned in section (1.2). Chapter 1 is a general introduction to highlight the importance of this study bridging the gap in *ET* knowledge, particularly in spatial and temporal challenging issues in heterogeneous environments. Chapter 2 examines the influence of using different spatial domains/model grid sizes to represent surface features in a heterogeneous canopy environment, namely vineyards using the *TSEB* model and *sUAS*. Chapter 3 evaluates different methodologies for daily

evapotranspiration (ET_d) estimation from *sUAS* over commercial vineyards of different climates, vine variety and trellis design. Chapter 4 deals with the issue of how to capture the spatial variability of the land surface to improve the ET estimation over a heterogeneous natural environment using high-resolution imagery from *sUAS*.

Chapter 5 provides a summary of this research work, shows the main conclusions drawn from the study, and presents some recommendations for further research.

References

1. Senkondo, W.; Munishi, S.E.; Tumbo, M.; Nobert, J.; Lyon, S.W. Comparing Remotely-Sensed Surface Energy Balance Evapotranspiration Estimates in Heterogeneous and Data-Limited Regions: A Case Study of Tanzania's Kilombero Valley. *Remote Sensing* 2019, *11*, 1289.
2. Allen, R.G.; Pereira, L.S.; Howell, T.A.; Jensen, M.E. Evapotranspiration Information Reporting: II. Recommended Documentation. *Agricultural Water Management* 2011, *98*, 921–929.
3. McCabe, M.F.; Wood, E.F. Scale Influences on the Remote Estimation of Evapotranspiration Using Multiple Satellite Sensors. *Remote Sensing of Environment* 2006, *105*, 271–285.
4. Geli, H.M.E. Modeling Spatial Surface Energy Fluxes of Agricultural and Riparian Vegetation Using Remote Sensing, Utah State University, 2012.
5. Grimmond, C.S.B.; Best, M.; Barlow, J.; Arnfield, A.J.; Baik, J.-J.; Baklanov, A.; Belcher, S.; Bruse, M.; Calmet, I.; Chen, F.; et al. Urban Surface Energy Balance Models: Model Characteristics and Methodology for a Comparison Study. *Meteorological and Air Quality Models for Urban Areas* 2009, 97–123.
6. Li, Z.-L.; Tang, R.; Wan, Z.; Bi, Y.; Zhou, C.; Tang, B.; Yan, G.; Zhang, X. A Review of Current Methodologies for Regional Evapotranspiration Estimation from Remotely Sensed Data. *Sensors* 2009, *9*, 3801–3853.
7. Nassar, A.; Torres-Rua, A.; Kustas, W.; Alfieri, J.; Hipps, L.; Prueger, J.; Nieto, H.; Alsina, M.M.; White, W.; McKee, L.; et al. Assessing Daily Evapotranspiration Methodologies from One-Time-of-Day sUAS and EC Information in the GRAPEX Project. *Remote Sensing* 2021, *13*, 2887.
8. Baldocchi, D.D. Assessing the Eddy Covariance Technique for Evaluating Carbon Dioxide Exchange Rates of Ecosystems: Past, Present and Future. *Global Change Biology* 2003, *9*, 479–492.
9. Zhang, B.; Kang, S.; Li, F.; Zhang, L. Comparison of Three Evapotranspiration Models to Bowen Ratio-Energy Balance Method for a Vineyard in an Arid Desert Region of Northwest China. *Agricultural and Forest Meteorology* 2008, *148*, 1629–1640.
10. Su, Z. The Surface Energy Balance System (SEBS) for Estimation of Turbulent Heat Fluxes. *Hydrology and Earth System Sciences* 2002, *6*, 85–100.
11. Belgiu, M.; Stein, A. Spatiotemporal Image Fusion in Remote Sensing. *Remote Sensing* 2019, *11*, 818.
12. Tsouros, D.C.; Bibi, S.; Sarigiannidis, P.G. A Review on UAV-Based Applications for Precision Agriculture. *Information* 2019, *10*, 349.

13. Watts, A.C.; Ambrosia, V.G.; Hinkley, E.A. Unmanned Aircraft Systems in Remote Sensing and Scientific Research: Classification and Considerations of Use. *Remote Sensing* 2012, 4, 1671–1692.
14. Kustas, W.P.; Norman, J.M.; Anderson, M.C.; French, A.N. Estimating Subpixel Surface Temperatures and Energy Fluxes from the Vegetation Index–radiometric Temperature Relationship. *Remote Sensing of Environment* 2003, 85, 429–440.
15. Kustas, W. Effects of Remote Sensing Pixel Resolution on Modeled Energy Flux Variability of Croplands in Iowa. *Remote Sensing of Environment* 2004, 92, 535–547.
16. University of California Agriculture; Natural Resources Growing Grapes (table, Wine, Raisins) in Your Backyard Available online: http://cagardenweb.ucanr.edu/Growing_Grapes_in_the_California_Garden/?uid=1&ds=436 (accessed on 14 July 2020).
17. Spacing Trees in an Orchard - Cooperative Extension: Tree Fruits - University of Maine Cooperative Extension Available online: <https://extension.umaine.edu/fruit/growing-fruit-trees-in-maine/spacing/> (accessed on 17 July 2020).
18. Zipper, S.C.; Loheide, S.P., II Using Evapotranspiration to Assess Drought Sensitivity on a Subfield Scale with HRMET, a High-Resolution Surface Energy Balance Model. *Agricultural and Forest Meteorology* 2014, 197, 91–102.
19. Tang, R.; Li, Z.-L.; Sun, X. Temporal Upscaling of Instantaneous Evapotranspiration: An Intercomparison of Four Methods Using Eddy Covariance Measurements and MODIS Data. *Remote Sensing of Environment* 2013, 138, 102–118.
20. Lian, J.; Li, D.; Huang, M.; Chen, H. Evaluation of Remote Sensing-Based Evapotranspiration Estimates Using a Water Transfer Numerical Simulation under Different Vegetation Conditions in an Arid Area. *Hydrological Processes* 2018, 32, 1801–1813.
21. Elhag, M.; Psilovikos, A.; Manakos, I.; Perakis, K. Application of the Sebs Water Balance Model in Estimating Daily Evapotranspiration and Evaporative Fraction from Remote Sensing Data Over the Nile Delta. *Water Resources Management* 2011, 25, 2731–2742.
22. - Soil Moisture and Evapotranspiration. *Environmental Hydrology* 2015, 144–193.
23. Nagler, P.; Scott, R.; Westenburg, C.; Cleverly, J.; Glenn, E.; Huete, A. Evapotranspiration on Western U.S. Rivers Estimated Using the Enhanced Vegetation Index from MODIS and Data from Eddy Covariance and Bowen Ratio Flux Towers. *Remote Sensing of Environment* 2005, 97, 337–351.
24. Tomaso, J.M.D.; Di Tomaso, J.M. Impact, Biology, and Ecology of Saltcedar (*Tamarix*spp.) in the Southwestern United States. *Weed Technology* 1998, 12, 326–336.

25. Kustas, W. Evaluating the Effects of Subpixel Heterogeneity on Pixel Average Fluxes. *Remote Sensing of Environment* 2000, 74, 327–342.

CHAPTER 2

INFLUENCE OF MODEL GRID SIZE ON THE ESTIMATION OF SURFACE FLUXES USING THE TWO SOURCE ENERGY BALANCE MODEL AND SUAS IMAGERY IN VINEYARDS

Abstract

Evapotranspiration (*ET*) is a key variable for hydrology and irrigation water management, with significant importance in drought-stricken regions of the western US. This is particularly true for California, which grows much of the high-value perennial crops in the U.S. The advent of small unmanned aerial system (*sUAS*) with sensor technology similar to satellite platforms allows for the estimation of high-resolution *ET* at plant spacing scale for individual fields. However, while multiple efforts have been made to estimate *ET* from *sUAS* products, the sensitivity of *ET* models to different model grid size / resolution in complex canopies, such as vineyards, is still unknown. The variability of row spacing, canopy structure, and distance between fields makes this information necessary because additional complexity processing individual fields. Therefore, processing the entire image at a fixed resolution that is potentially larger than the plant-row separation is more efficient. From a computational perspective, there would be an advantage to running models at much coarser resolutions than the very fine native pixel size from *sUAS* imagery for operational applications. In this study, the Two Source Energy Balance with a dual temperature (*TSEB-2T*) model, which uses remotely sensed soil/substrate and canopy temperature from *sUAS* imagery, was used to estimate *ET* and identify the impact of spatial domain scale under different vine phenological conditions. The analysis relies upon high-resolution imagery collected during multiple years and

times by the Utah State University *AggieAirTM* *sUAS* Program over a commercial vineyard located near Lodi, California. This project is part of the USDA-Agricultural Research Service Grape Remote Sensing Atmospheric Profile and Evapotranspiration eXperiment (*GRAPEX*). Original spectral and thermal imagery data from *sUAS* were at 10 cm and 60 cm per pixel, respectively, and multiple spatial domain scales (3.6, 7.2, 14.4, and 30 m) were evaluated and compared against eddy covariance (*EC*) measurements. Results indicated that the *TSEB-2T* model is only slightly affected in the estimation of the net radiation (R_n) and the soil heat flux (G) at different spatial resolutions, while the sensible and latent heat fluxes (H and LE , respectively) are significantly affected by coarse grid sizes. The results indicated overestimation of H and underestimation of LE values, particularly at Landsat scale (30 m). This refers to the non-linear relationship between the land surface temperature (LST) and the normalized difference vegetation index ($NDVI$) at coarse model resolution. Another predominant reason for LE reduction in *TSEB-2T* was the decrease in the aerodynamic resistance (R_A), which is a function of the friction velocity (u_*) that varies with mean canopy height and roughness length. While a small increase in grid size can be implemented, this increase should be limited to less than twice the smallest row spacing present in the *sUAS* imagery. The results also indicated that the mean LE at field scale is reduced by 10% to 20% at coarser resolutions, while the with-in field variability in LE values decreased significantly at the larger grid sizes and ranged between approximately 15% and 45%. This implies that, while the field-scale values of LE are fairly reliable at larger grid sizes, the with-in field variability limits its use for precision agriculture applications.

Keywords: evapotranspiration (*ET*); *GRAPEX*; *sUAS*; remote sensing; Two Source Energy Balance (*TSEB*) model; contextual spatial domain/resolution; data aggregation; eddy covariance (*EC*).

2.1 Introduction

Evapotranspiration (*ET*) is a key factor in the hydrologic cycle and in irrigation demand. Conventional methods for estimating *ET*, such as lysimeters and flux towers, are limited to sampling small areas on the order of 10^1 to 10^3 m². For that, a more efficient method is needed as *ET* varies spatially under different micrometeorological and vegetative conditions. Accordingly, spatially distributed data are important for mapping *ET* variations over large areas, particularly in agricultural regions containing many of crop types and growth stages. In recent decades, remote sensing products from various platforms and at various spatial resolutions have been applied in modeling different environmental processes (e.g., surface energy fluxes, water and carbon balance, net primary productivity) [1]. Improved sensor systems and methods in remote sensing, and particularly the advent of small unmanned aerial systems (*sUAS*), have made these technologies a valuable source of spatial information for *ET* estimation at the canopy level. *sUAS* can offer spatial coverage with sub-meter-resolution imagery for mapping canopy and soil temperature, which are the key surface states for estimating *ET* [2]. While satellites are characterized by either coarse resolution and high temporal frequency or by high spatial resolution and low repeatability [3], *sUAS* technology, in addition to offering high-resolution data [4,5,6], can be described as “flexible in timing” [7]. This means that remotely sensed information can be obtained when needed or on demand using *sUAS*. For these reasons, various methods are under development to employ *sUAS* data for *ET* estimation [2].

Remote sensing is a valuable source for accessing land surface spatial information [8]. Nonetheless, spatial scaling is recognized as a challenging issue, particularly in surface-atmosphere exchange [8,9], environmental modeling, and agricultural management [10] applications and research. Previous studies by Brunsell and Gillies [11] and Giorgi [12] indicated that spatial scaling becomes more complex in cases of heterogeneous land surfaces, and homogeneity is less likely to be met in reality [13]. Various models have been developed to describe aerodynamic or energy balance fluxes, but these models assume homogeneity in terms of agricultural type, surface roughness, surface temperature, and meteorological condition [13,14]. Heat fluxes, including latent heat flux (LE) and sensible heat flux (H), are highly influenced by land surface heterogeneity [15]. Therefore, the variability in land cover within a pixel or model grid size can result in significant error in the mean pixel or grid heat flux estimation [16]. Vegetated areas with partial canopy cover will have underlying soil/substrate affecting the remotely sensed data, and hence, require models that explicitly consider the different effects of these two sources on energy exchange and sensor integration [2]. Typically, remotely sensed data at different resolutions are employed as an approximation to describe the spatial variability of the interaction between surface and atmosphere [11]. Current and future developments in remote sensing, with information spanning from sub-meters to kilometers, are making upscaling (data aggregation) a crucial issue in scientific and methodological advances. This is particularly true for understanding the physics behind climate, weather, and the surface energy balance [13,17].

In general, spatial aggregation can be performed under two different procedures: forcing inputs to a coarser resolution or aggregating the derived fluxes from initial high-

resolution data (contextual spatial domain). Long et al. [18] pointed out that forcing spatial data aggregation from Landsat bands to *MODIS* (Moderate Resolution Imaging Spectroradiometer) resolution results in different statistical and spatial properties in *ET* estimates than at the original Landsat resolution. Study cases of *LE* resulted in inaccuracies [19,20] due to a reduction in surface variability at *MODIS* scale [11]. Moreover, the structure of vegetation and aerodynamic roughness influence the aggregation of turbulent fluxes and produce bias when *MODIS* data is used [15]. On the other hand, Bian and Butler [21] showed that low-resolution data could retain the statistical characteristics of the original data using specific aggregation techniques such as average and median. In addition, the spatial aggregation of *ET* inputs removes the effects of heterogeneity on the land surface. Still, scaling up energy fluxes from Landsat to *MODIS* scale is necessary in large-scale environmental models [22]. However, Landsat resolution is needed for validating modeled outputs using flux towers [23].

Several methods exist for spatial aggregation of *ET* data, but they are in the exploratory stage [24]. Ershadi et al. [14] demonstrated that *ET* results reduced by 15% when aggregating Landsat TM (Thematic Mapper) imagery by 50% using the Surface Energy Balance System (*SEBS*) model. The *ET* reduction was caused by the decrease in roughness parameterization [14]. This outcome was also supported by Brunsell and Gillies [11], who indicated that the land surface heterogeneity is highly influenced by the input forcing aggregation of Landsat TM data affecting the surface heat fluxes. In contrast, French et al. [25] found no significant difference in daily *ET* estimates when they used *METRIC* (Mapping EvapoTranspiration at high Resolution with Internalized Calibration) model and upscaled data acquired by aircraft to Landsat resolution. However, another study by Kustas

and Norman [16] that used a detailed soil-vegetation atmosphere simulation model along with the thermal-based Two Source Energy balance model found that varying the degree of heterogeneity within a pixel, either in terms of surface roughness, moisture status, or a combination thereof, can have a significant impact on the pixel aggregated flux.

A key question related to data aggregation was raised by Su et al. [26]: “How does the level of aggregation affect surface energy fluxes as fluxes are aggregated from the resolution at which they are observed to the coarse grid cell size of the atmospheric model?”. The study conducted by Guzinska and Nieto [27] aimed to estimate *ET* using a Two Source Energy Balance (*TSEB*) model. They reported that sharpening Sentinel 3 thermal imagery at 1-km pixel resolution to higher resolution (20 m) visible/near-infrared is indicative of the main issue of the lack of fine resolution thermal-IR (InfraRed) data for input to remote sensing-based *ET* models, particularly when applied to agricultural areas. In addition, Niu et al. [28] indicated that the *TSEB* model *ET* output using *sUAS* imagery gives more reliable estimates compared to coarse-resolution data because the model can separate between canopy and soil components. Moreover, most previous studies exploring the effects of sensor resolution on modeled *ET* have used semi-empirical models (e.g., Surface Energy Balance Algorithm for Land (*SEBAL*) model) [14], while physically-based *ET* models are required to quantify changes in the water and energy exchange due to changes in fractional vegetation cover, roughness, canopy structure, phenology, etc. that are occurring at plant scale [29]. In addition, it is common knowledge that vineyards and orchard fields do not have the same row spacing. The spacing varies from 6 ft to 12 ft for vineyards [30] and from 8 ft to 18 ft for orchards [31].

In the same context as the investigations discussed above on spatial resolution and surface heterogeneity, this study investigates the impact of grid-size resolution on *LE* outputs from *TSEB* model using the component soil/substrate and canopy temperature version (*TSEB-2T*) model applied to a complex agricultural canopy, namely a vineyard in California's Central Valley. The study directly quantifies the effect of sensor resolution on key *TSEB* model inputs (i.e., land surface temperature (*LST*), leaf area index (*LAI*), canopy height (h_c), canopy height-to-width ratio (w_c/h_c), and fractional cover (f_c)) for estimating surface energy balance/*ET*. High-resolution optical and thermal data were acquired by an *sUAS* platform for vine and cover crop phenological stages at several different times during the day. In this research effort, the topics investigated include determining (a) whether the separation between canopy and soil/substrate temperature (T_c and T_s , respectively) using *TSEB-2T* is valid for coarse spatial domains (e.g., towards Landsat scale); (b) the effect of spatial resolution of *TSEB-2T* inputs on the magnitude and spatial variation of *LE*; (c) if the different spatial domain scales/pixel resolutions under study (3.6, 7.2, 14.4 and 30 m) have an impact on the magnitude of the *LE* and quantify the discrepancies as a function of resolution.

2.1.1 *TSEB-2T* Model

TSEB-2T is a physically based approach developed by Norman et al. [32] that explicitly accommodates the difference between aerodynamic and radiometric surface temperature that affect the radiative and convective exchange of energy between soil and canopy systems and the lower atmosphere. The main concept underpinning the *TSEB-2T* approach is modeling of the partitioning of radiative and turbulent energy fluxes between canopy and soil systems. In this case, *H* is partitioned between soil and canopy, which is

dependent mainly on T_c and T_s differences with the overlying atmosphere and their respective aerodynamic coupling.

As shown in the Figure 2.1, the *TSEB-2T* model separates the surface energy balance between soil and vegetation as follows:

$$R_n = LE + H + G, \quad (2.1)$$

$$R_{nc} = H_c + LE_c, \quad (2.2)$$

$$R_{ns} = H_s + LE_s + G, \quad (2.3)$$

where R_n is the net radiation, H is the sensible heat flux, LE is the latent heat flux, and G is the soil heat flux. All units of fluxes are in W/m^2 . Subscripts of c and s represent the canopy and soil components, respectively. Because T_s and T_c can be derived from the *LST* with a high enough resolution of optical data, energy fluxes (R_n , H) can be calculated directly from the component temperatures (T_c and T_s) and estimated aerodynamic resistances of canopy and soil components, while G is parametrized as a portion of soil net radiation (R_{ns}). LE_c and LE_s are solved as residuals when (T_c and T_s) observations are available.

$$G = c_G R_{ns} \quad (2.4)$$

where c_G is an empirical coefficient changing over the daytime [2].

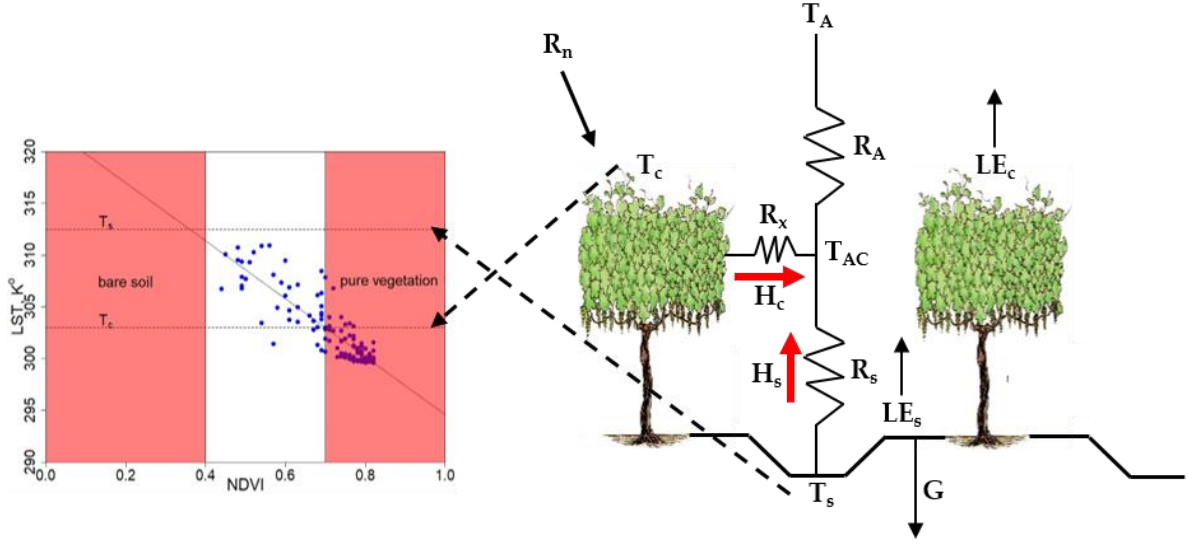


Figure 2.1 Schematic representation of *TSEB-2T* model.

To estimate the sensible heat flux for vegetation and canopy, Norman et al. [32] proposed a series of soil-vegetation resistance network as illustrated in Figure 2.1:

$$H = H_c + H_s = \rho_{air} C_p \frac{T_{AC} - T_A}{R_A} = \rho_{air} C_p \left[\frac{T_c - T_{AC}}{R_x} + \frac{T_s - T_{AC}}{R_s} \right] \quad (2.5)$$

$$R_A = \frac{\ln \left(\frac{z_T - d_0}{z_{0H}} \right) - \psi_h \left(\frac{z_T - d_0}{L} \right) + \psi_h \left(\frac{z_{0H}}{L} \right)}{\kappa' u_*} \quad (2.6)$$

where ρ_{air} is the air density (kg/m^3); C_p is the heat capacity of the air at constant pressure ($\text{J}/(\text{kg} \cdot \text{K})$); T_c and T_s are canopy and soil temperature (K), respectively; T_{AC} is the temperature of canopy-air space (K); and T_A is the temperature of air (K). R_A is the aerodynamic resistance to heat transport from the soil/canopy system (s/m), R_x is the boundary layer resistance of the canopy leaves (s/m), R_s is the aerodynamic resistance to heat transport in the boundary layer close to the soil surface (s/m), z_T is the measurement height for T_A , z_{0H} is the roughness length for heat transport, d_0 is the zero-plane displacement height (m), L is the Monin-Obukhov length (m), $\kappa' = 0.4$ is the von

Karman's constant, u_* is the friction velocity (m/s), and Ψ_h is the adiabatic correction factor for the momentum.

Key factors, including T_s and T_c , LAI , f_c , w_c/h_c , and h_c , are required as inputs for the *TSEB* model to parameterize the radiative and convective flux exchanges between soil/substrate and canopy. Other parameters related to micrometeorological data are also needed to run the model. In the study conducted by Chirouze et al. [33] comparing different remote sensing *ET* models, results indicated that *TSEB* is a better model for *ET* estimation compared to others, being less sensitive to roughness parameters. This lack of sensitivity to roughness parameters was also recently verified for vineyards by Alfieri et al. [34]. The *TSEB* model has been extensively tested for years over agroecosystems [35,36,37], natural ecosystems [38,39], and wetlands [40,41].

TSEB-2T was originally developed and evaluated by Kustas and Norman [42] using multiple thermal-IR radiometer viewing angles and was further refined and tested by Nieto et al. [2] applied to high resolution imagery from *sUAS* or other airborne sources. They found that *TSEB-2T* gave better agreement with tower fluxes compared to other versions of *TSEB*, including *TSEB-PT* (Priestly-Taylor), *TSEB-DTD* (Dual-time-difference), and *TSEB-2T-DMS* (Data-mining sharpening of temperature). *TSEB-PT* is one version of the *TSEB* model that assumes a composite radiometric temperature (T_{rad}) containing temperature contribution from the canopy and soil/substrate, which is typically provided by the radiometer. The decomposition of radiometric temperature (T_{rad}) between plant canopy and soil/substrate is based on f_c . *TSEB-DTD* is a further development of the *TSEB-PT* model described by Norman et al. [43]. The *TSEB-DTD* model is similar to the *TSEB-PT* model in that it divides the composite T_{rad} into T_c and T_s . However, *TSEB-DTD* uses

two observations of T_{rad} : the first observation obtained 1.5 h after the sunrise ($T_{rad,0}$) and the second one during the daytime ($T_{rad,1}$). This version is less sensitive to errors in absolute radiometric surface temperature or the use of non-local air temperature observations. *TSEB-2T-DMS* partitions T_s and T_c using a data-mining fusion algorithm [44] to sharpen the original *LST* to be similar to the optical data, which would allow a better discrimination between T_s and T_c .

The Nieto et al. [2] *TSEB-2T* approach is a contextual *TSEB* that estimates T_s and T_c from composite *LST* imagery using the relationship between vegetation index (*VI*) and *LST* for extracting T_s and T_c within a spatial domain. T_s and T_c are calculated by averaging the temperature of pixels that are considered pure soil/substrate and pure canopy in a contextual spatial domain, namely, a two-dimensional plot of *LST* versus *VI*, such as Normalized Difference Vegetation Index (*NDVI*) (see Figure 2.1). That is, each pixel of the spatial domain is assigned based on T_c and T_s corresponding to the average temperature of the 0.6-m grids that are considered pure vegetation and bare soil, respectively. Both soil/substrate or canopy features are determined using *NDVI* threshold values (or any other vegetation index). The selection criterion for detecting the *NDVI* threshold of pure soil for bare soil interrows or, for most of the growing season, a soil senescent and cover crop stubble mixture (substrate) ($NDVI_s$) can be further supported by other sources such as *NDVI* value from a *NDVI-LAI* curve when *LAI* in the interrows is nearly zero. The pure vine canopy *NDVI* threshold ($NDVI_v$) can be calculated as the mean value of pixels identified as pure vegetation in a binary (soil-vegetation) classification of a multispectral image. In cases of very dense vegetation where pure soil pixels do not exist or sparse vegetation lacking pure vegetation pixels inside the spatial domain, a linear fit between *LST* and *NDVI*

can be developed where T_s and T_c can be estimated by previously defining the $NDVI$ thresholds of canopy and bare soil (Figure 2.1).

2.1.2 *TSEB-2T* Main Inputs

2.1.2.1 Leaf Area Index (*LAI*)

LAI is one of the key inputs in *TSEB* influencing the computation of *ET* as leaves distribution is the driving factor in energy and mass exchange in this model. *LAI* is also difficult to acquire using ground-based leaf-scale measurements, due to the time-intensive effort required [45], complications using indirect methods in complex canopies, and lack of any spatial extent for mapping, even at the field scale [46]. Therefore, considerable efforts have been devoted to developing remote sensing approaches to estimate *LAI* [47].

Estimating spatial distribution of *LAI* is challenging in vineyards, with their rows of vines and interrows with little to no vegetation. A previous study conducted by Johnson [48] evaluated the *LAI-NDVI* relationship in vineyards using *IKONOS* satellite imagery with 1-m pixel resolution and comparing *NDVI* to ground-based *LAI* measurements. They concluded that *LAI* can be computed from *NDVI* using simple linear regression for the vineyard they studied planted with red grape in six blocks of different planting density, trellis, age, and cultivar. In addition, Johnson et al. [48] and Dobrowski et al. [49] showed that remotely sensed indices of soil and vegetation can be used to estimate *LAI*. However, a study by Fang [50] indicated that limitations exist when using vegetation indices (*VI*s) to describe the spatially distributed *LAI* due to sensitivity of the *LAI-VI*s relationship to vegetation type and substrate/soil type, and hence, will not be stable or applicable over large areas. Indeed, operational satellite retrievals of *LAI*, particularly for vineyards [51], have a level of uncertainty that could affect modeling fluxes using *TSEB*. Furthermore,

canopy phenological properties (i.e., chlorophyll content and average leaf angle), along with other factors such as atmospheric scattering, soil reflectance, and the effects of mixed pixel due to a composite of soil and vegetation that changes with time and from one place to another, affect the accuracy of *LAI* estimation [47]. To improve the *LAI-VIs* relationships, numerous studies have been conducted to estimate *LAI* using statistical approaches. Artificial Neural Network (*ANN*) was very promising and is simple to use [50]; however, this method does not allow for standardization of the *LAI* estimation [52]. As described by Gonsamo and Pellikka [53], there is currently no standard or arbitrary characteristic parameters, specific vegetation types, or data sources can be employed for *LAI* estimation. Thus, researchers must develop custom models by considering the sensitivity of parameters to *LAI* within an expected range [53].

2.1.2.2 Canopy Height (h_c)

The h_c value is representative (mean) over the area of interest, but it can also be incorporated from spatial sources. An estimate of h_c can be produced using high-resolution images from *sUAS* and other airborne sources processed with structure-from-motion (*SfM*) methods in Agisoft or Pix4D, among others, along with digital elevation models (*DEM*) and point clouds (*LiDAR*). The value of h_c is required for the *TSEB-2T* model to estimate surface aerodynamic roughness and radiation transmission in row crops and to calculate the foliage density, which are all required for the canopy wind attenuation model (Figure 2.2).

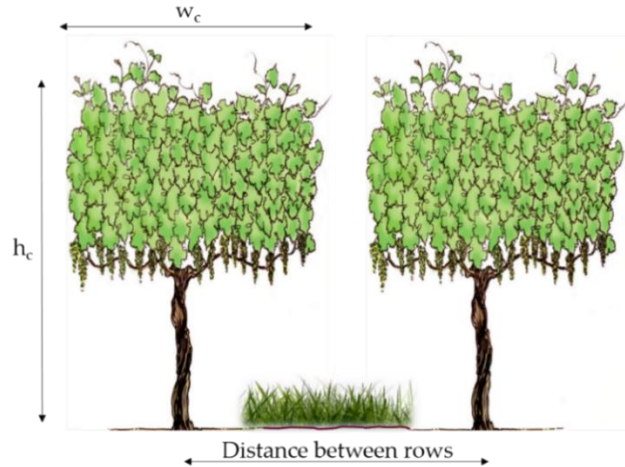


Figure 2.2 Schematic diagram for canopy w_c/h_c ratio.

2.1.2.3 Fractional Cover (f_c) and Canopy Width (w_c)

Fractional cover (f_c) is the proportional area of vine for each spatial domain under analysis, where values vary from 0 through 1. f_c is used to estimate w_c and the clumping index, which is a factor to adjust the remotely sensed LAI value, which is assumed to be uniformly distributed (homogeneous) over the landscape instead of being clumped [54]. These are used to estimate the actual canopy gap fraction, which is greater than the homogenous case. It is required as input for the radiation transmission and wind extinction algorithms through the canopy layer. The magnitude of w_c is a length scale representing the area occupied by vine leaves along the vine row, which varies spatially and temporally based on phenology and management (i.e., vine manipulation via the trellis system and pruning) (Figure 2.2).

2.1.2.4 w_c/h_c Ratio

In *TSEB* and *TSEB-2T* models, the w_c/h_c ratio is required as input to the radiation transmission and wind extinction algorithms through the canopy layer developed for

vineyards [2,55]. The w_c/h_c ratio value is obtained by simply calculating canopy width over canopy height (Figure 2.2).

2.2 Materials and Methods

The methodology to assess the impact of changes in the contextual spatial domain for the *TSEB-2T* model is graphically presented in Figure 2.3. The analysis was performed for wine grape growing seasons (May–August) using different spatial domain scales.

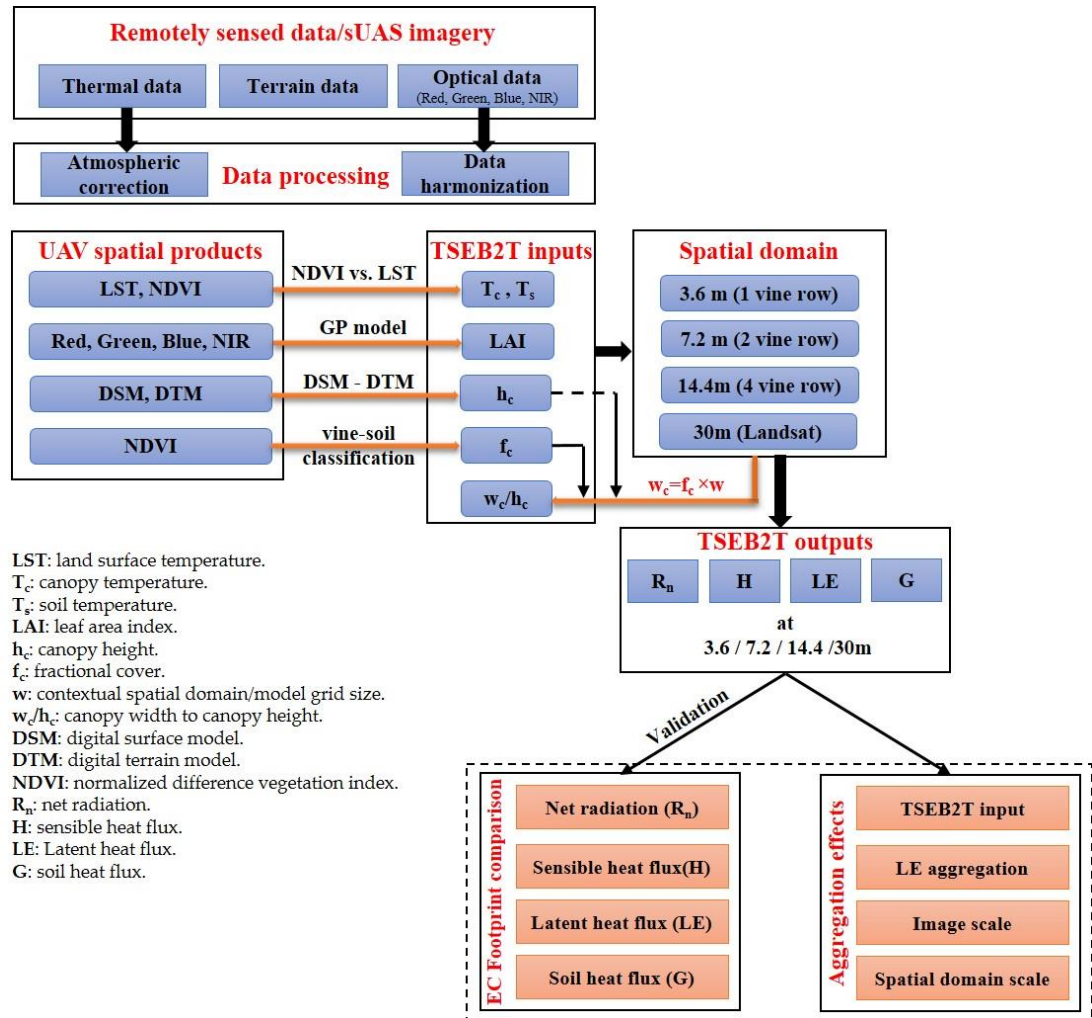


Figure 2.3 Study methodology for assessing the impact of the *TSEB-2T* contextual spatial domain.

2.2.1 Study Area and Data Sources

The study site is located near Lodi, California (38.29° N, 121.12° W) with an area of approximately 150 ha. The two vineyard blocks (north and south) are part of the Sierra Loma vineyard ranch (Figure 2.4). The north block was planted in 2009, while the south block was implemented in 2011, leading to different levels of vine maturity, and hence, biomass and grape production. Both vineyards are managed cooperatively by Pacific Agri-Lands Management. The plantation structure in both fields is the same, with vine rows having east–west orientation with a row width of 3.35 m (11 feet). A cover crop grows in the interrows, occupying ~ 2 m, with bare soil strips along the vine rows spanning ~ 0.7 m. The purpose of the cover crop is to deplete plant available water in the interrows from the fall and winter precipitation in order to control vine growth in the spring by irrigation. Typically, the vine height varies between 2 m and 2.5 m above ground level (*agl*) and vine biomass is concentrated mainly in the upper half of the vine canopy height. The actual vine canopy width varies spatially and temporally due to vine management practices. This study site is a part of the Grape Remote Sensing Atmospheric Profile and Evapotranspiration eXperiment (*GRAPEX*) project run by the USDA Agricultural Research Service in collaboration with E&J Gallo Winery, Utah State University, University of California in Davis, and others [56].

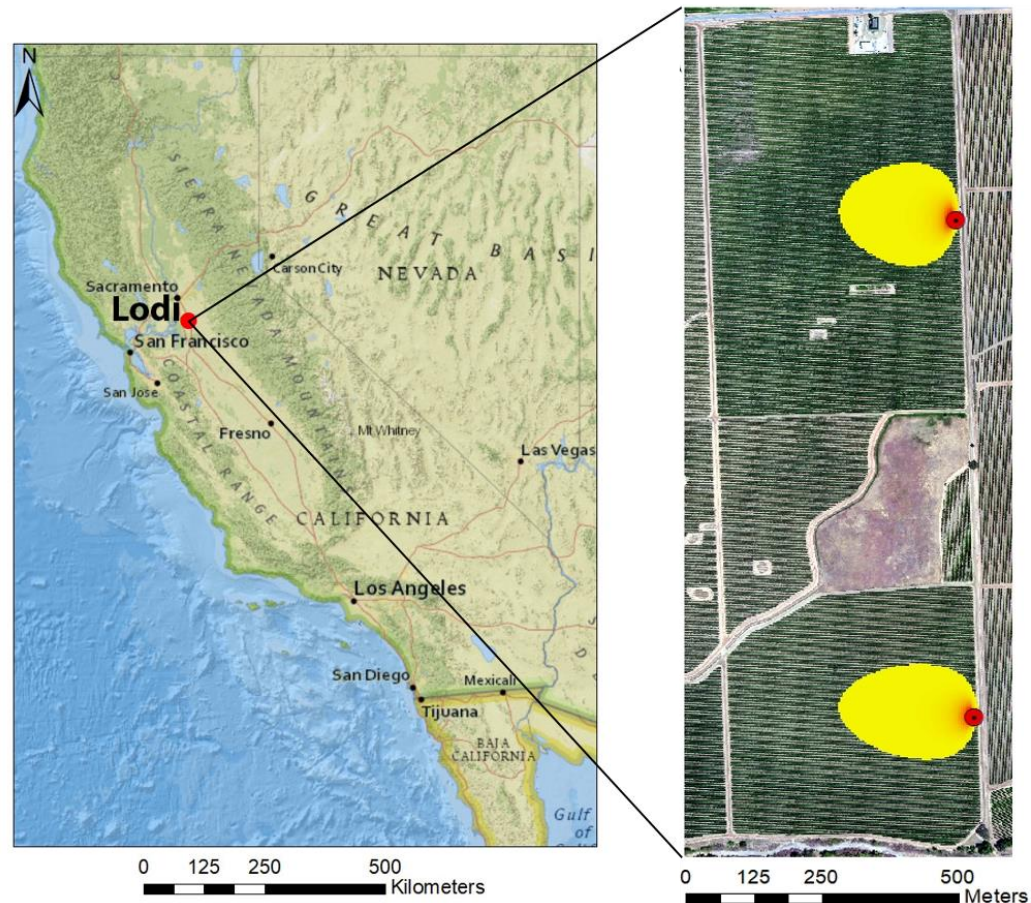


Figure 2.4 Layout of study area in Lodi, California, locations of *EC* towers and example of 90% of *EC* footprint at afternoon for June 02, 2015.

Flights campaigns were conducted by the *AggieAir sUAS* Program at Utah State University (<https://uwrl.usu.edu/aggieair/>). Optical and thermal high-resolution imagery of the study site were collected from different flights in 2014, 2015, and 2016. Vegetative and soil conditions changed between the field campaigns. The 2016 flight imagery represents the early part of the growing season, around the time phenologically of fruit set, while other flights in 2014 and 2015 represent full vine canopy development and grape vine phenology in the pre- and post-veraison stages. Table 2.1 lists information concerning the different flights. The pixel resolution of the *sUAS* imagery collected is 10 cm and 60 cm for the optical and thermal bands, respectively. The spectral range of the optical data is

similar to Landsat and includes visible bands (red, green, and blue) as well as near-infrared. However, the thermal band is different than Landsat, having a bandwidth spanning from 7 to 14 μm [57]. Thermal data, acquired using a lightweight micro-bolometer camera, were radiometrically calibrated [58].

Table 2.1 Dates and times of *AggieAir GRAPEX* flights used in this study.

Flight Date	Landsat time PST	Afternoon PST	Midafternoon PST
August 09, 2014	10:41 am		-
June 02, 2015	10:43 am	14:07 pm	-
July 11, 2015	10:35 am	14:14 pm	
May 02, 2016	-	12:05 pm	15:04 pm
May 03, 2016	-	12:48 pm	-

To evaluate the *ET* performance at different spatial domain scales, two eddy covariance (*EC*) flux systems were deployed for the measurements of turbulent fluxes, including *LE* and *H*, and the available energy terms of R_n and G . Both towers are located at the eastern edge of the fields, due to predominant winds from the west. Ground measurements, including soil temperature and soil moisture were also collected. A complete listing of all measurements on the towers is given by Kustas et al. [56]. Details of the post processing of the *EC* data as well as the available energy measurements are provided by Alfieri et al. and Agam et al. [59,60].

EC micrometeorological data also included wind speed, air temperature, vapor pressure, air pressure, and shortwave radiation. Hourly average values of these atmospheric forcing variables, as well as the components of the surface energy balance, were

computed. Table 2.2 illustrates the in-situ micrometeorological parameters and the name of the instruments used for the measurements.

Table 2.2 Description of in-situ micrometeorological measurements in this study.

ID	Micrometeorological parameters	Instrument name¹	Elevation
1	Water vapor concentration	Infrared gas analyzer (EC150, Campbell Scientific, Logan, Utah)	5 m <i>agl</i>
2	Wind velocity	Sonic anemometer (CSAT3, Campbell Scientific)	5 m <i>agl</i>
3	Net radiation	4-way radiometer (CNR-1, Kipp and Zonen, Delft, Netherlands)	6 m <i>agl</i>
4	Air temperature	Gill shielded temperature (Vaisala, Helsinki, Finland)	5 m <i>agl</i>
5	Water vapor pressure	Humidity probe (HMP45C, Vaisala, Helsinki, Finland)	5 m <i>agl</i>
6	Soil heat flux	Five plates (HFT-3, Radiation Energy Balance Systems, Bellevue, Washington)	-8 cm
7	Soil temperature	Thermocouples	-2 cm
8	Soil moisture	Soil moisture probe (HydraProbe, Stevens Water Monitoring Systems, Portland, Oregon)	-5 cm

¹ The use of trade, firm, or corporation names in this article is for the information and convenience of the reader. Such use does not constitute official endorsement or approval by the US Department of Agriculture or the Agricultural Research Service of any product or service to the exclusion of others that may be suitable.

Given the high fluctuation of atmospheric conditions during the daytime, the flux footprint or contributing source area of each *EC* tower was estimated for the hourly period encompassing *sUAS* flight campaigns using the two-dimensional (2D) flux footprint model developed recently by Kljun et al. [61]. Because a 100% *EC* footprint fetch could extend over the study area, a 90% footprint area (90% cutoff) was used for analysis. Then, the weighted footprint area was divided by 0.9.

2.2.2 Data Processing

In this study, images were acquired remotely by *sUAS*, and the data were terrain corrected using georeferencing based on ground control points (*GCPs*). Furthermore, both thermal and optical data were atmospherically corrected.

2.2.2.1 Thermal Data

Torres-Rua [57] indicated that the thermal data obtained from the *sUAS* thermal sensors in this study are adversely affected by changes in transmissivity and atmospheric radiance. For this reason, ground measurements of temperature were collected in the same timeframe as the *sUAS* flight and compared with the imagery to calibrate the thermal image data. More details about the calibration of temperature imagery related to this study can be found in Torres-Rua [57].

2.2.2.2 Optical Data

Radiometric agreement between remotely sensed data from different platforms constitutes one of the major challenges in image processing. Therefore, in this research, the images acquired by *sUAS* were upscaled and harmonized with Landsat using the point spread function (*PSF*). More details related to *sUAS* data harmonization can be found in Hassan-Esfahani et al. [62].

2.2.3 Energy Balance Closure Adjustment Methods for *EC*

While the *EC* technique provides measurements of turbulent fluxes H and LE , a lack of energy balance closure with the available energy terms R_n and G [63] is well documented. This results in $R_n - G > LE + H$ [64,65], and the computed closure ratio (CR) evaluates the energy balance discrepancy, $CR = (H + LE)/(R_n - G)$. This ratio varies

during the daytime, but for the *sUAS* flights [55] it was found to be above 0.8, except for the May 2 afternoon flight where it fell to around 0.7.

To avoid any bias when comparing the energy balance models with *EC* field measurements, the energy closure issue needs to be handled and resolved. Twine et al. [66] suggested a method for energy balance closure that assumes the Bowen ratio (H/LE) before and after adjustment are the same, while considering both R_n and G as reliable measurements. A modified H and LE can be calculated as:

$$LE^* = \frac{(R_n - G)}{(B + 1)} \quad (2.7)$$

$$H^* = \frac{(R_n - G)}{\left(\frac{1}{B} + 1\right)} \quad (2.8)$$

where LE^* and H^* denotes the closure adjusted latent and sensible heat flux, respectively.

2.2.4 Contextual Spatial Domain

The representative *TSEB-2T* modeling grid size for the vineyard blocks was taken at 3.6 m, which corresponds to encompassing 6 x 6 grid or 36 *sUAS* thermal pixels having a resolution of 0.6 m. At this grid size, the inputs to *TSEB-2T* incorporate the thermal-IR and optical bands of a vine row and adjusted interrows having a length scale of 3.35 m. Larger spatial domain scales were considered in this study, including 7.2 m, 14.4 m, and 30 m, to investigate the influence of domain size on the *TSEB-2T* estimates. These selected values correspond to multiple vine rows spacing of 7.2 m (two rows), 14.4 m (four rows), and 30 m (Landsat scale—nine rows).

2.2.5 TSEB-2T Inputs

The *TSEB-2T* model developed by Nieto et al. [2] and implemented in Python language and is available at <https://github.com/hectornieto/pyTSEB>.

2.2.5.1 Leaf Area Index (*LAI*)

To assess the spatial heterogeneity of *LAI*, an approach was developed in this study to calculate *LAI* using a genetic programming (*GP*) model using the Eureka software. The *GP* model associated *sUAS* imagery and *LAI* ground measurements collected with an indirect method using (*LAI-2200*, *LI-COR*, Lincoln, Nebraska) plant canopy analyzer measurements at several locations within the northern and southern vineyards with additional validation using destructive *LAI* sampling at several locations [46]. Before performing the *GP* model calculations, imagery features were classified into two categories, vine and interrow, and then statistical calculations were separately carried out for the optical properties of each category. The main optical reflectance used in this analysis comprise the original bands (red (*R*), green (*G*), blue (*B*), and near-infrared (*NIR*)), along with two conventional *VI*s (*NDVI* and *NIR/R*). Statistical computations were performed using the fine-resolution data inside the spatial domain scales (3.6 m, 7.2 m, 14.4 m, and 30 m), which included the maximum, minimum, area, mean, standard deviation, and sum. The *GP* model integrates all of these corresponding statistics to construct a relationship to *LAI* observations.

2.2.5.2 Canopy Height (h_c)

Spatial data from the digital terrain model (*DTM*) [67] and digital surface model (*DSM*) were aggregated into multiple spatial scales by employing a simple averaging

method; then, h_c was calculated using the expression: $h_c = DSM - DTM$. For example, in the case of a 7.2-m grid, the average values of DSM and DTM , $DSM_{(7.2)}$, and $DTM_{(7.2)}$, respectively, were computed inside the grid window, then the height of the canopy was computed as: $h_{c(7.2)} = DSM_{(7.2)} - DTM_{(7.2)}$.

2.2.5.3 Fractional Cover (f_c) and Canopy Width (w_c)

The north and south vineyard blocks were classified into two categories, vine and interrow, based on $NDVI$. Then the vine area inside each spatial domain was calculated and divided by the total area of the grid to calculate the f_c . w_c inside each spatial domain was computed using f_c and the width of the grid (w) under analysis, i.e., $w_c = f_c \times w$. To calculate the representative width of the vine canopy, the total width was rescaled and standardized at multiple spatial domain scales, depending on the number of rows inside each grid. For example, in the case of a 3.6-m grid, one vine row was counted inside, while in a 7.2-m grid, the number of rows was doubled.

2.2.5.4 w_c/h_c Ratio

w_c/h_c was calculated by simply dividing canopy width by canopy height at each contextual spatial domain.

2.2.6 Goodness-of-Fit Statistics

Evaluating the performance of the *TSEB-2T* model with the *sUAS* imagery for the four different modeling grid resolutions involved comparing the estimated fluxes with measurements from the *EC* towers. Computed statistical metrics included the root mean square error (*RMSE*), the normalized root mean square error (*NRMSE*), mean absolute error (*MAE*), mean absolute percentage error (*MAPE*), and Nash–Sutcliffe efficiency coefficient

(*NSE*). A value of $NSE = 1$ indicates perfect agreement between modeled and observed flux, while NSE approaching 0 means that the agreement is very poor, and $NSE < 0$ indicates unacceptable performance [68]. These statistical measurements are calculated as follows using LE as the flux:

$$RMSE = \sqrt{\frac{1}{N} \sum_{i=1}^N (LE_{m,i} - LE_{o,i})^2} \quad (2.9)$$

$$NRMSE = \frac{RMSE}{\sigma_o} \quad (2.10)$$

$$MAE = \frac{\sum_{i=1}^n |LE_{m,i} - LE_{o,i}|}{n} \quad (2.11)$$

$$MAPE = \frac{\sum_{i=1}^N \left| \frac{LE_{m,i} - LE_{o,i}}{LE_{o,i}} \right| * 100}{n} \quad (2.12)$$

$$NSE = 1 - \frac{\sum_{i=1}^n (LE_{m,i} - LE_{o,i})^2}{\sum_{i=1}^n (LE_{o,i} - \bar{LE}_{o,i})^2} \quad (2.13)$$

where LE_m denotes the modeled latent heat flux obtained from the *TSEB-2T* aggregated up for the estimated flux footprint/source area, LE_o denotes the observed values from the *EC* tower, and n represents the number of observations, σ_o denotes the standard deviation of observed values.

LE was used for evaluating the impact of spatial resolution or grid size on modeled fluxes. At field scale, the evaluation is done using the spatial mean and coefficient of variation (*CV*) statistics. For LE statistical characteristics, frequency and cumulative distribution curves were used. Finally, to evaluate the effect of aggregating LE at 3.6 m, 7.2 m, 14.4 m, and Landsat scale, relative difference (relative error) was used. Relative difference (relative error) is defined as the root mean square error (*RMSE*) between the

aggregated resolution and its reference grid size resolution of 3.6×3.6 m divided by the spatial mean (μ) value computed from the reference grid size ($3.6 \text{ m} \times 3.6 \text{ m}$), i.e., $E_r = RMSE/\mu$ [14]. Each grid value of aggregated data was compared to the $n \times n$ set of reference scale or resolution (3.6 m) grid using E_r .

2.3 Results and Discussion

2.3.1 TSEB-2T Contextual Spatial Domains Validation

2.3.1.1 EC Footprint Estimation

The results of footprint analysis using the 2D flux model developed by Kljun et al. [61] and described in section 2.2.1 are shown in Figure 2.5 for the different *sUAS* flights.

The orientation and size of each flux footprint/source area depends on the micrometeorological conditions at the site measured by the *EC* towers, which include the turbulence fluxes, friction velocity (u_*), and wind speed, which affect atmospheric stability, and canopy and *EC* measurement height, which affect the effective sampling height and wind direction that affects the orientation of the footprint. The total statistical weight of the footprint is taken to equal unity, although the actual area computed by the footprint model represents 90% of the contribution since the additional 10% essentially makes no measurable contribution. To compare the fluxes computed by the *TSEB-2T* model at the different spatial resolutions with the *EC* measurements, the source area estimated by the footprint model was multiplied by the corresponding modeled fluxes (R_n , H , LE , G) using *ArcGIS10.6*. Then, a comparison between the weighted fluxes at the different spatial resolutions or grid sizes from the *TSEB-2T* version of *TSEB* and *EC* measurements was performed to assess model performance.

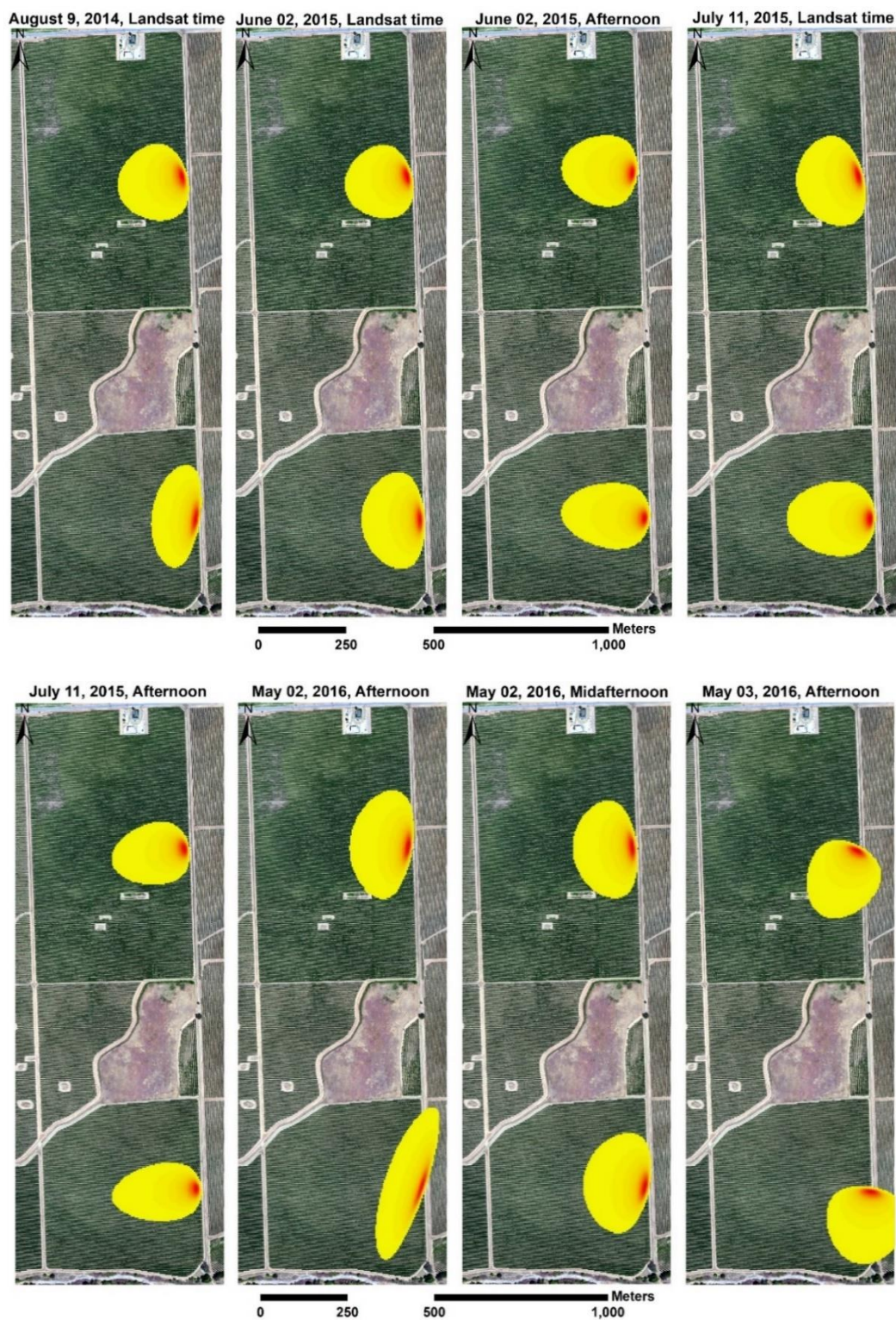


Figure 2.5 Layout of 90% *EC* footprints for two towers at different times considered by this study.

2.3.1.2 Statistical Performance

Table 2.3 lists the goodness-of-fit statistics between the energy fluxes using *TSEB-2T* at different spatial resolutions and *EC* tower observations, while Figure 2.6 shows the relationship between the modeled and measured fluxes. The results indicate a significant deterioration in model performance at the 30-m grid size. A major factor that may be responsible for this poor performance in the *TSEB-2T* model at 30-m resolution is that the size and dimension of the *EC* source area estimated by the footprint model cannot incorporate a representative range in the spatial variability in the fluxes at 30-m resolution. This conclusion agrees with a previous study conducted by Song et al. [69] that showed a major problem in comparing modeled and measured fluxes when there is a mismatch in pixel resolution or model grid size in the remotely sensed *ET* output and in the source area contributing to the *EC* tower measurements in a heterogeneous landscape.

Results in Table 2.3 also indicate that R_n and G across multiple aggregated grids demonstrated a close agreement between the *TSEB-2T* output and observed measurements, as indicated by lower *MAE* and *MAPE* with quite constant correlation (R^2). The *MAE* and *MAPE* in the R_n estimate at grid sizes of 3.6 m, 7.2 m, and 14.4 m accounted for less than 25 W/m² and 5%, respectively. However, at Landsat scale the *MAE* increased slightly to 29 W/m². A similar result was obtained for H , where *MAE* at the finer resolutions yielded values less than 45 W/m², while the coarser grid size of 30 m yielded a larger *MAE* of nearly 80 W/m². As shown in Table 2.3, the correlation of H is higher than G and LE , except for 30-m resolution/model grid. This implies that the performance of the 30-m resolution is different compared to the 3.6-m, 7.2-m, and 14.4-m resolutions. The results for LE indicated good agreement with the flux measurements at 3.6-m, 7.2-m, and 14.4-m

modeling grid sizes, while at the 30-m resolution, the *MAE* value was around 85 W/m². As demonstrated in Figure 2.6 (d), all values of *LE* are underestimated (below 1:1 line) with an NSE coefficient of 0.2. Furthermore, the highest *NRMSE* values were observed for *LE*, compared with other surface fluxes, particularly at 30-m resolution. The lowest *NRMSE* was obtained for *R_n* across different spatial domains/model grids.

Table 2.3 Goodness-of-fit statistics between the eddy covariance and the *TSEB-2T* fluxes at different spatial scales (3.6 m, 7.2 m, 14 m, and 30 m).

Spatial domain	Fluxes	RMSE (W/m ²)	NRMSE	MAE (W/m ²)	MAPE (%)	NSE	R ²
3.6m	<i>R_n</i>	28	0.3	25	5	0.9	0.94
	<i>LE</i>	69	1.2	58	20	0.5	0.49
	<i>H</i>	54	0.8	41	26	0.7	0.67
	<i>G</i>	34	0.9	30	51	0.6	0.56
7.2m	<i>R_n</i>	27	0.3	24	4	0.9	0.94
	<i>LE</i>	66	1.2	56	19	0.5	0.53
	<i>H</i>	51	0.7	36	24	0.7	0.67
	<i>G</i>	33	0.8	30	50	0.6	0.58
14.4m	<i>R_n</i>	25	0.3	20	4	0.9	0.95
	<i>LE</i>	79	1.4	56	18	0.1	0.21
	<i>H</i>	48	0.7	35	26	0.6	0.69
	<i>G</i>	32	0.8	29	49	0.6	0.59
30m	<i>R_n</i>	34	0.4	29	5	0.9	0.96
	<i>LE</i>	101	1.8	86	30	0.2	0.53
	<i>H</i>	93	1.3	78	67	-0.1	0.23
	<i>G</i>	31	0.8	28	48	0.6	0.60

With the *TSEB-2T* model and other remote sensing-based models using thermal-IR as the boundary condition, *LE* is solved as the residual component of the surface energy balance, $LE = R_n - H - G$. Therefore, an error in the calculation of energy fluxes (*R_n*, *H*,

and G) adversely affects the estimation of LE . Based on Figure 2.6, the LE estimation (or bias) is mainly influenced by the estimation of H . This conclusion was also reached by Kustas et al. [70], who showed the discrepancies between modeled and measured LE is due in large part, up to approximately 90%, to errors in modeled H .

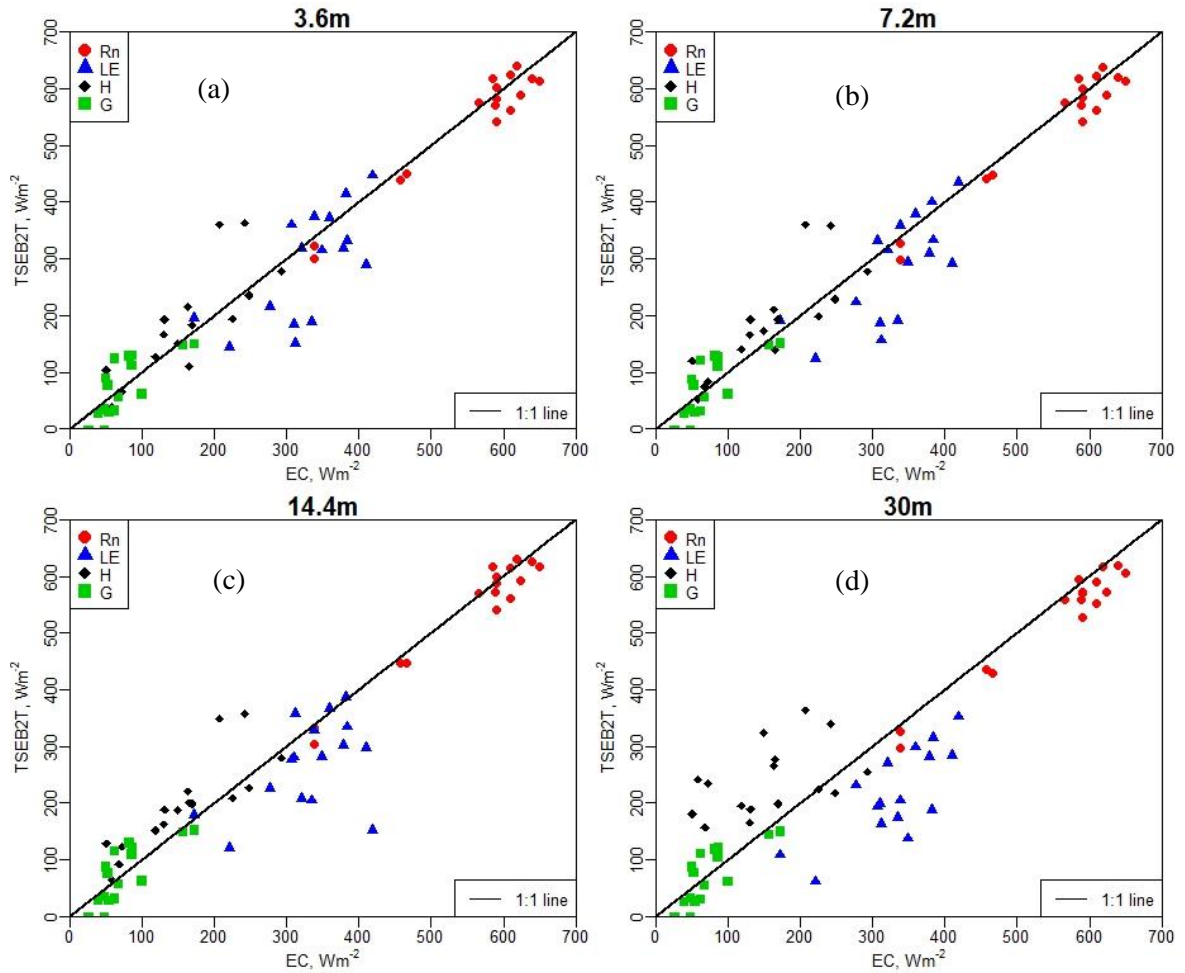


Figure 2.6 Scatterplot of observed versus estimated surface fluxes using different model grid sizes/resolution with the *TSEB-2T* model; (a) 3.6 m, (b) 7.2 m, (c) 14.4 m, and (d) 30 m.

2.3.2 Contextual Spatial Domain Aggregations Effects

2.3.2.1 The Effect of Model Grid Size on *TSEB-2T* Inputs

(a) Canopy and Soil Temperatures (T_c , T_s)

T_c and T_s were estimated based on a linear *LST-NDVI* relationship as described by Nieto et al. [2]. However, this relationship does not fulfill the homoscedasticity criterion when the spatial domain/resolution reaches a certain size (i.e., 30-m) as shown in Figure 2.7. For example, in the case of a 30-m grid size, a higher variability is observed in the *LST-NDVI* data compared with finer resolutions (3.6 m, 7.2 m, and 14.4 m). At micro-scale (e.g., 3.6 m), there are small number of pixels inside the spatial domain compared with others (7.2 m, 14.4 m, and 30 m), and exhibit an apparent linear relationship between *LST* and *NDVI*. However, at coarse resolution (e.g., 30 m), there are many more pixels, more rows of vineyard are included, and large vegetated and bare soil pixels exist inside the spatial domain. The result is a partially filled triangular shape. This indicates the relationship between *LST* and *NDVI* starts to resemble the “triangle method” [71] to estimate *ET* as the sampling domain increases.

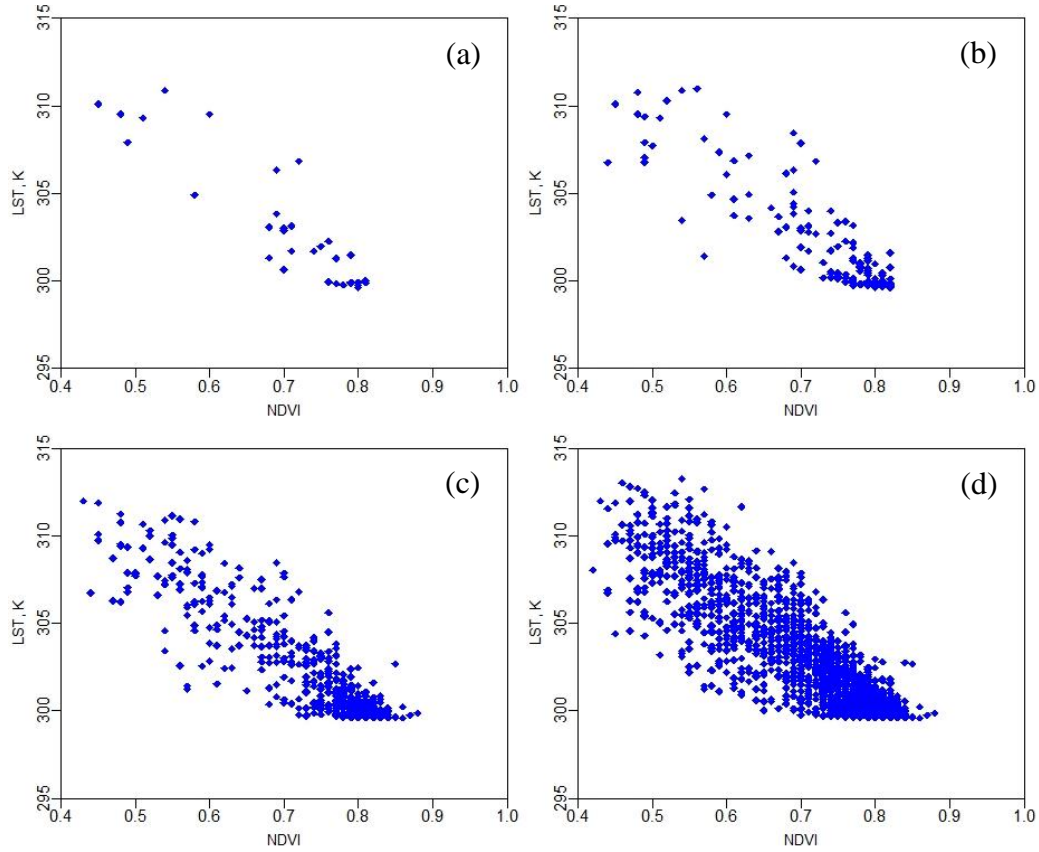
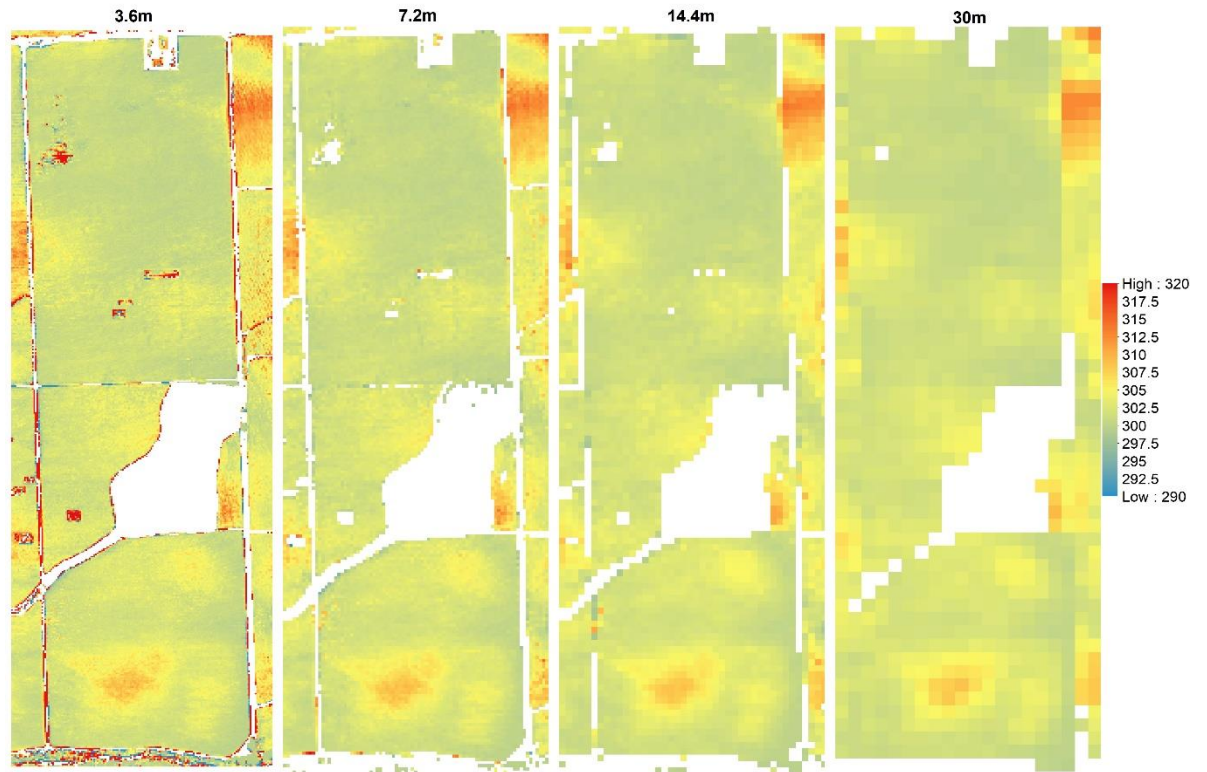


Figure 2.7 The LST - $NDVI$ relationship used for finding T_c and T_s as proposed by the $TSEB-2T$ model at different spatial domains (August 09, 2014). (a) 3.6 m, (b) 7.2 m, (c) 14.4 m, (d) 30 m.

Figure 2.8 illustrates the T_c and T_s maps at different resolutions, which provide an indication of the loss in spatial variability due to spatial aggregation. The ranges of T_c and T_s were between 290 K (16.85 °C) and 320 K (46.85 °C) for the $sUAS$ flight in 2014.

(a)



(b)

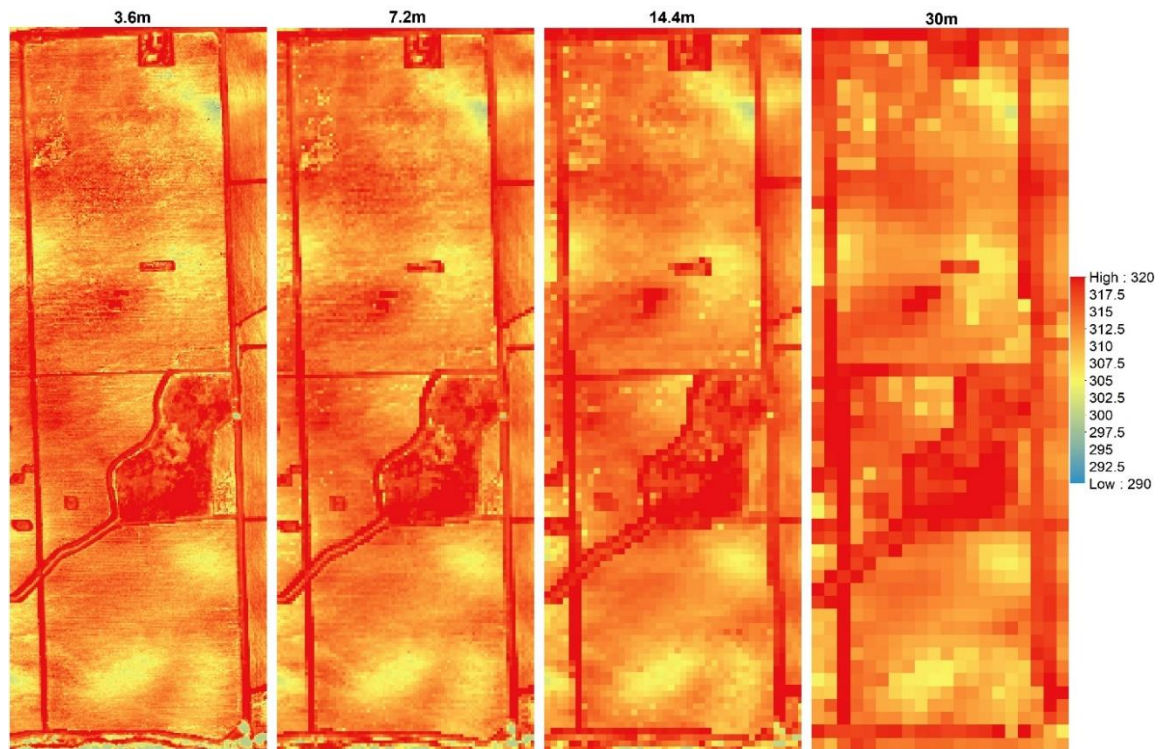


Figure 2.8 Example of (a) canopy temperature (T_c) and (b) soil temperature (T_s) in Kelvin (K) at different spatial domains for August 09, 2014.

(b) Leaf Area Index (*LAI*)

With the *GP* model results, it was found that the main estimators for computing *LAI* are the mean of *NIR/R* ratio of the vine, area of the vine, sum of *NDVI* of the vine, standard deviation of *NIR* of the interrow, and standard deviation of *NIR/R* ratio of the vine. The *GP* model (Equation 2.14) was applied to the remote-sensing imagery to map spatial *LAI* distribution across the study area.

$$LAI = 0.21NDVI_{v_area} - 0.004NDVI_{v_sum} + 0.34\left(\frac{NIR}{R}\right)_{v_mean} - \frac{0.94}{\exp\left(0.23(NDVI_{v_area})^2\right)} - 2.8NIR_{i_STD}\left(\frac{NIR}{R}\right)_{v_STD} - 0.7 \quad (2.14)$$

LAI values from the *GP* model compared with the actual *LAI* field measurements showed good agreement with an R^2 of 0.73.

To evaluate the difference between multiple model grid sizes of *LAI* for each flight, *LAI* maps at different resolutions were estimated (see Figure 2.9) and statistics including the spatial mean, standard deviation, and coefficient of variation (*CV*) were calculated as shown in Table 2.4. Figure 2.9 provides an indication of the loss in spatial variability in *LAI* images due to spatial aggregation. *LAI* at each contextual spatial domain/resolution was calculated using the *LAI* model (Eq 2.14). Each parameter in that equation was calculated based on the pixel values inside the model grid. The ranges of *LAI* were between 0 and 2.5 for the *sUAS* flight in 2014. As illustrated in Table 2.4, the spatial mean value (μ) is the same across different scales, with a slight decrease in *CV*. The exception is the flight on May 02, 2016, which represents the early growing stage of the vine canopy with active/live interrow cover crop, showing a higher *CV*. Hardin and Jensen [72] also found greater uncertainty in estimating *LAI* under low *LAI* conditions using *Vis*. The frequency

histogram in Figure 2.10 indicates the distribution of values is skewed such that the lower values are more pronounced for the flight of May, 2, 2016, with a non-significant change between curves from the different grid sizes, except the 30-m resolution spatial domain, which shows a higher variation compared with other scales. This behavior aligns with the decreasing CV values due to loss in internal or pixel variability of the LAI values. A similar trend of lower CV toward large scale (30 m) has been observed for other $TSEB-2T$ inputs including h_c , f_c , and w_o/h_c .

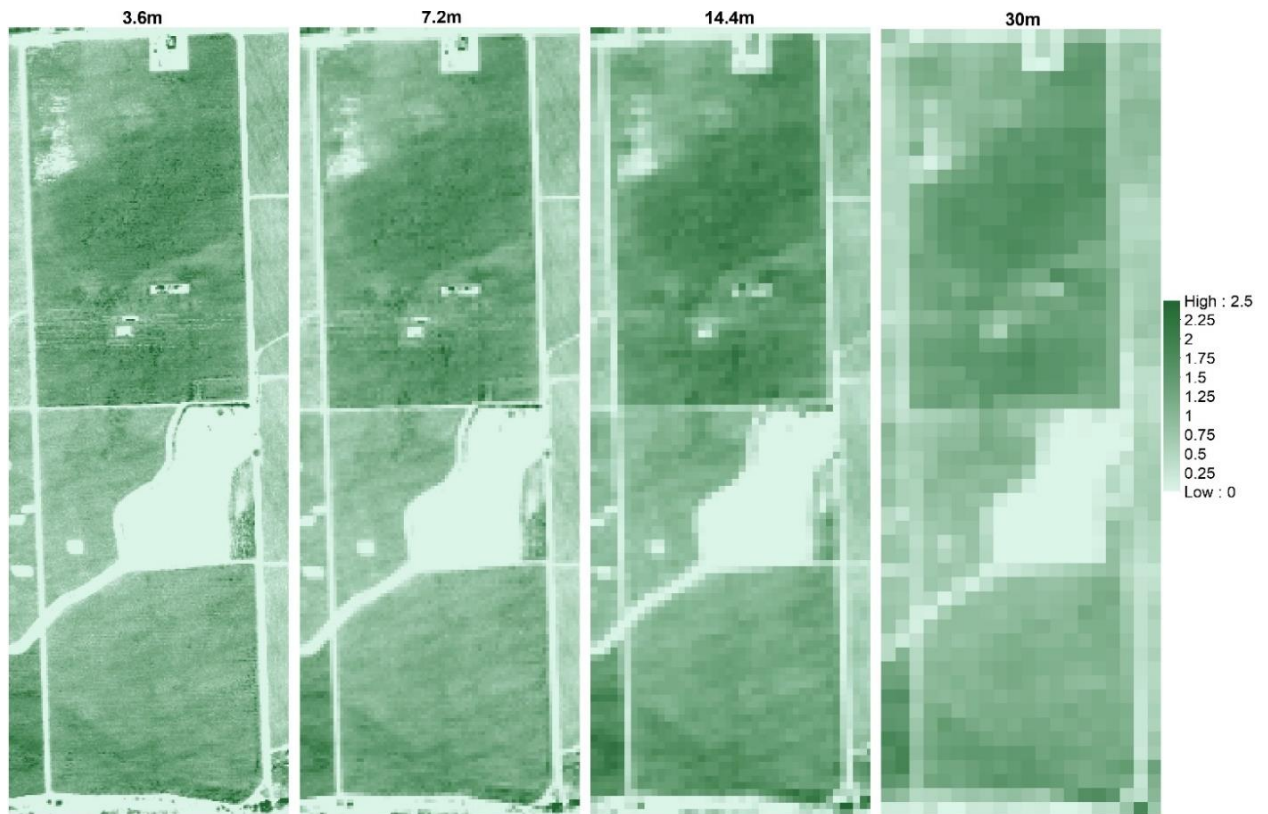


Figure 2.9 Example of modeled LAI (unitless) across different spatial domains for August 09, 2014.

Table 2.4 Spatial domain effect on *LAI* estimation.

Flight	Spatial domain	μ	σ	CV
August 09,2014	3.6m	0.91	0.56	0.61
	7.2m	0.91	0.54	0.59
	14.4m	0.91	0.52	0.57
	30.0m	0.91	0.48	0.53
June 02,2015	3.6m	0.57	0.38	0.66
	7.2m	0.57	0.33	0.58
	14.4m	0.57	0.30	0.52
	30.0m	0.57	0.27	0.47
July 11,2015	3.6m	0.52	0.39	0.75
	7.2m	0.52	0.36	0.69
	14.4m	0.52	0.34	0.65
	30.0m	0.52	0.31	0.60
May 02,2016	3.6m	0.06	0.11	1.90
	7.2m	0.06	0.10	1.75
	14.4m	0.06	0.10	1.66
	30.0m	0.06	0.09	1.59

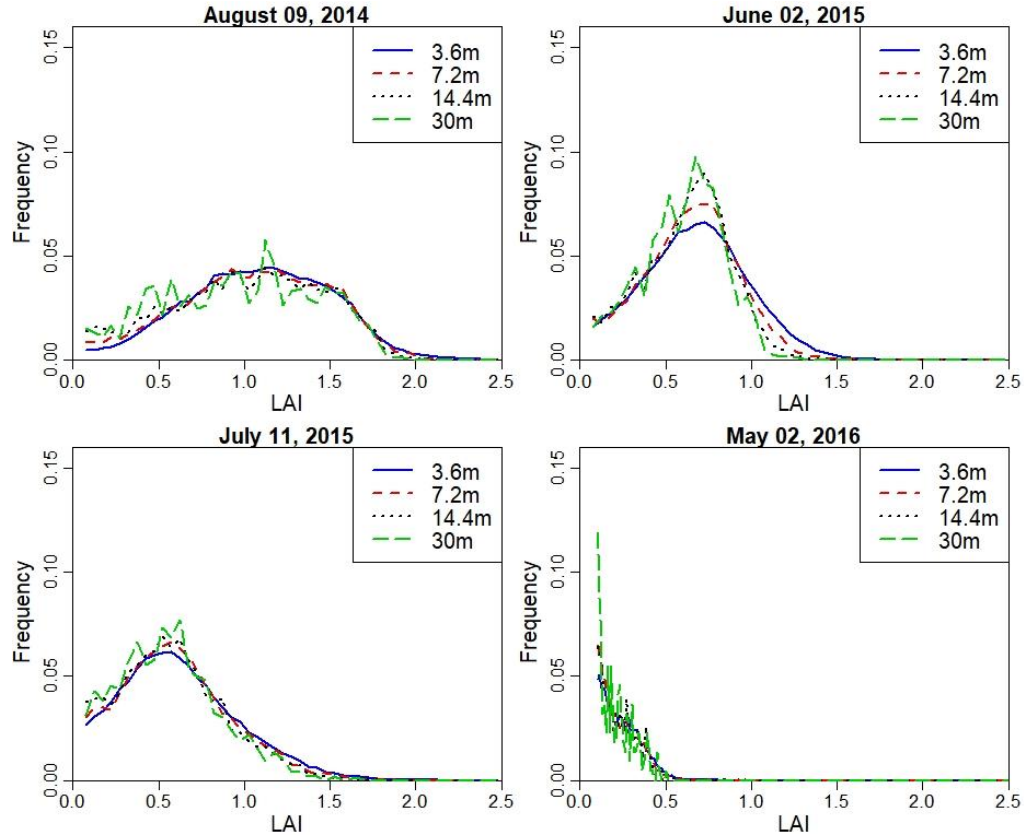


Figure 2.10 Frequency curve of *LAI* at different times from 3.6 m and 7.2 m, 14.4 m and 30 m.

2.3.2.2 Contextual Spatial Domain Effect on Field-Scale *LE* Estimation

An example of the maps of *LE* across different model grid sizes is shown in Figure 2.11. The maps of the energy balance components for 2014 flight at different resolutions are shown in Appendix A. The statistics (mean (μ) and coefficient of variation (*CV*)) for the *LE* maps at the different modeling resolutions are illustrated as bar graphs in Figure 2.12 and Figure 2.13, respectively. For *LE*, the highest mean value is on May 02, 2016, at midafternoon. Although the grapevine canopy is fully developed by June, *LE* in May at both overpass times is higher than the acquisition in June, July, and August. However, on May 3, the model yields the lowest *LE* values due to overcast conditions that day significantly reducing incoming solar radiation, and hence, the energy fluxes. The

phenocam data (<https://hrsl.ba.ars.usda.gov/awhite/CAM/>) indicate the high rate of *LE* on May 2 is the result of a rapidly developing vine canopy, together with a transpiring cover crop.

At a contextual spatial domain level, the magnitude of *LE* is degraded as shown in Figure 2.12 due to the data aggregation from the 3.6-m grid to Landsat scale (30 m). For example, the mean *LE* value from *TSEB-2T* on May 02, 2016 at midafternoon was 315 W/m^2 for the 3.6-m grid decreasing to 304 W/m^2 for the 7.2-m grid, then decreases further to 293 W/m^2 and 278 W/m^2 , respectively, for 14.4-m and 30-m grids. As shown in Figure 2.13, *CV* value slightly increases as the model grid scale/resolution size increases despite a decrease in variation of *LAI* and *LST* distribution as seen in section 2.3.2.1. While *LE* degrades, the *CV* values do not show significant differences. This can be due to internal *TSEB-2T* compensation of the energy balance components at the different evaluated scales.

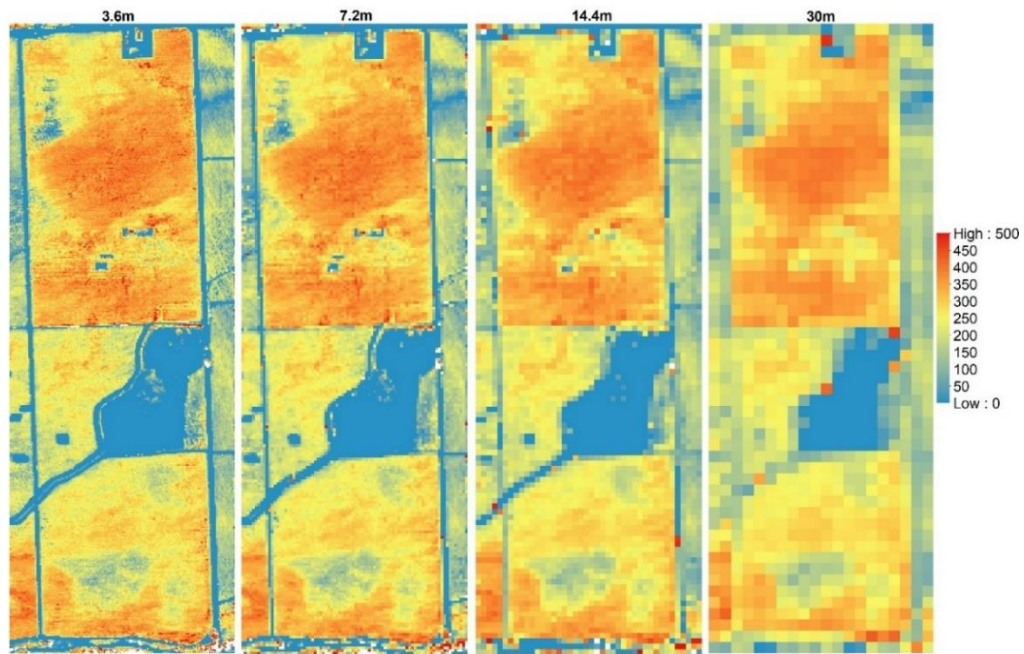


Figure 2.11 *LE* (W/m^2) aggregation at 3.6 m, 7.2 m, 14.4 m and 30 m for August 09, 2014.

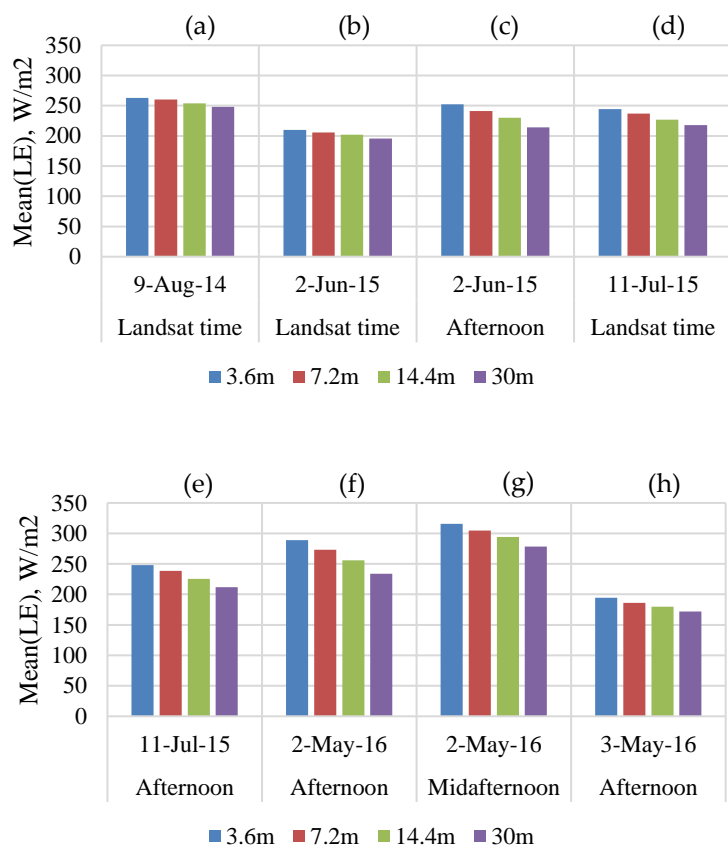
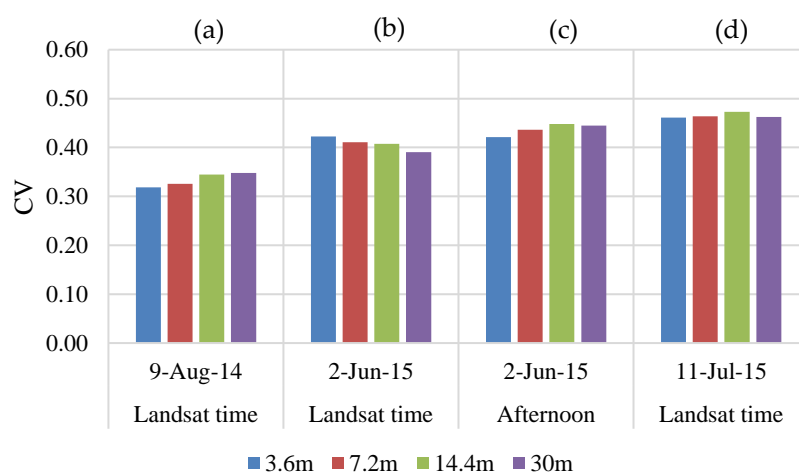


Figure 2.12 Spatial domain effect on the mean of LE spatial data at different times.



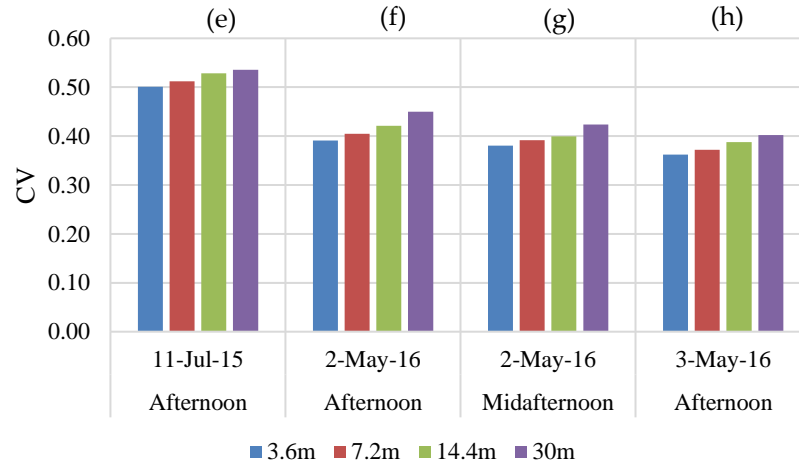


Figure 2.13 Spatial domain effect on the coefficient of variation (CV) of LE spatial data at different times.

2.3.2.3 Contextual Spatial Domain Effect on LE Statistical Characteristics

To provide quantitative evaluation of the impact of spatial aggregation of inputs on LE estimation for the resulting pixel values, frequency and cumulative distribution plots for the LE maps are illustrated in Figure 2.14. This figure shows that LE varies at different grid sizes. The cumulative frequency distribution curves indicate that, especially at the 30-m grid size, LE distribution tends to have the highest cumulative values at lower LE range (below 300 W/m^2). A magnitude shift towards lower LE persists across different times, with one exception. In the case of a 30-m grid on June 02, 2015, the frequency moved up then decreased below the frequency curves of other grid sizes (3.6 m, 7.2 m, and 14.4 m). In general, the results in Figure 2.14 show a reduction in LE distribution as the scale becomes coarser. Hong et al. [22] indicated that an increase in the peak of the LE histogram curve spans as much 10% to 20% as a response to spatial data aggregation using *SEBAL*. In the *TSEB* model, the soil and vegetation components of the scene are treated separately, while the *SEBAL* model uses a single source approach using the composite soil/canopy temperature and is contextual defining wet and dry ET limits based on the hot and cold

extremes in the *LST* field within the image [73]. Moreover, Ershadi et al. [14] pointed out three possible reasons behind the different results obtained from *ET* models: (a) the approach (e.g., contextual hot/cold surface temperature limits versus using absolute surface-atmosphere temperature differences) of each model to estimate *ET*, (b) the study area and eco-hydrological conditions of the surface, which may favor certain *ET* model parameterizations over others, or (c) the different models of aerodynamic resistance formulations and sensitivity to the roughness parameters.

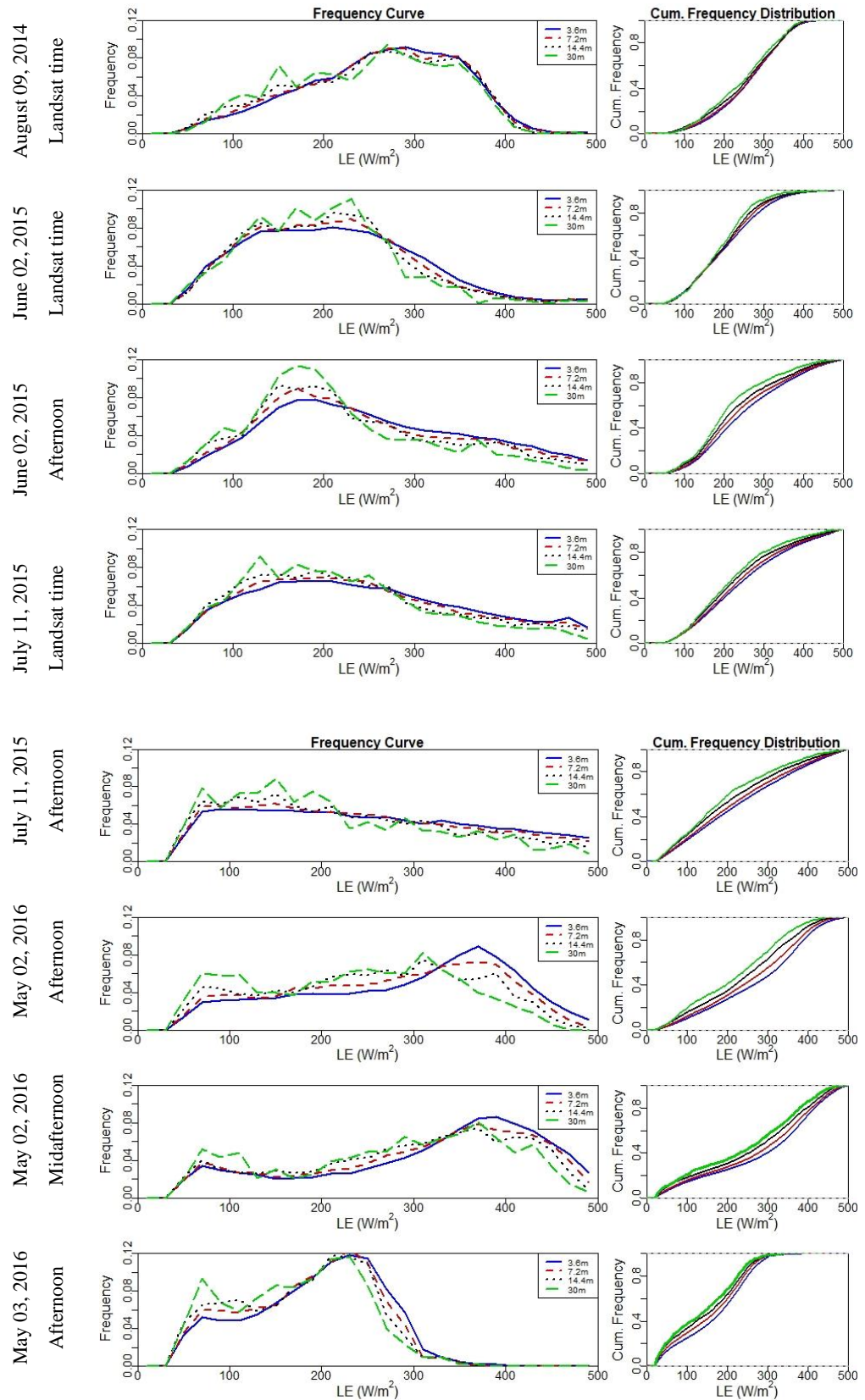


Figure 2.14 Frequency curve (left) and cumulative frequency distribution (right) plots of instantaneous LE for all sUAS flights at 3.6 m, 7.2 m, 14.4 m, and 30 m.

Increasing the spatial domain/resolution affects the estimation of *TSEB-2T* parameters as the fine details of the surface disappear. To test these claims, R_A (s/m) and *LST-NDVI* relationship were evaluated at different spatial domain/resolution; the latter is shown in section 2.3.2.1 (a). As shown in Figure 2.15, there is a decreasing trend in the relative spatial mean (μ_r) of R_A for all flights, ranging approximately from 20% to 60%. The high variability in R_A is related mainly to the variables that affect the friction velocity (u_*), which the mean canopy height and roughness length (z_{oH}), which are derived from the imagery at different resolution/spatial domain. This finding is in agreement with Ershadi et al. [14] and Moran et al. [15], who indicated that the reduction of R_A value at coarse spatial domain/resolution is a key factor behind the underestimation of *LE*.

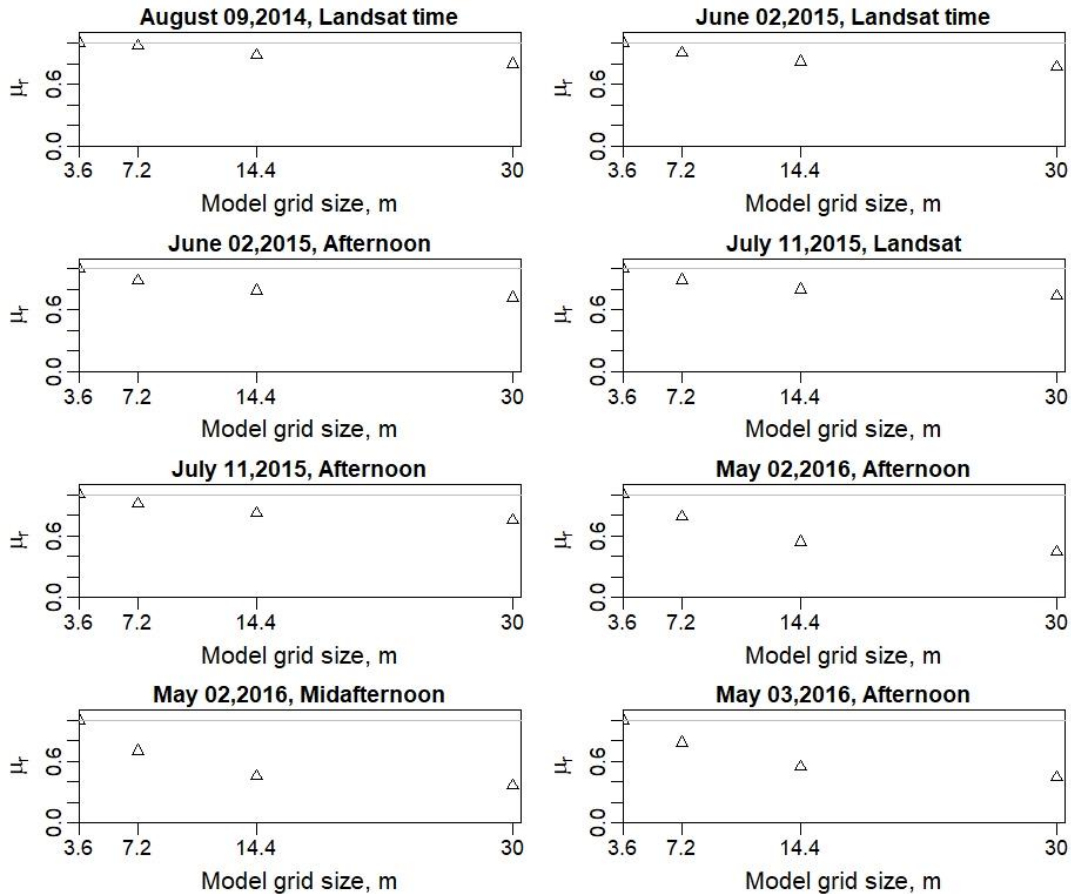


Figure 2.15 Variation of the relative spatial mean of R_A for different flights.

2.3.2.4 Effects of Model Grid Size on LE

To evaluate quantitatively the impact of model grid size via the resolution of key input data, the relative difference (relative error) (E_r) was computed using as the reference the LE at 3.6-m model grid size/resolution. For example, the LE value at the 7.2-m grid is compared to the LE at the 3.6-m grid size by resampling the 7.2-m grid to a 4×4 set of 3.6-m LE output which will have a uniform LE -value at the finer resolution, and taking the difference. As illustrated in Figure 2.16, E_r is calculated with the mean and percentiles (25th and 75th) for the coarser grid sizes used in the *TSEB-2T* model for the different *sUAS* acquisitions. The plots demonstrate an increasing trend in E_r as the model grid size/resolution increases/decreases. The largest E_r value was computed for the imagery on July 11, 2015 at afternoon at nearly 45% for the Landsat resolution. In contrast to July 11, 2015, the lowest range of relative error was observed on August 09, 2014, where the E_r ranged approximately between 15% for the 7.2-m grid and 25% for the 30-m grid. On an average, E_r value ranged from approximately 25% using the 7.2-m model grid size to 40% with the 30-m model resolution.

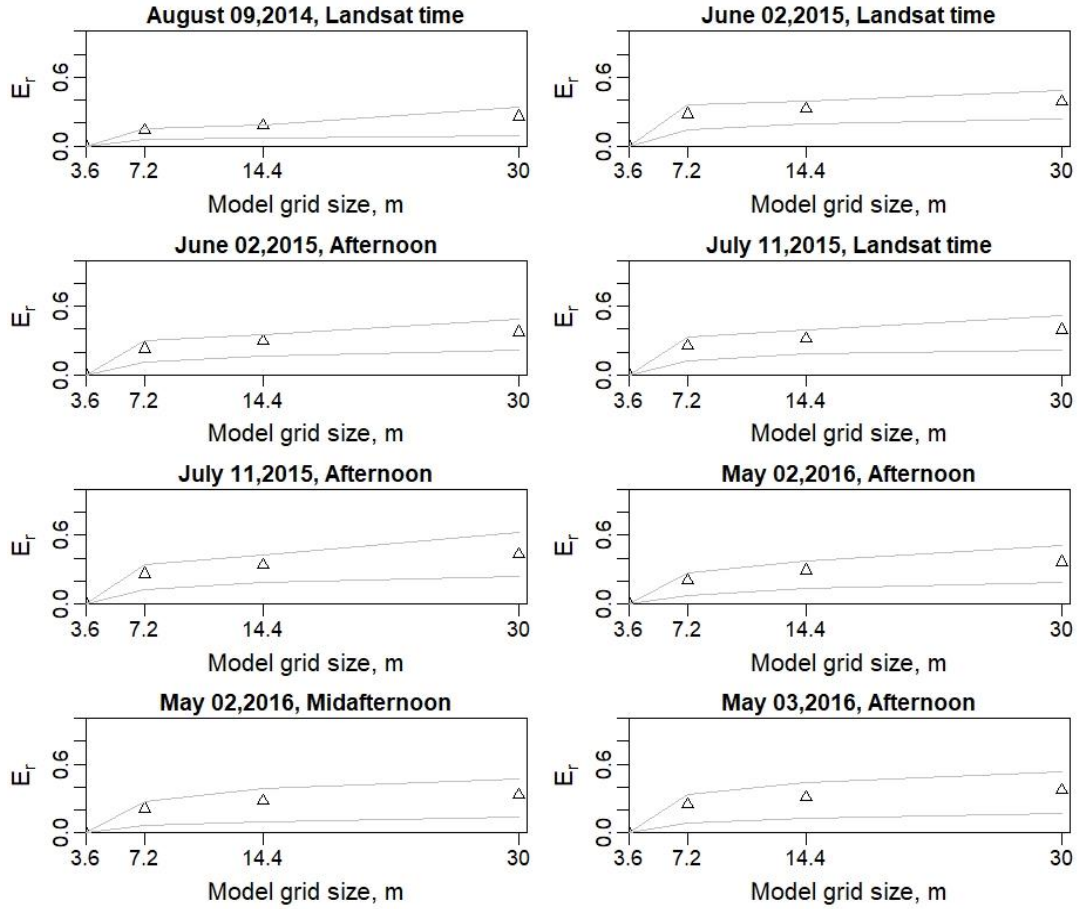


Figure 2.16 Relative error (E_r) at different spatial resolutions for LE with the triangle symbols indicating mean and light lines indicating the 25th and 75th percentiles for the coarse grid sizes.

These results are supported by an Ershadi et al. [14] study that found the E_r of LE varied between 20% and 40% when aggregating the Landsat data incrementally from 120 m to 960 m and using the $SEBS$ model to calculate surface heat fluxes. Furthermore, Moran et al. [15] indicated that a larger error could appear (larger than 50%) in H estimation over a heterogeneous area due to a mix of stable and unstable conditions and the variation in aerodynamic roughness, especially for highly unstable conditions. As previously mentioned in section 2.3.1, the underestimated LE could be influenced by overestimation in H , which implies that a large error is expected in the residual flux (LE) estimate at coarse

spatial domains [70]. Furthermore, the effect of model grid size on LE is also visible at the 25th and 75th percentiles, which immediately increases at the 7.2-m grid size and continues increasing towards the 30-m resolution, providing a clear indication of increasing discrepancy with the reference grid (3.6 m) LE estimates.

2.4 Conclusion

The objective of this study was to assess high-resolution LE estimation in vineyards at different model grid sizes or resolutions, specifically 3.6 m, 7.2 m, 14.4 m, and 30 m (Landsat scale), using a physically-based ET model known as $TSEB-2T$. The reference grid size of 3.6 m represents the finest pixel resolution that includes both vine canopy and interrow conditions, which is the resolution where the $TSEB$ model algorithms of soil/substrate and canopy temperature partitioning radiation and convective energy exchange are applicable [2]. Multiple statistical measures were used to assess the effect of decreasing the spatial resolution or increasing the model grid size 2, 4, and nearly 10 times the original 3.6 m resolution. These included validation of $TSEB-2T$ fluxes at the different model grid sizes with the EC measurements, comparing LE spatial statistics (mean and coefficient of variation, frequency distributions) and LE differences over the imaged domain at the different resolutions using LE at 3.6 m grid size as the reference. The results showed that separation of T_c and T_s , required in $TSEB-2T$, affects the $LST-NDVI$ linear trend as a function of resolution of the pixels. The validation results with the flux tower measurements indicate that R_n and G discrepancies do not change across different model grid sizes, while for H and LE there is an increase in model-measurement differences, particularly at the 30-m resolution. This is largely caused by an overestimation in H , causing an underestimation in LE (bias), particularly at the coarsest resolution (30-m grid

size). This refers mainly to the non-linear relationship of $LST-NDVI$ and the variability of R_a due to the variables that affect the u_* which are the mean canopy height and roughness length, which are derived from remote sensing imagery at different spatial domain/resolution.

The effects of model grid size were evaluated at field and at grid scale using the spatial mean and coefficient of variation and relative difference, respectively. At field scale, the results show small decreases in the spatial mean over the image, ranging approximately from 10% to 20%, as the data aggregated for model grid size increased from 3.6 m to 30 m. However, the relative differences with resolution indicate a significant decrease in LE , ranging approximately from 25% to 45%, when aggregating the data from 3.6 m to Landsat scale (30 m). This means that, while field values of LE may be adequate to use, the field variability reduction limits its use for precision agriculture applications, such as identifying areas within the field under actual stress conditions or being over irrigated. These results suggest that $TSEB-2T$ is only applicable using imagery with high enough resolution that can readily distinguish plant canopy and soil/substrate temperatures and the modeling grid size is at a resolution where it is appropriate to apply $TSEB-2T$ algorithms for modeling the radiative and convective energy exchange from both the vegetation and soil substrate systems. Aggregating inputs to $TSEB-2T$ to multiple grid sizes of the interrow/row spacings for vineyards is not advisable, since it is likely the accuracy of surface fluxes, particularly LE , will deteriorate. While this study was limited to evaluating different modeling grid sizes, a future comparison with Landsat and ECOstress ET products is also planned, which would provide a more comprehensive scaling assessment of ET estimates for $sUAS$ -Satellite ET integration. Furthermore, the effect of remote sensing resolution on the output

of other *TSEB* versions such as *TSEB-PT* may be less affected and will be evaluated in a future study.

References

1. Melesse, A.M.; Weng, Q.; Thenkabail, P.S.; Senay, G.B. Remote Sensing Sensors and Applications in Environmental Resources Mapping and Modelling. *Sensors* 2007, 7, 3209–3241.
2. Nieto, H.; Kustas, W.P.; Torres-Rúa, A.; Alfieri, J.G.; Gao, F.; Anderson, M.C.; White, W.A.; Song, L.; Alsina, M.D.M.; Prueger, J.H.; et al. Evaluation of TSEB turbulent fluxes using different methods for the retrieval of soil and canopy component temperatures from UAV thermal and multispectral imagery. *Irrig. Sci.* 2018, 37, 389–406.
3. Cammalleri, C.; Anderson, M.; Gao, F.; Hain, C.R.; Kustas, W.P. A data fusion approach for mapping daily evapotranspiration at field scale. *Water Resour. Res.* 2013, 49, 4672–4686.
4. McKee, M.; Torres-Rua, A.F.; Aboutalebi, M.; Nassar, A.; Coopmans, C.; Kustas, W.P.; Gao, F.; Dokoozlian, N.; Sanchez, L.; Alsina, M.M. Challenges that beyond-visual-line-of-sight technology will create for UAS-based remote sensing in agriculture (Conference Presentation). In *Autonomous Air and Ground Sensing Systems for Agricultural Optimization and Phenotyping IV.*; SPIE-The International Society for Optical Engineering: Bellingham, WA, USA, 2019; Volume 11008, p. 110080J.
5. Torres-Rue, A.F.; Aboutalebi, M.; Wright, T.; Nassar, A.; Guillevic, P.; Hipps, L.; Gao, F.; Jim, K.; Alsina, M.; Coopmans, C.; et al. Estimation of Surface Thermal Emissivity In A Vineyard For UAV Microbolometer Thermal Cameras Using NASA Hytes Hyperspectral Thermal, And Landsat And Aggieair Optical Data. *Autonomous Air and Ground Sensing Systems for Agricultural Optimization and Phenotyping IV.*; SPIE: Baltimore, MD, USA, 2019; pp.15–17.
6. Nassar, A.; Nieto, H.; Aboutalebi, M.; TorresRue, A.F.; McKee, M.; Kustas, W.P.; Prueger, J.H.; McKee, L.; Alfieri, J.G.; Hipps, L.; et al. *Pixel Resolution Sensitivity Analysis for the Estimation of Evapotranspiration Using the Two Source Energy Balance Model and sUAS Imagery under Agricultural Complex Canopy Environments*; American Geophysical Union (AGU): Washington, DC, USA, 2018;
7. Nassar, A.; Torres-Rue, A.F.; McKee, M.; Kustas, W.P.; Coopmans, C.; Nieto, H.; Hipps, L. *Assessment of UAV Flight Times for Estimation of Daily High Resolution Evapotranspiration in Complex Agricultural Canopy Environments*; Universities Council in Water Resources (UCOWR): Snowbird, UT, USA, 2019.
8. Wu, H.; Li, Z.-L. Scale Issues in Remote Sensing: A Review on Analysis, Processing and Modeling. *Sensors* 2009, 9, 1768–1793.

9. El Maayar, M.; Chen, J.M. Spatial scaling of evapotranspiration as affected by heterogeneities in vegetation, topography, and soil texture. *Remote. Sens. Environ.* 2006, *102*, 33–51.
10. Miu, M.; Zhang, X.; Dewan, M.A.A.; Wang, J. Aggregation and Visualization of Spatial Data with Application to Classification of Land Use and Land Cover. *Geoinformatics Geostat. Overv.* 2017, *5* (3).
11. Brunsell, N.; Gillies, R. Scale issues in land–atmosphere interactions: Implications for remote sensing of the surface energy balance. *Agric. For. Meteorol.* 2003, *117*, 203–221.
12. Giorgi, F. An Approach for the Representation of Surface Heterogeneity in Land Surface Models. Part I.; Theoretical Framework. *Mon. Weather Rev.* 1997, *125*, 1885–1899.
13. Sharma, V.; Kilic, A.; Irmak, S. Impact of scale/resolution on evapotranspiration from Landsat and MODIS images. *Water Resour. Res.* 2016, *52*, 1800–1819.
14. Ershadi, A.; McCabe, M.; Evans, J.; Walker, J. Effects of spatial aggregation on the multi-scale estimation of evapotranspiration. *Remote. Sens. Environ.* 2013, *131*, 51–62.
15. Moran, M.S.; Humes, K.S.; Pinter, P.J. The scaling characteristics of remotely-sensed variables for sparsely-vegetated heterogeneous landscapes. *J. Hydrol.* 1997, *190*, 337–362.
16. Kustas, W.; Norman, J.. Evaluating the Effects of Subpixel Heterogeneity on Pixel Average Fluxes. *Remote. Sens. Environ.* 2000, *74*, 327–342.
17. Verburg, P.H.; Crossman, N.; Ellis, E.C.; Heinimann, A.; Hostert, P.; Mertz, O.; Nagendra, H.; Sikor, T.; Erb, K.-H.; Golubiewski, N.; et al. Land system science and sustainable development of the earth system: A global land project perspective. *Anthropocene* 2015, *12*, 29–41.
18. Long, D.; Singh, V.P.; Li, Z. How sensitive is SEBAL to changes in input variables, domain size and satellite sensor? *J. Geophys. Res. Space Phys.* 2011, *116*, 116.
19. Goodchild, M.F.; Gopal, S. *The Accuracy of Spatial Databases*. CRC Press: Boca Raton, FL, USA, 1989.
20. Fritz, S.; See, L.; Rembold, F. Comparison of global and regional land cover maps with statistical information for the agricultural domain in Africa. *Int. J. Remote. Sens.* 2010, *31*, 2237–2256.
21. Bian, L.; Butler, R. Comparing effects of aggregation methods on statistical and spatial properties of simulated spatial data. *Photogramm. Eng. Remote Sens.* 1999, *65*, 73–84.

22. Hong, S.-H.; Hendrickx, J.M.; Borchers, B. Up-scaling of SEBAL derived evapotranspiration maps from Landsat (30m) to MODIS (250m) scale. *J. Hydrol.* 2009, *370*, 122–138.
23. Singh, R.K.; Senay, G.B.; Velpuri, N.M.; Bohms, S.; Verdin, J.P. On the Downscaling of Actual Evapotranspiration Maps Based on Combination of MODIS and Landsat-Based Actual Evapotranspiration Estimates. *Remote Sens.* 2014, *6*, 10483–10509.
24. Li, X.; Liu, S.; Li, H.; Ma, Y.; Wang, J.; Zhang, Y.; Xu, Z.; Xu, T.; Song, L.; Yang, X.; et al. Intercomparison of Six Upscaling Evapotranspiration Methods: From Site to the Satellite Pixel. *J. Geophys. Res. Atmos.* 2018, *123*, 6777–6803.
25. French, A.N.; Hunsaker, D.J.; Thorp, K.R. Remote sensing of evapotranspiration over cotton using the TSEB and METRIC energy balance models. *Remote Sens. Environ.* 2015, *158*, 281–294.
26. Su, Z.; Pelgrum, H.; Menenti, M. Aggregation effects of surface heterogeneity in land surface processes. *Hydrol. Earth Syst. Sci.* 1999, *3*, 549–563.
27. Guzinski, R.; Nieto, H. Evaluating the feasibility of using Sentinel-2 and Sentinel-3 satellites for high-resolution evapotranspiration estimations. *Remote Sens. Environ.* 2019, *221*, 157–172.
28. Niu, H.; Zhao, T.; Wang, D.; Chen, Y. Evapotranspiration Estimation with UAVs in Agriculture: A Review. *A Rev.* 2019. doi:10.20944/preprints201907.0124.v1.
29. Mauser, W.; Schädlich, S. Modelling the spatial distribution of evapotranspiration on different scales using remote sensing data. *J. Hydrol.* 1998, *212*, 250–267.
30. The California Garden Web, University of California. Available online: http://cagardenweb.ucanr.edu/Growing_Grapes_in_the_California_Garden/?uid=1&ds=436 (accessed on 16 September 2019).
31. Growing Fruit Trees in Maine, the University of Maine. Available online: <https://extension.umaine.edu/fruit/growing-fruit-trees-in-maine/spacing/> (accessed on 1 October 2019).
32. Norman, J.; Kustas, W.; Humes, K. Source approach for estimating soil and vegetation energy fluxes in observations of directional radiometric surface temperature. *Agric. For. Meteorol.* 1995, *77*, 263–293.
33. Chirouze, J.; Boulet, G.; Jarlan, L.; Fieuzal, R.; Rodríguez, J.C.; Ezzahar, J.; Er-Raki, S.; Bigeard, G.; Merlin, O.; Garatuza-Payan, J.; et al. Intercomparison of four remote-sensing-based energy balance methods to retrieve surface evapotranspiration and water stress of irrigated fields in semi-arid climate. *Hydrol. Earth Syst. Sci.* 2014, *18*, 1165–1188.

34. Alfieri, J.G.; Kustas, W.P.; Nieto, H.; Prueger, J.H.; Hipps, L.E.; McKee, L.G.; Gao, F.; Los, S. Influence of wind direction on the surface roughness of vineyards. *Irrig. Sci.* 2019, *37*, 359–373. doi:10.1007/s00271-018-0610-z.
35. Kustas, W.P.; Alfieri, J.G.; Nieto, H.; Wilson, T.G.; Gao, F.; Anderson, M.C. Utility of the two-source energy balance (TSEB) model in vine and interrow flux partitioning over the growing season. *Irrig. Sci.* 2019, *37*, 375–388. doi:10.1007/s00271-018-0586-8.
36. Bigeard, G.; Coudert, B.; Chirouze, J.; Er-Raki, S.; Boulet, G.; Ceschia, E.; Jarlan, L. Evapotranspiration monitoring based on thermal infrared data over agricultural landscapes: Comparison of a simple energy budget model and a SVAT model. *Hydrol. Earth Syst. Sci. Discuss.* 2018, *2018*, 1–44.
37. Kustas, W.; Anderson, M. Advances in thermal infrared remote sensing for land surface modeling. *Agric. For. Meteorol.* 2009, *149*, 2071–2081.
38. Yang, Y.; Qiu, J.; Zhang, R.; Huang, S.; Chen, S.; Wang, H.; Luo, J.; Fan, Y. Intercomparison of Three Two-Source Energy Balance Models for Partitioning Evaporation and Transpiration in Semiarid Climates. *Remote Sens.* 2018, *10*, 1149.
39. Andreu, A.; Kustas, W.P.; Polo, M.J.; Carrara, A.; González-Dugo, M.P. Modeling Surface Energy Fluxes over a Dehesa (Oak Savanna) Ecosystem Using a Thermal Based Two-Source Energy Balance Model (TSEB) I. *Remote Sens.* 2018, *10*, 567.
40. Yao, W.; Han, M.; Xu, S. Estimating the regional evapotranspiration in Zhalong wetland with the Two-Source Energy Balance (TSEB) model and Landsat7/ETM+ images. *Ecol. Inform.* 2010, *5*, 348–358.
41. Anderson, M.; Gao, F.; Knipper, K.; Hain, C.; Dulaney, W.; Baldocchi, D.; Eichelmann, E.; Hemes, K.; Yang, Y.; Medellín-Azuara, J.; et al. Field-Scale Assessment of Land and Water Use Change over the California Delta Using Remote Sensing. *Remote Sens.* 2018, *10*, 889.
42. Kustas, W.P.; Norman, J.M. A two-source approach for estimating turbulent fluxes using multiple angle thermal infrared observations. *Water Resour. Res.* 1997, *33*, 1495–1508.
43. Norman, J.M.; Kustas, W.P.; Prueger, J.H.; Diak, G.R. Surface flux estimation using radiometric temperature: A dual-temperature-difference method to minimize measurement errors. *Water Resour. Res.* 2000, *36*, 2263–2274.
44. Gao, F.; Kustas, W.P.; Anderson, M.C. A Data Mining Approach for Sharpening Thermal Satellite Imagery over Land. *Remote Sens.* 2012, *4*, 3287–3319.
45. Zheng, G.; Moskal, L.M. Retrieving Leaf Area Index (LAI) Using Remote Sensing: Theories, Methods and Sensors. *Sensors* 2009, *9*, 2719–2745.

46. White, W.A.; Alsina, M.M.; Nieto, H.; McKee, L.G.; Gao, F.; Kustas, W.P. Determining a robust indirect measurement of leaf area index in California vineyards for validating remote sensing-based retrievals. *Irrig. Sci.* 2019, 79, 269–280. doi:10.1007/s00271-018-0614-8.
47. Liu, K.; Zhou, Q.-B.; Wu, W.-B.; Xia, T.; Tang, H.-J. Estimating the crop leaf area index using hyperspectral remote sensing. *J. Integr. Agric.* 2016, 15, 475–491.
48. Johnson, L.F. Temporal stability of an NDVI-LAI relationship in a Napa Valley vineyard. *Aust. J. Grape Wine Res.* 2003, 9, 96–101.
49. Dobrowski, S.; Ustin, S.; Wolpert, J. Remote estimation of vine canopy density in vertically shoot-positioned vineyards: Determining optimal vegetation indices. *Aust. J. Grape Wine Res.* 2002, 8, 117–125.
50. Fang, H. Retrieving leaf area index using a genetic algorithm with a canopy radiative transfer model. *Remote Sens. Environ.* 2003, 85, 257–270.
51. Sun, L.; Gao, F.; Anderson, M.C.; Kustas, W.P.; Alsina, M.M.; Sanchez, L.; Sams, B.; McKee, L.; Dulaney, W.; White, W.A.; et al. Daily Mapping of 30 m LAI and NDVI for Grape Yield Prediction in California Vineyards. *Remote Sens.* 2017, 9, 317.
52. Kimes, D.; Knyazikhin, Y.; Privette, J.; Abuelgasim, A.; Gao, F. Inversion methods for physically-based models. *Remote Sens. Rev.* 2000, 18, 381–439.
53. Gonsamo, A.; Pellikka, P. The sensitivity based estimation of leaf area index from spectral vegetation indices. *ISPRS J. Photogramm. Remote Sens.* 2012, 70, 15–25.
54. Kustas, W.P.; Norman, J.M. Evaluation of soil and vegetation heat flux predictions using a simple two-source model with radiometric temperatures for partial canopy cover. *Agric. For. Meteorol.* 1999, 94, 13–29.
55. Nieto, H.; Kustas, W.P.; Alfieri, J.G.; Gao, F.; Hipps, L.E.; Los, S.; Prueger, J.H.; McKee, L.G.; Anderson, M.C. Impact of different within-canopy wind attenuation formulations on modelling sensible heat flux using TSEB. *Irrig. Sci.* 2019, 37, 315–331. doi:10.1007/s00271-018-0611-y.
56. Kustas, W.P.; Anderson, M.C.; Alfieri, J.G.; Knipper, K.; Torres-Rua, A.; Parry, C.K.; Nieto, H.; Agam, N.; White, W.A.; Gao, F.; et al. The Grape Remote Sensing Atmospheric Profile and Evapotranspiration Experiment. *Bull. Am. Meteorol. Soc.* 2018, 99, 1791–1812.
57. Torres-Rua, A. Vicarious Calibration of sUAS Microbolometer Temperature Imagery for Estimation of Radiometric Land Surface Temperature. *Sensors* 2017, 17, 1499.
58. McKee, M.; Nassar, A.; Torres-Rua, A.F.; Aboutaleb, M.; Kustas, W. Implications of sensor inconsistencies and remote sensing error in the use of small unmanned aerial systems for generation of information products for agricultural management.

Autonomous Air and Ground Sensing Systems for Agricultural Optimization and Phenotyping III; International Society for Optics and Photonics: Bellingham, WA, USA, 2018; Volume 10664, p. 1066402.

59. Alfieri, J.G.; Kustas, W.P.; Prueger, J.H.; McKee, L.G.; Hipps, L.E.; Gao, F. A multi-year intercomparison of micrometeorological observations at adjacent vineyards in California's Central Valley during GRAPEX. *Irrig. Sci.* 2019, *37*, 345–357. doi:10.1007/s00271-018-0599-3.
60. Agam, N.; Kustas, W.P.; Alfieri, J.G.; Gao, F.; McKee, L.M.; Prueger, J.H.; Hipps, L.E. Micro-scale spatial variability in soil heat flux (SHF) in a wine-grape vineyard. *Irrig. Sci.* 2019, *37*, 253–268.
61. Kljun, N.; Calanca, P.; Rotach, M.W.; Schmid, H.P. A simple two-dimensional parameterisation for Flux Footprint Prediction (FFP). *Geosci. Model Dev.* 2015, *8*, 3695–3713.
62. Hassan-Esfahani, L.; Ebtehaj, A.M.; Torres-Rua, A.; McKee, M. Spatial Scale Gap Filling Using an Unmanned Aerial System: A Statistical Downscaling Method for Applications in Precision Agriculture. *Sensors* 2017, *17*, 2106.
63. Moorhead, J.E.; Marek, G.W.; Colaizzi, P.D.; Gowda, P.H.; Evett, S.R.; Brauer, D.K.; Marek, T.H.; Porter, D.O. Evaluation of Sensible Heat Flux and Evapotranspiration Estimates Using a Surface Layer Scintillometer and a Large Weighing Lysimeter. *Sensors* 2017, *17*, 2350.
64. Imukova, K.; Ingwersen, J.; Hevart, M.; Streck, T. Energy balance closure on a winter wheat stand: Comparing the eddy covariance technique with the soil water balance method. *Biogeosciences Discuss.* 2015, *12*, 6783–6820.
65. Mauder, M.; Genzel, S.; Fu, J.; Kiese, R.; Soltani, M.; Steinbrecher, R.; Zeeman, M.; Banerjee, T.; De Roo, F.; Kunstmann, H. Evaluation of energy balance closure adjustment methods by independent evapotranspiration estimates from lysimeters and hydrological simulations. *Hydrol. Process.* 2017, *32*, 39–50.
66. Twine, T.; Kustas, W.; Norman, J.; Cook, D.; Houser, P.; Meyers, T.; Prueger, J.; Starks, P.; Wesely, M. Correcting eddy-covariance flux underestimates over a grassland. *Agric. For. Meteorol.* 2000, *103*, 279–300.
67. Al-Juaidi, A.E.M.; Nassar, A.M.; Al-Juaidi, O.E.M. Evaluation of flood susceptibility mapping using logistic regression and GIS conditioning factors. *Arab. J. Geosci.* 2018, *11*, 765.
68. Sun, H.; Yang, Y.; Wu, R.; Gui, D.; Xue, J.; Liu, Y.; Yan, D. Improving Estimation of Cropland Evapotranspiration by the Bayesian Model Averaging Method with Surface Energy Balance Models. *Atmosphere* 2019, *10*, 188.

69. Song, L.; Liu, S.; Kustas, W.P.; Zhou, J.; Xu, Z.; Xia, T.; Li, M. Application of remote sensing-based two-source energy balance model for mapping field surface fluxes with composite and component surface temperatures. *Agric. For. Meteorol.* 2016, *230*, 8–19.
70. Kustas, W.P.; Nieto, H.; Morillas, L.; Anderson, M.C.; Alfieri, J.G.; Hipps, L.E.; Villagarcía, L.; Domingo, F.; Garcia, M. Revisiting the paper “Using radiometric surface temperature for surface energy flux estimation in Mediterranean drylands from a two-source perspective.” *Remote Sens. Environ.* 2016, *184*, 645–653.
71. Carlson, T. An Overview of the “Triangle Method” for Estimating Surface Evapotranspiration and Soil Moisture from Satellite Imagery. *Sensors* 2007, *7*, 1612–1629.
72. Hardin, P.J.; Jensen, R.R. Neural Network Estimation of Urban Leaf Area Index. *GIScience Remote Sens.* 2005, *42*, 251–274.
73. Timmermans, W.J.; Kustas, W.P.; Anderson, M.C.; French, A.N. An intercomparison of the Surface Energy Balance Algorithm for Land (SEBAL) and the Two-Source Energy Balance (TSEB) modeling schemes. *Remote Sens. Environ.* 2007, *108*, 369–384.

CHAPTER 3

ASSESSING DAILY EVAPOTRANSPIRATION METHODOLOGIES FROM
ONE-TIME-OF-DAY SUAS AND *EC* INFORMATION IN THE *GRAPEX* PROJECT**Abstract**

Daily evapotranspiration (ET_d) plays a key role in irrigation water management and is particularly important in drought-stricken areas, such as California and high-value crops. Remote sensing allows for the cost-effective estimation of spatial evapotranspiration (ET), and the advent of small unmanned aerial systems ($sUAS$) technology has made it possible to estimate instantaneous high-resolution ET at the plant, row, and subfield scales. $sUAS$ estimates ET using “instantaneous” remote sensing measurements with half-hourly/hourly forcing micrometeorological data, yielding hourly fluxes in W/m^2 that are then translated to a daily scale (mm/day) under two assumptions: (a) relative rates, such as the ratios of ET -to-net radiation (R_n) or ET -to-solar radiation (R_s), are assumed to be constant rather than absolute, and (b) nighttime evaporation (E) and transpiration (T) contributions are negligible. While assumption (a) may be reasonable for unstressed, full cover crops (no exposed soil), the E and T rates may significantly vary over the course of the day for partially vegetated cover conditions due to diurnal variations of soil and crop temperatures and interactions between soil and vegetation elements in agricultural environments, such as vineyards and orchards. In this study, five existing extrapolation approaches that compute the daily ET from the “instantaneous” remotely sensed $sUAS$ ET estimates and the eddy covariance (EC) flux tower measurements were evaluated under different weather, grapevine variety, and trellis designs. Per assumption (b), the nighttime ET contribution was ignored. Each

extrapolation technique (evaporative fraction (EF), solar radiation (R_s), net radiation-to-solar radiation (R_n/R_s) ratio, Gaussian (GA), and Sine) makes use of clear skies and quasi-sinusoidal diurnal variations of hourly ET and other meteorological parameters. The $sUAS$ ET estimates and EC ET measurements were collected over multiple years and times from different vineyard sites in California as part of the USDA Agricultural Research Service Grape Remote Sensing Atmospheric Profile and Evapotranspiration eXperiment (*GRAPEX*). Optical and thermal $sUAS$ imagery data at 10 cm and 60 cm, respectively, were collected by the Utah State University *AggieAir* $sUAS$ Program and used in the Two Source Energy Balance ($TSEB$) model to estimate the instantaneous or hourly $sUAS$ ET at overpass time. The hourly ET from the EC measurements was also used to validate the extrapolation techniques. Overall, the analysis using EC measurements indicates that the R_s , EF , and GA approaches presented the best goodness-of-fit statistics for a window of time between 1030 and 1330 PST (Pacific Standard Time), with the R_s approach yielding better agreement with the EC measurements. Similar results were found using $TSEB$ and $sUAS$ data. The 1030–1330 time window also provided the greatest agreement between the actual daily EC ET and the extrapolated $TSEB$ daily ET , with the R_s approach again yielding better agreement with the ground measurements. The expected accuracy of the upscaled $TSEB$ daily ET estimates across all vineyard sites in California is below 0.5 mm/day, (EC extrapolation accuracy was found to be 0.34 mm/day), making the daily scale results from $TSEB$ reliable and suitable for day-to-day water management applications.

Keywords: evapotranspiration (ET); daily ET ; remote sensing; $sUAS$; vineyards; *GRAPEX*; eddy covariance (EC); $TSEB$; energy balance

3.1 Introduction

Evapotranspiration (*ET*) is a key component in the hydro-ecological process, which couples water and energy budgets, links the land surface and the atmosphere [1], and represents water consumption for biomass production [2]. Routine monitoring of actual *ET* is important for a variety of applications, including water resource management, drought monitoring, climate change, and the efficiency of crop irrigation [3–6]. Numerous methods have been used over the past decades to measure *ET*, including lysimeters, Bowen ratio, and eddy covariance (*EC*) flux towers. However, these methods represent limited sampling areas [7], and the measurements are best interpreted for homogeneous surfaces [8]. Spatial techniques are needed to accurately quantify *ET* for improved irrigation scheduling and water management decision support, particularly in complex canopies such as vineyards, which have non-uniform and complex vertical canopy structure, wide and variable row spacing, and deep and complex rooting systems [9]. This canopy structure produces large diurnal changes in solar radiation exposure to soil and plants [9] and requires sophisticated radiation extinction modeling [10,11]. Meanwhile, row spacing ranges between 2.4 m and 3.6 m for vineyards [12], and between 3.6 m and 6 m for orchards trees [13]. Water-limiting conditions across different vineyards in drought-stricken areas, such as California, necessitate the assessment of irrigation demand to set up agricultural water management strategies and decisions [14]. According to the USDA, California produces over 90% of U.S. wine, with a steady growth reaching 635,000 acres [15] in 2019. The high evaporative demand with limited rainfall in the vineyard growing season (May–September), along with the need to achieve grapevine stress targets, constitutes a significant challenge for irrigation scheduling to ensure vineyard productivity [16].

Advances in methods for measuring and modeling the interactions of vineyards with the environment require a better understanding of the processes influencing energy, water, and carbon exchange for highly organized and complex structure perennial crops. Various remote sensing platforms, including satellites, manned aircraft, and small unmanned aerial systems (*sUAS*), improve the potential availability of surface information for estimating *ET* at different spatial scales [17]. However, spatial information from satellites has limitations for *ET* estimation, including spatial and temporal resolutions, the presence of clouds at overpass time, and imagery delivery time [18]. These issues make satellite data challenging to use for the continuous mapping of daily *ET* (*ET_d*) and for real-time irrigation scheduling [19]. However, data fusion methodologies using multiple satellite platforms have improved capabilities for generating daily *ET* on a more routine basis [20,21] and for irrigation scheduling [22]. While manned aircraft have the ability to gather high-resolution data on demand at different times of the day, they are usually cost-prohibitive and, therefore, unlikely to be used to conduct multiple flights over an area of interest [23]. The advent of advanced *sUAS* remote sensing technology with lightweight sensors could overcome some of the previously mentioned remote sensing platform limitations. Compared to satellites, *sUAS* can be described as “flexible in timing”, in that they can be operated as needed at almost any time [7]. Additionally, *sUAS* can provide high spatial and temporal resolution data at sub-meter and multispectral resolutions, although data quality and data processing workflows must be enhanced before *sUAS* can become an efficient data collection platform [24]. Moreover, the areal coverage from *sUAS* is limited compared to satellites. For example, the Landsat 8 scene size is 185 km × 180 km, while an *sUAS* is nearly 1.6 km × 1.6 km, depending on the sensor type and flight height.

Whether using satellite or aerial imagery, the ability to reliably extrapolate from one-time-of-day instantaneous ET (ET_i) to daily ET (ET_d) is most useful [25] and relevant for the water management of agricultural crops [3]. Although numerous daily ET datasets are available for different applications, these products are often calculated based on the Penman-Monteith approach, the Priestley-Taylor method, or the integration of multiple ET estimates at a coarse resolution ($\geq 0.25^\circ$) [26]. *EEFLUX* (Earth Engine Evapotranspiration Flux) is another source for obtaining daily ET information at 30-m spatial resolution using Landsat data and an energy balance model. However, its temporal resolution of 16 days [27] limits its capability for continuously monitoring ET and identifying the spatial variability in irrigation practices that can occur in less than one week. Many current research efforts are being directed towards daily ET estimation using surface energy balance models, among them the Two Source Energy Balance (*TSEB*) model. However, the *TSEB* model provides hourly surface energy fluxes, which requires a scaling/extrapolation approach for generating daily ET information. Several studies have compared different daily ET methods with an assumption that the ratio of latent heat flux (LE) to one energy balance term is constant throughout the day, yet no universal approach has been identified as suitable for all types of land surfaces. Previous studies have indicated that the accuracy of that approach (upscaling daily ET) is a function of land surface type. For example, the evaporative fraction (EF) approach produced the best agreement in bare soil [28] and soybean [19], while the incoming solar radiation (R_s) approach was deemed to be more efficient in estimating daily ET in grassland and woody savanna [29]. Another crucial issue for precise daily ET estimation is the proper selection of the time-of-day window. In the study conducted by Colaizzi et al. [28], the best time window for

extrapolating the hourly ET to a daily scale was shown to be within 1 or 2 h of solar noon. This conclusion was also supported by Jackson et al. [30], who identified the time-of-day window for acquiring the ET for daily ET estimation as within 2 h of solar noon. Therefore, some concerns, such as actual and potential satellite overpass times and cloudiness vs. time of day, should be identified clearly to avoid any error propagation in the daily ET estimation.

The need for accurate daily ET (ET_d) estimates raises two fundamental questions: (1) which daily ET extrapolation approach at grapevine row scales can provide reliable values under a variety of crop and environmental conditions and thermal-based ET models like $TSEB$? and (2) what time window for acquiring a remotely-sensed ET provides the most reliable daily ET using an extrapolation approach? Multiple efforts have been made to estimate ET_d for different crops; however, computing ET_d for complex canopies, such as vineyards and grapevine row scales, has not been adequately addressed. In this study, different extrapolation approaches from the literature were assessed for estimating daily ET from instantaneous $sUAS$ ET estimates for several vineyard sites across California. Specifically, this paper (a) assessed the performance of several daily ET extrapolation approaches using EC observations and $sUAS$ information, and (b) determined an optimal time window for ET upscaling from a single to a daily estimate.

3.1.1 Daily ET Upscaling Approaches

ET upscaling is commonly performed by assuming conservation of some ET metric over the daytime, generally known as a ratio between instantaneous ET and a reference variable at a specific time of day, and that nighttime E and T contributions (soil evaporation and plant transpiration) are negligible or represent some small percentage of the daytime

ET (on the order of 10%). This hypothesis is commonly known as energy self-preservation [29,31,32] and includes EF , R_s , and R_n/R_s ratio approaches. The second assumption in flux upscaling procedures is that cloud-free conditions persist throughout the daytime [28,33]. However, the clear-sky condition cannot be assured necessarily throughout the season. Other ET_d extrapolation approaches are characterized by a quasi-sinusoidal shape, such as Gaussian (GA) and Sine. These approaches assume that the diurnal variation of ET is similar to the solar irradiance, with the peak value at solar noon. A description of each approach is presented below.

3.1.1.1 Evaporative Fraction (EF) Approach

One of the most common schemes to extrapolate instantaneous evapotranspiration to a daily value is the evaporative fraction (EF) [34]. EF is defined as the ratio of latent heat flux (LE) to the available energy (the difference between net radiation, R_n , and soil heat flux, G), assumed to be constant throughout daytime hours. The EF approach is presented in Equation (3.1), as follows:

$$ET_d = \left(\frac{LE}{R_n - G} \right) \left(\frac{c}{\rho_w \lambda} \right) (R_n - G)_d \quad (3.1)$$

where ET_d is the daily ET (mm/day), LE is the instantaneous latent heat flux (W/m^2), R_n is the instantaneous net radiation (W/m^2), G is the instantaneous soil heat flux (W/m^2), ρ_w is the water density (kg/m^3), λ is the latent heat of vaporization for water (MJ/kg), $(R_n - G)_d$ is the total daily available energy ($MJ/m^2/day$), and c is a factor equal to 1000 to convert meters to millimeters.

Numerous studies have considered the tendency of the EF to be nearly constant during the daytime [35]; however, the combination of soil moisture, weather conditions,

topography, and biophysical conditions has an impact on the conservation (or variability) of the EF in the daytime [31]. According to Hoedjes et al. [36], self-preservation of the EF approach is applicable under dry conditions, while under wet conditions, the EF is no longer valid. Nonetheless, a previous study by Crago [32], which used Bowen ratio stations over natural grassland, indicated that, for clear days, the midday EF is a good indicator of the daytime average value of the EF compared with cloudy days, but the values are still underestimated from the daytime average EF due to the concave-up shape of the diurnal variation of the EF . This finding is also supported by Li et al. [37], who found that the EF is relatively close to the daily average EF in the 1000 to 1500 timeframe, and could be used to guide vineyard irrigation practices in arid regions. However, the study by Zhang and Lemeur [38], which used 12 surface network stations called *Système Automatique de Mesure de l'Evaporation Réelle (SAMER)* over an area composed of forest (40%) and mixed agriculture (60%), indicated that the EF varies during the daytime and could not be used as a guide for ET_d estimates due to factors such as available energy, soil moisture, and other environmental variables. According to the study by Gentine et al. [39], which examined the influence of environmental factors (incoming solar radiation, wind speed, air temperature, soil water content, and leaf area index) on the diurnal behavior of the EF over wheat and olive, indicated that EF is strongly linked to soil moisture availability and canopy cover. As such, the EF increases with increasing the soil moisture and/or fractional cover. On the other hand, they found that the phase difference between net radiation (R_n) and the soil heat flux (G) must be well-characterized in application models that invoke the EF daytime self-preservation.

3.1.1.2 Solar Radiation (R_s) Approach

Another approach for extrapolating ET_i to ET_d is the R_s approach, which is similar to the EF but replaces the available energy ($(R_n - G)$, instantaneous or daily) term with the incoming solar radiation (R_s) as a reference variable. This approach, developed by Jackson et al. [30], assumes that the diurnal ET variation is similar to the solar radiation ($ET \sim R_s$), that is, the ET is highly correlated and proportional to the R_s . Equation (3.2) demonstrates the expressions for calculating ET_d using the R_s approach.

$$ET_d = \left(\frac{LE}{R_s} \right) \left(\frac{c}{\rho_w \lambda} \right) R_{s_d} \quad (3.2)$$

where R_{s_d} is the daily solar radiation ($\text{MJ/m}^2/\text{day}$), and R_s is the instantaneous solar radiation (W/m^2). Other parameters are similar to the EF approach.

According to Van Neil et al. [40], the R_s approach is robust when upscaling ET_i to multiple timeframes (e.g., daily, 8-day, and monthly). Moreover, many studies have indicated that solar radiation (R_s) is the most robust scalar approach that explains the ratio between the ET_d and ET_i [41].

3.1.1.3 Ratio of Net Radiation-to-Solar Radiation (R_n/R_s) Approach

The R_n/R_s approach is another approach to scale up ET_i to ET_d using the evaporative fraction (EF) and the ratio of net radiation-to-solar radiation (R_n/R_s) [42]. The R_n/R_s approach is presented in Equation (3.3).

$$ET_d = \left(\frac{LE}{R_n - G} \right) \left(\frac{R_n}{R_s} \right) \left(\frac{c}{\rho_w \lambda} \right) R_{s_d} \quad (3.3)$$

The parameters of this approach are explained in the EF and R_s approaches.

3.1.1.4 Sine Approach

The Sine approach, developed by Jackson et al. [30], showed that the generic trend of the ET_i during the daylight period is similar to the solar irradiance and could be approximated by a Sine function, where the maximum irradiance occurs at solar noon (~12 p.m.). For cloudy days, the daily ET estimates using the Sine approach are less reliable or may be invalid. This implies that the ET_i responds strongly to solar radiation [38]. The approach has been investigated by Zhang and Lemeur [38], who found the Sine approach to be preferable to others for upscaling instantaneous ET values.

$$ET_d = ET_i \left(\frac{2N}{\pi \sin(\pi t/N)} \right) \quad (3.4)$$

where ET_i represents the instantaneous ET (mm/hr), N is the total time from sunrise to sunset (h) and can be calculated using Equation (3.5), and t is the time elapsed since sunrise (h).

$$N = 0.945\{a + b \sin^2[\pi(D + 10)/365]\} \quad (3.5)$$

In Equation (3.5), a and b are latitude-dependent constants, while D is the day of the year. For parameters a and b , Jackson et al. [30] developed a regression model that is a function of the latitude of the location, as shown in Equations (3.6) and (3.7), respectively.

$$a = 12.0 - 5.69 \times 10^{-2}L - 2.02 \times 10^{-4}L^2 + 8.25 \times 10^{-6}L^3 - 3.15 \times 10^{-7}L^4 \quad (3.6)$$

And

$$b = 0.123L - 3.10 \times 10^{-4}L^2 + 8.0 \times 10^{-7}L^3 + 4.99 \times 10^{-7}L^4 \quad (3.7)$$

where L is the latitude in decimal degrees.

3.1.1.5 Gaussian (GA) Approach

The Gaussian (GA) approach has been used recently by Liu et al. [43] to retrieve the ET_d from remotely sensed instantaneous ET . The study used ET_i observations from an EC system and found that the ET diurnal variation follows a Gaussian-fitting curve. When comparing this approach to the Sine and EF approaches, results from the study of Liu et al. [43] indicated that GA is more accurate using the eddy covariance (EC) system.

$$ET_d = w \sqrt{\frac{\pi}{2}} \times ET_i \times e^{2((t_i - t_c)^2 / w^2)} \quad (3.8)$$

where w is the width that equals 2δ , δ is the standard deviation of ET_i values, t_i is the time of the instantaneous ET (ET_i), and t_c is the time when ET_i arrives at maximum value in the diurnal variation.

3.1.2 Two Source Energy Balance (TSEB) Model

The $TSEB$ model was developed by Norman et al. [44] to explicitly accommodate the difference between radiometric and aerodynamic surface temperatures that affect the energy exchange between soil and canopy systems and the lower atmosphere at instantaneous time scales. In the $TSEB$ model, turbulent energy fluxes are partitioned between canopy and soil, with different versions applied to separate between those components. These versions include the $TSEB-PT$ (Priestly-Taylor), the $TSEB-DTD$ (Dual Time Difference), $TSEB-2T-DMS$ (Data-Mining Sharpening of temperature), and $TSEB-2T$ (Dual Temperature). The $TSEB-PT$ version assumes a composite radiometric temperature (T_{rad}) that contains temperature contributions from the soil/substrate and canopy and is decomposed based on the vegetation fractional cover (f_c). The $TSEB-DTD$ version, developed by Norman et al. [45], uses two observations of T_{rad} : the first

observation obtained 1.5 h after the sunrise ($T_{rad,0}$), and the second one during the daytime ($T_{rad,1}$). The *TSEB-DTD* version uses the same approach as *TSEB-PT* to divide the composite T_{rad} between the soil/substrate and canopy temperatures. Using *TSEB-DTD* could reduce the error in flux estimations when uncertainty exists in local air temperature observations and absolute T_{rad} [46]. *TSEB-2T-DMS* uses a data-mining fusion algorithm to sharpen the land surface temperature (*LST*), which allows better discrimination between the soil/substrate and canopy temperatures [47]. The *TSEB-2T* approach was originally developed by Kustas and Norman [48] and was further refined and tested by Nieto et al. [49]. The main concept underpinning the *TSEB-2T* approach is to estimate the T_s and T_c from composite *LST* imagery using the relationship between the vegetation index (*VI*) and the *LST* to extract the T_s and T_c within a spatial domain. An early attempt at estimating vineyard water use at a field scale using aerial imagery with *TSEB* and a simple thermal-based contextual scheme suggests the *TSEB* is a robust approach for vineyard *ET* estimation [50]. In this study, the *TSEB* model was used to calculate the instantaneous *ET* at the time of the *sUAS* overpass, and the various schemes were used to extrapolate this one-time-of-day *ET* to a daily value. The *TSEB-2T* model was used for the Sierra Loma vineyard analysis, while the *TSEB-PT* was used for Ripperdan and Barrelli due to limitations in applying the *TSEB-2T* model to those two sites. The average value of the *LAI* was used for these sites, but the *TSEB-2T* requires the *LAI* spatial information to identify the threshold values of *NDVI* of soil, which is based on the empirical relationship between the *NDVI* and *LAI*. More details about the *TSEB-2T* can be found in Nieto et al. [49]. Applying the energy conservation and balance principles, the energy budget in the *TSEB* model can be described in the following equations:

$$R_n = LE + H + G, \quad (3.9)$$

$$R_{nc} = H_c + LE_c, \quad (3.10)$$

$$R_{ns} = H_s + LE_s + G, \quad (3.11)$$

where R_n is the net radiation, and G is the soil heat flux. H and LE are heat fluxes, where H is the sensible heat flux and LE is the latent heat flux. All flux units are expressed in W/m^2 . Subscripts of c and s represent the canopy and soil components, respectively. To estimate the sensible heat flux for soil and canopy, Norman et al. [44] proposed a series of soil vegetation resistive schemes (following an analogy with Ohm's law), as illustrated in Figure 3.1.

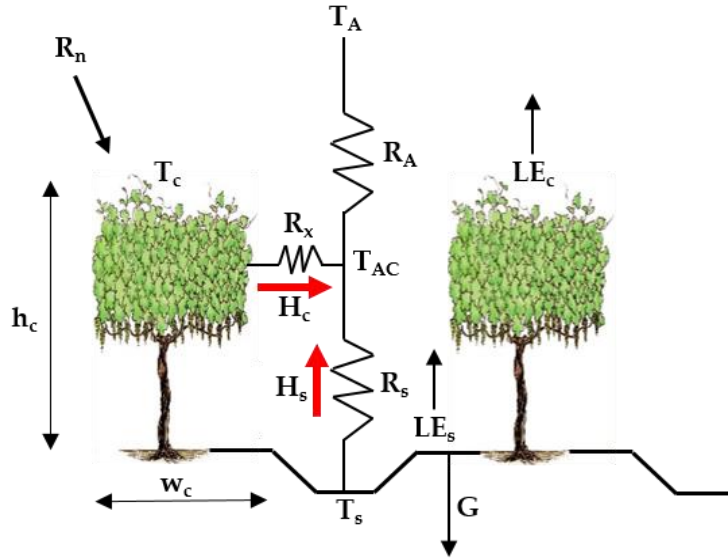


Figure 3.1 Schematic representation of the Two Source Energy Balance (*TSEB*) model.

$$H = H_c + H_s = \rho_{air} C_p \frac{T_{AC} - T_A}{R_A} = \rho_{air} C_p \left[\frac{T_c - T_{AC}}{R_x} + \frac{T_s - T_{AC}}{R_s} \right] \quad (3.12)$$

where ρ_{air} is the air density (kg/m^3), C_p is the heat capacity of the air at constant pressure ($J/kg/K$), T_A is the air temperature (Kelvins), T_c and T_s are the canopy and soil temperatures

(Kelvins), respectively, and T_{AC} is the temperature of the canopy air space (Kelvins), which is calculated with Equation (3.13).

$$T_{AC} = \frac{\frac{T_A}{R_A} + \frac{T_C}{R_x} + \frac{T_s}{R_s}}{\frac{1}{R_A} + \frac{1}{R_x} + \frac{1}{R_s}} \quad (3.13)$$

where R_A is the aerodynamic resistance to heat transport from the soil/canopy system, R_x is the boundary layer resistance of the canopy leaves, and R_s is the aerodynamic resistance to heat transport in the boundary layer close to the soil surface. All resistances are expressed in (s/m). The mathematical expressions used to compute the resistance network are detailed in Equations (3.14) – (3.16).

$$R_A = \frac{\ln\left(\frac{z_T - d_0}{z_{0M}}\right) - \psi_h\left(\frac{z_T - d_0}{L}\right) + \psi_h\left(\frac{z_{0M}}{L}\right)}{\kappa' u_*} \quad (3.14)$$

$$R_x = \frac{C'}{LAI} \sqrt{\left(\frac{l_w}{U_{d_0 + z_{0M}}}\right)} \quad (3.15)$$

$$R_s = \frac{1}{c(T_s - T_A)^{1/3} + bu_s} \quad (3.16)$$

where u_* is the friction velocity, calculated as the following:

$$u_* = \frac{\kappa' u}{\ln\left(\frac{z_u - d_0}{z_{0M}}\right) - \psi_m\left(\frac{z_u - d_0}{L}\right) + \psi_m\left(\frac{z_{0M}}{L}\right)} \quad (3.17)$$

In Equation (3.17), z_u and z_T are the measurement heights for wind speed (u) and air temperature (T_A), respectively, d_0 is the zero-plane displacement height, and z_{0M} is the roughness length for momentum. The unit of z_{0M} is expressed in m. In the *TSEB* model versions, the roughness length of momentum (z_{0M}) is assumed to equal the roughness

length for heat transport (z_{0H}), as the aerodynamic resistance of the canopy elements (R_x) already takes into account the different efficiencies between momentum and heat transport. κ' represents the von Karman's constant, which is equal to 0.4. Ψ_h and Ψ_m are the adiabatic correction factors for heat and momentum, respectively. The details of these two factors are described in Brutsaert [51]. In Equation (3.15), C' is assumed to be $90 \text{ s}^{1/2}/\text{m}$ and l_w represents the average width of leaf (m). The coefficients (b and c) in Equation (3.16) depend on the turbulent length scale in the canopy, the soil-surface roughness, and the turbulence intensity in the canopy. More details can be found in the work by Nieto et al. (2019a), Nieto et al. (2019b), Kustas et al., and Kondo and Ishida [11,49,52,53].

3.2 Methodology

3.2.1 Study Area

The experiment was conducted within three different climate regions located in California, as shown in Figure 3.2. All of these sites are part of the Grape Remote Sensing Atmospheric Profile and Evapotranspiration eXperiment (*GRAPEX*) project [54], led by the USDA ARS in collaboration with E&J Gallo Winery, University of California in Davis, Utah State University, NASA, and others. The overall objective of the *GRAPEX* project is to provide the vineyard manager and grower with spatially distributed, remotely sensed *ET* information for improving irrigation water use efficiency and detecting crop stress in multiple vineyard blocks. This would facilitate water conservation efforts in California's Central Valley, which has been experiencing frequent and severe drought conditions. The project began in 2013 at two pinot noir blocks located within the Sierra Loma Vineyard near Lodi, California (38.29° N , 121.12° W) in Sacramento County (see Figure 3.2) [7]. The two vineyard blocks, north and south, differed in maturity and age, having been

implemented in 2009 and 2011, respectively. The configuration of the trellising system in both fields is the same, with vine trellises 3.35 m apart and an east–west orientation. In 2017, the *GRAPEX* project extended the observations to include two additional vineyards: Barrelli vineyard ($38.75^{\circ} N, 122.98^{\circ} W$), located near Cloverdale, California, and Ripperdan vineyard ($36.84^{\circ} N, 120.21^{\circ} W$), located near Madera, California. With the expansion of the *GRAPEX* project from Sierra Loma to the Barrelli site to the north and Ripperdan to the south, a large range in trellis designs, climate regions, vine varieties, canopy structure, and vine physiology are represented. The Ripperdan vineyard was planted in 2009, whereas the Barrelli vineyard was implemented in 2010. Both the Barrelli and Ripperdan vineyards employ different plantation structures and vine varieties. The vine rows in Barrelli have a northeast–southwest row orientation, with a row spacing of 3.35 m and predominately Cabernet Sauvignon vine variety, while in Ripperdan, the row direction is east–west, with a row spacing of 2.74 m growing Chardonnay and Merlot. Data collection campaigns/intensive observation periods (*IOPs*) in these sites were conducted in the veraison period (from mid-July to early August), when the crop evaporative demand increases.

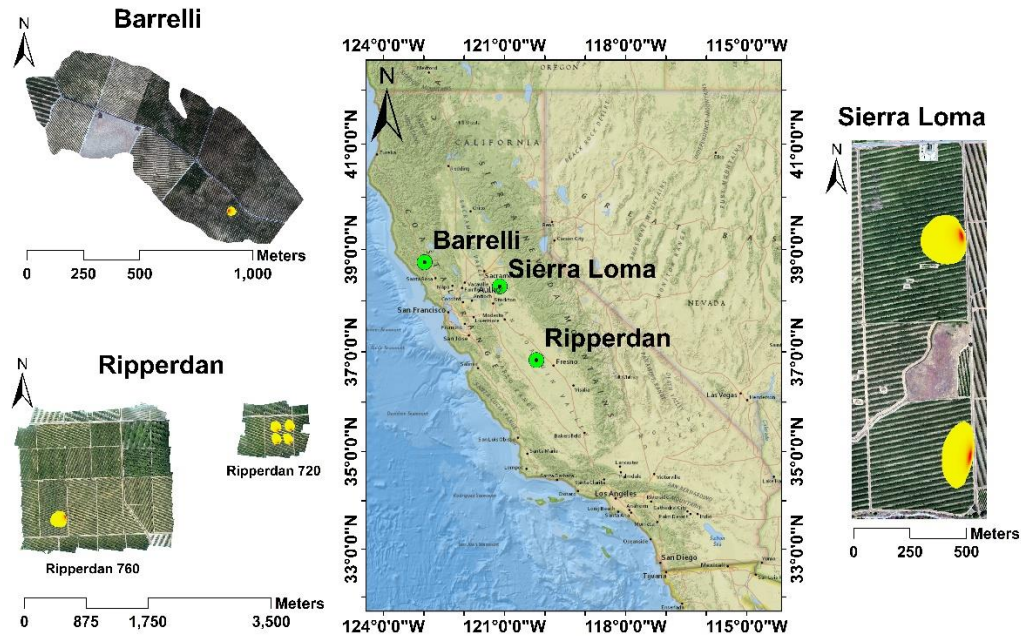


Figure 3.2 Layout of study vineyards in Central Valley, California with estimated typical flux footprint/source area for the *EC* towers.

3.2.2 Procedure

Figure 3.3 illustrates the procedure used for this study. First, available eddy covariance (*EC*) flux tower data was filtered to select cloud-free days only. Then, five different ET_d approaches were applied to the *LE* fluxes from the *EC* measurements for upscaling the *ET* to the daily timescale. The analysis was performed using *EC* observations at different vine phenological stages (April–May, June–August, and September–October). Finally, daily *sUAS ET* information, produced using the *TSEB* model, and results from the five approaches for upscaling/extrapolating the daily *ET* were compared against the measured ET_d from the *EC* tower data. Two time windows were selected for the daily *ET* estimation: the first was near solar noon (1030–1330), and the second was in the afternoon (1430–1630). The reasons for these selections were (a) satellite overpass time, (b) *sUAS* flexibility, which allows for flights at different hours, including mid to late afternoon, and

(c) an opportunity to assess the suitability of using later (2+ hours after solar noon) *sUAS* flights for the estimation of daily *ET*.

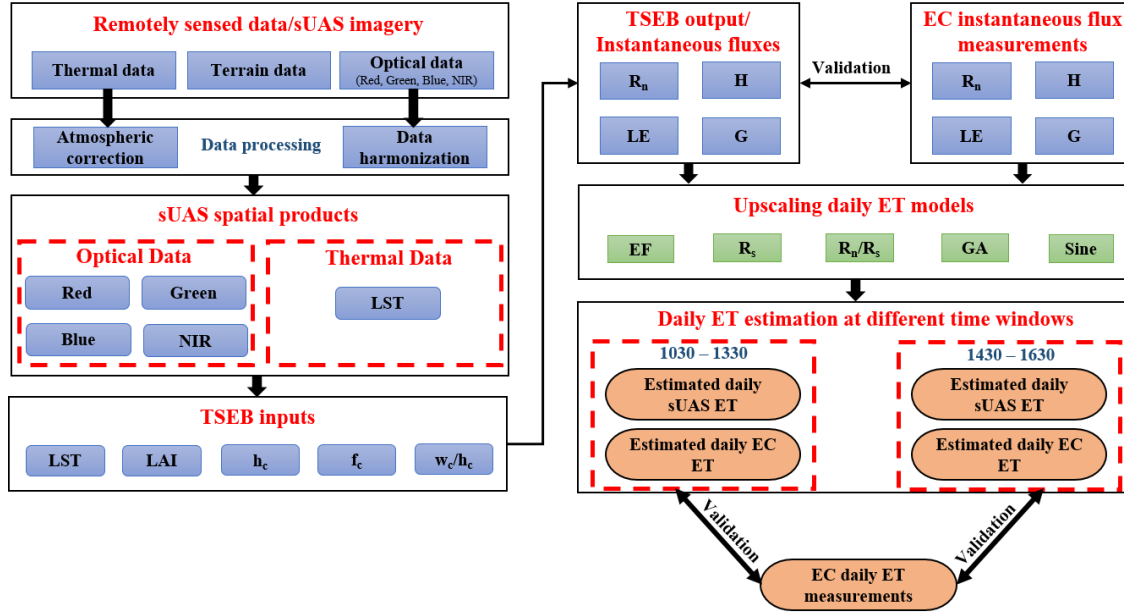


Figure 3.3 Study methodology for assessing different upscaling daily *ET* methods in *sUAS*.

3.2.2.1 *sUAS* Data Processing

The *AggieAir sUAS* Program at Utah State University (<https://uwrl.usu.edu/aggieair/>) [55] acquired high-resolution imagery at 450 m above ground level (*agl*), resulting in visible and near-infrared data at a 0.10 m spatial resolution, and a thermal spatial resolution at 0.6 m. The spectral range of the visible and near-infrared data was similar to Landsat; however, the thermal band range was wider, with a bandwidth spanning from 7 to 14 μm . Thermal data was acquired using a radiometrically calibrated micro-bolometer camera. Table 3.1 lists the information concerning the different *AggieAir sUAS* flights. In this study, the obtained *sUAS* images were georectified using ground control points (*GCPs*). Details of the optical and thermal information are presented below.

(a) Thermal Data

Changes in the transmissivity and atmospheric radiance can adversely affect the *sUAS* thermal data [56]. Details about thermal data calibration can be found in the work by Torres-Rua [56], while the work by Torres-Rua et al. [57] shows that the *TSEB* model is insensitive to surface emissivity. The *AggieAir sUAS* Program has a thermal protocol to use over 90% of overlap for thermal raw imagery collected after *sUAS* launching but before mission data collection upon internal lens temperature stabilization of the microbolometer camera. These two steps address potential vignetting as well as the temperature drifting effect observed in other *sUAS* applications.

(b) Optical Data

Radiometric agreement between different remote sensing platforms is important for further integration. An internal evaluation of the optical data obtained from different *sUAS* flights was performed by aggregating the high-resolution imagery up to Landsat scale using a point-spread function (*PSF*). The resulting 30-m pixels were found to agree with Landsat reflectance information. This is due to the use of different sensors than the ones used by Hassan-Esfahani et al. [58].

Table 3.1 Dates and times of *AggieAir sUAS* flights used in this study.

Site	Date	Time PST ¹	Spectral Bands ²	Satellite's Overpass
Sierra Loma	9 August 2014	1041	RGBNIR	Landsat
Sierra Loma	2 June 2015	1043	RGBNIR	Landsat
Sierra Loma	2 June 2015	1407	RGBRE	NA
Sierra Loma	11 July 2015	1035	RGBNIR	Landsat
Sierra Loma	11 July 2015	1414	RGB	NA
Sierra Loma	2 May 2016	1205	REDNIR	NA
Sierra Loma	2 May 2016	1504	REDNIR	NA
Sierra Loma	3 May 2016	1248	REDNIR	NA
Barrelli	8 August 2017	1052	RGBNIR	Landsat
Barrelli	9 August 2017	1043	RGBNIR	Landsat
Ripperdan 760	24 July 2017	1035	RGBNIR	Sentinel3
Ripperdan 760	25 July 2017	1035	RGBNIR	Landsat
Ripperdan 760	25 July 2017	1357	RGBNIR	NA
Ripperdan 760	25 July 2017	1634	RGBNIR	NA
Ripperdan 760	26 July 2017	1426	RGBNIR	NA
Ripperdan 760	5 August 2018	1044	RGBNIR	Landsat
Ripperdan 760	5 August 2018	1234	RGBNIR	NA
Ripperdan 720	5 August 2018	1044	RGBNIR	Landsat
Ripperdan 720	5 August 2018	1234	RGBNIR	NA

¹ PST: Pacific Standard Time. ² Spectral Bands explanation: R/RED = red, G = green, B = blue, RE = red edge, NIR = near infrared. ³ All *sUAS* flights included thermal information.

3.2.2.2 Eddy Covariance (*EC*) Fluxes

Surface energy fluxes (*LE* and *H*) were calculated from the *EC* measurements of the sonic temperature, water vapor, and vertical wind speed. In this study, the measurements obtained from the *EC* were averaged over a 60-min time interval to ensure appropriate averaging time for calculating the *H* and *LE*. The sensible heat flux was calculated from the product of the air density, the specific heat of air, and the covariance between the vertical wind speed and sonic temperature. The expression used to calculate *H* is shown in Equation (3.18).

$$H = \rho_a C_p (\overline{U_z' T_s'}) \quad (3.18)$$

where ρ_a is the air density (kg/m^3), C_p is the heat capacity of the air at constant pressure (J/kg/K), U_z' is the vertical wind speed (m/s), and T_s' is the sonic temperature (Kelvins).

The latent heat flux (*LE*) was calculated from the product of the latent heat of vaporization (λ) and the covariance between the vertical wind speed (U_z') and the water vapor density (ρ_v'). The formula used to calculate the *LE* is illustrated in Equation (3.19).

$$LE = \lambda (\overline{U_z' \rho_v'}) \quad (3.19)$$

where ρ_v' is the water vapor density (kg/m^3).

Table 3.2 describes the *EC* towers installed at the different vineyard sites to monitor *ET*. The *EC* measurements (April to October) obtained are the surface energy fluxes (R_n , *H*, and *LE*) and micrometeorological data. More details about the in-situ micrometeorological measurements can be found in the work by Nassar et al. [7].

Table 3.2 Description of *EC* towers in vineyards that were part of this study.

Vineyard	Number of <i>EC</i> Towers	Elevation (agl)	<i>EC</i> Tower Name	Latitude ¹	Longitude ¹	Period of Data (Years)
Sierra Loma	2	5	1	38° 16' 49.76"	−121° 7' 3.35"	5
			2	38° 17' 21.62"	−121° 7' 3.95"	5
Ripperdan 760	1	3.5	1	36° 50' 20.52"	−120° 12' 36.60"	2
Ripperdan 720	4	3.5	1	36° 50' 57.27"	−120° 10' 26.50"	1
			2	36° 50' 51.40"	−120° 10' 26.69"	1
			3	36° 50' 57.26"	−120° 10' 33.83"	1
			4	36° 50' 51.39"	−120° 10' 34.02"	1
Barrelli	1	3.5	1	38° 45' 4.91"	−122° 58' 28.77"	2

¹ coordinates are in WGS1984.

In Sierra Loma, each *EC* tower monitors grapevines of different ages, while 4 flux towers in Ripperdan 720 measure different water management approaches at 4 different blocks. In this study, the footprint analysis of each *EC* tower was performed to validate the results obtained from the *TSEB* model. The Kljun et al. [59] model was used for describing the fetch of the *EC* contribution area for the hourly period encompassing the *sUAS* flight times. The shape and orientation of the *EC* footprint depend on multiple micrometeorological conditions that are observed by the *EC* towers installed at the sites, which include the friction velocity, wind speed, wind direction, roughness length, standard deviation of the crosswind velocity, and Monin–Obukhov length as well as the *EC* tower height. In this study, the authors did not include any energy balance closure to the *EC* information to minimize biases.

3.2.3 Goodness-of-Fit Statistics

3.2.3.1 Quantitative Statistics

The performance indices to evaluate the daily *ET* approaches in this study involved comparisons of the modeled *ET* from the five different approaches against daily *ET* measurements from the *EC* towers. Computed statistical metrics included the root mean square error (*RMSE*), mean absolute error (*MAE*), mean absolute percentage error (*MAPE*), Nash–Sutcliffe efficiency coefficient (*NSE*), and the coefficient of determination (R^2). The *NSE* coefficient checks the capability of the model to reproduce the following statistical components: correlation coefficient of (r), mean (μ), and variance (s). *NSE* values range between $-\infty$ and 1, where 1 represents a perfect agreement, while a value of 0 means that the model results are not better than the average of the variable of interest, and values < 0 indicate unacceptable model performance [60].

$$RMSE = \sqrt{\frac{\sum_{i=1}^N (O_i - P_i)^2}{N}} \quad (3.20)$$

$$MAE = \frac{\sum_{i=1}^N |O_i - P_i|}{N} \quad (3.21)$$

$$MAPE = \frac{\sum_{i=1}^N \left| \frac{O_i - P_i}{O_i} \right| \times 100}{N} \quad (3.22)$$

$$NSE = 1 - \frac{\sum_{i=1}^N (O_i - P_i)^2}{\sum_{i=1}^N (O_i - \bar{O})^2} \quad (3.23)$$

$$R^2 = \left[\frac{\sum_{i=1}^N (O_i - \bar{O})(P_i - \bar{P})}{\sqrt{\sum_{i=1}^N (O_i - \bar{O})^2} \sqrt{\sum_{i=1}^N (P_i - \bar{P})^2}} \right]^2 \quad (3.24)$$

where O_i denotes the observed value, P_i denotes the modeled value, \bar{O} denotes the mean observed value, \bar{P} denotes the mean modeled value, and N represents the number of observations.

3.2.3.2 Graphical Representations

Different graphical representations were used to visualize and evaluate the datasets from the *EC* towers and the performance of the extrapolation techniques. Boxplots were created to describe the variance of surface energy fluxes (R_n , H , LE , and G) at each hour in the dataset. Boxplots were also used to evaluate the performance of the five daily *ET* extrapolation schemes by presenting the distribution of relative error at each individual hour during the daytime, as shown in Appendix B. Moreover, scatterplots were used to compare the modeled fluxes from *TSEB* and the measurements from *EC* systems to evaluate model performance.

3.3 Results and Discussion

3.3.1 Diurnal Variation of Energy Fluxes from *EC* Measurements

An example of the diurnal variation of surface energy fluxes (R_n , H , LE , and G) is shown in Figure 3.4 for the Sierra Loma vineyard. Diurnal variation plots for the other vineyard study sites (Ripperdan 760, Ripperdan 720, and Barrelli) are shown in Appendix Sections B.2.1, B.3.1, and B.4.1. The boxplot at each individual hour represents the seasonal variation (April to October) of surface fluxes due to changes in the irrigation scheduling and variations in weather conditions (wind speed, air temperature, vapor pressure deficit, and soil moisture) [61]. Overall, the behavior of R_n diurnal variation is similar among the different sites, as the solar radiation is relatively consistent. As shown

in Figure 3.4, R_n values are negative in the nighttime and late evening. In the daytime, R_n values vary, with maximum values of nearly 700 W/m^2 at solar noon depending on the daily solar radiation. The diurnal pattern of R_n is almost systematic with a peak value appearing during midday, around 1200 standard time. The diurnal distribution of both H and LE exhibits a typical concave-down shape, with minimums in the early morning and late afternoon. The peak value appears near solar noon, between 1030 and 1330. Overnight, the H is almost negative, while the LE is approximately equal to zero, as the incoming solar radiation (R_s) value is 0 at night. Although this is not always the case, the approximation may be acceptable for night [62]. In summertime, the LE value overnight is very small and rarely exceeds 5–10% of the daily total [63]. The study by Shapland et al. [64], which was conducted to estimate the ET over vineyards in California, assumed that the turbulent fluxes are zero during the night to avoid the uncertainty associated with the flux measurement. Another study by Tolk et al. [65], which aimed to quantify the nighttime evapotranspiration $ET_{N\text{-to-}24\text{-h } ET}$ (ET_{24}) of irrigated and dryland cotton in a semiarid climate, indicated that the ratio of $ET_{N\text{-to-}ET_{24}}$ ranged from an average of 3% for a dryland cotton crop to around 7% for irrigated alfalfa. The contribution of $ET_{N\text{-to-}ET_{24}}$ was the result of a relatively high nighttime vapor pressure deficit (VPD) and wind speed.

Flux observations indicated that the LE values were higher than the H across the different vineyards, as shown in Figure 3.4 and Appendix Sections B.2.1, B.3.1, and B.4.1. These results stem from the fact that the vineyards are drip irrigated and, during most of the growing season, the cover crop is senescent, so ET is largely controlled by the vine canopy and, hence, mainly affected by the vine leaf stomatal conductance. The diurnal variation of soil heat flux (G) does not follow symmetric behavior, having a right skewness.

As demonstrated in Figure 3.4 and Appendix Sections B.2.1, B.3.1, and B.4.1, the G value is much lower than other energy fluxes (R_n , H , and LE), where the peak does not persist across different vineyard sites. For overnight and later evening, G is negative and could yield values around -100 W/m^2 , as shown in Figure 3.4d at Sierra Loma vineyard, with similar results obtained at the other vineyard sites included in this study. In the energy balance, usually, the G value is estimated as a portion of R_n ($\sim 0.35 R_n$) for remote sensing ET models. Meanwhile, the G value is highly affected by the LAI , canopy architecture, row direction, and trellis design, as well as the incoming solar radiation. Reducing the canopy fractional cover results in an increased daytime soil heat flux (G), while increasing the areal coverage of vegetation leads to decreased soil heat flux and greater above-canopy latent heat fluxes, as long as there is ample root zone soil moisture to meet the atmospheric demand.

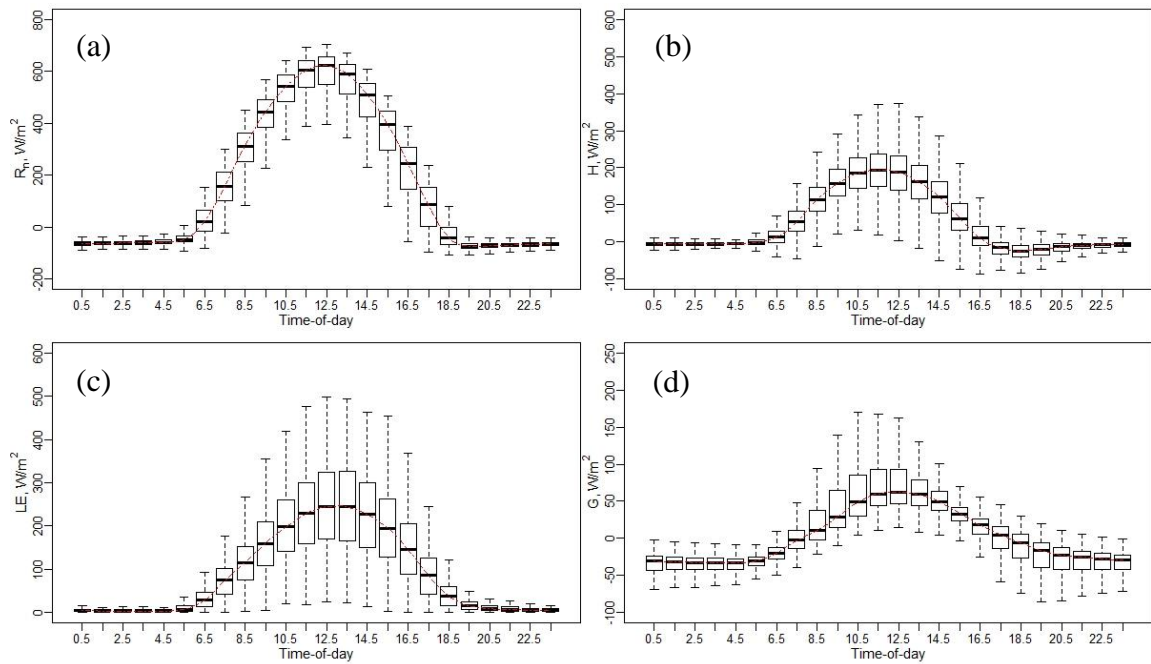


Figure 3.4 Diurnal variations of energy fluxes at Sierra Loma Sites 1 and 2 for the years 2014 to 2018, from the April to October irrigation season. (a) Net radiation (R_n), (b) sensible heat flux (H), (c) latent heat flux (LE), (d) soil heat flux (G).

Figure 3.5 shows the LE diurnal variation at each individual EC tower included in this study. The boxplot at every hour represents the seasonal variation from April to October due to weather changes and irrigation scheduling. Overall, the general temporal trend of the LE has a shape that resembles solar radiation at different vineyard sites, with a peak value near solar noon, between 1030 and 1330. In early morning and overnight, the LE values were close to zero. Comparing the diurnal variation of LE at different vineyards, the Barrelli site had the lowest LE values. The Barrelli vineyard is located near the Pacific Coast shoreline, which brings cool maritime air that cools the warm interior valleys. The cool and moist air over Barrelli is associated with a decrease in the vapor pressure deficit (VPD) and more cloudiness, which causes a decrease in ET demand. In Sierra Loma and Ripperdan, the VPD and air temperature were higher than Barrelli, as both sites are exposed to a warm Mediterranean climate, which is characterized by abundant sunshine and a large day-to-night temperature difference and, therefore, increases the ET demand [66].

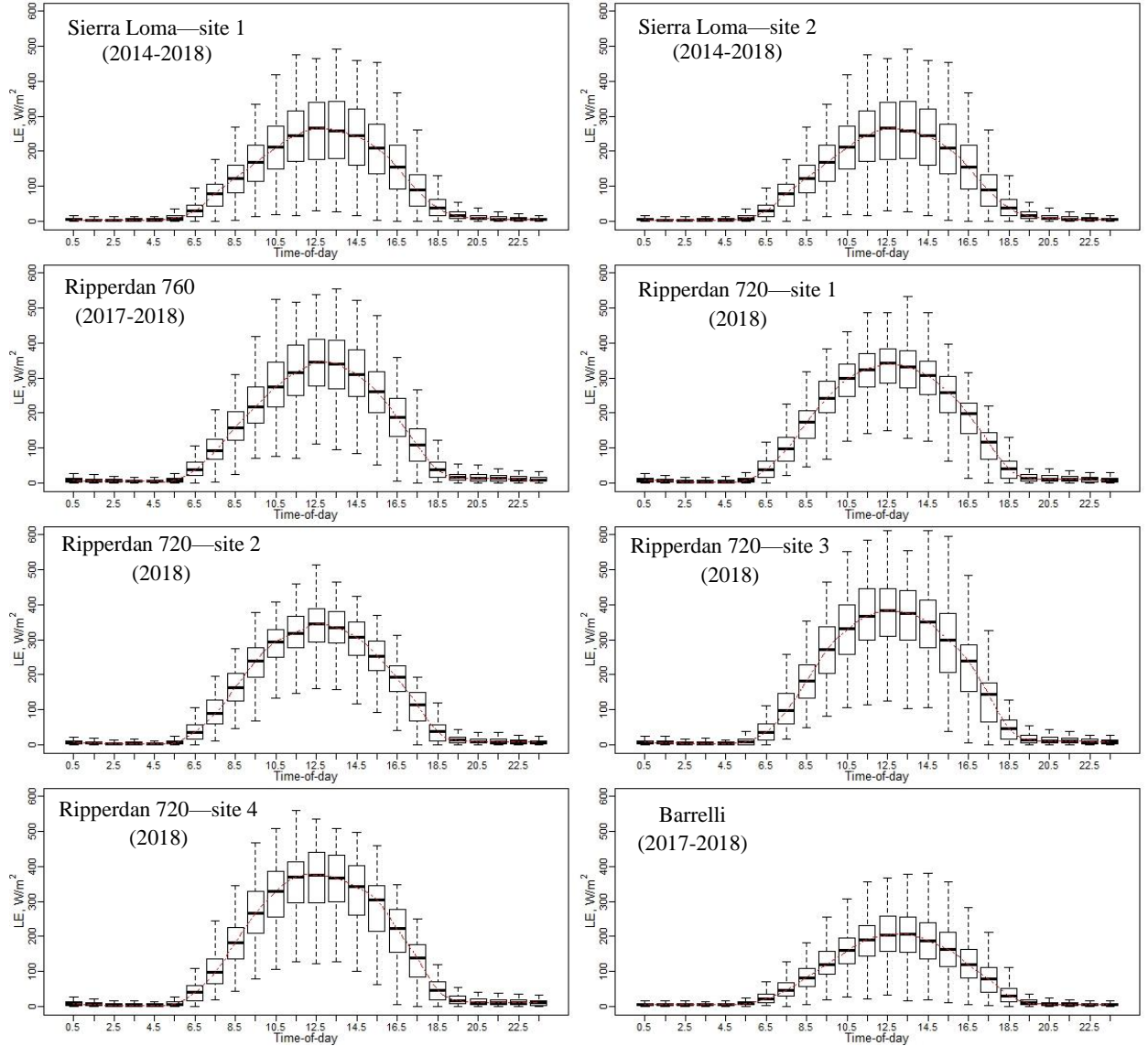


Figure 3.5 Diurnal variations of LE for each EC included in this study for the years 2014 to 2018, from the April to October irrigation season.

To compare the contribution of the ET at different hours to the daily ET , additional statistics were included, such as the ratio of hourly ET (ET_h)-to-daily ET (ET_h/ET_d) and the ratio of ET_h -to-maximum hourly ET ($ET_{h(max)}$) ($ET_h/ET_{h(max)}$). An example of the diurnal variation of both ratios (ET_h/ET_d and $ET_h/ET_{h(max)}$) at different phenological vine stages (bloom, April–May; veraison, June–August; and post-harvest, September–October) is shown in Figure 3.6 for the Sierra Loma vineyard, while the figures of other sites are shown

in Appendix Sections B.2.2, B.2.3, B.3.2, B.3.3, B.4.2, and B.4.3. The general trends of ET_h/ET_d and $ET_h/ET_{h(max)}$ resemble a Gaussian behavior, with peak values at solar noon. The results also indicate that the vine phenological stage could affect both ratios in terms of the variation at each individual hour during the daytime. In the veraison stage, low variation was observed in the ET_h/ET_d and $ET_h/ET_{h(max)}$ compared with the bloom and post-harvest stages. In the early growing season (April), the inter-row cover crop was at peak greenness, which was senesced by early June as the vines' leaves were fully developed (see the phenocam data at different study sites showing the different vine phenological stages: <https://hrsl.ba.ars.usda.gov/awhite/CAM/>). This transition resulted in the main source of transpiration from the inter-rows, where the turbulent exchange was relatively suppressed to the vines with high potential coupled with the atmosphere [67]. On the other hand, the high variability observed in ET_h/ET_d and $ET_h/ET_{h(max)}$ ratios in the time period between September and October were due to vines senescence and stress in the post-harvest stage due to a lack of irrigation and low atmospheric demand, where the daily ET decreased significantly. Moreover, as shown in Figure 3.6, the results of the ET_h/ET_d indicate that the major contribution of the daily ET came from the midday time between 1030 to 1530, which represents at least 65% of the daily total. However, in early morning (~0630 to 0930) and evening (~1630 to 1930), the value of ET_h/ET_d was low, which together represents 25–35% of the daily ET .

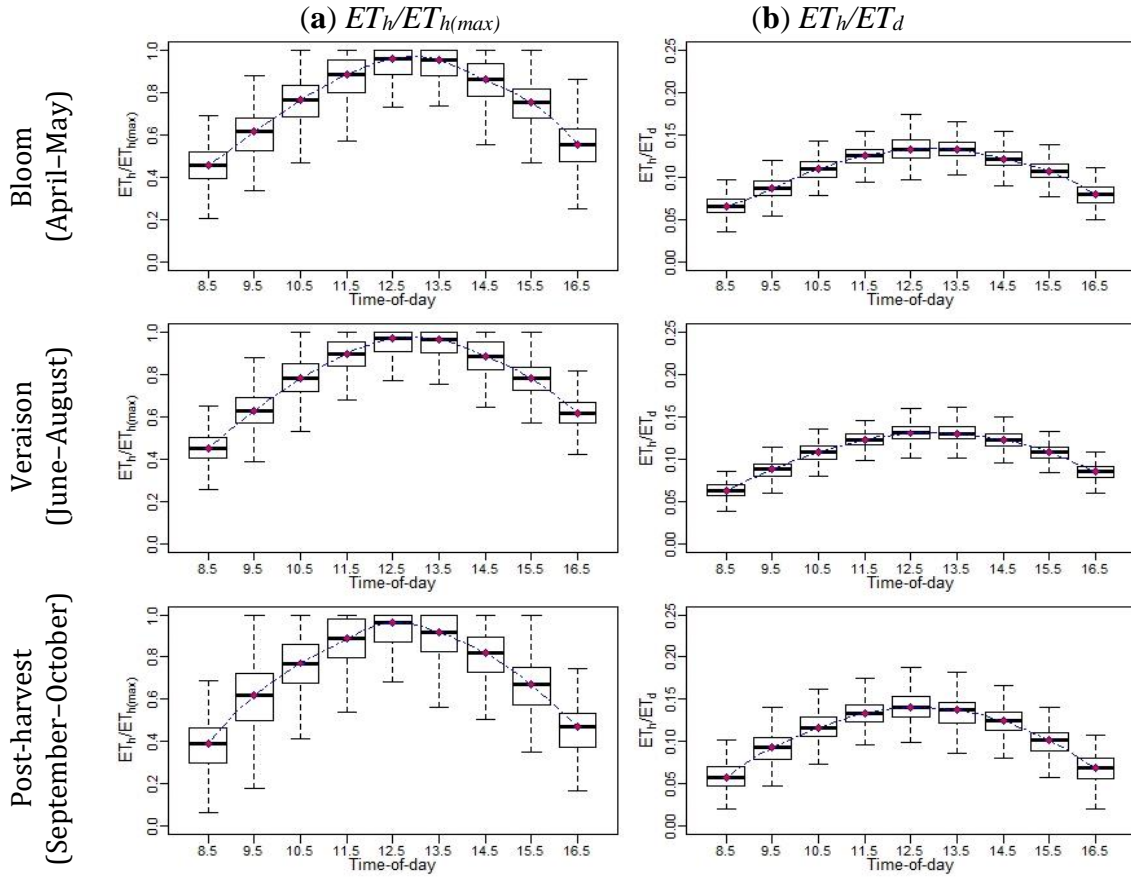


Figure 3.6 An example of the diurnal variations of (a) $ET_h/ET_{h(max)}$ and (b) ET_h/ET_d at different phenological vine stages for Sierra Loma Sites 1 and 2 between 2014 and 2018.

3.3.2 Comparison between Different ET_d Extrapolation Approaches Using the EC Measurements

Table 3.3 lists the goodness-of-fit statistics comparing the five different extrapolation approaches used to compute daily ET from the hourly EC at two different time windows: near solar noon (1030–1330) and afternoon (1430–1630) PST. The detailed statistics for $RMSE$ and E_r at each individual hour at the different vineyard sites are shown in Appendix Sections B.1.1, B.1.2, B.2.4, B.2.5, B.3.4, B.3.5, B.4.4, and B.4.5. The analysis also considered all months segregated into three vine stages/periods (April–May, June–August, and September–October) to investigate how vine phenology could affect the accuracy of estimated daily ET due to the timing of both water uptake and growth. In general, the results

indicate that the performance of the methods had different utility in computing an accurate daily ET at different vine canopy development and grapevine phenological stages (bloom, veraison, and post-harvest). As shown in Table 3.3, the $MAPE$ was lower during the summer months (June–August) compared with the early growing season (April–May) of the vine crop and after harvesting time. Meanwhile, the results indicate that the extrapolated EC -derived ET_d could be affected by the time during the day, as a better agreement was observed using instantaneous (hourly) EC ET between 1030 and 1330 PST than within the second time window (1430–1630 PST). Across multiple ET_d upscaling approaches during the veraison stage and in the 1030–1330 time window, the $MAPE$ yielded values ranging between 8% and 22%, while in the 1430–1630 time window, the $MAPE$ range increased and yielded values between 15% and 35%.

The results indicate that three methods (R_s , GA , and EF) among the five daily ET models have the best performance (low $RMSE$ and $MAPE$ values and a high NSE value). The R_s showed better agreement with the ground measurements among the other extrapolation approaches and was less sensitive to LE variation due to seasonal and climate differences, and particularly when using the one-time-of-day ET in the time window between 1030 and 1330. Using the R_s approach, $RMSE$ values were less than 0.4 mm/day, while the NSE value was higher than 0.9 for all vine stages (season). These results are also supported by a previous study conducted by Cammalleri et al. [29], which compared several upscaling daily ET methods using observations from flux towers within the United States and were evaluated over multiple seasonal cycles. They reported that using solar radiation (R_s) for converting the instantaneous to a daily ET value is more robust. Comparing the less accurate daily ET extrapolation techniques, the Sine method marginally

outperformed the R_n/R_s approach in terms of moderate to high error within the time window (1030–1330) in the bloom and veraison stages, while in the post-harvest stage, the R_n/R_s method gave better results than the Sine approach. Using these approaches increased the $RMSE$, which yielded values above 0.65 mm/day, while the $MAPE$ values were greater than 20% in the time window between 1030 and 1330 for all vine stages (season). This implies that the Sine and R_n/R_s techniques do not work properly for a daily ET estimate in vineyards.

Table 3.3 Goodness-of-fit statistics of daily ET extrapolation methods at two different time windows (1030–1330 and 1430–1630 PST) using only EC tower information in California.

Vine Stage	Method	1030–1330					1430–1630				
		RMSE (mm/day)	MAE (mm/day)	MAPE (%)	NSE	R ²	RMSE (mm/day)	MAE (mm/day)	MAPE (%)	NSE	R ²
Bloom (April–May)	<i>EF</i>	0.36	0.28	10	0.83	0.85	1.02	0.71	29	−0.75	0.55
	<i>R_s</i>	0.35	0.26	10	0.85	0.87	0.64	0.50	19	0.31	0.81
	<i>R_n/R_s</i>	1.33	0.82	29	−1.25	0.15	1.49	1.13	43	−2.68	0.06
	<i>GA</i>	0.38	0.30	11	0.81	0.87	0.87	0.72	28	−0.26	0.77
	<i>Sine</i>	0.56	0.47	18	0.60	0.86	0.50	0.39	15	0.59	0.82
Veraison (June–August)	<i>EF</i>	0.47	0.32	9	0.81	0.85	0.97	0.70	21	0.07	0.63
	<i>R_s</i>	0.38	0.29	8	0.88	0.89	0.70	0.57	17	0.51	0.83
	<i>R_n/R_s</i>	1.67	0.90	22	−1.41	0.17	1.78	1.26	35	−2.14	0.08
	<i>GA</i>	0.43	0.33	9	0.84	0.87	1.12	0.96	29	−0.23	0.72
	<i>Sine</i>	0.65	0.53	14	0.64	0.86	0.63	0.51	15	0.61	0.84
Post-harvest (September–October)	<i>EF</i>	0.28	0.21	13	0.93	0.95	2.53	0.68	55	−6.76	0.10
	<i>R_s</i>	0.25	0.19	11	0.94	0.95	0.49	0.37	23	0.71	0.92
	<i>R_n/R_s</i>	0.47	0.31	16	0.80	0.88	1.02	0.63	42	−0.27	0.62
	<i>GA</i>	0.40	0.31	17	0.86	0.95	0.53	0.41	25	0.66	0.93
	<i>Sine</i>	0.77	0.64	36	0.45	0.92	0.31	0.24	16	0.88	0.92
All stages (Season)	<i>EF</i>	0.41	0.29	10	0.91	0.92	1.50	0.70	31	−0.57	0.43
	<i>R_s</i>	0.34	0.26	9	0.93	0.94	0.64	0.51	19	0.71	0.90
	<i>R_n/R_s</i>	1.38	0.73	22	−0.08	0.37	1.56	1.08	38	−0.71	0.23
	<i>GA</i>	0.41	0.32	12	0.90	0.93	0.95	0.77	28	0.37	0.86
	<i>Sine</i>	0.67	0.55	21	0.75	0.91	0.54	0.42	15	0.80	0.91

Numbers in bold are the best statistical results for each timeframe and vine stage.

3.3.3 Assessing the Instantaneous *TSEB ET* Versus *EC* Measurements

As a first step toward evaluating the performance of the *TSEB* model, a comparison between the field observations from the *EC* and modeled fluxes using the *TSEB* and the *sUAS* (Table 3.1) at four different study sites are presented in Figure 3.7. A more detailed model performance assessment for each energy flux term is shown in Table 3.4. Surface fluxes were estimated from the *sUAS* based on the *TSEB* model, averaged over the *EC* footprint, and then compared against the measured fluxes. As shown in Figure 3.7, the estimated fluxes derived from the *TSEB* model generally align along the 1:1 line at the different vineyard sites, indicating good agreement between the modeled and measured fluxes. Net radiation (R_n) demonstrates a close agreement with the in-situ measurement, as indicated by lower *RMSE*, *MAE*, and *MAPE* values, and a high *NSE* value. The *MAE* and *MAPE* for R_n estimates at the different vineyard sites were less than 40 W/m² and 10%, respectively, while the *RMSE* ranged between 26 W/m² and 43 W/m². The *NSE* yielded high values at the Sierra Loma and Ripperdan 760 sites, accounting for more than 0.85; however, at the Ripperdan 720 and Barrelli vineyards, the values decreased to less than 0.2 and 0.6, respectively. The results for H agreed well with the *EC* observations at the Sierra Loma and Ripperdan sites, with the *MAE* and *MAPE* values less than 43 W/m² and 28%, respectively, while the *RMSE* values were less than 55 W/m². However, at the Barrelli vineyard, the *RMSE* and *MAE* increased to 62 W/m² and 46 W/m², respectively, while the *MAPE* value was 22%. However, this site had only 2 samples to compute the difference statistics, making it difficult to reach any conclusions concerning the model performance in relation to the other sites. The results for LE indicate a slight increase in the *RMSE* compared to the H , varying between 51 W/m² and 58 W/m² at the Sierra Loma and

Ripperdan vineyards. However, the Barrelli site results indicate that the *RMSE* of the *LE* was less than the *H*. Overall, the higher values of the *RMSE* obtained for the *LE* are attributed mainly to the *TSEB* method for calculating the *LE*, which is solved as the residual component of the surface energy balance, $LE = R_n - H - G$. Therefore, the uncertainties associated with the calculation of energy fluxes (R_n , H , and G) within the *TSEB* method can adversely affect the estimation of the *LE*. Another potential uncertainty could be related to the no use of flux closure in the eddy covariance (*EC*) data. According to previous studies (e.g., Neale et al. 2012) [68], heat fluxes (H and LE) are acceptable when the *RMSE* ranged between 20 W/m² and 60 W/m². This implies that the results of the H and LE obtained from the *TSEB* model across different vineyards were within an acceptable range and similar to prior studies [50]. The results for G indicate poor performance across the different vineyard sites, except for Ripperdan 720 vineyard, which had a *MAPE* of less than 25%. Part of these discrepancies between the modeled and observed G can be attributed to the assumption used in this study for calculating G , which is that as a portion of the soil net radiation (R_{ns}), $G = 0.35 R_{ns}$. This value was obtained based on a proposed method by Nieto et al. [49], which takes into consideration the diurnal variation of the G/R_{ns} and found high scattering/uncertainty in the relationship, with an average value of 0.35 near solar noon. In this study, most of the flights were between 1000 and 1500, and at these time intervals around solar noon, the G/R_{ns} fraction remained rather constant at ~0.35 (see Figure 4 in Nieto et al. (2019)) [49]. Therefore, for the sake of simplicity, and considering that the sinusoidal approach might be site-dependent, the constant fraction at 0.35 was used. This value is also broadly applied over a wide range of crops and environments. Meanwhile, vineyards are characterized by strong heterogeneity, which

causes spatial and temporal variability in G values. According to Kustas et al. [69], the simple remote sensing methods for estimating G as a portion of R_n have significant uncertainty due to temporal variability in the G/R_n ratio.

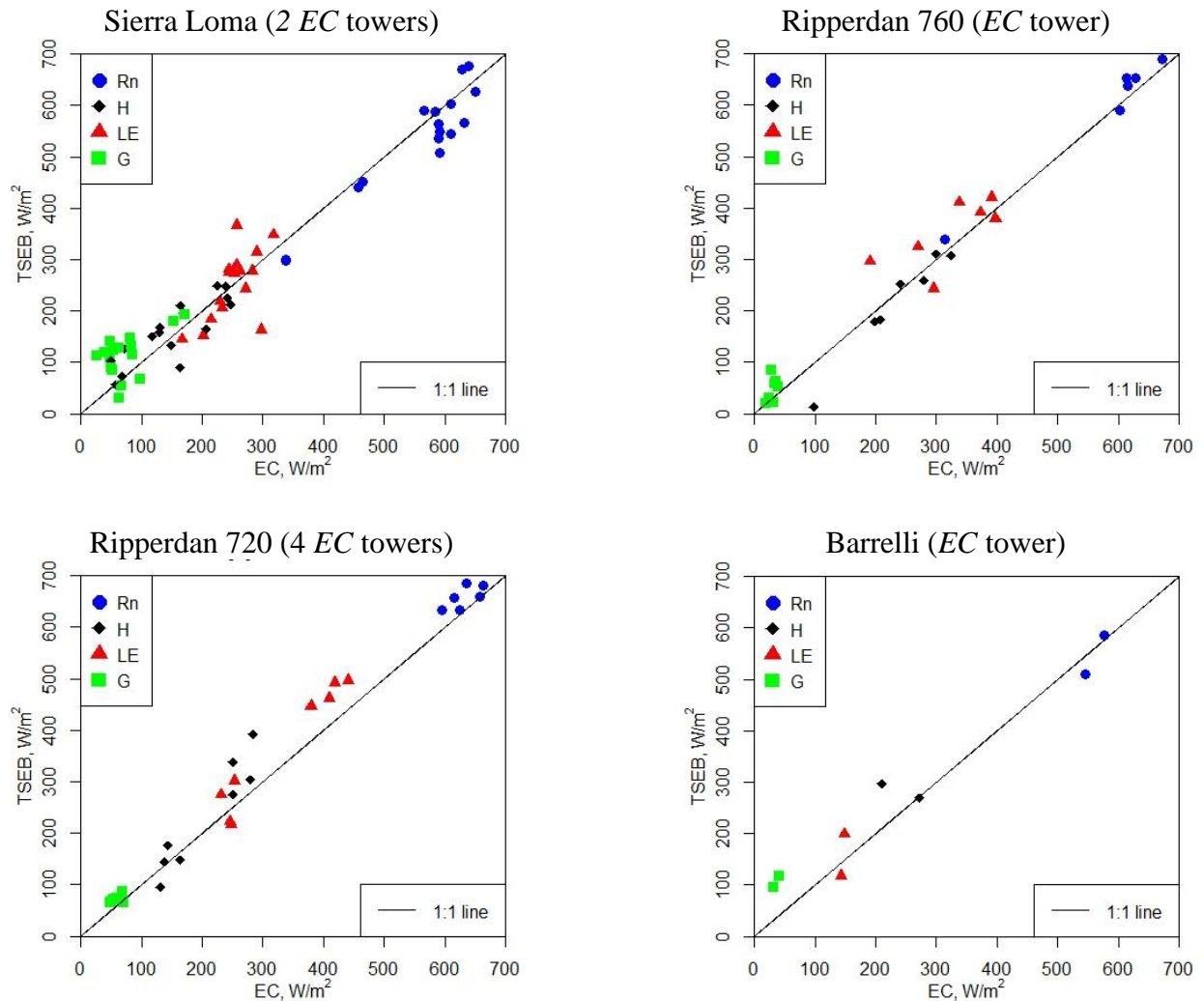


Figure 3.7 Comparison of instantaneous $TSEB$ $sUAS$ energy fluxes against EC measurements (without flux closure). The presented subplots include the available $sUAS$ imagery, as described in Table 3.1.

Table 3.4 Goodness-of-fit statistics between the eddy covariance (*EC*) and the instantaneous *TSEB sUAS* fluxes at the different vineyard sites of this project.

Site	Fluxes	RMSE (W/m ²)	MAE (W/m ²)	MAPE (%)	NSE	R ²
Sierra Loma	R_n	43	36	7	0.85	0.90
	H	37	31	27	0.61	0.70
	LE	51	38	15	0.40	0.40
	G	55	50	96	0.08	0.30
Ripperdan 760	R_n	36	31	5	0.91	0.96
	H	37	27	19	0.86	0.96
	LE	58	50	19	0.28	0.52
	G	27	20	66	0.11	0.21
Ripperdan 720	R_n	35	28	4	0.17	0.53
	H	54	42	20	0.73	0.90
	LE	52	49	15	0.81	0.94
	G	14	14	23	-0.01	0.31
Barrelli	R_n	26	23	4	0.58	NA ¹
	H	62	46	22	-0.92	NA
	LE	40	38	26	0.11	NA
	G	71	71	196	0.01	NA
All vineyards	R_n	39	32	6	0.90	0.90
	H	43	34	23	0.80	0.80
	LE	52	43	17	0.70	0.80
	G	45	36	78	0.20	0.40

¹ NA because we had only two *sUAS* flights.

3.3.4 Assessment of the Daily *ET* Extrapolation Approaches Using *TSEB sUAS* Results

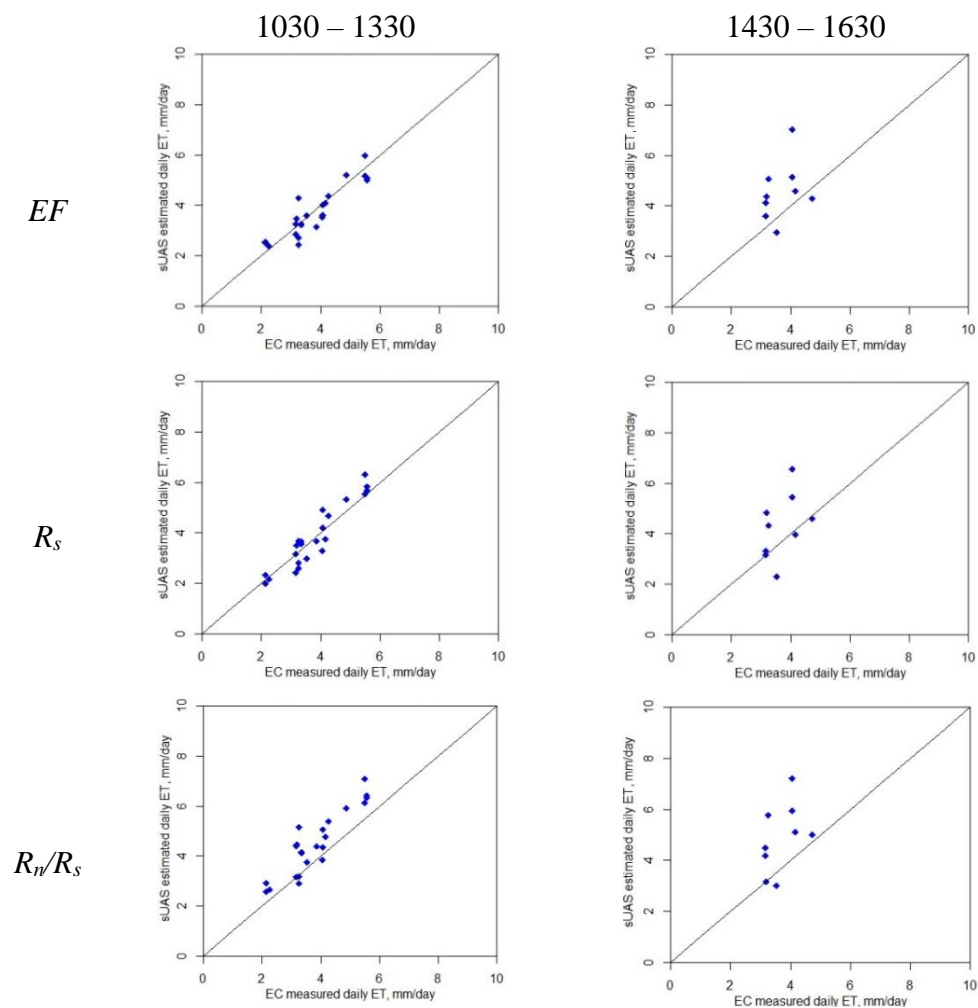
The accuracy of the daily high-resolution *ET* from the *TSEB* depends largely on an accurate instantaneous *ET* estimate at the time of acquisition of the *sUAS* imagery, as well as the reliability of the approach used to scale up the *TSEB*-derived *ET* to a daily value.

The five daily *ET* methods (*EF*, *R_s*, *R_n/R_s*, *GA*, and Sine) were applied using the modeled energy fluxes derived from the *TSEB* and compared against the *EC*-derived daily value, *ET_d*, calculated by integrating the daytime *LE* fluxes measured by *EC* towers. Table 3.5 lists the goodness-of-fit statistics between the modeled daily *ET* using *sUAS* data sets and the ground-based *EC* daily measurements at two time windows during the day: 1030–1330 and 1430–1630. Figure 3.8 shows the relationship between the modeled and measured fluxes. Overall, the results indicate that the modeled *ET_d* values have better agreement across different upscaling methods using the time window of 1030–1330 PST, while a significant deterioration was observed in the performance of all methods using the 1430–1630 period for upscaling. The *RMSE* and *MAPE* statistics yielded values greater than 1.2 mm/day and 25%, respectively, in the 1430–1630 time window; however, these values decreased to less than 1 mm/day and 20% across different methods using the *TSEB* output in the 1030–1330 timeframe, with one exception. In the case of the Sine approach, the *RMSE* and *MAPE* yielded values of 1.32 mm/day and 26%, respectively. These findings align with the results obtained when comparing different *ET_d* methods using measurements from the *EC* tower (see Section 3.2), where *RMSE* and *MAPE* yielded values greater than 0.5 mm/day and 14% in the time window 1430–1630. However, using the time window of 1030–1330, the values of *RMSE* and *MAPE* decreased to less than 0.7 mm/day and 23%, respectively. The larger *RMSE* and *MAPE* values obtained in the *sUAS ET_d* compared to the *EC ET_d* are due to the bias in the *TSEB*-derived *ET* compared to the *EC* measurements. These results are also supported by previous studies conducted by Jackson et al. [30] and Colaizzi et al. [28], where scaling instantaneous *ET* to daily values showed better agreement when the measurement was taken within about 1–2 h of solar noon.

Although the results indicate that three (GA , EF , and R_s) out of the five methods for daily ET upscaling agree reasonably well with the ground-based measurements, the R_s technique yielded better agreement at all three sites (Sierra Loma, Ripperdan 720, and Barrelli). This approach generated a robust ET_d when a single remote sensing-based ET estimate was taken within 1–2 h of solar noon and provided a close agreement with the ground truth ET measurement. This result also aligns with the EC ET_d analysis, which indicates that the R_s approach has better statistical performance (see Table 3.3). Using the R_s approach for all vineyards, the $RMSE$ values were 0.45 mm/day, and the $MAPE$ was 10%, while the R^2 was 0.88 for the time window of 1030–1330 (see Table 3.5, All Vineyards section).

These results agree with a previous study conducted by Wandera et al. [41], which showed that the R_s -based approach was better for upscaling compared with the EF method. That study was carried out over 41 FLUXNET validation sites for two different times of day, including 1100 and 1330. Furthermore, the found results are also supported by Cammalleri et al. [29], when comparing different daily extrapolation methods. Cammalleri et al. [29] found that the incoming solar radiation (R_s) was the most robust method with the least error when using EC data collected at different flux tower sites within the United States and over multiple seasons. The R_s approach for ET upscaling is highly recommended in situations where obtaining the daily net radiation is not possible [19] or, in some cases, where the modeled R_n is overestimated/underestimated, which will adversely affect the EF ratio. On the other hand, the G is more difficult to estimate than the R_s and R_n , which could limit the accuracy of the EF method. This might explain why the R_s method has a slightly higher agreement than the EF . Comparing the approaches with the lowest performance, the

Sine method demonstrated the worst performance, with the largest $RMSE$ and $MAPE$ values and the lowest NSE value in the time window between 1030 and 1330. However, between 1430 and 1630, the results indicate that Sine performed slightly better than R_n/R_s . Still, the $RMSE$ and $MAPE$ values were high and the NSE and R^2 values were very low. The hypothesis is that the heterogeneity in the field, due to vine biomass, cover crop, and bare soil, has a larger impact on the R_n/R_s and Sine approaches than other methods.



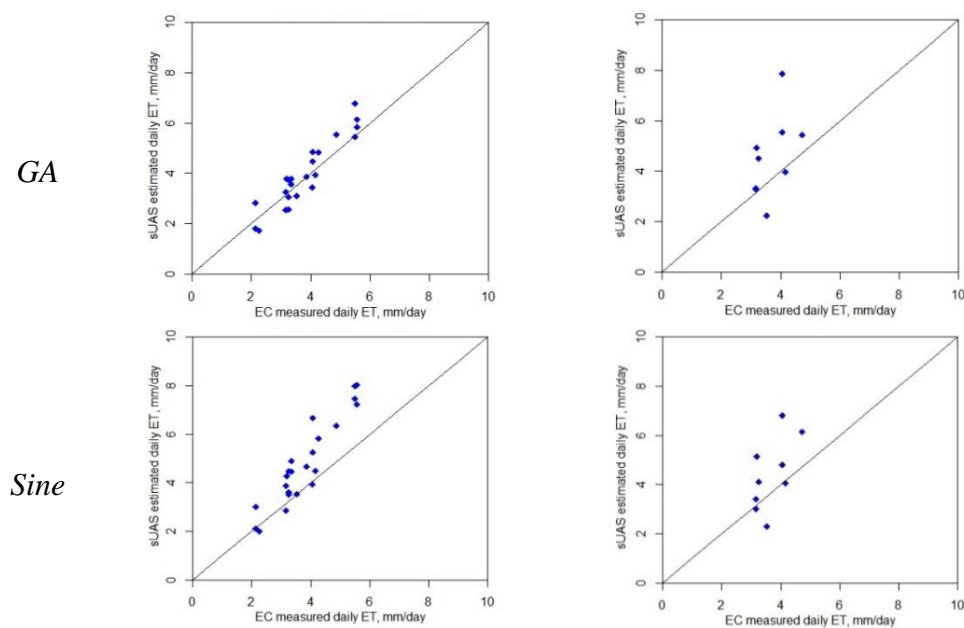


Figure 3.8 Comparison between daily *ET* from *TSEB sUAS* and *EC* at two different time windows (1030–1330 and 1430–1630).

Table 3.5 Goodness-of-fit statistics comparing multiple daily *ET* methods at two different time windows (1030–1330 and 1430–1630).

Sites	Method	1030–1330					1430–1630				
		RMSE (mm/day)	MAE (mm/day)	MAPE (%)	NSE	R ²	RMSE (mm/day)	MAE (mm/day)	MAPE (%)	NSE	R ²
Sierra Loma	<i>EF</i>	0.44	0.32	10	0.57	0.63	1.02	0.89	27	−7	0.00
	<i>R_s</i>	0.38	0.32	10	0.67	0.78	0.95	0.72	22	−6	0.00
	<i>R_n/R_s</i>	0.95	0.77	23	−0.96	0.67	1.30	1.05	31	−12.08	0.05
	<i>GA</i>	0.44	0.39	13	0.58	0.82	1.02	0.79	24	−7.02	0.01
	<i>Sine</i>	0.80	0.63	18	−0.41	0.79	1.01	0.76	24	−6.93	0.00
Rippperdan 760	<i>EF</i>	0.39	0.34	8	0.24	0.93	1.85	1.5	36	−33.52	0.55
	<i>R_s</i>	0.62	0.55	13	−0.82	0.45	1.65	1.34	33	−26.54	0.69
	<i>R_n/R_s</i>	0.73	0.62	14	−3.43	0.70	2.12	1.77	43	−44.70	0.67
	<i>GA</i>	0.63	0.61	14	−2.26	0.55	2.39	1.99	48	−56.82	0.28
	<i>Sine</i>	1.60	1.34	31	−20.18	0.19	1.83	1.63	38	−33	0.04
Rippperdan 720	<i>EF</i>	0.49	0.44	11	0.80	0.92	No flights				
	<i>R_s</i>	0.44	0.36	9	0.85	0.93					
	<i>R_n/R_s</i>	0.83	0.73	16	0.44	0.92					
	<i>GA</i>	0.59	0.47	11	0.72	0.91					
	<i>Sine</i>	1.68	1.47	31	−1.26	0.94					
Barrelli	<i>EF</i>	0.41	0.41	19	NA	NA ¹					
	<i>R_s</i>	0.19	0.19	9	NA	NA					
	<i>R_n/R_s</i>	0.78	0.78	36	NA	NA					
	<i>GA</i>	0.67	0.67	31	NA	NA					
	<i>Sine</i>	0.86	0.86	40	NA	NA					
All vineyards	<i>EF</i>	0.45	0.37	10	0.81	0.82	1.35	1.1	30	−14.29	0.11
	<i>R_s</i>	0.45	0.37	10	0.80	0.88	1.23	0.93	25	−11.65	0.19
	<i>R_n/R_s</i>	0.87	0.73	20	0.29	0.82	1.62	1.29	35	−21.06	0.22
	<i>GA</i>	0.54	0.47	13	0.71	0.87	1.61	1.19	32	−20.72	0.25
	<i>Sine</i>	1.32	1.05	26	−0.68	0.87	1.34	1.05	28	−14.10	0.37

¹ NA because we have only two observations. Numbers in bold are the best statistical results for each timeframe and vine stage.

3.4 Conclusion

The objective of this study was to assess existing methodologies for upscaling *ET* from single time-of-day information to daily estimates over commercial vineyards in California's Central Valley using *EC* flux measurements and the *TSEB* model with *sUAS* imagery. The extrapolation approaches included the evaporative fraction (*EF*), solar radiation (R_s), net radiation to incoming solar radiation (R_n/R_s), the Gaussian (*GA*), and Sine technique. First, analysis was performed using flux observations collected at eight *EC* towers located at three vineyards in California's Central Valley: Sierra Loma, Ripperdan, and Barrelli. These sites are characterized by different climates, soils, vine variety, and trellis designs. The analysis also considered months of the growing season to coincide with three vine phenological stages (April–May (rapid vine growth, bloom/berry establishment), June–August (berry development/veraison), and September–October (harvest/post-harvest/vine senescence)) to investigate how vine phenology could affect the accuracy of the modeled daily *ET* due to timing of both water uptake and growth.

The *EC* analysis results indicate that three daily *ET* approaches (*EF*, R_s , and *GA*) out of five have a reasonable agreement with the *EC*-based measurements, with the R_s approach being preferred for daytime upscaling of *ET* across different stages of vine phenology, as it yielded the highest accuracy among the tested methods. Moreover, the results demonstrate that the methods could perform differently at different vine canopy development and grapevine phenology stages and at different time windows during the day. In the time window between 1030 and 1330, *MAPE* yielded values of 8% when using the R_s approach in the veraison stage, whereas this value increased to 17% between 1430 and 1630 h. In the bloom and post-harvest vine stages, the *MAPE* yielded values of 10%

and 11%, respectively, when using R_s within the 1030–1330 time window, which then increased to 19% and 23%, respectively, between 1430 and 1630.

A similar result was obtained when applying the five ET upscaling methods using instantaneous $TSEB$ -derived ET . The results reported that the R_s , out of the other methods, has better agreement with the ground measurements to extrapolate the instantaneous ET at the time of the $sUAS$ acquisition to daily values, with an $RMSE$ of 0.45 mm/day and an $MAPE$ of 10% in the time window between 1030 and 1330 PST. The EF and GA methods performed relatively well, with a $MAPE$ of 10% and 13%, respectively, in the same time window. However, between 1430 and 1630, the results indicate a significant deterioration in the performance of all methods, with the $RMSE$ and $MAPE$ values greater than 1.2 mm/day and 25%, respectively. The range in climate, vine variety, soils, trellis designs, and times when $sUAS$ imagery was collected support the general results that the R_s extrapolation method can provide reliable daily ET estimates, particularly if the modeled ET is extrapolated from imagery collected 1–2 h before/after solar noon.

References

1. Yang, H.; Yang, D.; Lei, Z.; Sun, F. New Analytical Derivation of the Mean Annual Water-Energy Balance Equation. *Water Resour. Res.* 2008, *44*, doi:10.1029/2007wr006135.
2. Housh, M.; Cai, X.; Ng, T.L.; McIsaac, G.F.; Ouyang, Y.; Khanna, M.; Sivapalan, M.; Jain, A.K.; Eckhoff, S.; Gasteyer, S.; et al. System of Systems Model for Analysis of Biofuel Development. *J. Infrastruct. Syst.* 2015, *21*, 04014050.
3. Jiang, Y.; Jiang, X.; Tang, R.; Li, Z.-L.; Zhang, Y.; Huang, C.; Ru, C. Estimation of Daily Evapotranspiration Using Instantaneous Decoupling Coefficient from the MODIS and Field Data. *IEEE J. Sel. Top. Appl. Earth Obs. Remote Sens.* 2018, *11*, 1832–1838.
4. Allen, R.G.; Tasumi, M.; Morse, A.; Trezza, R. A Landsat-Based Energy Balance and Evapotranspiration Model in Western US Water Rights Regulation and Planning. *Irrig. Drain. Syst.* 2005, *19*, 251–268.
5. Anderson, M.C.; Kustas, W.P.; Norman, J.M.; Hain, C.R.; Mecikalski, J.R.; Schultz, L.; González-Dugo, M.P.; Cammalleri, C.; d’Urso, G.; Pimstein, A.; et al. Mapping Daily Evapotranspiration at Field to Continental Scales Using Geostationary and Polar Orbiting Satellite Imagery. *Hydrol. Earth Syst. Sci.* 2011, *15*, 223–239.
6. Anderson, M.C.; Allen, R.G.; Morse, A.; Kustas, W.P. Use of Landsat Thermal Imagery in Monitoring Evapotranspiration and Managing Water Resources. *Remote Sens. Environ.* 2012, *122*, 50–65.
7. Nassar, A.; Torres-Rua, A.; Kustas, W.; Nieto, H.; McKee, M.; Hipps, L.; Stevens, D.; Alfieri, J.; Prueger, J.; Alsina, M.M.; et al. Influence of Model Grid Size on the Estimation of Surface Fluxes Using the Two Source Energy Balance Model and sUAS Imagery in Vineyards. *Remote Sens. Basel* 2020, *12*, 342.
8. Drexler, J.Z.; Snyder, R.L.; Spano, D.; U, K.T.P. A Review of Models and Micrometeorological Methods Used to Estimate Wetland Evapotranspiration. *Hydrol. Process.* 2004, *18*, 2071–2101.
9. Ortega-Farias, S.; Carrasco, M.; Olioso, A.; Acevedo, C.; Poblete, C. Latent Heat Flux over Cabernet Sauvignon Vineyard Using the Shuttleworth and Wallace Model. *Irrig. Sci.* 2006, *25*, 161–170.
10. Parry, C.K.; Nieto, H.; Guillevic, P.; Agam, N.; Kustas, W.P.; Alfieri, J.; McKee, L.; McElrone, A.J. An Intercomparison of Radiation Partitioning Models in Vineyard Canopies. *Irrig. Sci.* 2019, *37*, 239–252.
11. Nieto, H.; Kustas, W.P.; Alfieri, J.G.; Gao, F.; Hipps, L.E.; Los, S.; Prueger, J.H.; McKee, L.G.; Anderson, M.C. Impact of Different within-Canopy Wind Attenuation Formulations on Modelling Sensible Heat Flux Using TSEB. *Irrig. Sci.* 2019, *37*, 315–331.

12. University of California Agriculture; the California Garden Web. Available online: <http://cagardenweb.ucanr.edu> (accessed on 25 December 2020).
13. Mitcham, E.J.; Elkins, R.B. *Pear Production and Handling Manual*; UCANR Publications: 2007, ISBN 9781879906655.
14. Prueger, J.H.; Parry, C.K.; Kustas, W.P.; Alfieri, J.G.; Alsina, M.M.; Nieto, H.; Wilson, T.G.; Hipps, L.E.; Anderson, M.C.; Hatfield, J.L.; et al. Crop Water Stress Index of an Irrigated Vineyard in the Central Valley of California. *Irrig. Sci.* 2019, 37, 297–313.
15. USDA—National Agricultural Statistics Service—California. Available online: <http://www.nass.usda.gov/ca> (accessed on 25 December 2020).
16. Alfieri, J.G.; Kustas, W.P.; Nieto, H.; Prueger, J.H.; Hipps, L.E.; McKee, L.G.; Gao, F.; Los, S. Influence of Wind Direction on the Surface Roughness of Vineyards. *Irrig. Sci.* 2019, 37, 359–373.
17. Nassar, A.; Torres-Rua, A.F.; Nieto, H.; Alfieri, J.G.; Hipps, L.E.; Prueger, J.H.; Alsina, M.M.; McKee, L.G.; White, W.; Kustas, W.P.; et al. Implications of Soil and Canopy Temperature Uncertainty in the Estimation of Surface Energy Fluxes Using TSEB2T and High-Resolution Imagery in Commercial Vineyards. In Proceedings of the SPIE, 26 May 2020.
18. Niu, H.; Zhao, T.; Wang, D.; Chen, Y. Evapotranspiration Estimation with UAVs in Agriculture: A Review. *Preprints* 2019, doi:10.20944/preprints201907.0124.v1.
19. Chávez, J.L.; Neale, C.M.U.; Prueger, J.H.; Kustas, W.P. Daily Evapotranspiration Estimates from Extrapolating Instantaneous Airborne Remote Sensing ET Values. *Irrig. Sci.* 2008, 27, 67–81.
20. Cammalleri, C.; Anderson, M.C.; Gao, F.; Hain, C.R.; Kustas, W.P. A Data Fusion Approach for Mapping Daily Evapotranspiration at Field Scale. *Water Resour. Res.* 2013, 49, 4672–4686.
21. Cammalleri, C.; Anderson, M.C.; Gao, F.; Hain, C.R.; Kustas, W.P. Mapping Daily Evapotranspiration at Field Scales over Rainfed and Irrigated Agricultural Areas Using Remote Sensing Data Fusion. *Agric. For. Meteorol.* 2014, 186, 1–11.
22. Knipper, K.R.; Kustas, W.P.; Anderson, M.C.; Alsina, M.M.; Hain, C.R.; Alfieri, J.G.; Prueger, J.H.; Gao, F.; McKee, L.G.; Sanchez, L.A. Using High-Spatiotemporal Thermal Satellite ET Retrievals for Operational Water Use and Stress Monitoring in a California Vineyard. *Remote Sens.* 2019, 11, 2124.
23. Tsouros, D.C.; Bibi, S.; Sarigiannidis, P.G. A Review on UAV-Based Applications for Precision Agriculture. *Information* 2019, 10, 349.
24. Nielsen, H.H.M. *Evapotranspiration from UAV Images: A New Scale of Measurements*; Department of Geosciences and Natural Resource Management, Faculty of Science, University of Copenhagen: Copenhagen, Denmark, 2016.

25. Nassar, A.; Torres-Rue, A.F.; McKee, M.; Kustas, W.P.; Coopmans, C.; Nieto, H.; Hipps, L. *Assessment of UAV Flight Times for Estimation of Daily High Resolution Evapotranspiration in Complex Agricultural Canopy Environments*; Universities Council in Water Resources (UCOWR): Snowbird, UT, USA, 2019.
26. Zhang, C.; Long, D.; Zhang, Y.; Anderson, M.C.; Kustas, W.P.; Yang, Y. A Decadal (2008–2017) Daily Evapotranspiration Data Set of 1 Km Spatial Resolution and Spatial Completeness across the North China Plain Using TSEB and Data Fusion. *Remote Sens. Environ.* 2021, 262, 112519.
27. Allen, G.; Morton, C.; Kamble, B.; Kilic, A.; Huntington, J.; Thau, D.; Gorelick, N.; Erickson, T.; Moore, R.; Trezza, R.; et al. 2015 EEFlux: A Landsat-Based Evapotranspiration Mapping Tool on the Google Earth Engine. In Proceedings of the 2015 ASABE/IA Irrigation Symposium: Emerging Technologies for Sustainable Irrigation—A Tribute to the Career of Terry Howell, Sr. Conference Proceedings, 2015.
28. Colaizzi, P.D.; Evett, S.R.; Howell, T.A.; Tolk, J.A. Comparison of Five Models to Scale Daily Evapotranspiration from One-Time-of-Day Measurements. *Trans. ASABE* 2006, 49, 1409–1417.
29. Cammalleri, C.; Anderson, M.C.; Kustas, W.P. Upscaling of Evapotranspiration Fluxes from Instantaneous to Daytime Scales for Thermal Remote Sensing Applications. *Hydrol. Earth Syst. Sci.* 2014, 18, 1885–1894.
30. Jackson, R.D.; Hatfield, J.L.; Reginato, R.J.; Idso, S.B.; Pinter, P.J. Estimation of Daily Evapotranspiration from One Time-of-Day Measurements. *Agric. Water Manag.* 1983, 7, 351–362.
31. Crago, R.D. Conservation and Variability of the Evaporative Fraction during the Daytime. *J. Hydrol.* 1996, 180, 173–194.
32. Crago, R.D. Comparison of the Evaporative Fraction and the Priestley-Taylor α for Parameterizing Daytime Evaporation. *Water Resour. Res.* 1996, 32, 1403–1409.
33. Delogu, E.; Boulet, G.; Olioso, A.; Coudert, B.; Chirouze, J.; Ceschia, E.; Le Dantec, V.; Marloie, O.; Chehbouni, G.; Lagouarde, -P.J. Reconstruction of Temporal Variations of Evapotranspiration Using Instantaneous Estimates at the Time of Satellite Overpass. *Hydrol. Earth Syst. Sci.* 2012, 16, 2995–3010.
34. Suleiman, A.; Crago, R. Hourly and Daytime Evapotranspiration from Grassland Using Radiometric Surface Temperatures. *Agron. J.* 2004, 96, 384.
35. Shuttleworth, W.J.; Gurney, R.J.; Hsu, A.Y.; Ormsby, J.P. FIFE: The Variation in Energy Partition at Surface Flux Sites. *IAHS Publ.* 1989, 186, 523–534.
36. Hoedjes, J.C.B.; Chehbouni, A.; Jacob, F.; Ezzahar, J.; Boulet, G. Deriving Daily Evapotranspiration from Remotely Sensed Instantaneous Evaporative Fraction over Olive Orchard in Semi-Arid Morocco. *J. Hydrol.* 2008, 354, 53–64.

37. Li, S.; Kang, S.; Li, F.; Zhang, L.; Zhang, B. Vineyard Evaporative Fraction Based on Eddy Covariance in an Arid Desert Region of Northwest China. *Agric. Water Manag.* 2008, *95*, 937–948.
38. Zhang, L.; Lemeur, R. Evaluation of Daily Evapotranspiration Estimates from Instantaneous Measurements. *Agric. For. Meteorol.* 1995, *74*, 139–154.
39. Gentine, P.; Entekhabi, D.; Chehbouni, A.; Boulet, G.; Duchemin, B. Analysis of Evaporative Fraction Diurnal Behaviour. *Agric. For. Meteorol.* 2007, *143*, 13–29.
40. Van Niel, T.; McVicar, T.; Roderick, M.; Dijk, A.; Beringer, J.; Hutley, L.; Gorsel, E. Upscaling Latent Heat Flux for Thermal Remote Sensing Studies: Comparison of Alternative Approaches and Correction of Bias. *J. Hydrol.* 2012, *468–469*, 35–46.
41. Wandera, L.; Mallick, K.; Kiely, G.; Rouspard, O.; Peichl, M.; Magliulo, V. Upscaling Instantaneous to Daily Evapotranspiration Using Modelled Daily Shortwave Radiation for Remote Sensing Applications: An Artificial Neural Network Approach. *Hydrol. Earth Syst. Sci.* 2017, *21*, 197–215, doi:10.5194/hess-2016-344-supplement.
42. French, A.N.; Fitzgerald, G.; Hunsaker, D.; Barnes, E.; Clarke, T.; Lesch, S.; Roth, R.; Pinter, P. Estimating Spatially Distributed Cotton Water Use from Thermal Infrared Aerial Imagery. *Impacts Glob. Clim. Chang.* 2005, doi:10.1061/40792526.
43. Liu, S.; Su, H.; Zhang, R.; Tian, J.; Chen, S.; Wang, W.; Yang, L.; Liang, H. Based on the Gaussian Fitting Method to Derive Daily Evapotranspiration from Remotely Sensed Instantaneous Evapotranspiration. *Adv. Meteorol.* 2019, *2019*, 1–13.
44. Norman, J.M.; Kustas, W.P.; Humes, K.S. Source Approach for Estimating Soil and Vegetation Energy Fluxes in Observations of Directional Radiometric Surface Temperature. *Agric. For. Meteorol.* 1995, *77*, 263–293.
45. Norman, J.M.; Kustas, W.P.; Prueger, J.H.; Diak, G.R. Surface Flux Estimation Using Radiometric Temperature: A Dual-Temperature-Difference Method to Minimize Measurement Errors. *Water Resour. Res.* 2000, *36*, 2263–2274.
46. Kustas, W.P.; Alfieri, J.G.; Anderson, M.C.; Colaizzi, P.D.; Prueger, J.H.; Evett, S.R.; Neale, C.M.U.; French, A.N.; Hipps, L.E.; Chávez, J.L.; et al. Evaluating the Two-Source Energy Balance Model Using Local Thermal and Surface Flux Observations in a Strongly Advective Irrigated Agricultural Area. *Adv. Water Resour.* 2012, *50*, 120–133.
47. Gao, F.; Kustas, W.; Anderson, M. A Data Mining Approach for Sharpening Thermal Satellite Imagery over Land. *Remote Sens.* 2012, *4*, 3287–3319.
48. Kustas, W.P.; Norman, J.M. A Two-Source Approach for Estimating Turbulent Fluxes Using Multiple Angle Thermal Infrared Observations. *Water Resour. Res.* 1997, *33*, 1495–1508.
49. Nieto, H.; Kustas, W.P.; Torres-Rúa, A.; Alfieri, J.G.; Gao, F.; Anderson, M.C.; White, W.A.; Song, L.; Del Mar Alsina, M.; Prueger, J.H.; et al. Evaluation of TSEB Turbulent Fluxes Using Different Methods for the Retrieval of Soil and Canopy

- Component Temperatures from UAV Thermal and Multispectral Imagery. *Irrig. Sci.* 2019, 37, 389–406.
50. Xia, T.; Kustas, W.P.; Anderson, M.C.; Alfieri, J.G.; Gao, F.; McKee, L.; Prueger, J.H.; Geli, H.M.E.; Neale, C.M.U.; Sanchez, L.; et al. Mapping Evapotranspiration with High-Resolution Aircraft Imagery over Vineyards Using One- and Two-Source Modeling Schemes. *Hydrol. Earth Syst. Sci.* 2016, 20, 1523–1545.
 51. Brutsaert, W. Aspects of Bulk Atmospheric Boundary Layer Similarity under Free-Convective Conditions. *Rev. Geophys.* 1999, 37, 439–451.
 52. Kustas, W.P.; Nieto, H.; Morillas, L.; Anderson, M.C.; Alfieri, J.G.; Hipps, L.E.; Villagarcía, L.; Domingo, F.; Garcia, M. Revisiting the Paper “Using Radiometric Surface Temperature for Surface Energy Flux Estimation in Mediterranean Drylands from a Two-Source Perspective.” *Remote Sens. Environ.* 2016, 184, 645–653.
 53. Kondo, J.; Ishida, S. Sensible Heat Flux from the Earth’s Surface under Natural Convective Conditions. *J. Atmos. Sci.* 1997, 54, 498–509.
 54. Kustas, W.P.; Anderson, M.C.; Alfieri, J.G.; Knipper, K.; Torres-Rua, A.; Parry, C.K.; Nieto, H.; Agam, N.; White, W.A.; Gao, F.; et al. The Grape Remote Sensing Atmospheric Profile and Evapotranspiration Experiment. *Bull. Am. Meteorol. Soc.* 2018, 99, 1791–1812.
 55. Utah State University AggieAir. Available online: <https://uwrl.usu.edu/aggieair/index> (accessed on 25 December 2020).
 56. Torres-Rua, A. Vicarious Calibration of sUAS Microbolometer Temperature Imagery for Estimation of Radiometric Land Surface Temperature. *Sensors* 2017, 17, 1499, doi:10.3390/s17071499.
 57. Torres-Rua, A.F.; Ticlavilca, A.M.; Aboutaleb, M.; Nieto, H.; Alsina, M.M.; White, A.; Prueger, J.H.; Alfieri, J.G.; Hipps, L.E.; McKee, L.G.; et al. Estimation of Evapotranspiration and Energy Fluxes Using a Deep-Learning-Based High-Resolution Emissivity Model and the Two-Source Energy Balance Model with sUAS Information. In Proceedings of the SPIE, Online, 14 May 2020.
 58. Hassan-Esfahani, L.; Ebtehaj, A.M.; Torres-Rua, A.; McKee, M. Spatial Scale Gap Filling Using an Unmanned Aerial System: A Statistical Downscaling Method for Applications in Precision Agriculture. *Sensors* 2017, 17, 2106.
 59. Kljun, N.; Calanca, P.; Rotach, M.W.; Schmid, H.P. A simple two-dimensional parameterisation for Flux Footprint Prediction (FFP). *Geosci. Model Dev.* 2015, 8, 3695–3713.
 60. Sun, H.; Yang, Y.; Wu, R.; Gui, D.; Xue, J.; Liu, Y.; Yan, D. Improving Estimation of Cropland Evapotranspiration by the Bayesian Model Averaging Method with Surface Energy Balance Models. *Atmosphere* 2019, 10, 188.
 61. Li, S.; Tong, L.; Li, F.; Zhang, L.; Zhang, B.; Kang, S. Variability in Energy Partitioning and Resistance Parameters for a Vineyard in Northwest China. *Agric. Water Manag.* 2009, 96, 955–962.

62. Brutsaert, W.; Chen, D. Diurnal Variation of Surface Fluxes During Thorough Drying (or Severe Drought) of Natural Prairie. *Water Resour. Res.* 1996, *32*, 2013–2019.
63. Sugita, M.; Brutsaert, W. Daily Evaporation over a Region from Lower Boundary Layer Profiles Measured with Radiosondes. *Water Resour. Res.* 1991, *27*, 747–752.
64. Shapland, T.M.; Snyder, R.L.; Smart, D.R.; Williams, L.E. Estimation of Actual Evapotranspiration in Winegrape Vineyards Located on Hillside Terrain Using Surface Renewal Analysis. *Irrig. Sci.* 2012, *30*, 471–484.
65. Tolk, J.A.; Howell, T.A.; Evett, S.R. Nighttime Evapotranspiration from Alfalfa and Cotton in a Semiarid Climate. *Agron. J.* 2006, *98*, 730–736.
66. Knipper, K.R.; Kustas, W.P.; Anderson, M.C.; Nieto, H.; Alfieri, J.G.; Prueger, J.H.; Hain, C.R.; Gao, F.; McKee, L.G.; Mar Alsina, M.; et al. Using High-Spatiotemporal Thermal Satellite ET Retrievals to Monitor Water Use over California Vineyards of Different Climate, Vine Variety and Trellis Design. *Agric. Water Manag.* 2020, 106361.
67. Semmens, K.A.; Anderson, M.C.; Kustas, W.P.; Gao, F.; Alfieri, J.G.; McKee, L.; Prueger, J.H.; Hain, C.R.; Cammalleri, C.; Yang, Y.; et al. Monitoring Daily Evapotranspiration over Two California Vineyards Using Landsat 8 in a Multi-Sensor Data Fusion Approach. *Remote Sens. Environ.* 2016, *185*, 155–170.
68. Neale, C.M.U.; Geli, H.M.E.; Kustas, W.P.; Alfieri, J.G.; Gowda, P.H.; Evett, S.R.; Prueger, J.H.; Hipps, L.E.; Dulaney, W.P.; Chávez, J.L.; et al. Soil Water Content Estimation Using a Remote Sensing Based Hybrid Evapotranspiration Modeling Approach. *Adv. Water Resour.* 2012, *50*, 152–161.
69. Kustas, W.P.; Prueger, J.H.; Hatfield, J.L.; Ramalingam, K.; Hipps, L.E. Variability in Soil Heat Flux from a Mesquite Dune Site. *Agric. For. Meteorol.* 2000, *103*, 249–264.

CHAPTER 4

CHARACTERIZING THE SPATIAL HETEROGENEITY IN A RIVER CORRIDOR
TO EVALUATE ITS IMPACT ON EVAPOTRANSPIRATION ESTIMATES USING
THE TSEB MODEL AND SUAS INFORMATION

Abstract

Understanding the spatial variability in highly heterogeneous natural environments such as savannas and river corridors is an important issue in characterizing and modeling energy fluxes, particularly for evapotranspiration (*ET*) estimates. The natural environment is characterized by variation in vegetation types, soil strata and properties, and other geomorphological processes. Various land surface and hydrological models can be applied to estimate *ET* in such environments; however, model performance may be affected due to the lack of robust methods of accounting for the spatial variability in the vegetation and soil. Remote sensing-based surface energy balance (*SEB*) models are applied widely and routinely in agricultural settings to obtain *ET* information on an operational basis for use in water resources management. However, the application of these models in natural environments is challenging due to spatial heterogeneity in vegetation cover and complexity in the number of vegetation species existing within a biome. The analysis in this study relies upon multispectral images acquired through multiple campaigns over different seasons (June, July, and October) by the *AggieAirTM* small unmanned aerial systems (*sUAS*) program at Utah State University (<https://uwrl.usu.edu/aggieair/>) specifically in the San Rafael River corridor in Utah, which is part of the Upper Colorado River Basin. The study area is characterized by arid conditions and variations in soil moisture status and the type and height of vegetation (treated tamarisk, cottonwood,

willow, grass, and other vegetation species). Optical data in red, green, blue, and near infrared bands were acquired at 2.5-cm spatial resolution, while thermal data were acquired at 15 cm using a microbolometer camera. The micrometeorological data were obtained from a weather station installed in the field during the flight dates. In this research effort, *sUAS* data were used to study the influence of land surface spatial heterogeneity on the modeling of *ET* using high-resolution information. First, a spatial variability analysis was performed using a discrete wavelet transform (*DWT*) to identify a representative spatial resolution/model grid size for adequately solving energy balance components to derive *ET*. Next, the Two Source Energy Balance (*TSEB*) model, a physically based *ET* model, was implemented over different vegetation/soil conditions and times at two different scales, 6 m and 15 m. Lastly, the instantaneous (hourly) latent heat flux (*LE*) was extrapolated/upscaled to daily *ET* values using the incoming solar radiation (R_s) method. Results indicate that spatial resolutions between 6 m and 15 m are suitable for representing fluxes in the study area. The results also indicate small differences in the *LE* values between 6-m and 15-m resolutions, with a slight decrease in detail at 15 m due to losses in spatial variability. For daily *ET* estimation, the results indicate that willow and cottonwood have the highest *ET* rates, followed by grass/shrubs and treated tamarisk.

Keywords: evapotranspiration (*ET*); natural environment; spatial heterogeneity; wavelet energy; discrete wavelet transform (*DWT*); *sUAS*; Remote Sensing; *TSEB* model; Upper Colorado River Basin; San Rafael River corridor

4.1 Introduction

Evapotranspiration (*ET*) is of paramount importance for terrestrial water balance as it represents the second largest component after precipitation and it links climate, hydrology, and ecosystem processes that couple water and energy budgets [1]. Spatial *ET* information has been shown to play a critical part in monitoring the spatial and temporal variation of agricultural drought on monthly and annual scales [2] to improve water resources planning and management. Accurate *ET* estimation is necessary, particularly in drought-stricken areas, to monitor the impacts on the natural environment. Direct measurements of *ET* using ground instrumentation such as eddy covariance (*EC*) or lysimeters only work appropriately for homogenous surfaces and are limited to small sampling areas [3]. At large scales, such as watersheds or biomes, these methods are difficult to employ due to the complexity of hydrometeorological processes [4]. Challenges associated with natural ecosystem scales usually arise from spatial heterogeneity in soils and vegetation species, in addition to other biophysical processes that affect the surface-atmosphere exchanges of water and energy [5]. Therefore, to understand the spatial heterogeneity of the landscape for accurate estimation of surface energy fluxes, particularly latent heat flux (*LE*) or evapotranspiration (*ET*), advanced techniques are needed. To address these needs, the scientific community has developed land surface models, mathematical representations of land-atmosphere exchange, to quantify surface energy and water balance, which drive climatic and earth system processes [6]. These models are helpful tools that can provide vital information to track ecosystem response to dynamic changes in climate and environmental components [7,8].

Simple and complex land surface and hydrological models [9] have been applied to estimate *ET* in heterogeneous environments [10]. Currently, remote sensing-based energy balance models are widely and routinely applied to produce spatial *ET* information on an operational basis for use in water resources management [11]. These models use thermal infrared (*TIR*) data as a boundary condition and solve *LE* as a residual component of the surface energy balance (*SEB*) [12]. Generally, two types of *SEB* models are applied, both of which use optical and *TIR* remote sensing information to calculate *ET* through the radiation and energy balance equations. The first is the One-Source Energy Balance (*OSEB*) model, which treats the canopy-substrate surface as a single layer [13]. The second is the dual source, such as the Two-Source Energy Balance (*TSEB*) model [14], which partitions the energy fluxes between canopy and soil/substrate [15]. The *TSEB* model was originally developed for homogenous partial vegetation cover, and then the framework was upgraded to accommodate the effects of heterogeneous partial vegetation, as opposed to the *OSEB* models [16,17]. However, both model types tend to show greater uncertainty in cases of heterogeneous landscapes and/or natural environments [18,19]. From an operational perspective, identifying individual fields and other small hydrological features in a heterogeneous environment requires a more advanced technology that can provide high-resolution data in a timely manner. Satellite remote sensing can provide radiometric surface temperature and optical observations at a spatial scale of 10 to 10^3 m²; however, satellite measurements are affected by various landscape features and require semi-empirical algorithms to convert radiances to physical quantities for *SEB* modeling [20]. Although satellite data fusion has improved the information, the presence of clouds during satellite overpass can limit its operational application [20]. The development of small

unmanned aerial systems (*sUAS*) with novel instrumentations and lightweight sensors has made high multispectral resolution possible without the previously mentioned limitations. Additionally, these systems are “flexible in timing” [3].

Remote sensing offers access to a wide range of spatial information, but the high spatial resolution is also recognized as a challenging issue for energy flux modeling, particularly for *ET* estimates. According to Brunsell and Gillies (2003) [21], spatial scaling becomes more complicated in heterogeneous landscapes. Considering the spatial variability of surface and environmental properties such as canopy height, vegetation cover, and land surface temperature (*LST*), the spatial resolution of remote sensing products should have a significant impact on the adequacy and accuracy of *ET* estimates. Previous studies assessing the effects of different satellite sensors on *ET* estimation found discrepancies among the various spatial scales [22,23]. To a large extent, this is a function of the scale of variability in land cover relative to the resolution of the pixel information [24,25]. Therefore, analyses to evaluate the effects of spatial scale on surface properties and states that affect surface energy balance (*SEB*) modeling for different heterogeneous landscapes are required [26].

In natural environments that are characterized by a heterogeneous natural ecosystem and low precipitation, such as the San Rafael River corridor in Utah, the major component of the water balance is vegetation transpiration (*T*) and soil evaporation (*E*) or the combined evapotranspiration (*ET*). This location also exhibits significant high spatial variability in *ET* information due to several factors that include soil moisture availability, groundwater depth, leaf area, topography, land surface temperature and vegetation species [27]. Moreover, the San Rafael River corridor is dominated by treated tamarisk, which

increases the complexity of the ecosystem's water use and poses additional difficulties beyond the previously mentioned challenges due to the high variability of this vegetation in space and time.

The presence of treated tamarisk and other riparian vegetation in the river corridor changes the river hydraulics by increasing the channel roughness, which can result in slower water flow and increased flood frequency. Efforts are underway to restore habitats by removing tamarisk in the river corridor to foster a more ecologically acceptable state, which may also have an impact on the evapotranspiration rate [28]. These efforts target mechanical whole tree removal on riverbanks lined with mature trees to encourage lateral scour and channel widening within channelized sections. A tracked excavator with a grapple attachment removes the tamarisk at or below the soil surface. This method has proven effective in removing the tamarisk root system and minimizing re-sprouting in subsequent years. Tamarisk removal is conducted in the winter months to reduce upland soil disturbance and avoid impacts to migratory birds. After removal, tamarisk is stacked and left to dry for later burning or is left onsite to provide brush pile habitat. Areas disturbed during mechanical treatment and newly opened areas are seeded in the autumn following removal.

According to a 2011 study by Neale et al. [27] conducted over the Mojave River, California, to estimate *ET* using high-resolution airborne multispectral imagery, tamarisk and cottonwood plants had the highest *ET* rate compared with other vegetation species. Furthermore, although a vast amount of information is available on water use by different types of riparian species, plant physiological processes and sources of available water that control water use are still disputed and poorly understood [27]. Hence, further insights into

the amount of available water used in such heterogeneous systems would benefit natural and water resources managers and decision makers. In this research effort, the topics investigated include (a) determining which spatial resolution(s)/scale(s) are most appropriate to represent the two ecosystems (river corridor and surrounding arid vegetation) for *ET* estimation, (b) examining the effects of different spatial resolutions for *TSEB* inputs on the magnitude and spatial variation in *LE*, and (c) calculating the daily *ET* of vegetation species using the incoming solar radiation (R_s) method.

4.2 Methodology

Figure 4.1 illustrates the research methodology used for this study. First, the spatial domain/model grid size to represent the San Rafael River corridor was identified using discrete wavelet transform (*DWT*) analyses and *sUAS NDVI* information. Next, we derived the input data required by the *TSEB* model to calculate energy fluxes, mainly *LE*. Finally, the daily *ET* was calculated for each vegetation type using the R_s method.

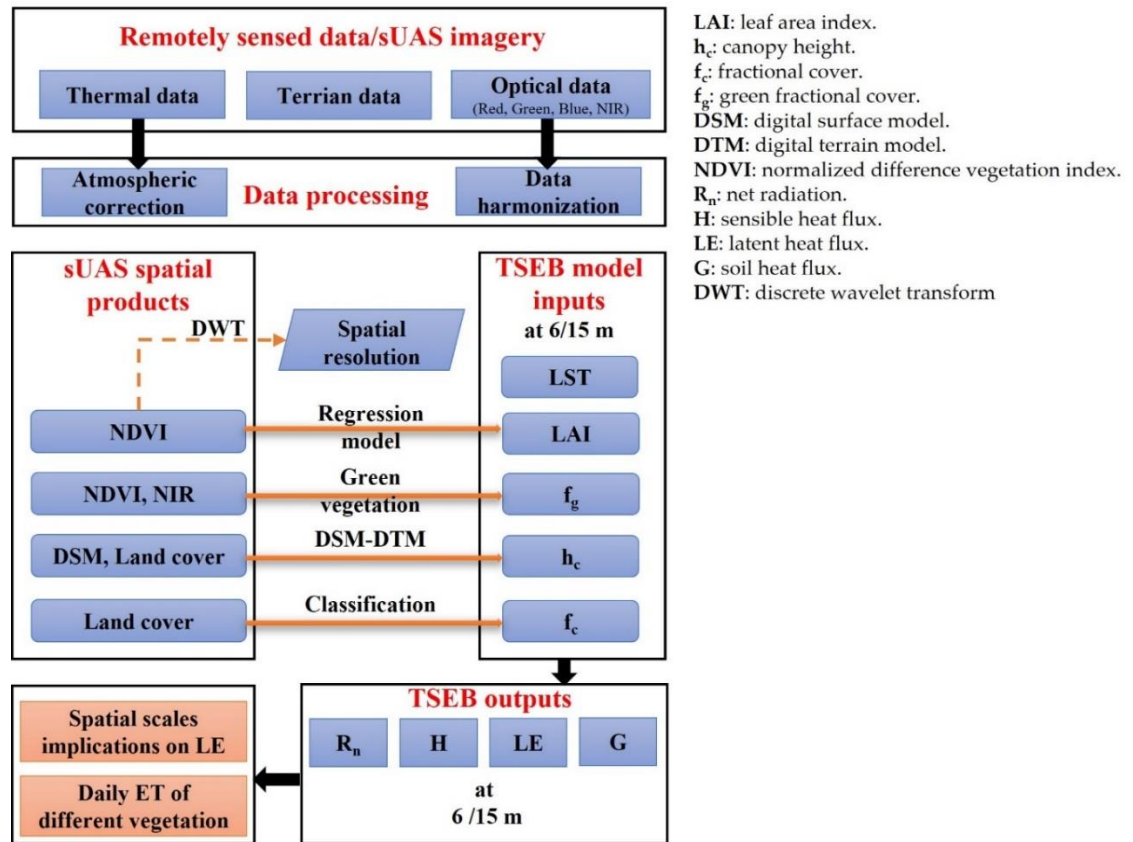


Figure 4.1 Flowchart of the methodology followed in this study.

4.2.1 Site Description

The study location is the San Rafael River corridor located in east central Utah (38°46'31" N, 110°06'17" W), as shown in Figure 4.2. The San Rafael River drains approximately 4,500 km² in south central Utah, including the northern Swell, which makes up part of the San Rafael Swell, a giant dome-shaped anticline. The river originates from the merging of three tributaries: Huntington Creek, Cottonwood Creek, and Ferron Creek. The San Rafael is one of the most over-allocated rivers in the State of Utah, with some 360 dams and 800 surface points of diversion. The underlying geology within the region consists of sandstone, shale, and limestone, which are consistently eroded by infrequent but powerful flash floods. In recent times, fragmentation, dewatering, non-native species,

and channelization have heavily impacted the river. The combination of altered hydrology, reductions in the magnitude and duration of snowmelt floods, and vegetation colonization has led to a narrowing and confinement of the river into a single-thread channel with steep banks, a low width-to-depth ratio, and a loss of habitat complexity [29]. Dewatering in this drainage is sometimes so severe that it results in a complete lack of flow for up to two months during the summer period [30]. The main riparian vegetation species in the San Rafael River corridor are treated tamarisk, willow, cottonwood, and grass/shrubs. The treatment of tamarisk involves spraying all sides of the canopy stems from the soil surface to a height of 12–18 inches using oil-soluble forms of triclopyr (Garlon 4 Ultra) herbicide and an approved oil (i.e., JBL Oil Plus). Willows are abundant along the river, and treated tamarisk are generally set back from the channel edge and dominate the floodplain. Multiple age classes of cottonwood exist on the lower floodplain surface, while grass and shrubs are scattered across the landscape.

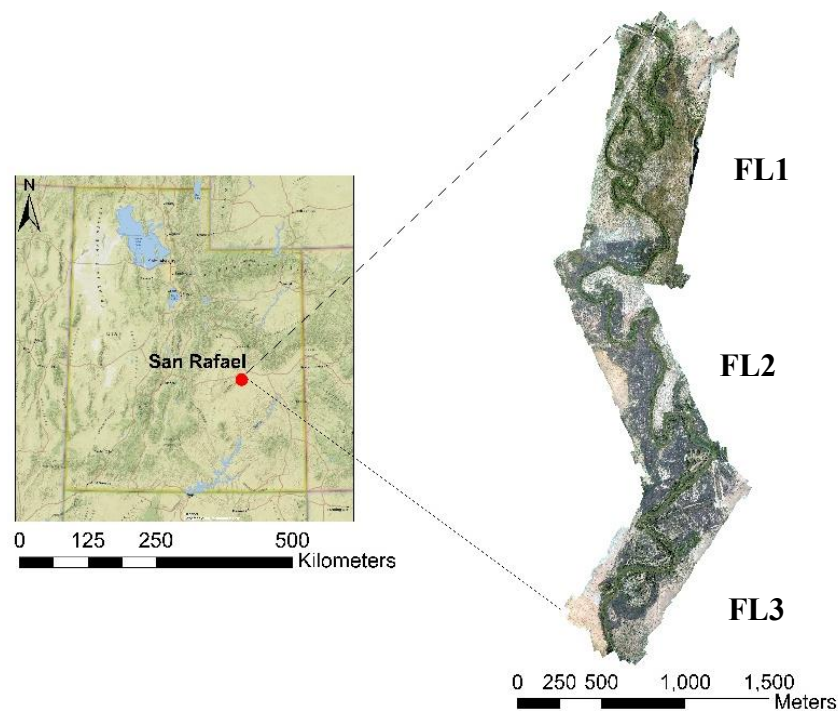


Figure 4.2 Layout of a section of the San Rafael River corridor area of study.

The analyses in this study rely on multiple flight campaigns implemented by the *AggieAir sUAS* Program at Utah State University (<https://uwrl.usu.edu/aggieair/>). Remote sensing data with multispectral images have been acquired through many *sUAS* campaigns over different seasons (see Table 4.1). Optical data, including red, green, blue, and near infrared bands, were acquired at 2.5-cm spatial resolution. Thermal data were acquired at 15 cm during the same flights at 400-ft elevation using a microbolometer camera. Each individual scene was mosaicked to generate a calibrated image (reflectance and temperature) covering the study area. The micrometeorological data was obtained from a weather station installed in the field during the flight dates. The technical specifications of the weather station used for this study are illustrated in Table 4.2. In this study, wind and temperature data obtained from the weather station (~2-m height) were extrapolated to 20 m above ground level (*agl*) to address the tall tree (mainly cottonwood) heights. For the calculation of the adjusted wind speed at 20 m *agl*, a logarithmic wind speed profile was used as shown in equation (4.1), while the air temperature was reduced using adiabatic lapse rate (ca. 6K/1km)

$$u_2 = u_z \frac{4.7}{\ln(67.8z - 5.42)} \quad (4.1)$$

where u_2 wind speed at 2 m *agl* (m/s), u_z measured wind speed at specific height (m/s), z height of measurement *agl* (m).

Table 4.1 Dates and times (launch and landing) of *AggieAir* flights at the San Rafael River corridor.

Date	Flight 1 (<i>FL1</i>)		Flight 2 (<i>FL2</i>)		Flight 3 (<i>FL3</i>)	
	Launch	Landing	Launch	Landing	Launch	Landing
June 19, 2019	11:34	12:07	13:52	14:20	-	-
July 22, 2019	9:49	10:20	12:36	13:02	14:50	15:18
October 26, 2019	11:38	12:03	13:00	13:23		

All times are expressed in Daylight-Saving Time zone.

Table 4.2 The technical specifications of the weather station used for this study.

Parameter	Instrumentation
Wind Speed	Solid state magnetic sensor
Wind Direction	Wind vane with potentiometer
Rain Collector	Tipping spoon
Temperature	PN Junction Silicon Diode
Relative Humidity	Film capacitor element

4.2.2 Characterizing the Spatial Heterogeneity Using Wavelet Analysis

The availability of different remote sensing platforms (satellites, manned aircrafts, and *sUAS*) with various spatial resolutions allows for assessment of the spatial heterogeneity in the landscape using vegetation indices such as *NDVI* [31]. While *sUAS* provides spatial information at a fine scale (i.e., plant scale), *SEB* models need to have adequate spatial resolutions/model grid sizes that are associated with the model parameterizations in deriving energy fluxes, particularly given challenges associated with accurately representing heterogeneous domains. For example, agricultural fields such as vineyards and orchards have an organized plant pattern with uniform vegetation row spacing, making it easy to identify the dominant scale based on the distance between plant

rows. In contrast, specifying the representative spatial resolution/model grid size in natural environments is more difficult as the perennial vegetation is more randomly spaced and largely clumped, creating significant gaps of bare soil with annuals emerging when water is available.

In this study, we used the discrete wavelet transform (*DWT*) along with *sUAS NDVI* data to characterize the spatial heterogeneity over the San Rafael River corridor, a heterogeneous natural environment. Wavelet analysis has been introduced successfully in different applications over the last two decades, particularly in signal processing and computational statistics [32]. In ecological/ecosystem applications, a few studies have addressed wavelet analysis [33]. The earliest study, conducted by Bradshaw and Spies (1992) [34], aimed to characterize forest canopy structure along a transect. Another application of the wavelet analysis sought to identify the dominant resolution/model grid size (e.g., Murwira and Skidmore 2010) [35] by decomposing the *2D* image into different scales for detecting the spatial pattern at each scale [36].

Wavelet energy [37] was used to characterize the spatial variability in the San Rafael River corridor by quantifying the intensity and the dominant resolution/model grid size of spatial heterogeneity in *NDVI* images from different dates (see Table 4.1). The calculation of wavelet energy begins with a wavelet transform, a linear filter that can be described by two functions: the scaling/smoothing function (also referred to as the father wavelet) and the detail function (or mother wavelet). These two functions are used to decompose the image to multiple wavelet transform coefficients to evaluate the degree of similarity between the wavelet template and the image structure/pattern. The Haar *DWT* was used for its ability to detect boundary, edges, and abrupt discontinuity in the data such

as changes and gaps in the vegetation cover [34]. At each level of decomposition, the wavelet transform produces two types of coefficients, “smooth” and “detail,” at successive bases (2^j with $j = 0, 1, 2, \dots, J$), as shown in Figure 4.3. Smoothing coefficients represent an averaged version of the original data, whereas detail coefficients describe the deviances from the average value in horizontal (h), vertical (v) and diagonal (d) directions. A high absolute value of the coefficients represents a good match between the wavelet and the image data (e.g., a change in vegetation cover), while small or zero values represent a poor match. Given an image, $F(x, y)$, the wavelet approximations, $\hat{F}(x, y)$, are calculated as a sum of the smooth and detail coefficients at different bases.

$$\hat{F}(x, y) = S_j(x, y) + \sum_{j=1}^J \sum_{dir} D_j^{dir}(x, y) \quad (4.2)$$

where S_j is the smooth coefficients and D_j^{dir} is the directional detail coefficients.

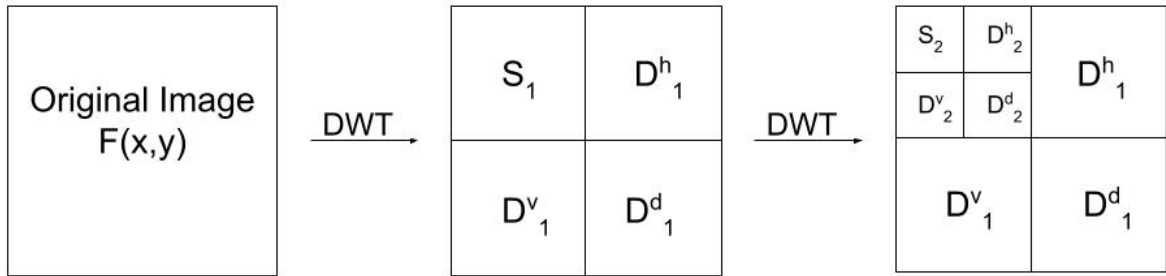


Figure 4.3 Schematic diagram of *DWT* for 2D image.

The wavelet energy is calculated as the sum of squares of the coefficients at a level of decomposition, 2^j , divided by the sum of squares all of the coefficients in $\hat{F}(x, y)$. The formula describes the wavelet energy as shown in Equation (4.3).

$$E_j^d = \frac{1}{E} \sum_{k=1}^{n/(2^j)^2} d_{j(x,y)}^2, j = 1, 2, 3, \dots, J \quad (4.3)$$

where $d_{j(x,y)}$ is the detail wavelet coefficient at level j and position (x,y) , E is the total wavelet energy calculated as the sum of squares of the coefficients in $\hat{F}(x,y)$, and $n/(2^j)^2$ is the number of coefficients at level j . High energy values represents the presence of larger coefficients and therefore identify dominant patterns at a given spatial resolution/model grid size.

4.2.3 Image Classification

Coarse resolution imagery, such as Landsat at 30-m or SPOT at 20-m, may not be enough to capture the spatial heterogeneity in natural environment [38]. However, the recent development of *sUAS* remote sensing technology with spatial resolutions of 10 cm or less allows for the capture of spatial variability in the riparian vegetation in locations such as the San Rafael River corridor. In this study, multispectral images from several flight campaigns acquired by *AggieAir sUAS* were classified to identify and map the features/classes of interest in riparian scenes using supervised classification, in which the spectral signatures/training samples from the image are extracted by specifying the known or visibly distinct features. Training samples were extracted from the images using ArcGIS 10.7 and then used to classify the entire map into several features, including willow, water, treated tamarisk, bare ground, developed/road, grass/shrubs, and cottonwood. Flight images show distinct spectral variations between different vegetation types, mostly willow (dense with green tones), treated tamarisk (represented by a dark brown color), and cottonwood (large green leaves and thick foliage).

4.2.4 ET Estimation Using the Two Source Energy Balance (TSEB) Model

4.2.4.1 Model Overview

The *TSEB* model was developed originally by Norman et al. (1995) [14] to calculate energy fluxes, mainly the latent heat flux (*LE*). *TSEB* considers the combined emissions from vegetation and soil to compose the total temperature emitted by the surface, weighted based on the fractional cover as described in Equation (4.4)

$$\sigma T_{rad}^4(\theta) = f_c(\theta)\sigma T_c^4 + [1 - f_c(\theta)]\sigma T_s^4 \quad (4.4)$$

where $f_c(\theta)$ is the vegetation fractional cover observed by the *TIR* sensor at specific angle (θ). T_c and T_s are the canopy and soil temperature, respectively, in (Kelvin). $T_{rad}(\theta)$ is the directional radiometric surface temperature. As the temperature is separated into soil and canopy temperatures (T_s and T_c), the energy balance is decoupled into two layers and can be described in the following equations

$$R_{nc} = H_c + LE_c, \quad (4.5)$$

$$R_{ns} = H_s + LE_s + G, \quad (4.6)$$

where R_n is net radiation, LE is latent heat flux, H is sensible heat flux, and G is the soil heat flux. All flux units are expressed in W/m^2 , and subscripts c and s represent the canopy and soil components, respectively. Radiative transfer and absorption through canopy are simulated using an extinction coefficient approach, which is a function of the amount of canopy foliage (i.e. LAI) and canopy architecture (i.e. X_{LAD}) along with the incident solar angle. In the radiative transfer model, the incoming shortwave radiation is separated into direct and diffused radiation, along with separation between visible and near-infrared (*VIS-NIR*) spectral ranges due to drastic changes in reflectivity and transmissivity between

canopy and soil features. *TSEB* simulated the longwave (*LW*) radiation transfer model similarly without considering a diffusion from the *TIR* region.

When estimating the sensible heat flux for soil and canopy (H_s and H_c), both layers are assumed to interact with each other and with the atmosphere using their respective temperatures along with a series of soil-vegetation resistive schemes (following an analogy with Ohm's law).

$$H = H_c + H_s = \rho_{air} C_p \frac{T_{AC} - T_A}{R_A} \quad (4.7)$$

$$H_c = \rho_{air} C_p \left[\frac{T_c - T_{AC}}{R_x} \right] \quad (4.8)$$

$$H_s = \rho_{air} C_p \left[\frac{T_s - T_{AC}}{R_s} \right] \quad (4.9)$$

where H is the sensible heat flux (W/m^2); ρ_{air} is the air density (kg/m^3); C_p is the heat capacity of the air at constant pressure (J/kg/K); T_A is the air temperature (Kelvin); T_c and T_s are canopy and soil temperature (Kelvin), respectively; and T_{AC} is the temperature of the canopy-air space (Kelvin) calculated from the component temperature of each source (T_c and T_s) along with aerodynamic resistances, R_A , R_s and R_x , as described mathematically in Equation (4.10).

$$T_{AC} = \frac{\frac{T_A}{R_A} + \frac{T_c}{R_x} + \frac{T_s}{R_s}}{\frac{1}{R_A} + \frac{1}{R_x} + \frac{1}{R_s}} \quad (4.10)$$

where R_A is the aerodynamic resistance to heat transfer based on the Monin-Obukhov similarity theory, R_x is the boundary layer resistance of the canopy leaves, and R_s is the aerodynamic resistance to heat transport in the boundary layer above the soil layer. All

resistances are expressed in (s/m). More details about the *TSEB* model and updates/revisions to algorithms can be found in Kustas et al. (1999), Kustas et al. (1999), and Nieto et al. (2019) [39,40,41], and the details of radiation formulations can be found in Campbell and Norman (1998) [42].

4.2.4.2 Retrieving the Biophysical *TSEB* Inputs

The *TSEB* model requires vegetation biophysical properties as inputs. In natural environments such as the San Rafael River corridor, deriving the spatial information of biophysical parameters is challenging due to spatial heterogeneity in the vegetation species, terrain formation, and environmental characteristics.

(a) Fractional Cover (f_c)

In the *TSEB* model, fractional cover (f_c) is used as a proxy for canopy clumpiness, which is defined as the nadir-looking fraction of vegetation (both green and standing dead vegetation elements) per unit ground. Together with total *LAI*, f_c mainly affects how irradiance is effectively intercepted by the vegetation and/or transmitted through the background/soil. To calculate the f_c in this study, the high resolution *RGB* image was first classified into multiple features/classes, then f_c was estimated as the portion of vegetation (green and standing dead) within the spatial domain / model grid size.

(b) Green Ground Cover (f_g)

Green ground cover (f_g) is defined as the fraction of leaves or vegetation elements that could actively transpire. It represents the fraction of *LAI* that is actually green and hence mainly contributing to latent heat flux, while the rest of the dead vegetation elements

$(1 - f_g)$ are mainly contributing to sensible heat flux. For the June and July flights, *NDVI* was used to separate vegetation pixels (classified previously for the f_c calculation) to calculate the proportion of green and dead elements at different spatial resolutions (6-m and 15-m), whereas the *NIR* band was used for October flights as most vegetation is in a dry and/or dead condition.

(c) Canopy Height (h_c)

Generating h_c maps for the San Rafael River corridor was challenging due to the high variation in the land surface topography. Canopy height (h_c) was calculated as the difference between the digital surface model (*DSM*) and the digital terrain model (*DTM*). The *DSM* was obtained from *sUAS* flights at different dates, while the *DTM*, which represents the ground elevation, was generated by selecting the elevation of pure bare soil pixels and then creating a *DTM* map covering the study area using an interpolation model (Kriging).

(d) Leaf Area Index (*LAI*)

LAI is an important state variable in ecosystem modeling as it influences the energy fluxes between the land surface and atmosphere. Estimating spatial distribution of *LAI* is challenging in heterogeneous natural environments with a variety of vegetation types, such as the San Rafael River corridor. In this study, the ground-based *LAI* measurements were collected using a *LiCOR* plant canopy analyzer at multiple locations. Due to the variability within the canopy as shown in Figure 4.4, the *LAI* was placed near the bottom of the canopy at each location and was moved to different spots (4 – 6) at the base of the canopy to provide a representative sample. For each measurement, a 45° view cap was placed over the lens, restricting the view to an eighth of a hemisphere.

LAI was estimated as a point measurement for individual canopy (LAI_{shrub}). The primary goal was to have the LAI value represent the spatial domain/model grid size (including bare ground and vegetation), and this was calculated as $LAI = f_c \times f_g \times LAI_{shrub}$ [43]. Next, a regression model (exponential equation) between LAI and the vegetation indices, particularly $NDVI$, was used to derive spatial maps of LAI in the June and July flights. However, using the regression model for October flights resulted in a weak correlation due to senescent condition with low LAI values. For the October flights, a specific LAI value was used for each vegetation type based on in-situ measurements.



Figure 4.4 Example of in-situ LAI measurements taken in the San Rafael River corridor.

4.3 Results and Discussion

4.3.1 Land Cover/Land Use Classification

The $sUAS$ images, in conjunction with ground-based observations, were used to discriminate riparian vegetation classes in the San Rafael River corridor. The results of the land cover/land use classification are summarized into six categories: water, bare ground, treated tamarisk, cottonwood, willow, and grass/shrubs. The distribution of the

vegetation has distinct patterns across the San Rafael floodway. Dense vegetation stands of treated tamarisk (non-native) represent the second dominant riparian plant species in the study area. Willows/phragmites (also called common reed) were identified along the river and dominate the river channel margin occupying the riparian berm that extends laterally to a width of 2 to 10 m. Some cottonwood trees are scattered across the floodplain. Most of the cottonwood trees are designated within the old age class, with height varying between 8 and 12 m above ground level (*agl*). Swaths of grass and desert shrubs are observed along the dry riverside, and other areas are dominated by sand dunes.

Figure 4.5 shows the proportion of the different plants mapped across the San Rafael River corridor. The results indicate that grass/shrubs are widespread throughout the entire study area, representing nearly 37%. Treated tamarisk is the second dominant vegetation species, which represents 23% of the study area. In contrast, the classified map shows the percentage of cottonwood and willow to be relatively small compared with the other vegetation species, accounting for 2% and 3% of total area, respectively. Of the remaining three land cover/land use classes, bare ground constitutes nearly 31%, and water, 3%, while the developed (Road) class is far less prevalent across the study area, accounting for 1%.

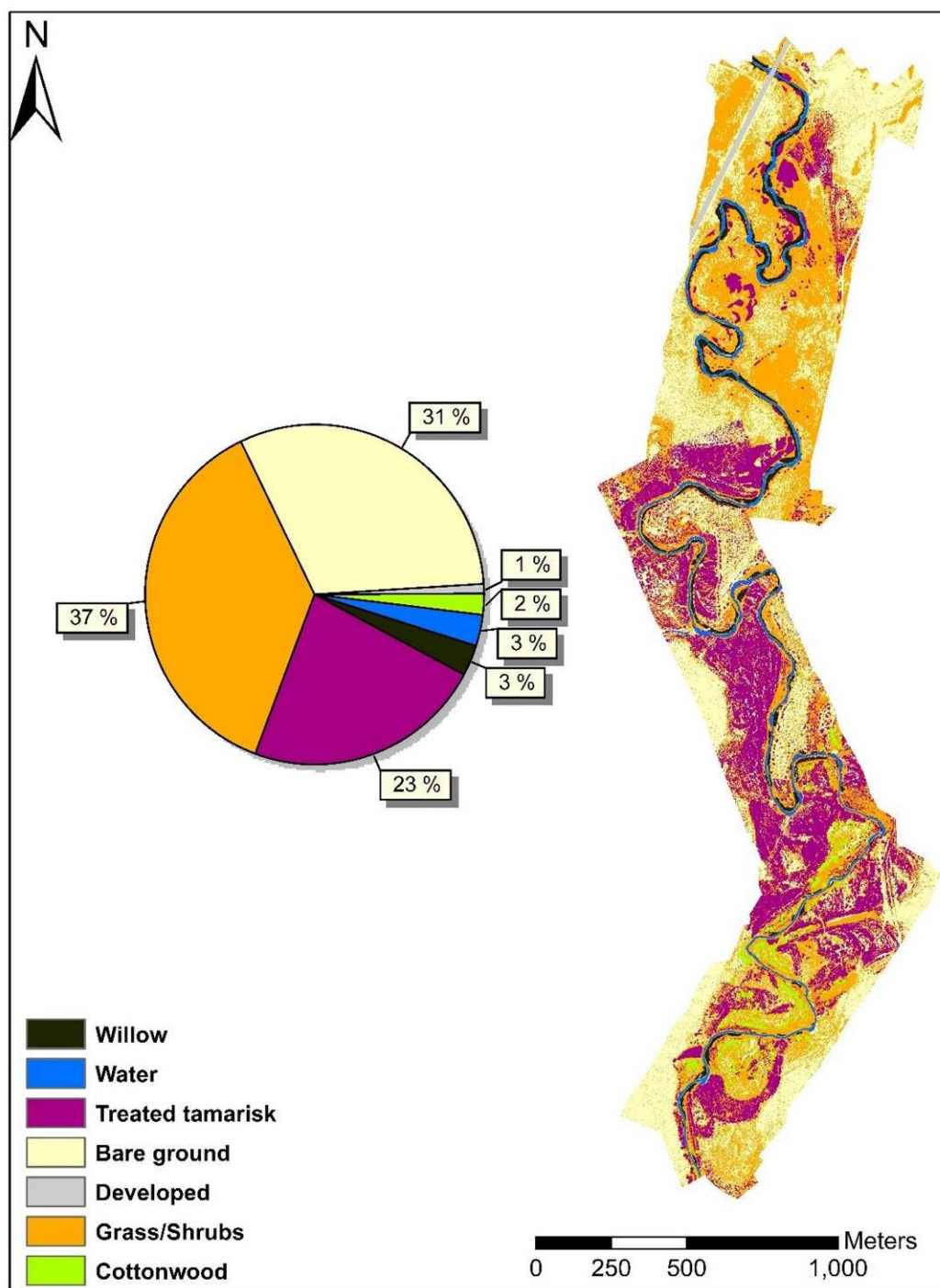


Figure 4.5 Vegetation classification map of the San Rafael River corridor.

4.3.2 Spatial Heterogeneity Using Wavelet Analysis

Understanding the role of landscape heterogeneity is essential for identifying the representative spatial resolution/model grid size to estimate surface fluxes, mainly *LE*. In this study, *NDVI*, as one of the most common vegetation indices, was used to investigate spatial heterogeneity in the San Rafael River corridor. As shown in Figure 4.6, high spatial variability was observed in the *NDVI* due to high landscape heterogeneity within the different features/classes, including water, vegetation, and bare soil. Other environmental factors that could increase the *NDVI* spatial variability are the variation in soil properties (such as soil salinity) and/or soil moisture [44]. High *NDVI* values correspond to green vegetation, particularly along the river corridor, whereas bare soil and standing dead vegetation are characterized by low *NDVI*. For example, the *NDVI* increases dramatically in cottonwood and high-density vegetation such as willow/ phragmites with values above 0.75. Sparse vegetation such as grass/shrubs result in moderate values of *NDVI* ranging between 0.4 and 0.7. In cases of soil and dead and/or dry vegetation, *NDVI* is less than 0.35. Negative values of *NDVI* correspond to the waterbody.

Figure 4.7 shows the wavelet energy of *NDVI* for two different features, the river corridor and the remaining area surrounding the river corridor (non-river corridor). Each plot describes the change in the wavelet energy (%) in the various directions (horizontal, vertical, diagonal) corresponding to multiple spatial resolutions/model grid sizes. The comparison of the wavelet energy curves for the two features shows that they have completely different shapes for all flights (June, July, and October). For the area adjacent to the river (river corridor), wavelet energy resembles a concave down shape with highest values of energy appearing in the vertical (north-south) direction, medium in the horizontal

(east-west) direction, and lowest in the diagonal (northeast-southwest and northwest-southeast) direction. Based on Figure 4.7, the vertical and horizontal curves show the presence of two dominant scales of spatial heterogeneity, depicted by two wavelet energy maxima ranging between 6.4 and 12.8 m for all *sUAS* flights. The wavelet energy values at 6.4-m and 12.8-m spatial resolutions are relatively close, with a slight increase at 12.8 m. However, in the diagonal orientation, the wavelet energy values are very low, with the wavelet-based dominant scale peaking at 12.8 m. In the non-river corridor area, the wavelet energy curves in the various directions (vertical, horizontal, and diagonal) flatten out without the presence of a dominant spatial resolution/scale, with one exception. *FLI* on June 19, 2019, shows a high wavelet energy value present at very low spatial resolution, which may occur as a result of different vegetation patterns and types existing in that area.

The different wavelet energy curves between the river corridor and the remaining area (non-river corridor) are caused mainly by the fact that green vegetation is present along the river, while the surrounding area is characterized by different surface types (soil, standing dead vegetation, shrubs or others). The *NDVI* of the canopy has a much higher value than any surface type, which causes a larger variation and more wavelet energy. However, for the second feature (non-river corridor), which is characterized by scattered shrubs and canopies, the wavelet energy is very low with a flat curve. This indicates that considerable wavelet energy is present at all spatial resolutions/model grid sizes. One explanation for the flat shape in the wavelet energy curve across the different flights could be the low variation in the *NDVI* values of dead plants and soil. Even the shrubs present within the domain do not seem to have a significant influence on the general trend of the wavelet energy curve due to the large distances between them.

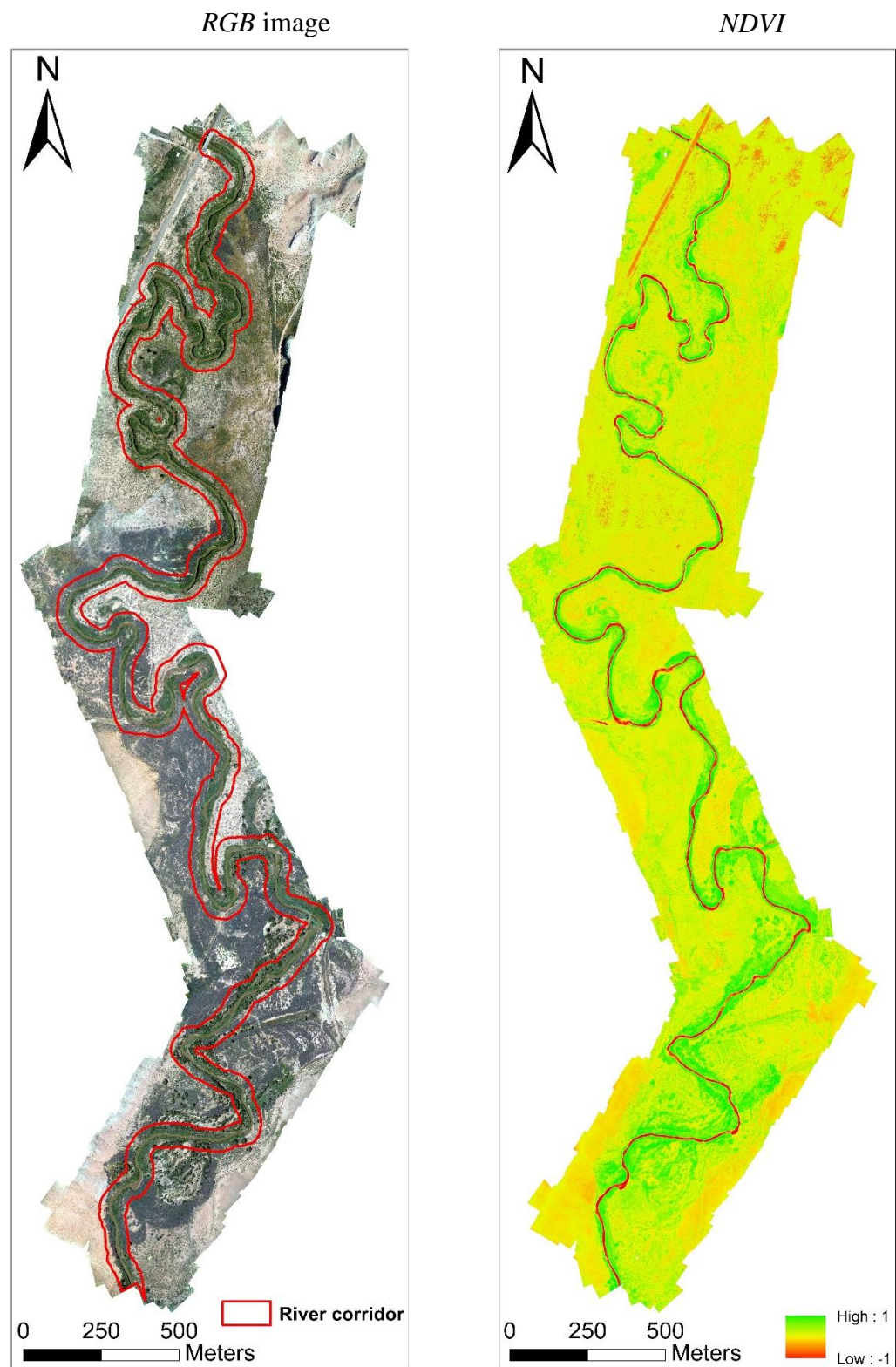
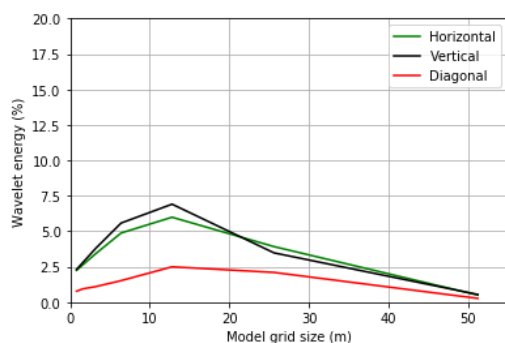
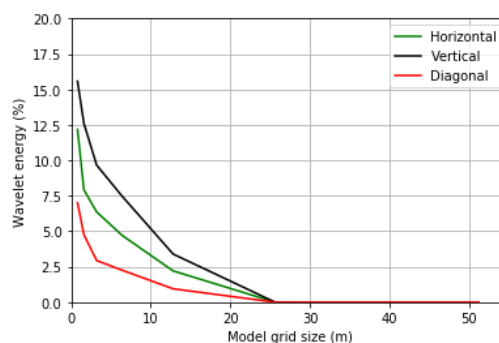
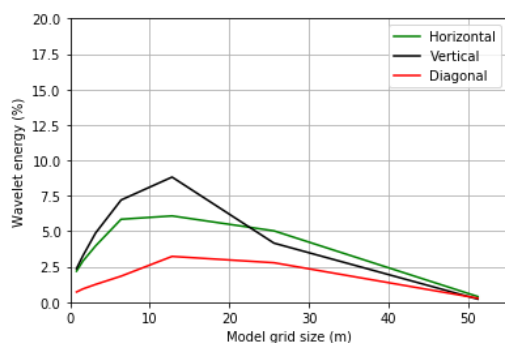
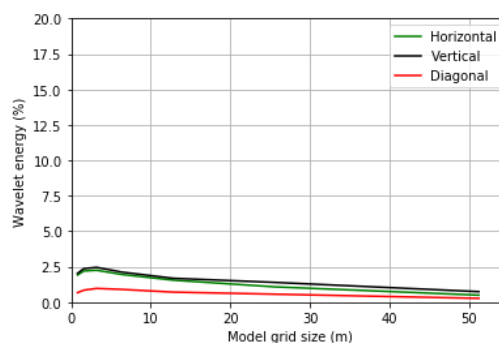
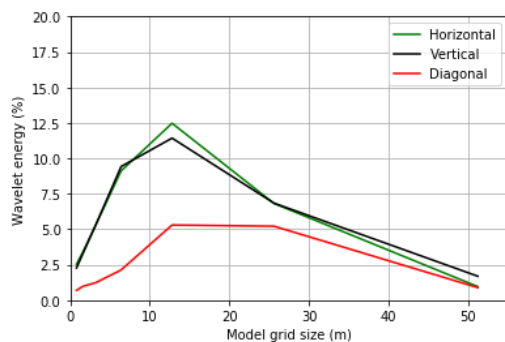
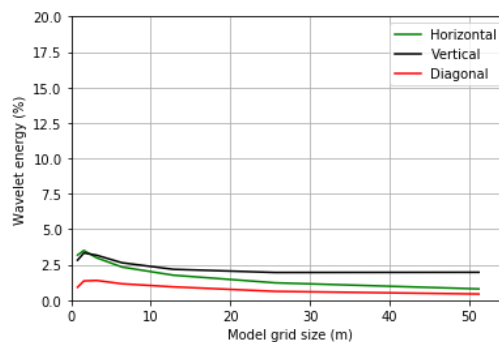
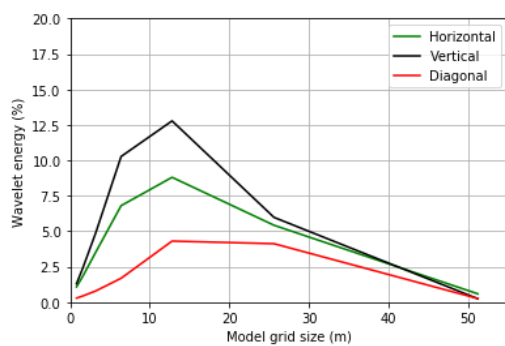
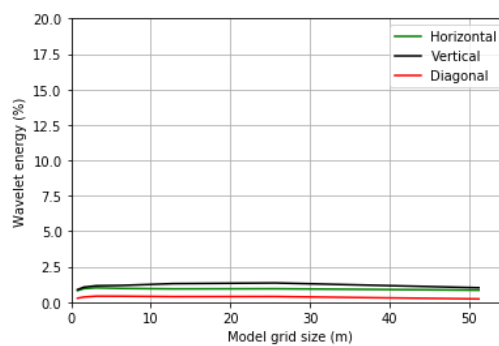


Figure 4.6 Layout of river corridor and non-river corridor area for wavelet analysis.

June 19, 2019 – *FL1* (River Corridor)June 19, 2019 – *FL1* (Non-River Corridor)June 19, 2019 – *FL2* (River Corridor)June 19, 2019 – *FL2* (Non-River Corridor)July 22, 2019 – *FL1* (River Corridor)July 22, 2019 – *FL1* (Non-River Corridor)July 22, 2019 – *FL2* (River Corridor)July 22, 2019 – *FL2* (Non-River Corridor)

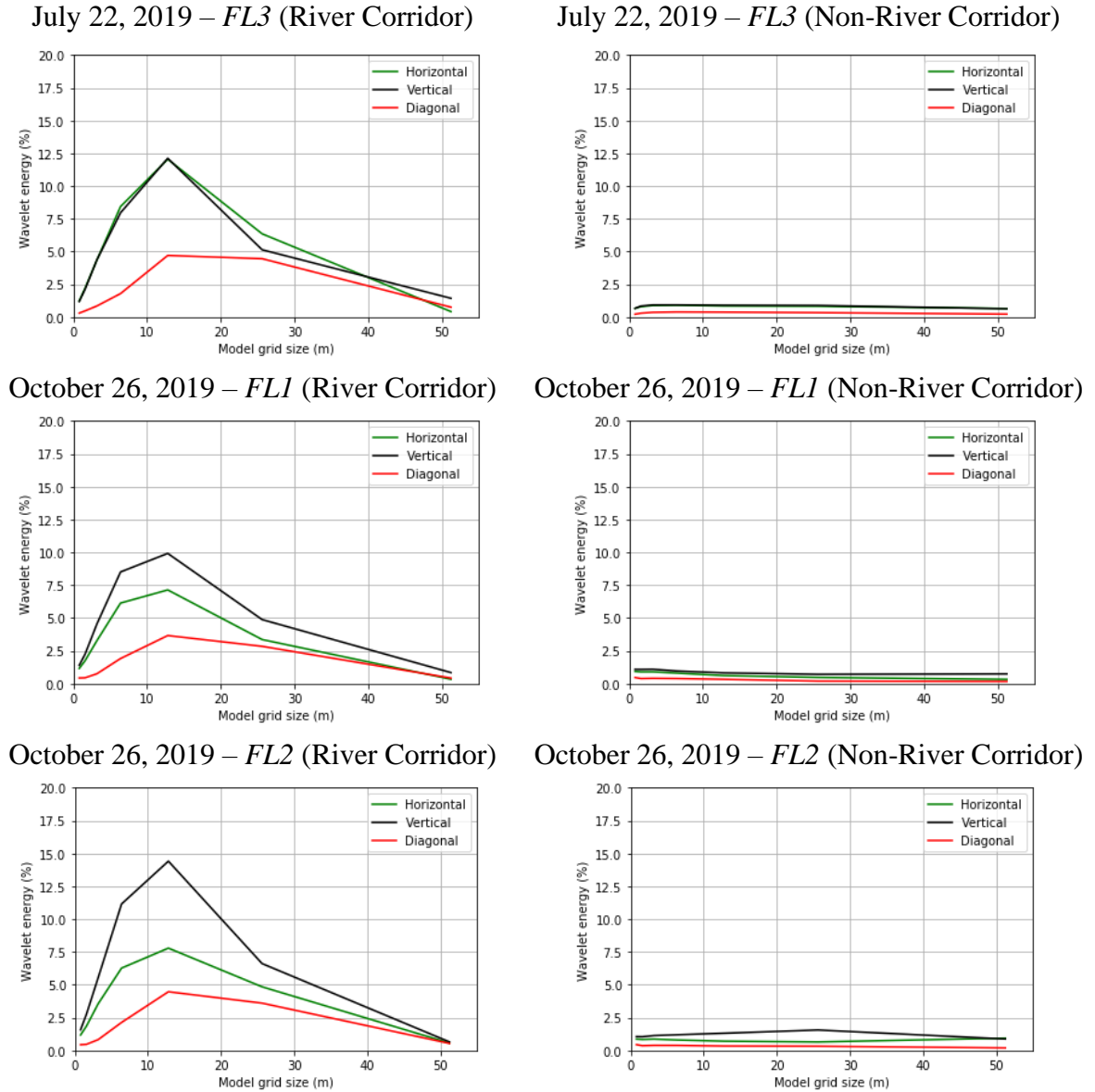


Figure 4.7 Wavelet energy at multiple spatial domains for different flights.

4.3.3 Retrieving the Biophysical Parameters

Figure 4.8 shows an example of each biophysical parameter (f_c , f_g , LAI , and h_c) used for the *TSEB* model. the f_c parameter was calculated using the percentage of vegetative pixels (stand dead and green) within each contextual spatial domain/resolution and ranged between 0 and 1 for the *sUAS* flight in July 2019. As shown in Figure 4.8a, the highest f_c values were observed along the river corridor, which is dominated by green vegetation.

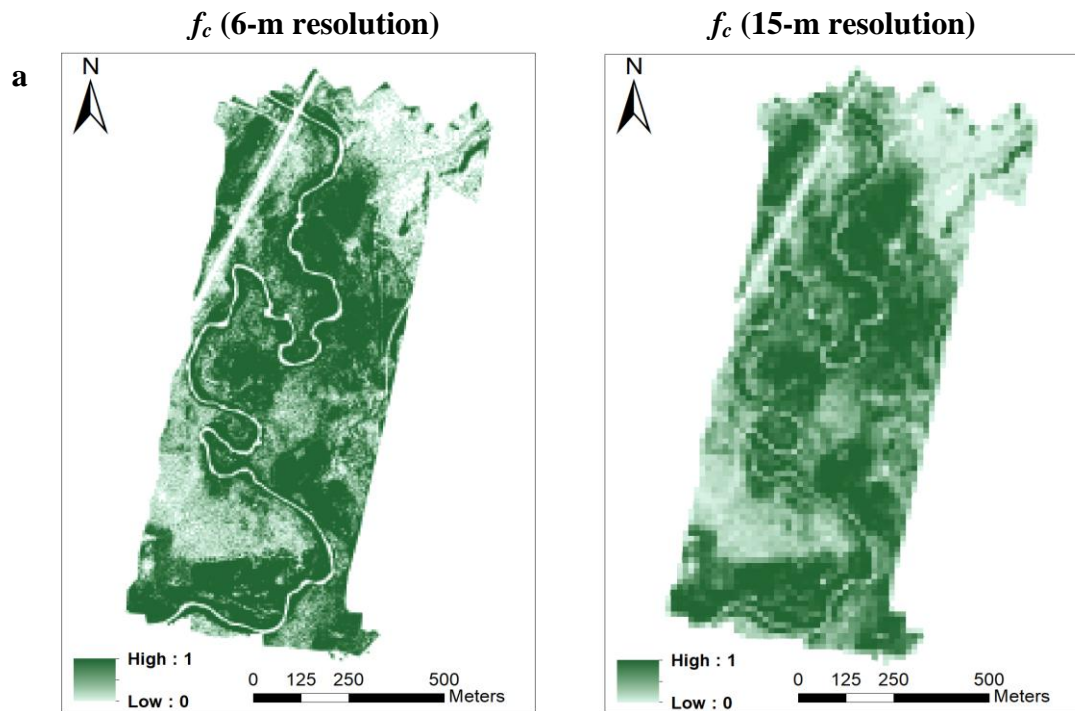
The comparison of the f_c maps at the two spatial resolutions (6 m and 15 m) shows a non-significant difference, with a slight decrease at 15 m due to the loss in spatial variability.

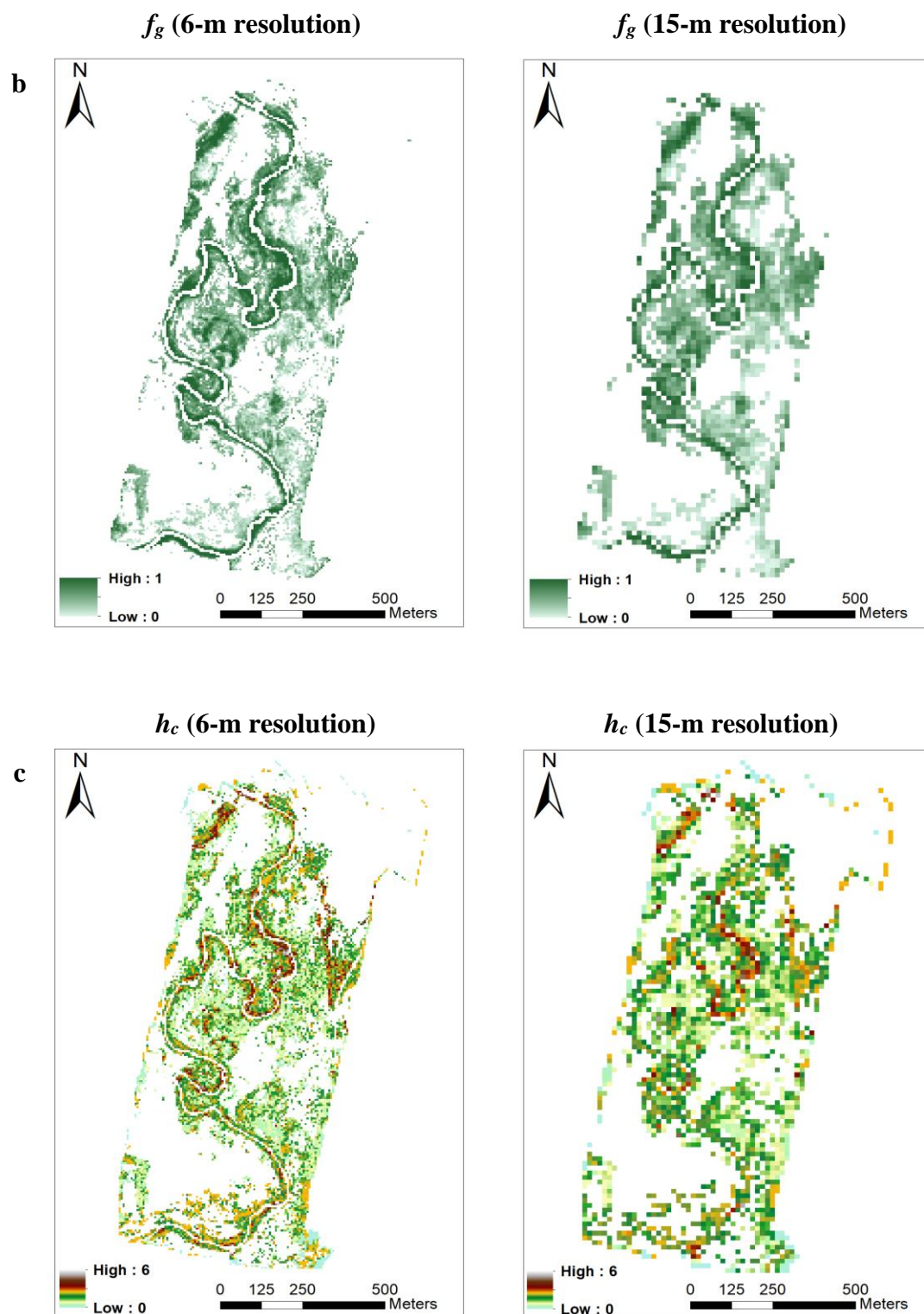
Green fractional cover (f_g) was calculated as the percentage of green vegetation only. *NDVI* threshold values were used to distinguish between the dead and green vegetation for the *sUAS* flights in June and July, whereas the *NIR* band was used for the October flight because most vegetation is in a dry condition at that time. Figure 4.8b illustrates the ranges of f_g , which are between 0 and 1 for the *sUAS FLI* on July 22, 2019. The highest f_g values were observed along the river corridor, whereas the lowest values are present in the treated tamarisk patches, which are in a dead/dry condition. Comparing the f_g values between the 6-m and 15-m spatial scales revealed a slight difference caused by aggregation issues.

Canopy height (h_c) maps were generated based on the differences between the *DSM* and *DTM*. Overall, h_c values showed high spatial variability due to the number of vegetation types (treated tamarisk, cottonwood, willow, grass/shrubs) that exist in the study area. The highest h_c values correspond to cottonwood, varying between 8 and 12 m, whereas the lowest h_c values were observed in grass/shrubs, ranging between 0.2 and 0.5 m, depending on the vegetation development stage. Figure 4.9 shows an example of canopy height calculation. The *DSM* profile represents the elevation of canopy above mean sea level (*AMSL*) at 25-cm spatial resolution, whereas the h_c profile represents canopy height derived at a 1-m spatial domain. A comparison of the two profiles indicates similarities in the shapes of both curves.

LAI calculation was challenging in this study because of the landscape complexity in the San Rafael River corridor. Figure 4.8 shows an example of the *LAI* maps at different

resolutions for *sUAS FLI* on July 22, 2019. The highest *LAI* values were observed in willow and cottonwood, whereas the lowest values exist in grass/shrubs. Comparing the *LAI* maps at the two scales, the values at 15-m spatial resolution are lower due to the mix of different vegetation types within the spatial domain/resolution. Wu et al. (2016) [45] found that *LAI* scaling is influenced not only by the spatial heterogeneity of *NDVI* but also by the nonlinearity model used for retrieving *LAI*. The study also found that the logarithmic regression model results in overestimation in *LAI* values, whereas the exponential regression function leads to underestimation of *LAI* values within the heterogeneous spatial domain. For this study, we found reasonable agreement between the *NDVI* and ground *LAI* measurements using the exponential equation as explained in the methodology section.





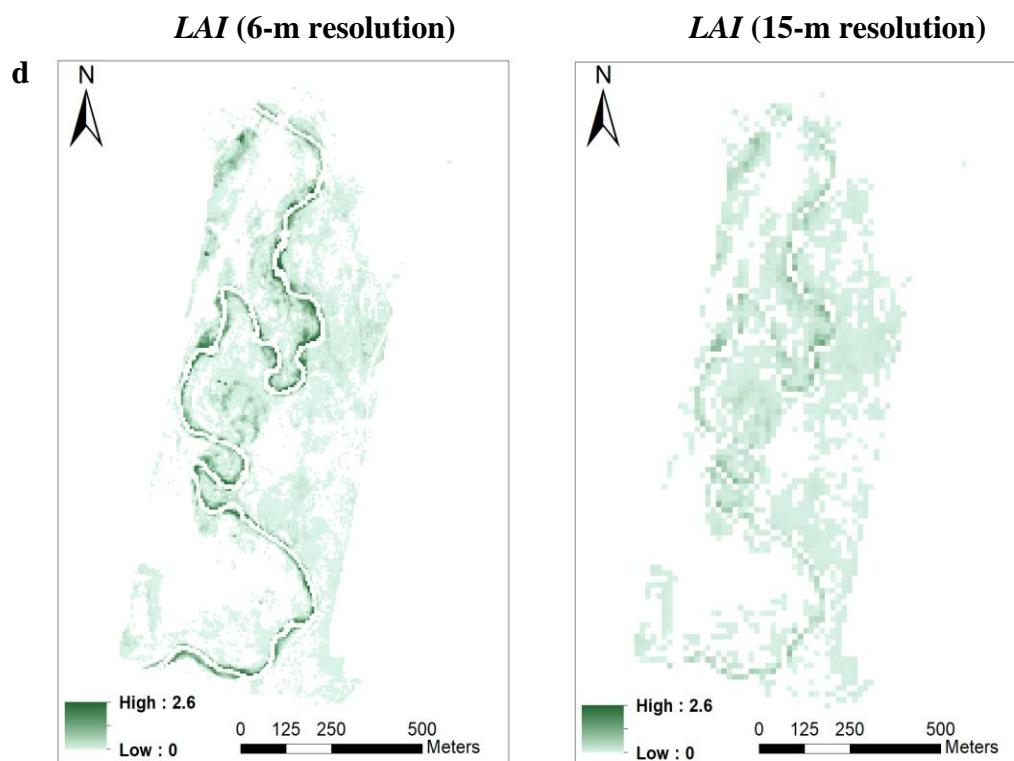


Figure 4.8 Example of the spatial maps for biophysical parameters at 6-m and 15-m resolutions for *FLI* (July 22, 2019).

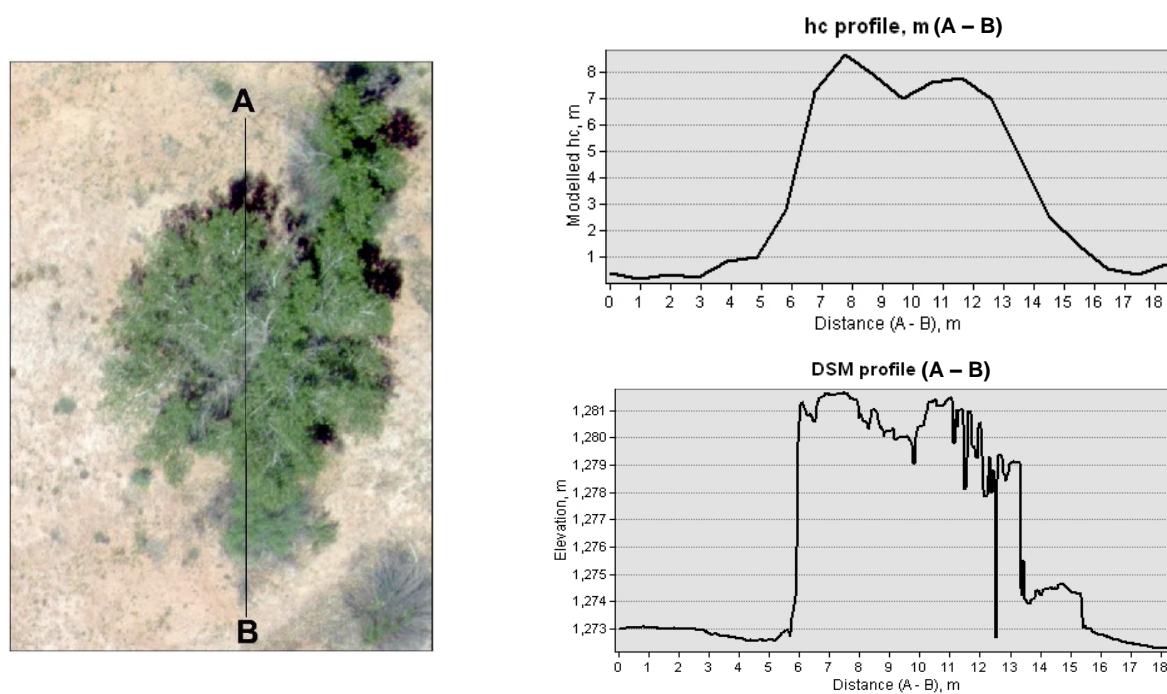


Figure 4.9 Example of *DEM* and h_c profiles in the study site.

4.3.4 Spatial Scale Implications on *LE*

The *TSEB* model was applied at two selected spatial resolutions/model grid sizes, 6 m and 15 m, both of which are considered suitable to represent the San Rafael River corridor domain according to the wavelet analysis (see section 4.3.2). To represent differences in roughness for the vegetation types within the two model grid sizes/spatial domains (6 m and 15 m), different canopy heights were weighted by their fractional cover. To evaluate the influence of the two resolutions on *LE* energy fluxes using the *sUAS* information, an example of the *LE* map along with other statistics, including the frequency curve, spatial mean, and standard deviation, were calculated and presented in Table 4.3 and Figure 4.10. Overall, the results indicate low statistical discrepancies in the *LE* values at the two different scales, 6 m and 15 m, for the multiple *sUAS* flights. The statistics (spatial mean (μ) and standard deviation (σ)) of the two resolutions are close, with a slight decrease at 15 m due to losses in spatial variability. For example, the spatial mean *LE* value for *FL1* on July 22, 2019, was 126 W/m² at 6-m resolution/model grid size but decreased to 122 W/m² at 15-m resolution. Similarly, the standard deviation decreases slightly from 68 W/m² at 6-m resolution to 64 W/m² at 15-m resolution. Figure 4.11 shows the frequency curves of *LE* at 6-m and 15-m spatial resolutions/model grid sizes for the area covered by each flight (*FL1*, *FL2*, and *FL3*). The plots demonstrate different trends due to different vegetation patterns and types that dominate each flight. For example, grass and shrubs dominate in *FL1*, whereas treated tamarisk is widespread in *FL2* and *FL3*. Moreover, the frequency histogram in Figure 4.11 indicates a non-significant change between the two curves at the two different scales for each single flight. This behavior aligns with the results obtained from the spatial mean and standard deviation. One explanation for the similarities

in LE values could be that both resolutions are able to capture the heterogeneity in the study site domain.

Figure 4.10 shows an example of modeled instantaneous LE (W/m^2) at 6-m and 15-m resolutions for $FL1$ on July 22, 2019. The maps show high spatial variability in LE values, varying between $0 W/m^2$ and $330 W/m^2$. A similar trend in spatial variances has been observed for other LE maps at different dates and times. Many factors related to soil moisture and differences in vegetation species and vegetation cover could potentially cause these variations in LE . High LE values correspond to the vegetation along the river corridor due to the presence of dense patches that reach full green ground cover. This is true for all of the vegetation along the riverbank.

Table 4.3 Spatial resolution effect on LE estimation.

Flight data	Flight number	Spatial mean (μ) (W/m^2)		Standard deviation (σ) (W/m^2)	
		6 m	15 m	6 m	15 m
June, 19, 2019	<i>FL1</i>	181	168	93	86
June, 19, 2019	<i>FL2</i>	203	184	132	122
July 22, 2019	<i>FL1</i>	126	122	68	64
July 22, 2019	<i>FL2</i>	218	197	143	134
July 22, 2019	<i>FL3</i>	274	255	154	145
October 26, 2019	<i>FL1</i>	206	204	50	50
October 26, 2019	<i>FL2</i>	232	230	56	52

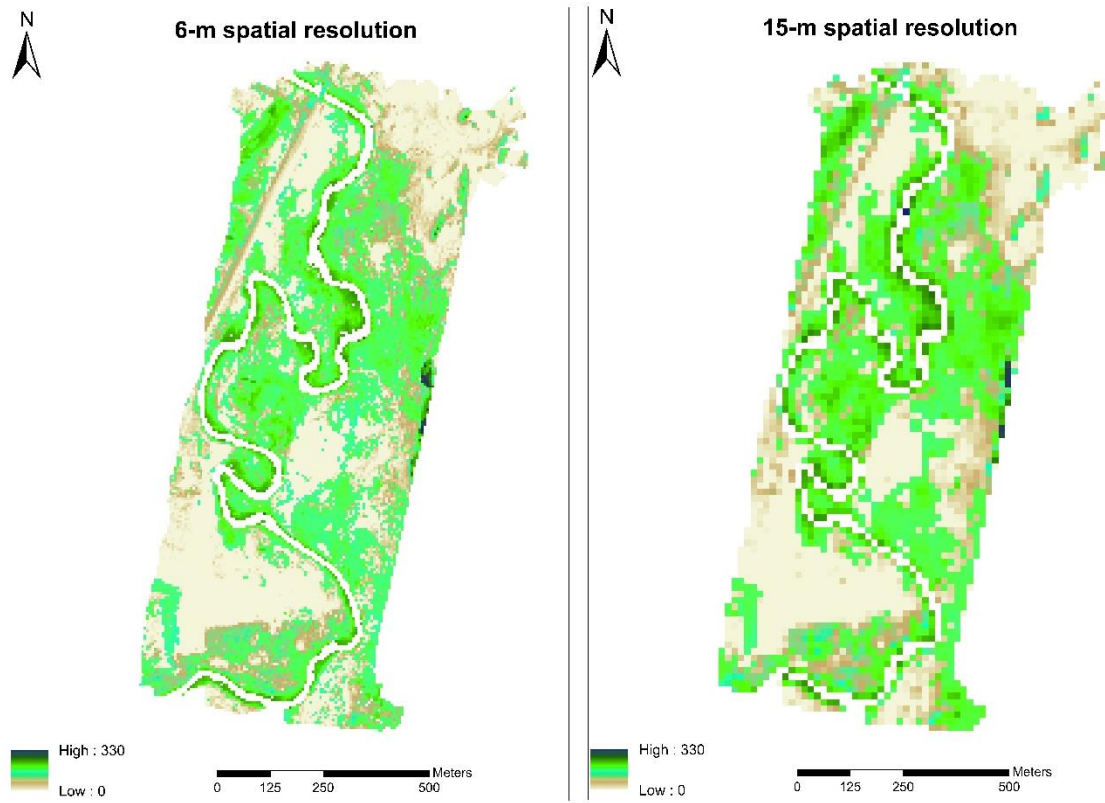


Figure 4.10 Example of modeled instantaneous LE (W/m^2) at 6-m and 15-m resolutions for July 22, 2019 at 10:05 am.

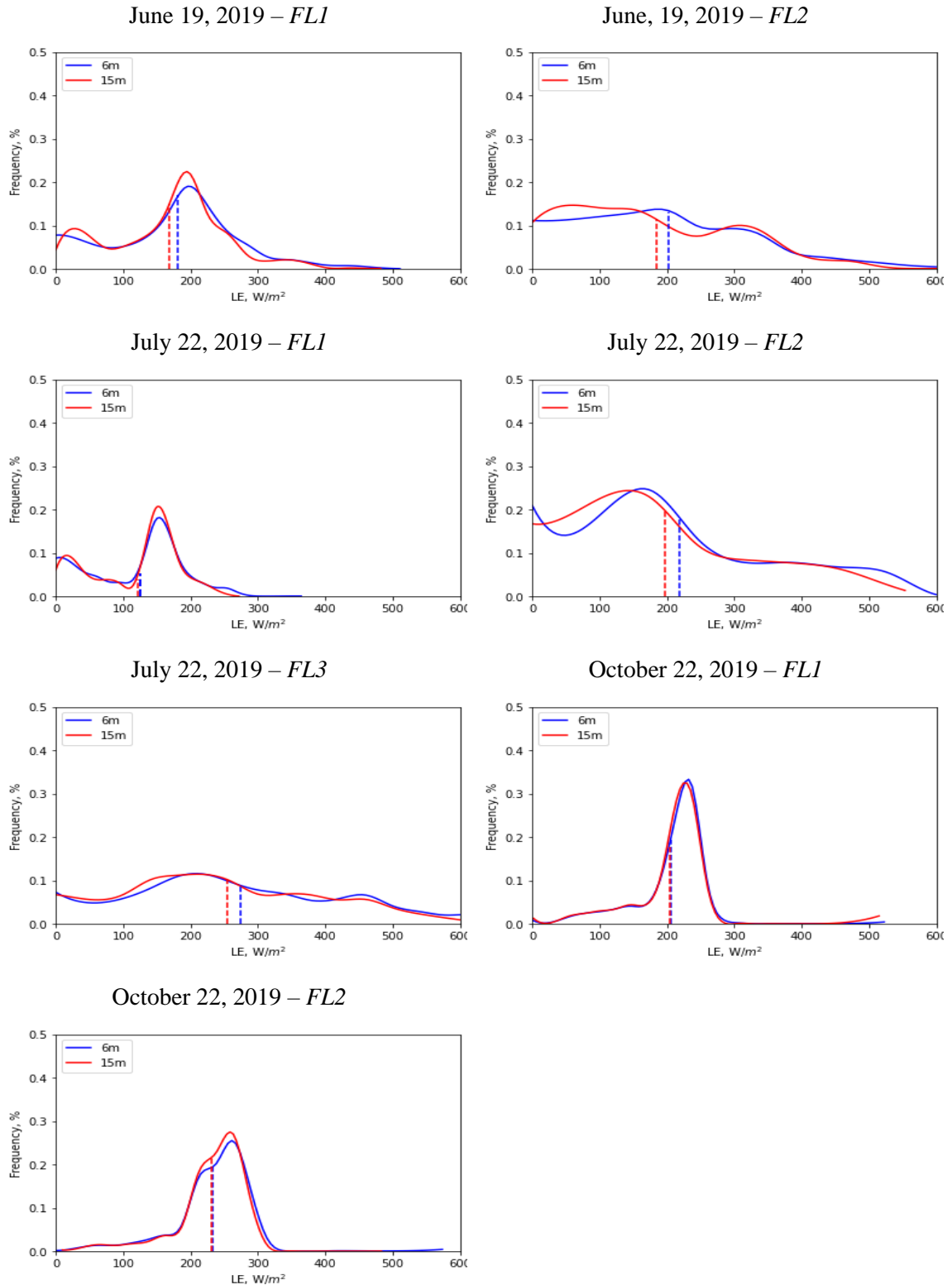


Figure 4.11 Frequency curves of instantaneous LE (W/m^2) for all $sUAS$ flights at 6 m and 15 m. Note: Blue dashed line represents the spatial mean of LE at 6-m resolution, the red represents the 15-m resolution.

4.3.5 Daily ET Calculation for Vegetation Types

The instantaneous (hourly) latent heat flux (LE) was obtained using the *TSEB* model then extrapolated/upscaled to daily ET (ET_d) values using the incoming solar radiation (R_s) method, which is the recommended method for use in complex canopy environments [46]. Moreover, a study conducted by Cammalleri et al. (2014) [47] indicated that the R_s approach is the best for extrapolating the instantaneous ET to daily values in grassland and woody savanna. To evaluate the difference in daily ET for each vegetation type on the different dates (June 19, 2019; July 22, 2019; October 26, 2019), spatial mean (μ) and standard deviation (σ) were calculated as shown in Table 4.4, while LE variability is illustrated as boxplots in Figure 4.12. Overall, the results indicate only a small difference in the spatial mean of ET_d between June 19, 2019, and July 22, 2019, with a significant decrease in standard deviation. For example, the mean daily ET value for cottonwood on June 19, 2019, and July 22, 2019, was 4.9 mm/day and 5 mm/day, respectively, and then decreased to 2.7 mm/day on October 26, 2019. Similarly, willow daily ET was 5 mm/day and 4.9 mm/day, respectively, for June 19 and July 22 and then decreased to 2.6 mm/day on October 26. The low values of ET on October 26 across different vegetation types are due to the dry condition of vegetation observed on that date. The exception is the treated tamarisk, which is in a dry/dead condition across all of the different dates.

As shown in Figure 4.13, the highest ET was observed in willow, which dominates the river corridor, and cottonwood. According to Neale et al. (2011) [27], cottonwood has the highest ET among the vegetation types studied (saltcedar/tamarisk, mesophytes, arundo, mesquite, conifer and desert scrub). In contrast, the lowest ET in this study was observed in treated tamarisk, which represents the second largest vegetation area after

grass/shrubs, with an average value of nearly 2.1 mm/day. Although the treated tamarisk is in dead and/or dry condition across different dates, green vegetation growing underneath contributed to a magnitude value of *ET* for tamarisk as shown in Figure 4.14. Generally, the estimation of actual water use in tamarisk is complicated in that it varies from one location to another and is strongly influenced by the measurement period [48] due to several factors related plant size, water quality and salinity, and depth to groundwater. The average *ET* rate of grass/shrubs was found to be between 2.2 mm/day and 2.8 mm/day across the different dates. These results are similar to Neale et al. (2011) [27], which showed daily *ET* ranging between 2 mm/day and 3.3 mm/day. The large *ET* rate estimated for grass/shrubs corresponds to the vegetation along the river corridor (see Figure 4.13).

Table 4.4 Average daily *ET* estimation for different vegetation types on different dates for the study area.

Vegetation type	June 19, 2019		July 22, 2019		October 26, 2019	
	μ (mm/day)	σ (mm/day)	μ (mm/day)	σ (mm/day)	μ (mm/day)	σ (mm/day)
Cottonwood	4.9	1.7	5	1.1	2.7	0.2
Willow	5	1.25	4.9	0.7	2.6	0.1
Grass/Shrubs	2.7	1.3	2.8	1.2	2.2	0.4
Treated tamarisk	2	1.1	2	1.1	2.3	0.4

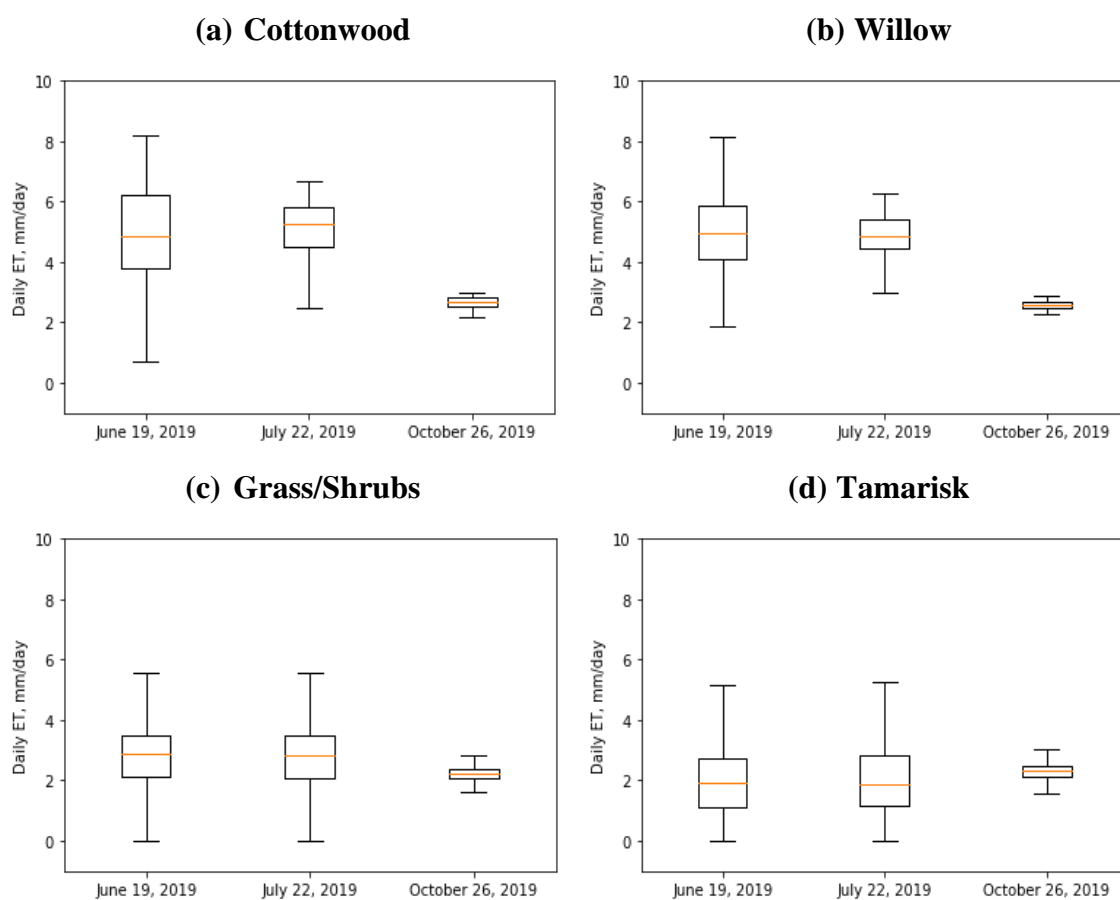


Figure 4.12 Daily *ET* estimation for each vegetation type on different *sUAS* flight dates in the study area.

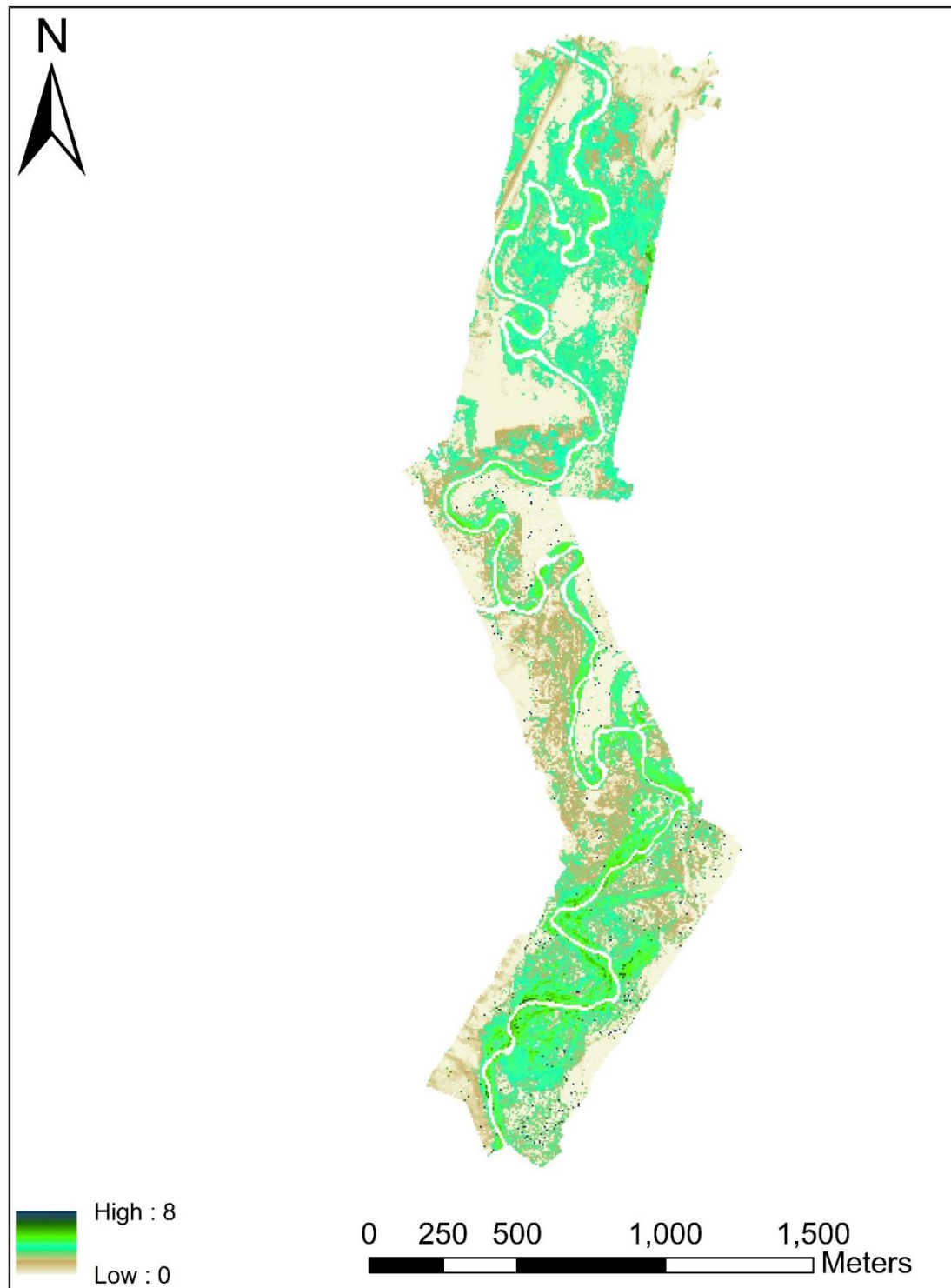


Figure 4.13 Example of modeled daily *ET* for July 22, 2019.



Figure 4.14 Example of *RGB sUAS* image from each flight date (June, July, and October).

4.4 Conclusion

Spatial resolution/scale is one of the challenges related to *ET* estimation, particularly in heterogeneous natural environments such as the San Rafael River corridor, which has a wide range of vegetation types and other ground features. The objective of this study was to characterize the spatial heterogeneity in a natural environment to evaluate its impact on *ET* estimation using the *TSEB* model and high-resolution data acquired by *sUAS*. Retrieving the biophysical parameters (LAI , f_c , f_g , and h_c) required as inputs to the *TSEB* model constitutes a challenging issue in this study due to landscape heterogeneity. The discrete wavelet transform (*DWT*) was used along with *sUAS NDVI* to identify the suitable spatial resolution to represent the study area. Wavelet analysis was considered for two different features from multiple *sUAS* flights; the river corridor and the remaining area (non-river corridor) that surrounds the river corridor. Multiple plots were used to describe the changes in wavelet energy (%) in the different directions (horizontal, vertical, and diagonal) corresponding to different spatial resolutions. The results showed that the maximum wavelet energy is between 6.4 m and 12.8 m for the river corridor area, while

the non-river corridor area, which is characterized by different surface types and random vegetation, does not show a peak value. One explanation for the flat shape in the wavelet energy in the non-river corridor area is the low variation in *NDVI* values for the dead/dry vegetation and soil.

Secondly, to evaluate the effect of spatial resolution on *LE* estimation using the *TSEB* model, spatial scales of 6 m and 15 m instead of 6.4 m and 12.8 m, respectively, were used to simplify the derivation of model inputs. Multiple statistical measures (frequency curve, spatial mean, standard deviation) were used to assess the effect of spatial resolutions. The results indicated low statistical differences in the *LE* values at the two different scales, 6 m and 15 m, for the multiple *sUAS* flights. Furthermore, the results showed that the high spatial variability in *LE* values within each single flight was due to many environmental factors, including soil moisture, different vegetation types, and fractional cover.

Lastly, to estimate the water use for each vegetation type in the study area, the instantaneous (hourly) latent heat flux (*LE*) obtained from the *TSEB* model was extrapolated to a daily scale using the R_s method. The highest *ET* was observed in willow, which dominates the river corridor, as well as cottonwood, followed by grass/shrubs and treated tamarisk. Although most of the treated tamarisk vegetation is in dead/dry condition, the green vegetation growing underneath resulted in a magnitude value of *ET*.

This study is an initial step toward a continued effort to explore and improve *TSEB* inputs for better *ET* estimates in such heterogeneous natural environments. Future research work should include ground-based energy flux measurements such as from an eddy covariance (*EC*) tower to validate further the results obtained from the *TSEB* model.

References

1. Glenn, E.P.; Huete, A.R.; Nagler, P.L.; Hirschboeck, K.K.; Brown, P. Integrating Remote Sensing and Ground Methods to Estimate Evapotranspiration. *Critical Reviews in Plant Sciences* 2007, 26, 139–168.
2. González-Dugo, M.P.; Chen, X.; Andreu, A.; Carpintero, E.; Gómez-Giraldez, P.J.; Carrara, A.; Su, Z. Long-Term Water Stress and Drought Monitoring of Mediterranean Oak Savanna Vegetation Using Thermal Remote Sensing.
3. Nassar, A.; Torres-Rua, A.; Kustas, W.; Nieto, H.; McKee, M.; Hipps, L.; Stevens, D.; Alfieri, J.; Prueger, J.; Alsina, M.M.; et al. Influence of Model Grid Size on the Estimation of Surface Fluxes Using the Two Source Energy Balance Model and sUAS Imagery in Vineyards. *Remote Sens (Basel)* 2020, 12, 342.
4. Saadi, S.; Boulet, G.; Bahir, M.; Brut, A.; Delogu, É.; Fanise, P.; Mougenot, B.; Simonneaux, V.; Chabaane, Z.L. Assessment of Actual Evapotranspiration over a Semiarid Heterogeneous Land Surface by Means of Coupled Low-Resolution Remote Sensing Data with an Energy Balance Model: Comparison to Extra-Large Aperture Scintillometer Measurements. *Hydrology and Earth System Sciences* 2018, 22, 2187–2209.
5. Giorgi, F.; Avissar, R. Representation of Heterogeneity Effects in Earth System Modeling: Experience from Land Surface Modeling. *Reviews of Geophysics* 1997, 35, 413–437.
6. Bonan, G.B.; Doney, S.C. Climate, Ecosystems, and Planetary Futures: The Challenge to Predict Life in Earth System Models. *Science* 2018, 359, eaam8328.
7. Krinner, G.; Viovy, N.; de Noblet-Ducoudré, N.; Ogée, J.; Polcher, J.; Friedlingstein, P.; Ciais, P.; Sitch, S.; Colin Prentice, I. A Dynamic Global Vegetation Model for Studies of the Coupled Atmosphere-Biosphere System. *Global Biogeochemical Cycles* 2005, 19.
8. Richardson, A.D.; Keenan, T.F.; Migliavacca, M.; Ryu, Y.; Sonnentag, O.; Toomey, M. Climate Change, Phenology, and Phenological Control of Vegetation Feedbacks to the Climate System. *Agricultural and Forest Meteorology* 2013, 169, 156–173.
9. Guzinski, R.; Nieto, H.; Stisen, S.; Fensholt, R. Inter-Comparison of Energy Balance and Hydrological Models for Land Surface Energy Flux Estimation over a Whole River Catchment. *Hydrology and Earth System Sciences* 2015, 19, 2017–2036.
10. Kite, G.; Droogers, P. Comparing Evapotranspiration Estimates from Satellites, Hydrological Models and Field Data. *Journal of Hydrology* 2000, 229, 1–2.
11. Kjaersgaard, J.; Allen, R.; Irmak, A. Improved Methods for Estimating Monthly and Growing Season ET Using METRIC Applied to Moderate Resolution Satellite Imagery. *Hydrological Processes* 2011, 25, 4028–4036.

12. Kustas, W.P. Estimates of Evapotranspiration with a One- and Two-Layer Model of Heat Transfer over Partial Canopy Cover. *Journal of Applied Meteorology* 1990, 29, 704–715.
13. Acharya, B.; Sharma, V. Comparison of Satellite Driven Surface Energy Balance Models in Estimating Crop Evapotranspiration in Semi-Arid to Arid Inter-Mountain Region. *Remote Sensing* 2021, 13, 1822.
14. Norman, J.M.; Kustas, W.P.; Humes, K.S. Source Approach for Estimating Soil and Vegetation Energy Fluxes in Observations of Directional Radiometric Surface Temperature. *Agricultural and Forest Meteorology* 1995, 77, 263–293.
15. Gao, R.; Torres-Rua, A.F.; Nassar, A.; Alfieri, J.; Aboutaleb, M.; Hipps, L.; Ortiz, N.B.; McElrone, A.J.; Coopmans, C.; Kustas, W.; et al. Evapotranspiration Partitioning Assessment Using a Machine-Learning-Based Leaf Area Index and the Two-Source Energy Balance Model with sUAV Information. *Autonomous Air and Ground Sensing Systems for Agricultural Optimization and Phenotyping VI* 2021.
16. Gonzalez-Dugo, M.P.; Neale, C.M.U.; Mateos, L.; Kustas, W.P.; Prueger, J.H.; Anderson, M.C.; Li, F. A Comparison of Operational Remote Sensing-Based Models for Estimating Crop Evapotranspiration. *Agricultural and Forest Meteorology* 2009, 149, 1843–1853.
17. Timmermans, W.J.; Kustas, W.P.; Anderson, M.C.; French, A.N. An Intercomparison of the Surface Energy Balance Algorithm for Land (SEBAL) and the Two-Source Energy Balance (TSEB) Modeling Schemes. *Remote Sensing of Environment* 2007, 108, 369–384.
18. Cleugh, H.A.; Leuning, R.; Mu, Q.; Running, S.W. Regional Evaporation Estimates from Flux Tower and MODIS Satellite Data. *Remote Sensing of Environment* 2007, 106, 285–304.
19. Jung, M.; Henkel, K.; Herold, M.; Churkina, G. Exploiting Synergies of Global Land Cover Products for Carbon Cycle Modeling. *Remote Sensing of Environment* 2006, 101, 534–553.
20. Kustas, W.P.; Norman, J.M. Use of Remote Sensing for Evapotranspiration Monitoring over Land Surfaces. *Hydrological Sciences Journal* 1996, 41, 495–516.
21. Brunsell, N.A.; Gillies, R.R. Scale Issues in Land–atmosphere Interactions: Implications for Remote Sensing of the Surface Energy Balance. *Agricultural and Forest Meteorology* 2003, 117, 203–221.
22. Hong, S.-H.; Hendrickx, J.M.H.; Borchers, B. Down-Scaling of SEBAL Derived Evapotranspiration Maps from MODIS (250 M) to Landsat (30 M) Scales. *International Journal of Remote Sensing* 2011, 32, 6457–6477.
23. Sharma, V.; Kilic, A.; Irmak, S. Impact of Scale/resolution on Evapotranspiration from Landsat and MODIS Images. *Water Resources Research* 2016, 52, 1800–1819.

24. Anderson, M.C.; Norman, J.M.; Mecikalski, J.R.; Torn, R.D.; Kustas, W.P.; Basara, J.B. A Multiscale Remote Sensing Model for Disaggregating Regional Fluxes to Micrometeorological Scales. *Journal of Hydrometeorology* 2004, 5, 343–363.
25. Li, F.; Kustas, W.P.; Anderson, M.C.; Prueger, J.H.; Scott, R.L. Effect of Remote Sensing Spatial Resolution on Interpreting Tower-Based Flux Observations. *Remote Sensing of Environment* 2008, 112, 337–349.
26. Kustas, W. Evaluating the Effects of Subpixel Heterogeneity on Pixel Average Fluxes.
27. Neale, C.M.U.; Geli, H.; Taghvaeian, S.; Masih, A.; Pack, R.T.; Simms, R.D.; Baker, M.; Milliken, J.A.; O'Meara, S.; Witherall, A.J. Estimating Evapotranspiration of Riparian Vegetation Using High Resolution Multispectral, Thermal Infrared and Lidar Data. *Remote Sensing for Agriculture, Ecosystems, and Hydrology XIII* 2011.
28. Keller, D.L.; Laub, B.G.; Birdsey, P.; Dean, D.J. Effects of Flooding and Tamarisk Removal on Habitat for Sensitive Fish Species in the San Rafael River, Utah: Implications for Fish Habitat Enhancement and Future Restoration Efforts. *Environmental Management* 2014, 54, 465–478.
29. Fortney, Stephen T. 2015. "A Century of Geomorphic Change of the San Rafael River and Implications for River Rehabilitation." Utah State University. <https://digitalcommons.usu.edu/etd/4363>.
30. Budy, Phaedra. 2009. "Habitat Needs, Movement Patterns, and Vital Rates of Endemic Utah Fishes in a Tributary to the Green River, Utah." In Utah Cooperative Fish and Wildlife Research Unit Department of Watershed Sciences Utah State University. https://digitalcommons.usu.edu/wats_facpub/870.
31. Seto, K.C.; Fleishman, E.; Fay, J.P.; Betrus, C.J. Linking Spatial Patterns of Bird and Butterfly Species Richness with Landsat TM Derived NDVI. *International Journal of Remote Sensing* 2004, 25, 4309–4324.
32. Morettin, P.A. From Fourier to Wavelet Analysis of Time Series. *COMPSTAT* 1996, 111–122.
33. Csillag, F.; Kabos, S. Wavelets, Boundaries, and the Spatial Analysis of Landscape Pattern. *Écoscience* 2002, 9, 177–190.
34. Bradshaw, G.A.; Spies, T.A. Characterizing Canopy Gap Structure in Forests Using Wavelet Analysis. *The Journal of Ecology* 1992, 80, 205.
35. Murwira, A.; Skidmore, A.K. Comparing Direct Image and Wavelet Transform-Based Approaches to Analysing Remote Sensing Imagery for Predicting Wildlife Distribution. *International Journal of Remote Sensing* 2010, 31, 6425–6440.
36. Cazelles, B.; Chavez, M.; Berteaux, D.; Ménard, F.; Vik, J.O.; Jenouvrier, S.; Stenseth, N.C. Wavelet Analysis of Ecological Time Series. *Oecologia* 2008, 156, 287–304.

37. Bruce, A.; Gao, H.-Y. *Applied Wavelet Analysis with S-PLUS*; Springer, 1996; ISBN 9780387947143.
38. Neale, C.M.U. Classification and Mapping of Riparian Systems Using Airborne Multispectral Videography. *Restoration Ecology* 2008, 5, 103–112.
39. Kustas, W.P.; Norman, J.M. Evaluation of Soil and Vegetation Heat Flux Predictions Using a Simple Two-Source Model with Radiometric Temperatures for Partial Canopy Cover. *Agricultural and Forest Meteorology* 1999, 94, 13–29.
40. Kustas, W.P.; Norman, J.M. Reply to Comments about the Basic Equations of Dual-Source Vegetation–atmosphere Transfer Models. *Agricultural and Forest Meteorology* 1999, 94, 275–278.
41. Nieto, H.; Kustas, W.P.; Alfieri, J.G.; Gao, F.; Hipps, L.E.; Los, S.; Prueger, J.H.; McKee, L.G.; Anderson, M.C. Impact of Different within-Canopy Wind Attenuation Formulations on Modelling Sensible Heat Flux Using TSEB. *Irrigation Science* 2019, 37, 315–331.
42. Campbell, G.S.; Norman, J.M. *An Introduction to Environmental Biophysics* 1998.
43. White, M.A.; Asner, G.P.; Nemani, R.R.; Privette, J.L.; Running, S.W. Measuring Fractional Cover and Leaf Area Index in Arid Ecosystems. *Remote Sensing of Environment* 2000, 74, 45–57.
44. Garrigues, S.; Allard, D.; Baret, F.; Weiss, M. Quantifying Spatial Heterogeneity at the Landscape Scale Using Variogram Models. *Remote Sensing of Environment* 2006, 103, 81–96.
45. Wu, L.; Qin, Q.; Liu, X.; Ren, H.; Wang, J.; Zheng, X.; Ye, X.; Sun, Y. Spatial Up-Scaling Correction for Leaf Area Index Based on the Fractal Theory. *Remote Sensing* 2016, 8, 197.
46. Nassar, A.; Torres-Rua, A.; Kustas, W.; Alfieri, J.; Hipps, L.; Prueger, J.; Nieto, H.; Alsina, M.M.; White, W.; McKee, L.; et al. Assessing Daily Evapotranspiration Methodologies from One-Time-of-Day sUAS and EC Information in the GRAPEX Project. *Remote Sensing* 2021, 13, 2887.
47. Cammalleri, C.; Anderson, M.C.; Kustas, W.P. Upscaling of Evapotranspiration Fluxes from Instantaneous to Daytime Scales for Thermal Remote Sensing Applications. *Hydrology and Earth System Sciences* 2014, 18, 1885–1894.
48. Cleverly, J.R.; Dahm, C.N.; Thibault, J.R.; Gilroy, D.J.; Allred Coonrod, J.E. Seasonal Estimates of Actual Evapo-Transpiration from Tamarix Ramosissima Stands Using Three-Dimensional Eddy Covariance. *Journal of Arid Environments* 2002, 52, 181–197.

CHAPTER 5

SUMMARY, CONCLUSIONS, AND RECOMMENDATIONS

5.1 Summary and Conclusions

The western U.S., including California and Utah, has always presented harsh climate conditions, but the combination of global climate change and a rapidly growing population exacerbates the impacts and shows the importance of water sustainability as a cross-cutting priority for hydrological, agricultural and ecological dimensions. From season to season, there is significant variation in precipitation and river flow as a result of climate change effects on the hydrological cycle, leading to decreased precipitation in some areas. The agriculture in that region mainly depends on diversions of water for irrigation, as rainfall is insufficient to grow the crop without supplemental water. Therefore, adequate estimation of consumptive water use by the crop or evapotranspiration (*ET*) is essential for balancing water supplies and water demand, particularly in arid regions such as western U.S., to avoid fragility and severe damage to the natural environment. To achieve that level of adequacy, it is necessary to explore emergent technologies that can assess water use by vegetation, such as *sUAS* that can provide detailed information and can be used to continuously monitor water use in agricultural and natural environments along other technologies (ground and satellite).

This dissertation contributes to improving the means for the use of spatial and temporal *ET* information for complex environments, particularly vineyards and natural areas. Heterogeneous landscapes and non-ideal surface conditions present challenges for adequate characterization of water and energy processes and require advanced analysis to estimate *ET*.

The need for accurate spatiotemporal *ET* estimation raised two fundamental questions: 1) What representative spatial scale/model grid size can describe the spatial heterogeneity in complex agricultural and natural environments, and how does this influence surface energy fluxes/*ET* estimates? and 2) Which data collection times and *ET* upscaling approach is appropriate for instantaneous to daily estimates and is reliable? The analysis relies upon high-resolution data acquired by *sUAS*, which is used for deriving key inputs (i.e., vegetation cover, *LST*, and canopy height) needed for an energy balance model, called *TSEB*, to estimate *ET*.

This dissertation is designed in five chapters. The first chapter is a general introduction addressing the importance of producing accurate *ET* for complex environments such as vineyards and natural areas.

The second chapter presents the influence of model grid size/spatial resolution on energy fluxes over the vineyard environment in California's Central Valley using the *TSEB-2T* model. Multiple spatial resolutions/domains were considered for the analysis, which corresponded to one, two, four, and nine vine rows, respectively. The results indicated that the separation of canopy and soil/substrate temperatures (T_c and T_s) using the *LST-NDVI* relationship is highly influenced by the spatial domain. At small scale, a linear relationship between the *LST* and *NDVI* was found due to small number of pixels exist inside the spatial domain; however, at the coarse resolution (i.e, Landsat scale), there are many more pixels, more rows of vineyard are included, and the *LST-NDVI* relationship starts to resemble a triangle shape, which results in a weak *LST-NDVI* correlation. The validation results using the eddy covariance (*EC*) flux measurements indicated that the difference between the *TSEB LE* and *EC LE* increased at different spatial resolutions,

particularly at the coarsest resolution (Landsat scale). This large difference in LE at Landsat scale was due to overestimation in H , causing an underestimation in LE , which refers mainly to the non-linear relationship $LST-NDVI$ at that coarse resolution. Another explanation for that difference is the variability of aerodynamic resistance (R_A) due to the variables that affect the friction velocity (u^*) - the mean canopy height and roughness length, which were derived from remote sensing imagery at different spatial domains/resolutions.

The third chapter assesses different daily evapotranspiration methodologies from a single time-of-day $sUAS$ and EC information over multiple vineyard sites characterized by different climate, soils, vine variety, and trellis design. Five existing methods that estimate daily ET from instantaneous measurements were evaluated. Each approach (evaporative fraction (EF), solar radiation (R_s), net radiation to solar radiation (R_n/R_s) ratio, Gaussian (GA), and Sine) takes advantage of clear skies and quasi-sinusoidal diurnal variation of hourly ET and other meteorological parameters as documented by eddy covariance (EC) sensors. The analysis also considered different growing seasons of vine (bloom (April – May), veraison (June – August), and post-harvest (September – October))) to investigate how vine phenology could affect the accuracy of modeled daily ET . Overall, the results obtained from the EC -derived ET_d and $TSEB$ -derived ET_d analysis indicated that three out of five methods (GA , EF , and R_s) reasonably agree with the ground observations from EC , with the R_s approach yielding better agreement across different stages in the season. Moreover, the results showed that the approaches could perform differently at different vine canopy development and grape vine phenology stages, and at different time windows during the day. The modeled ET_d values obtained from the time window 1030 – 1330

showed better agreement with the ground measurements than the second time window (1430 – 1630). This implies that *sUAS* imagery should be collected 1 – 2 hours before/after solar noon for generating accurate daily *ET* estimations.

The fourth chapter investigated the effect of the spatial heterogeneity of the natural environment on the *ET*. The study area is the San Rafael River corridor, which is characterized by extreme heterogeneous landscape described by a variety of vegetation species interspersed with bare soil and high spatial variability in canopy height, root zone, and soil moisture. First, spatial variability analysis was performed for identifying the spatial resolution/model grid size that can represent the study area using the discrete wavelet transform (*DWT*). Results indicated that spatial resolution between 6 m and 15 m is suitable for capturing the spatial heterogeneity in the San Rafael River corridor. Then, the *TSEB* model was used to evaluate the effect of the two different spatial resolutions (6 m and 15 m) on the *LE* estimates where the results showed low statistical discrepancies in the *LE* values at the two scales, with a slight decrease at 15 m due to loss in spatial variability. Lastly, to quantify the daily *ET* for the riparian vegetation, the instantaneous *TSEB LE* values were extrapolated to daily *ET* scale. The results indicated that willow and cottonwood vegetation have the highest *ET*, followed by grass/shrubs and treated (dead) tamarisk.

5.2 Recommendations

Remote sensing is a valuable source for having accurate *ET* spatial information, particularly in complex environments such as vineyards and natural areas. However, further investigation is needed for other complex agricultural environments, such as orchards (e.g., almonds and oranges), which are also characterized by a complex canopy

structure. Moreover, the analysis in this study relies upon the high-resolution data acquired by *sUAS* to explore the influence of different spatial resolutions on the *ET* estimates. Future work should include other remote sensing data from different platforms (e.g., satellites) to compare them to the *sUAS ET* products, which could provide a more comprehensive scaling assessment of *ET* estimates.

The first paper in this dissertation was limited to evaluating the influence of the model grid size/spatial resolution on the surface energy fluxes using *TSEB-2T* version. It is recommended to use other versions of the *TSEB* model, such as *TSEB-PT*, which may have less effect on scaling issues. *TSEB-2T* is highly influenced by the *LST-NDVI* relationship, which is used to separate canopy and soil/substrate temperature (T_c and T_s). In the *TSEB-PT* version, the decomposition of radiometric temperature (T_{rad}) between plant canopy and soil/substrate is based on fractional cover (f_c).

The second paper assessed multiple approaches for upscaling the instantaneous *ET* to daily values in vineyards. It will also be important to study the extrapolation/upscaling of instantaneous *ET* to daily *ET* estimates over natural areas, which are characterized by extreme heterogeneous landscape. Moreover, the nighttime *ET* contribution was neglected due to some uncertainties in the *EC* measurements at that time. Future research work should consider the *LE* fluxes overnight, which could provide a more comprehensive assessment to the daily *ET* estimates using different upscaling approaches.

The third paper focused on characterizing the spatial heterogeneity in natural environments to evaluate its impact on the *ET* estimation without ground observations. Future investigations in such heterogeneous environment should include results verification using ground-based measurements such as *EC* towers. This will help in

evaluating the performance of *TSEB* model in such environments where random distribution of vegetation presents with different types and heights.

APPENDICES

Appendix A: Supplemental Figures for Chapter 2

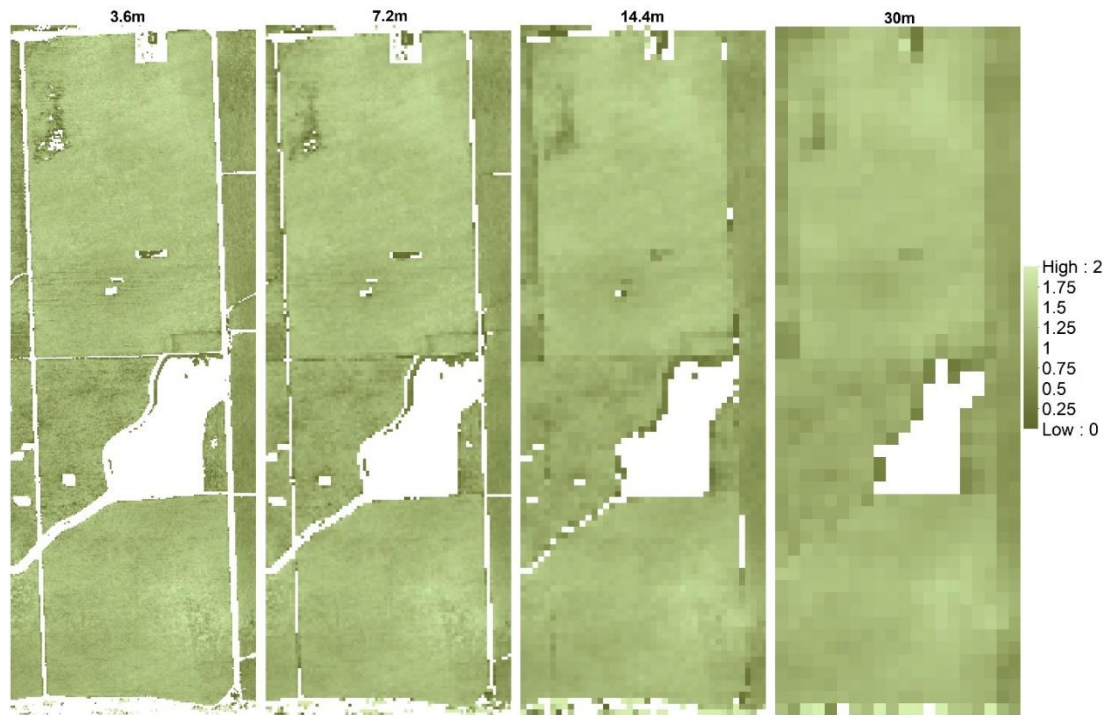


Figure A1 Example of modeled h_c (m) across different spatial domains for August 09, 2014.

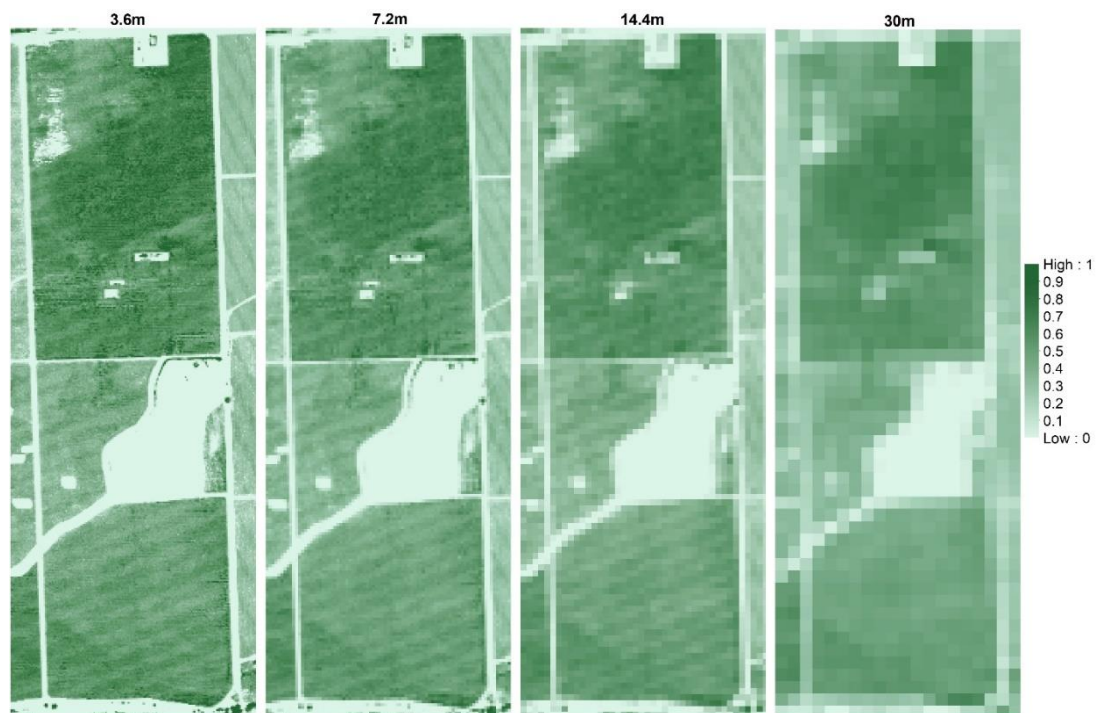


Figure A2 Example of modeled f_c across different spatial domains for August 09, 2014.

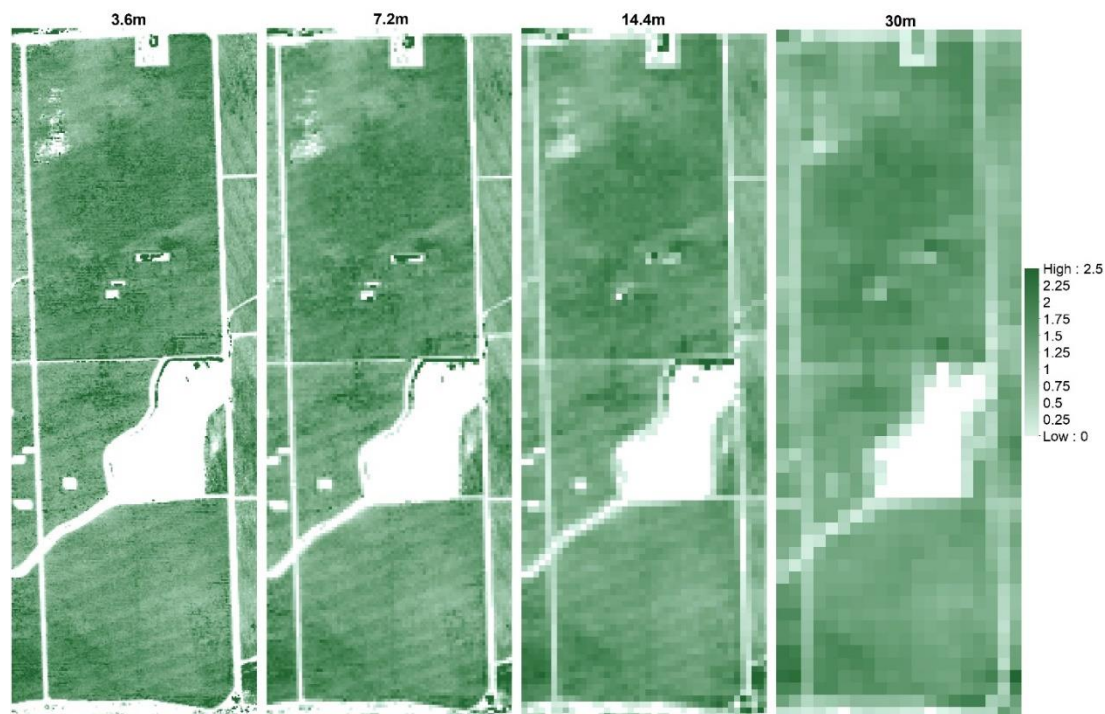
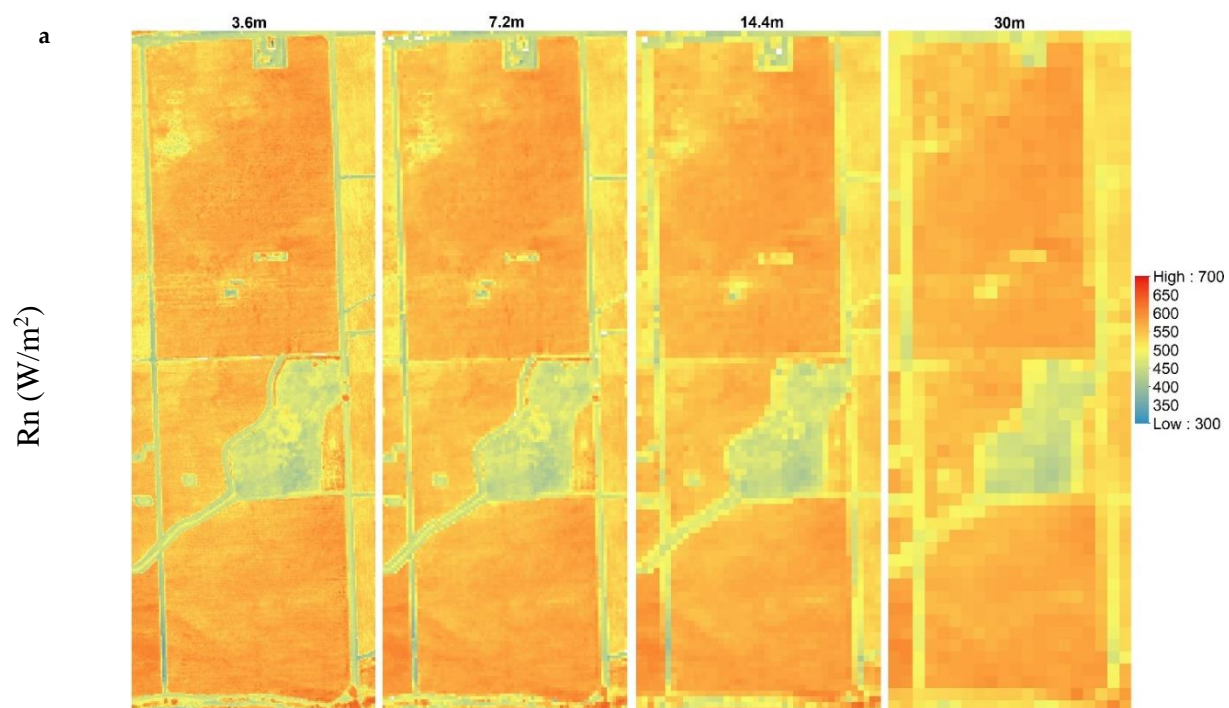
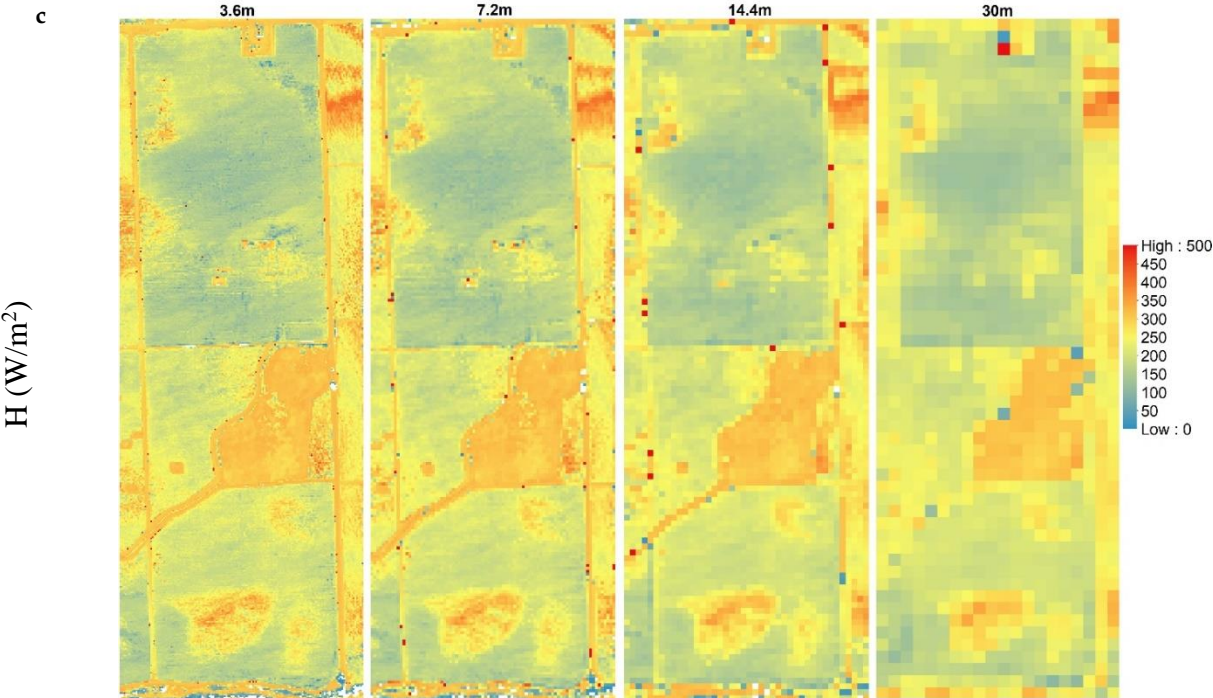
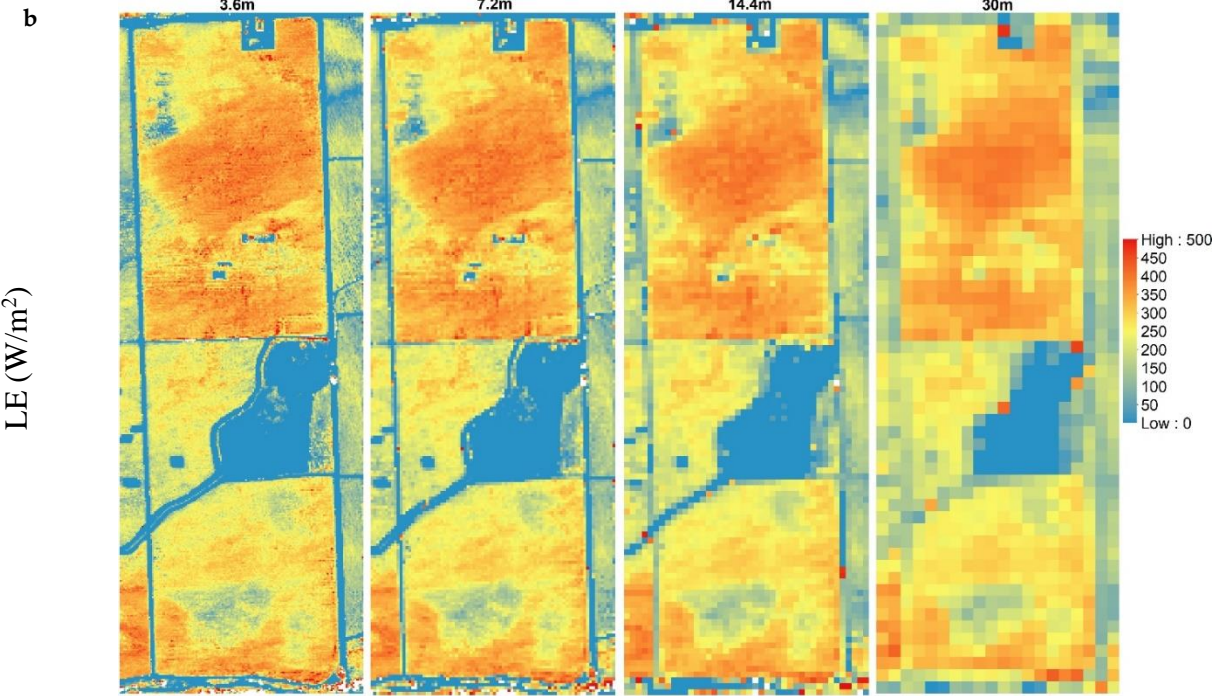


Figure A3 Example of Modeled w_e/h_c different spatial domains for August 09, 2014





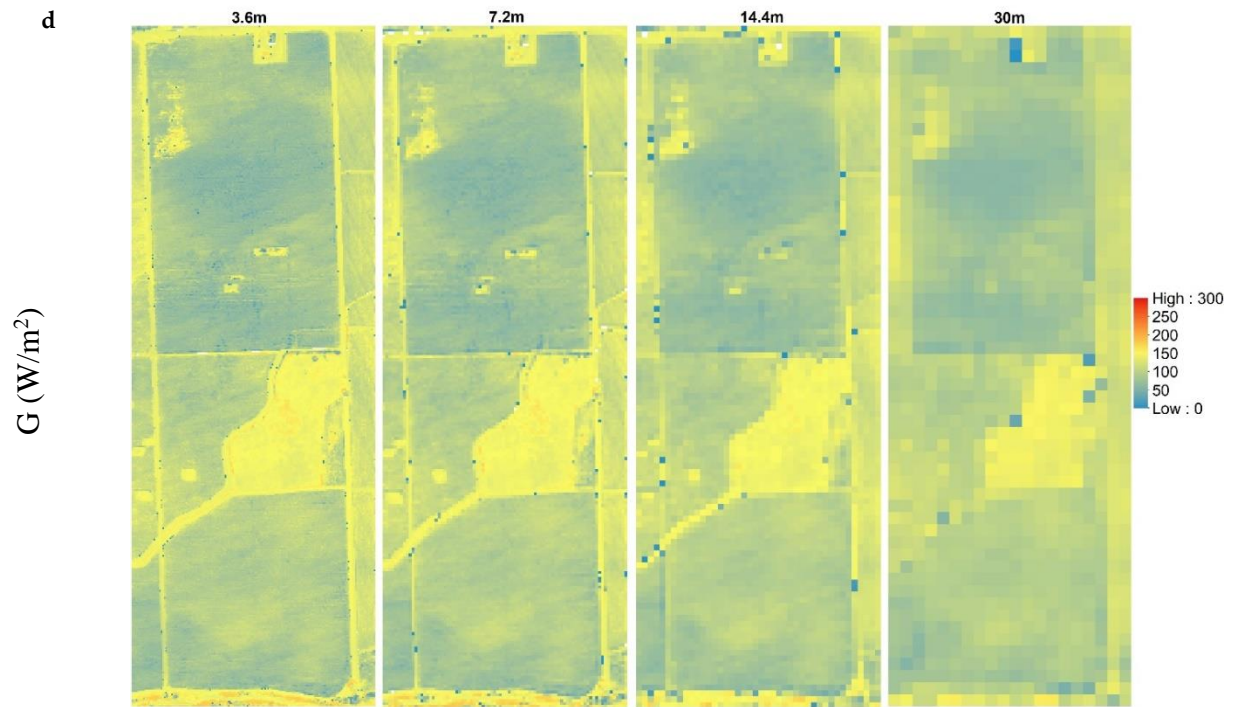


Figure A4 Aggregation of surface energy fluxes across different spatial domain (3.6m, 7.2m, 14.4 m, and 30 m) on August 09, 2014: (a) R_n , (b) LE , (c) H , and (d) G .

Appendix B: Supplemental Figures for Chapter 3

Appendix B.1 Daily ET Analysis at Sierra Loma Vineyard Near Lodi, California

Appendix B.1.1 Relative Error (E_r) at Hourly Scale for EC Measurements

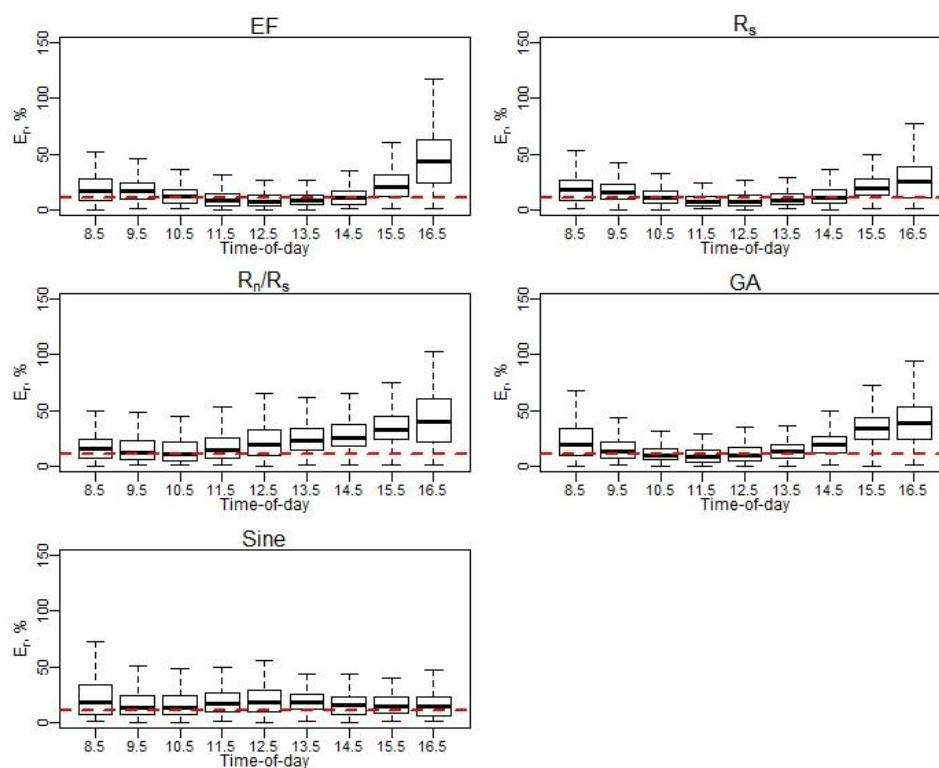


Figure B1 E_r of daily EC ET (April–May).

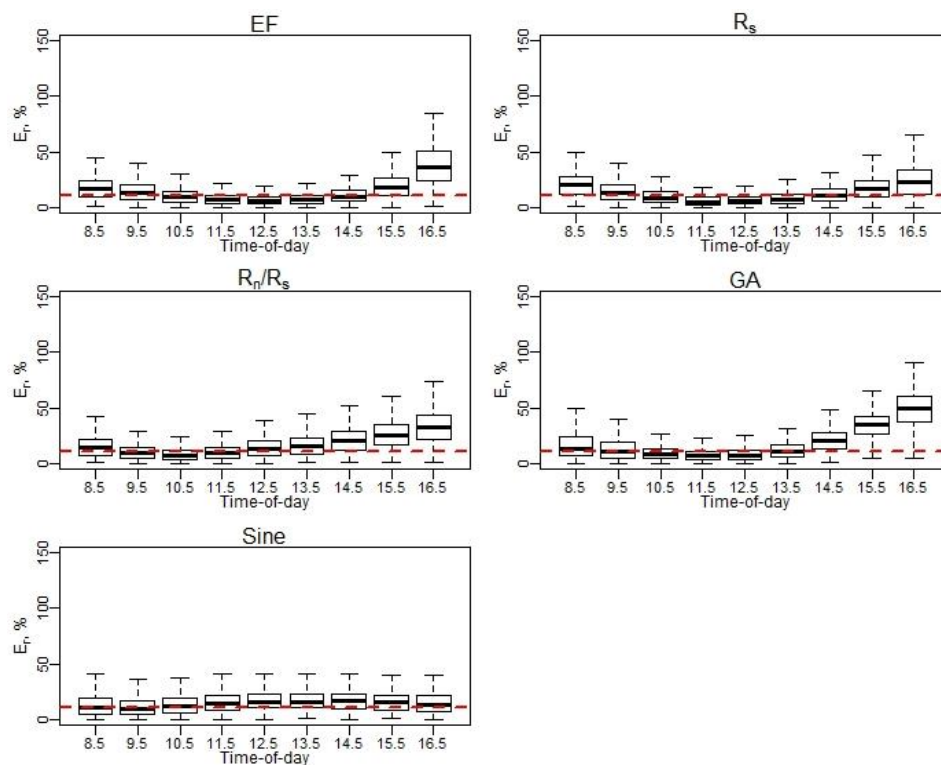


Figure B2 E_r of daily $EC\ ET$ (June–August).

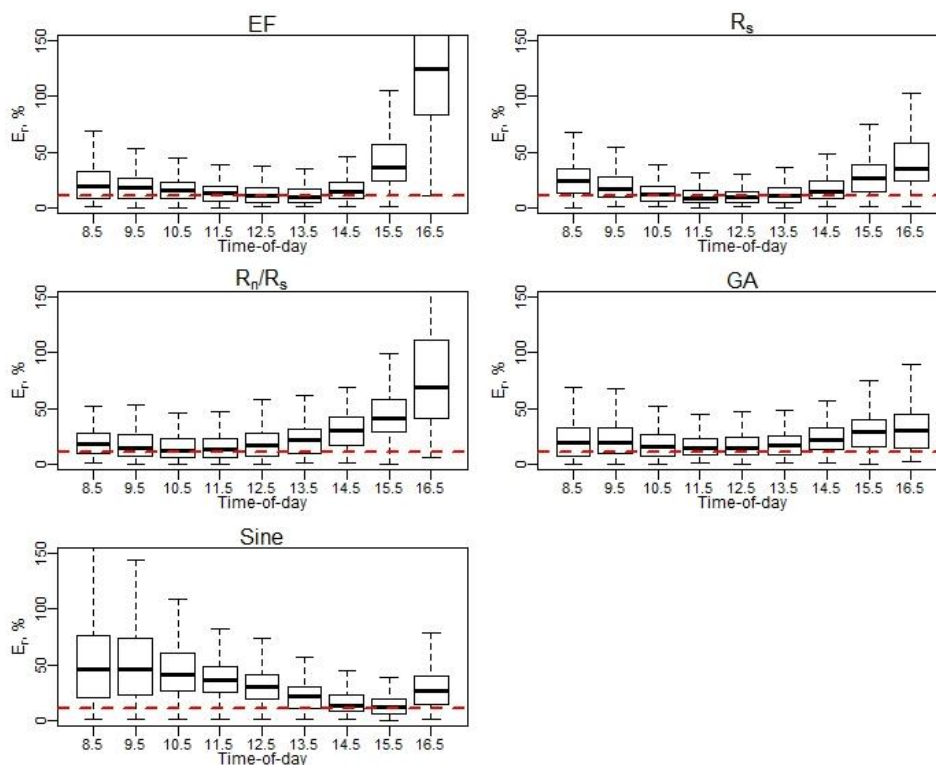


Figure B3 E_r of daily $EC\ ET$ (September–October). Note: Red dash line represents a 10% relative error (E_r).

Appendix B.1.2 Daily *RMSE* Performance Using Hourly *EC ET* Values

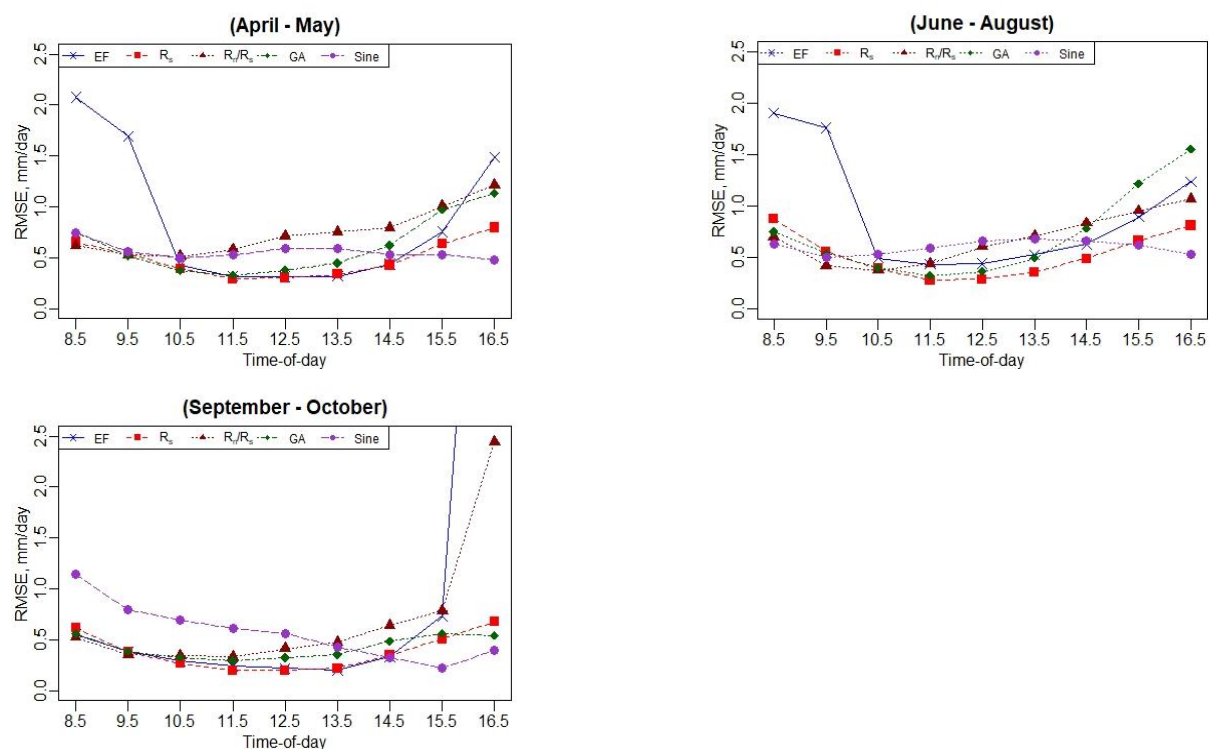


Figure B4 Daily *RMSE* performance using hourly *EC ET* values.

Appendix B.2 Daily *ET* Analysis at Ripperdan 760 Vineyard, California

Appendix B.2.1 Diurnal Variation of Surface Energy Fluxes (R_n , H , LE , and G)

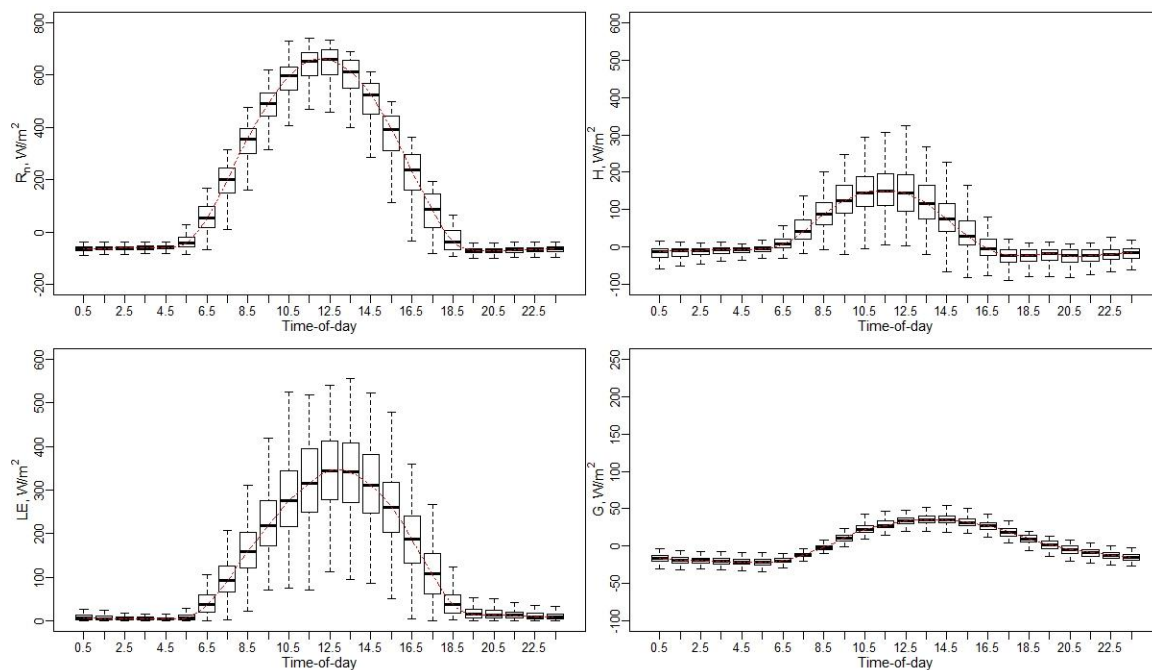


Figure B5 Diurnal variation of surface energy fluxes (R_n , H , LE , and G).

Appendix B.2.2 Hourly ET to Maximum Hourly ET ratio ($ET_h/ET_{h(max)}$) Variation Using EC Measurements

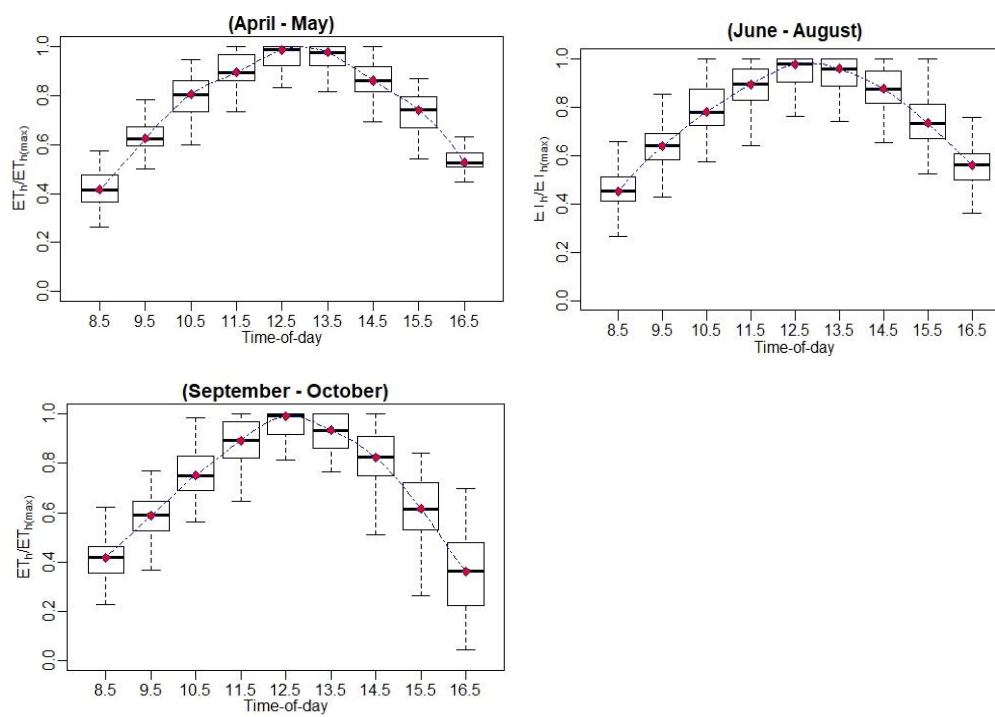


Figure B6 Hourly ET -to-maximum hourly ET ratio ($ET_h/ET_{h(max)}$) variation using EC measurements.

Appendix B.2.3 Hourly ET -to-Daily ET Ratio (ET_h/ET_d) variation Using EC

Measurements

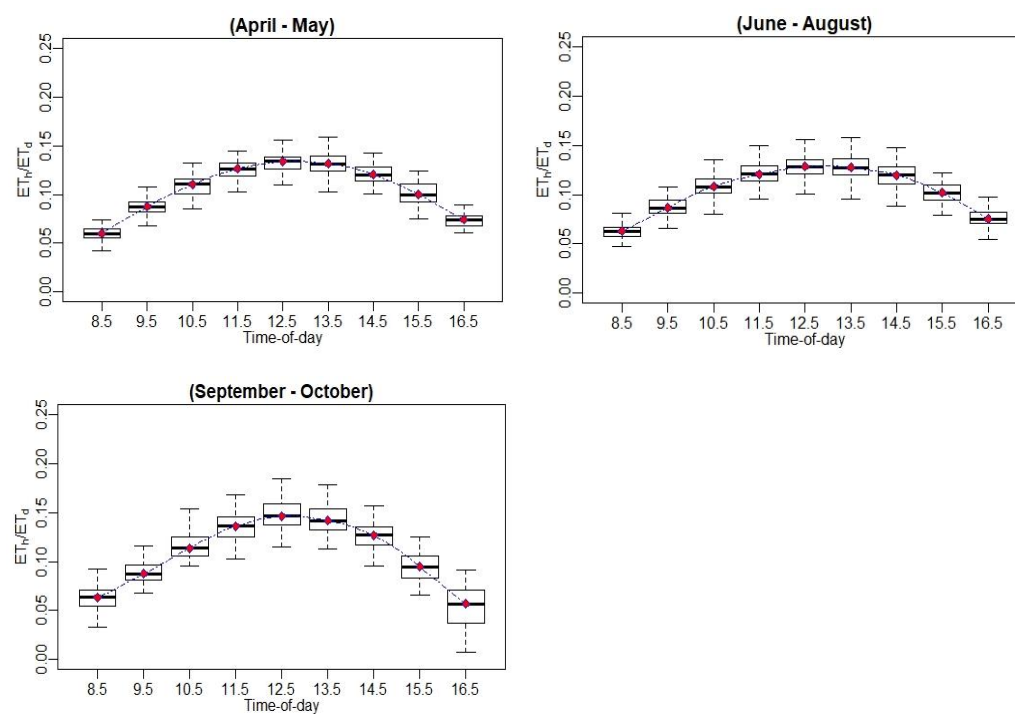


Figure B7 Hourly ET to daily ET ratio (ET_h/ET_d) variation using EC measurements.

Appendix B.2.4 Relative Error (E_r) at Hourly Scale for EC Measurements

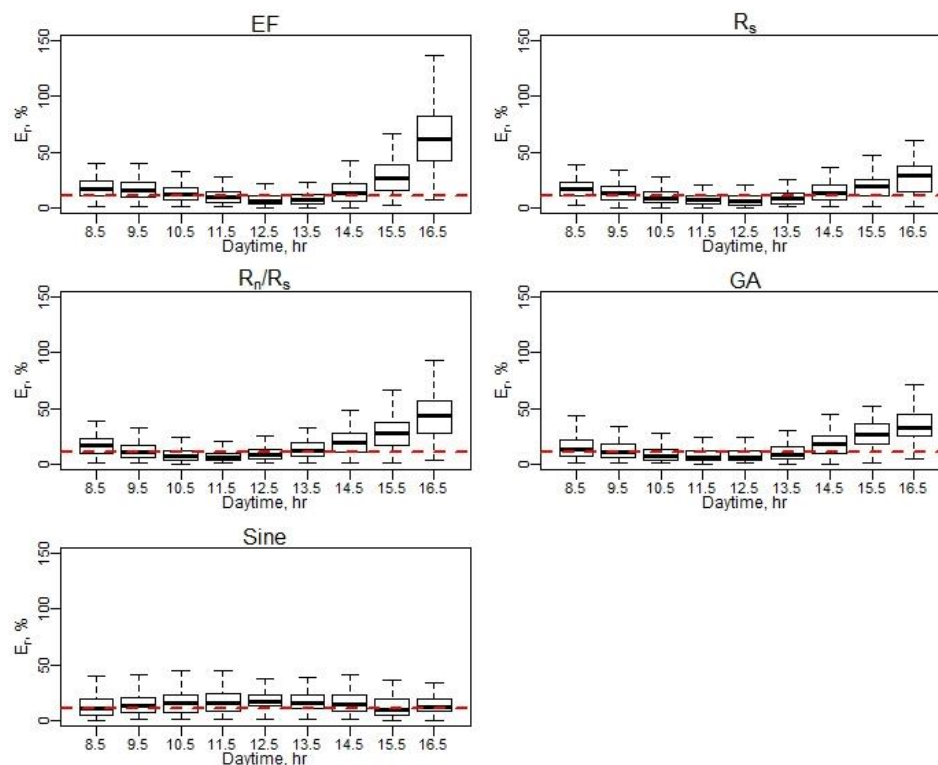


Figure B8 E_r of daily EC ET (April–May).

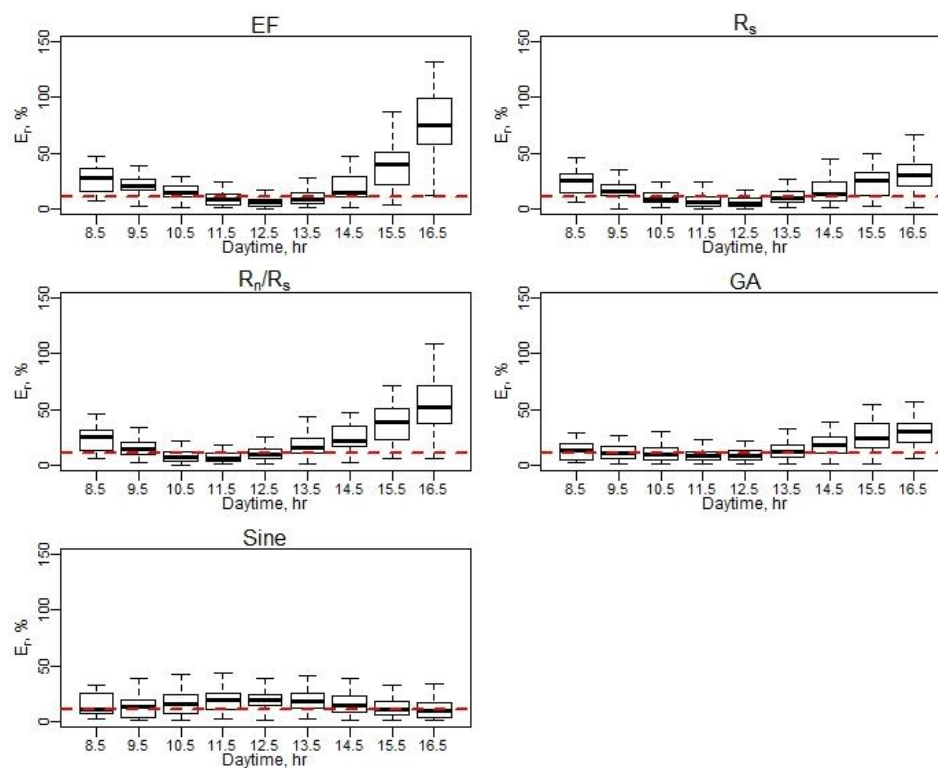


Figure B9 E_r of daily EC ET (June–August).

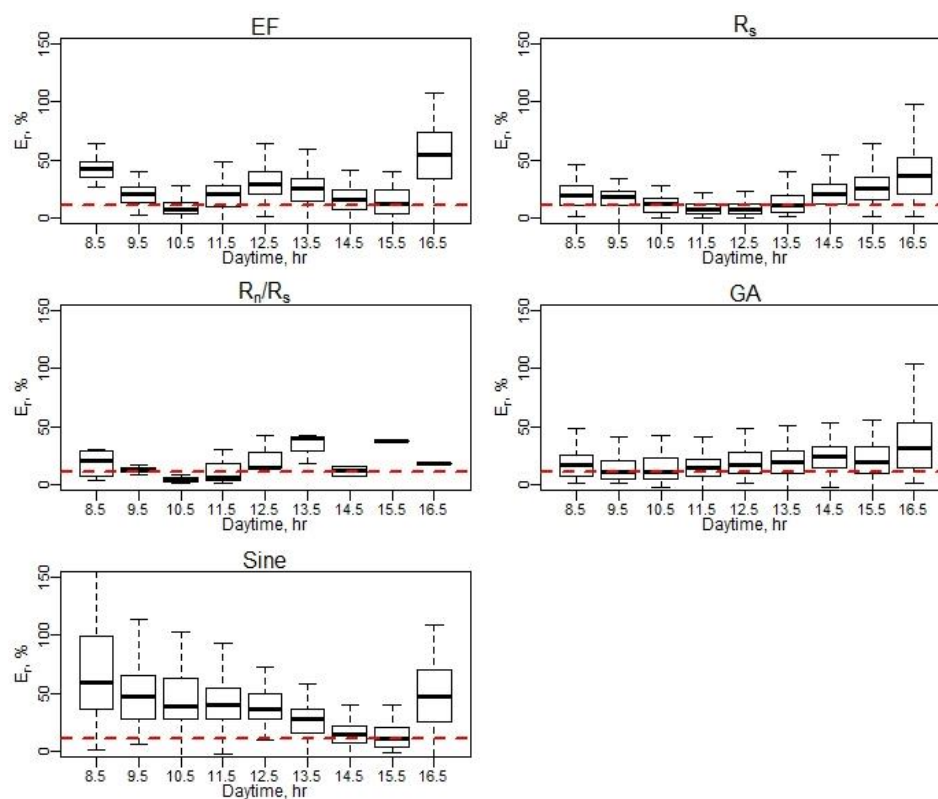


Figure B10 E_r of daily EC ET (September–October). Note: Red dash line represents a 10% relative error (E_r).

Appendix B.2.5 Daily *RMSE* Performance Using Hourly *EC ET* Values

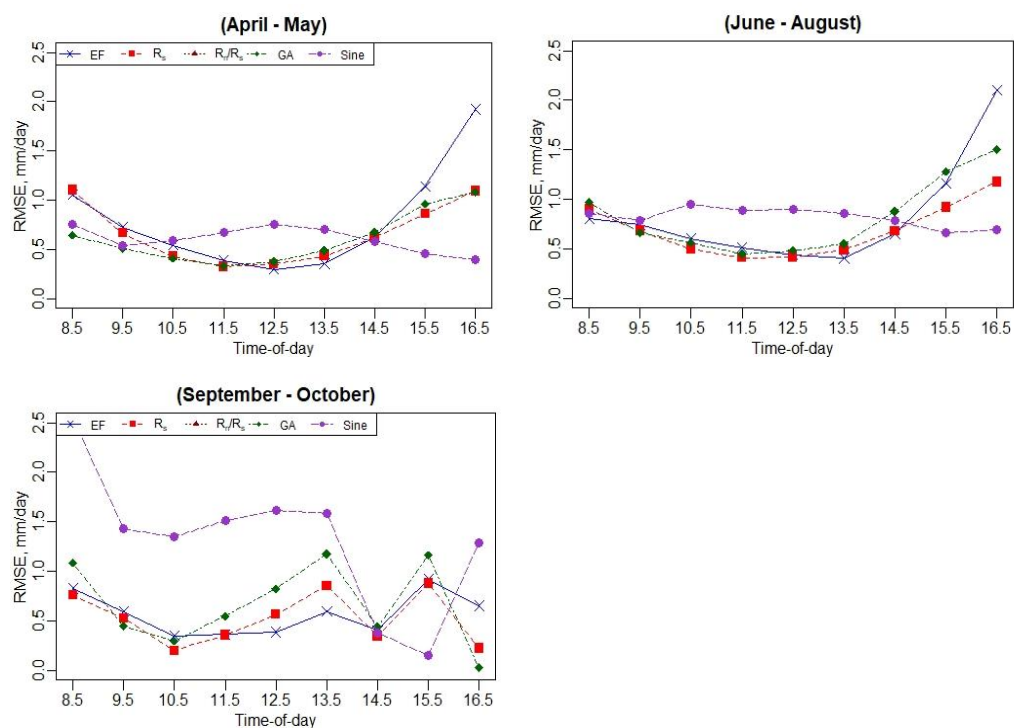


Figure B11 Daily *RMSE* performance using hourly *EC ET* values.

Appendix B.3 Daily *ET* Analysis at Ripperdan 720 Vineyard, California

Appendix B.3.1 Diurnal Variation of Surface Energy Fluxes (R_n , H , LE , and G)

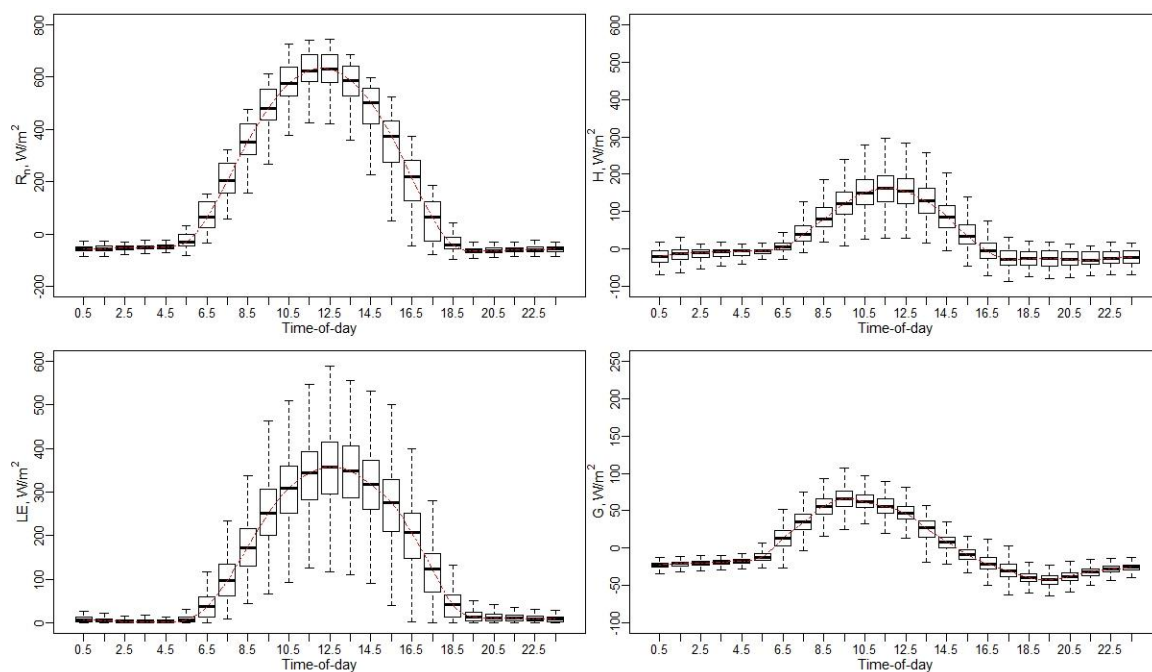


Figure B12 Diurnal variation of surface energy fluxes (R_n , H , LE , and G).

Appendix B.3.2 Hourly ET -to-Maximum Hourly ET Ratio ($ET_h/ET_{h(max)}$) Variation Using EC Measurements

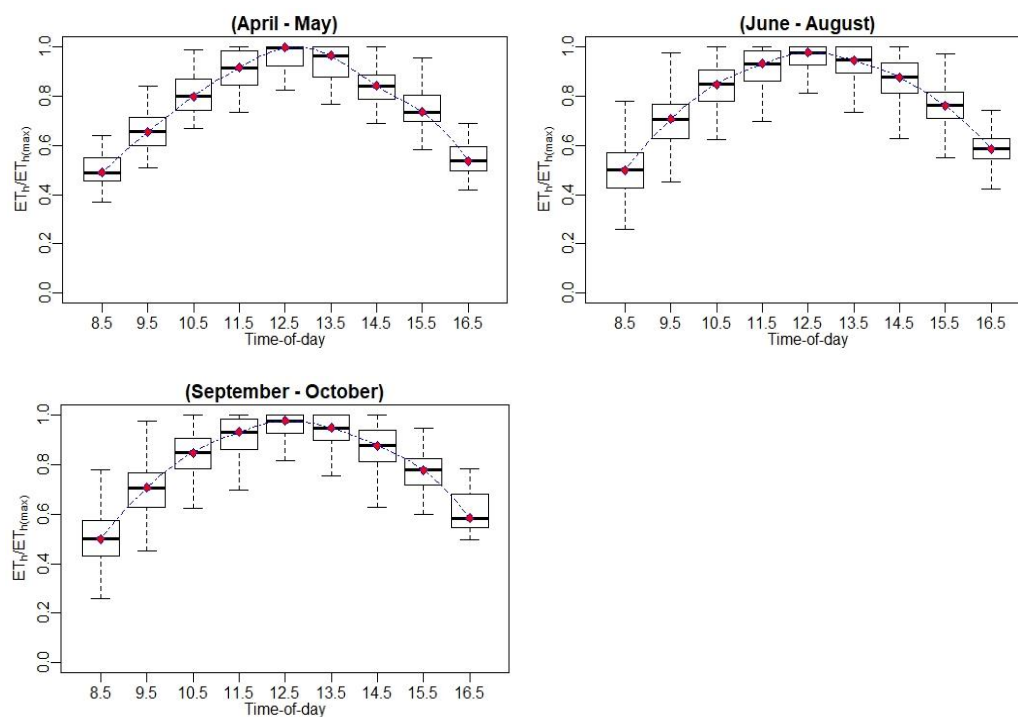


Figure B13 Hourly ET -to-maximum hourly ET ratio ($ET_h/ET_{h(max)}$) variation using EC measurements.

Appendix B.3.3 Hourly ET -to-Daily ET Ratio (ET_h/ET_d) Variation Using EC

Measurements

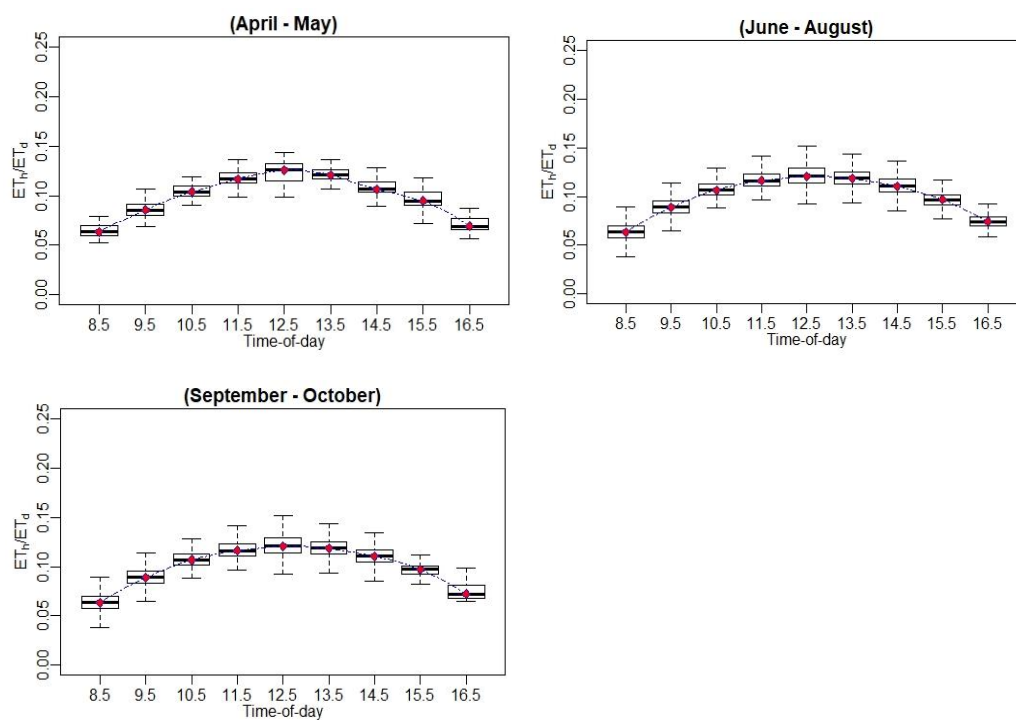


Figure B14 Hourly ET -to-daily ET ratio (ET_h/ET_d) variation using EC measurements.

Appendix B.3.4 Relative Error (E_r) at Hourly Scale for EC Measurements

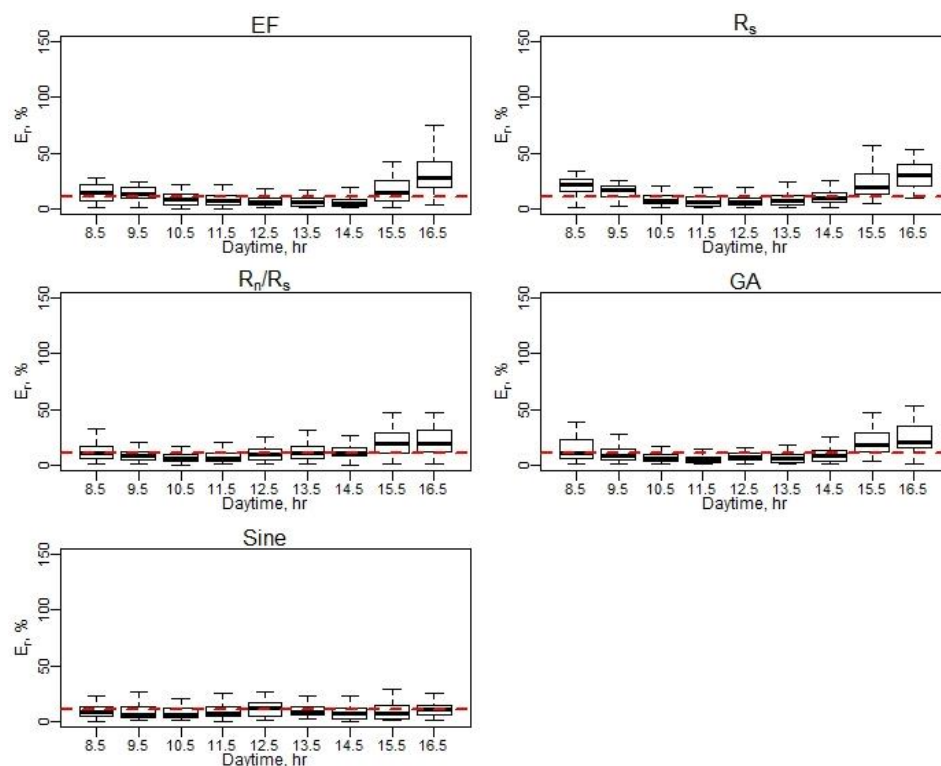


Figure B15 E_r of daily EC ET (April–May).

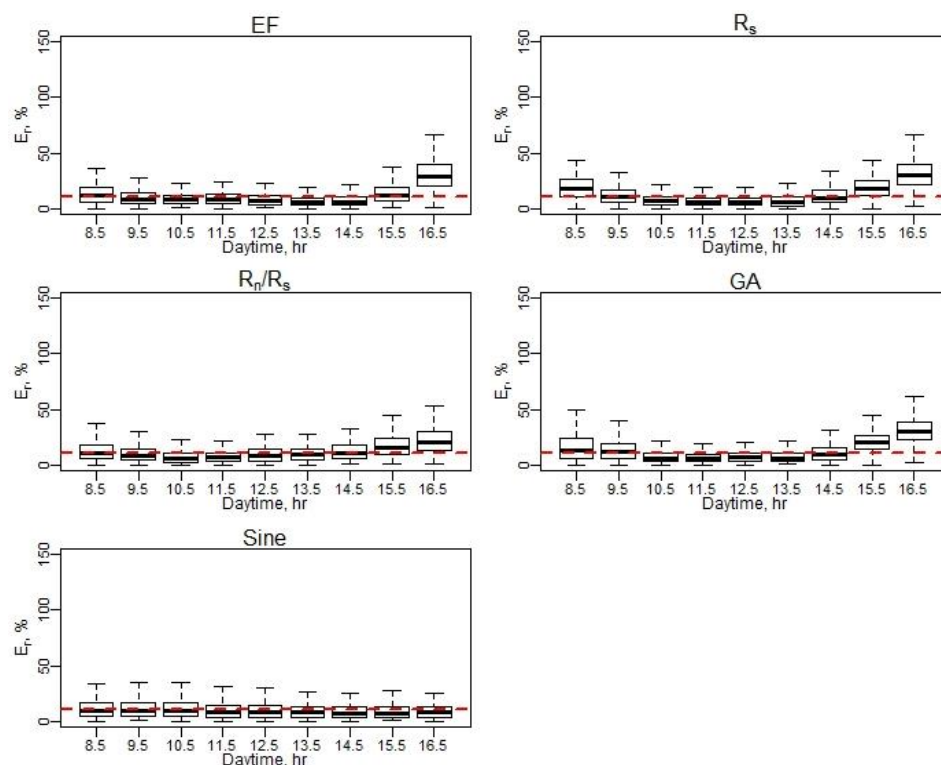


Figure B16 E_r of daily EC ET (June–August).

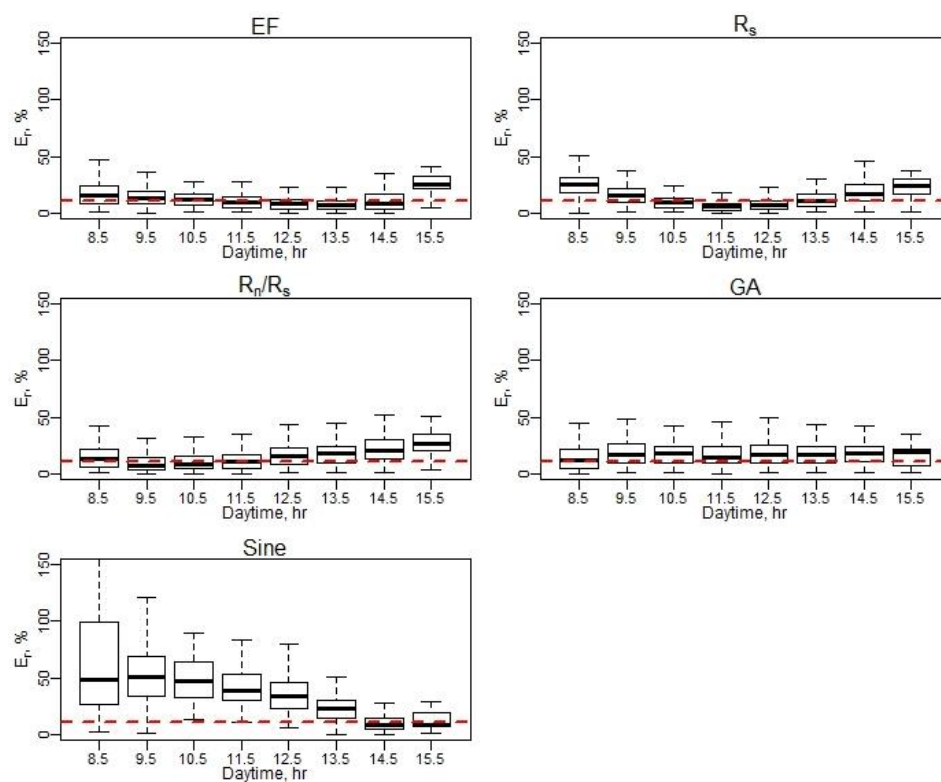


Figure B17 E_r of daily $EC\ ET$ (September–October). Note: Red dash line represents a 10% relative error (E_r).

Appendix B.3.5 Daily *RMSE* Performance Using Hourly *EC ET* Values

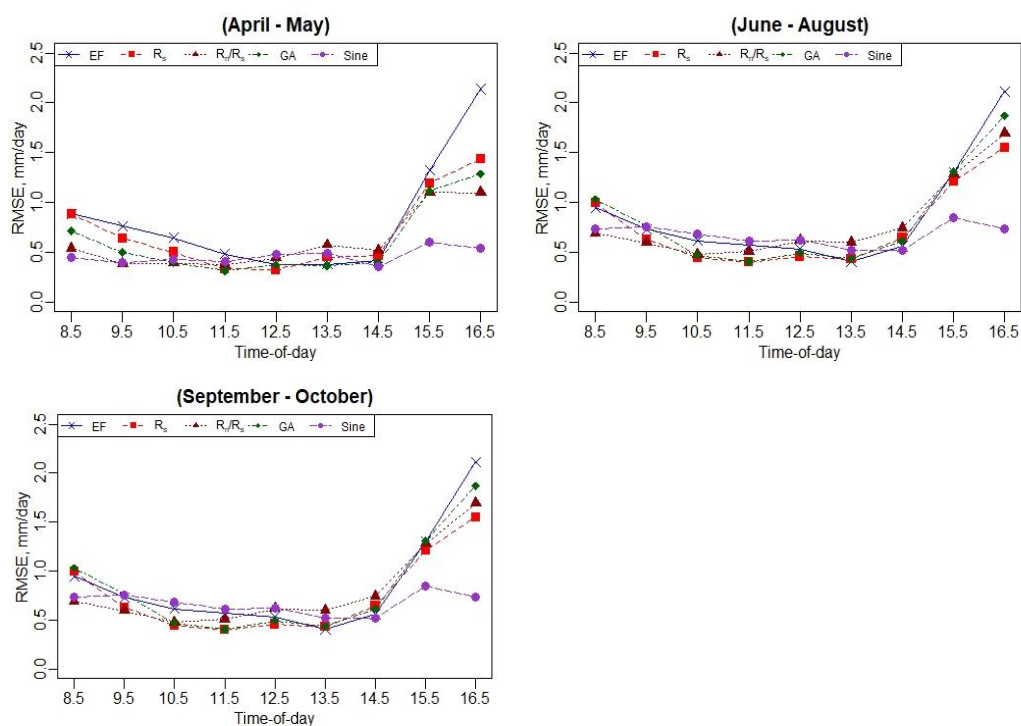


Figure B18 Daily *RMSE* performance using hourly *EC ET* values.

Appendix B.4 Daily *ET* analysis at Barrelli Vineyard, California

Appendix B.4.1 Diurnal Variation of Surface Energy Fluxes (R_n , H , LE , and G)

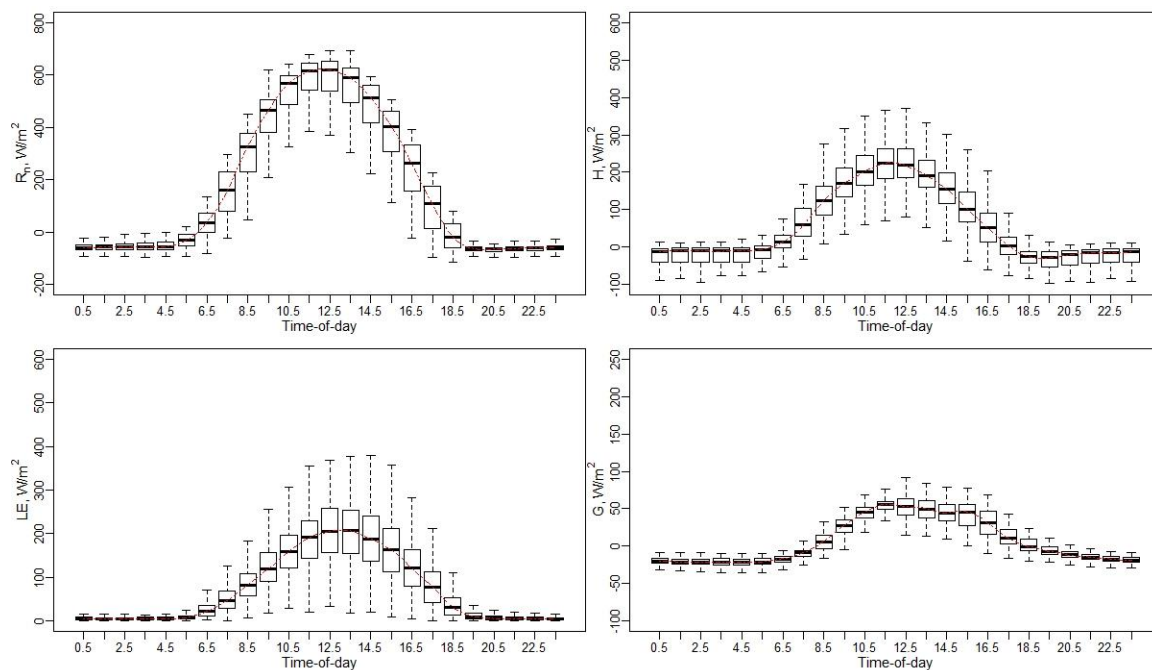


Figure B19 Diurnal variation of surface energy fluxes (R_n , H , LE , and G).

Appendix B.4.2 Hourly ET -to-Maximum Hourly ET Ratio ($ET_h/ET_{h(max)}$) Variation Using EC Measurements.

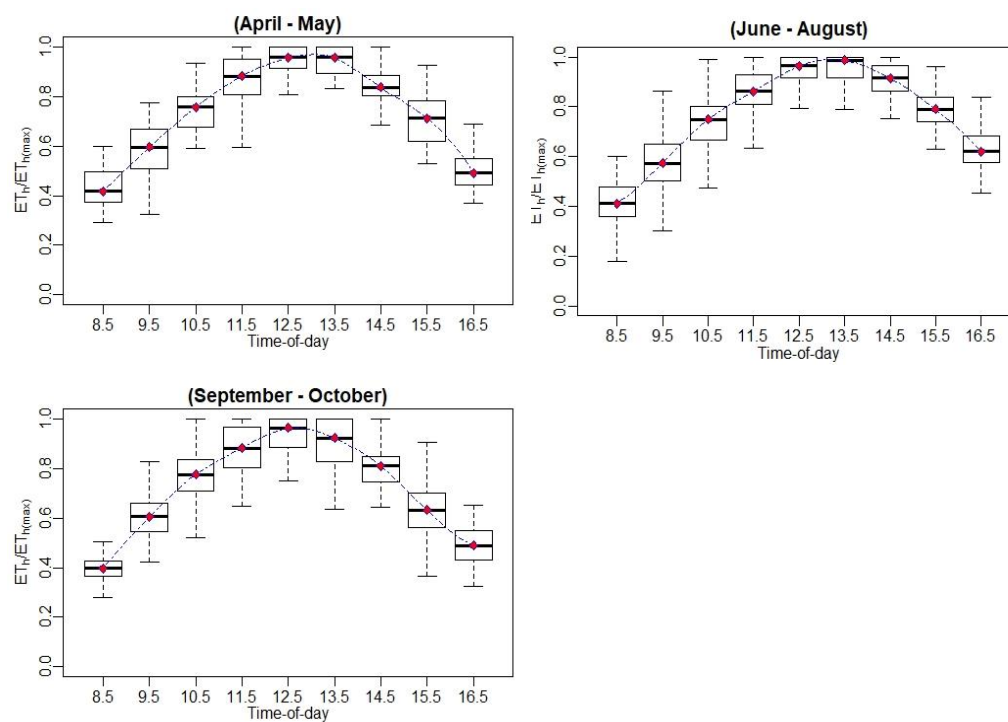


Figure B20 Hourly ET -to-maximum hourly ET ratio ($ET_h/ET_{h(max)}$) variation using EC measurements.

Appendix B.4.3 Hourly ET -to-Daily ET Ratio (ET_h/ET_d) Variation Using EC

Measurements

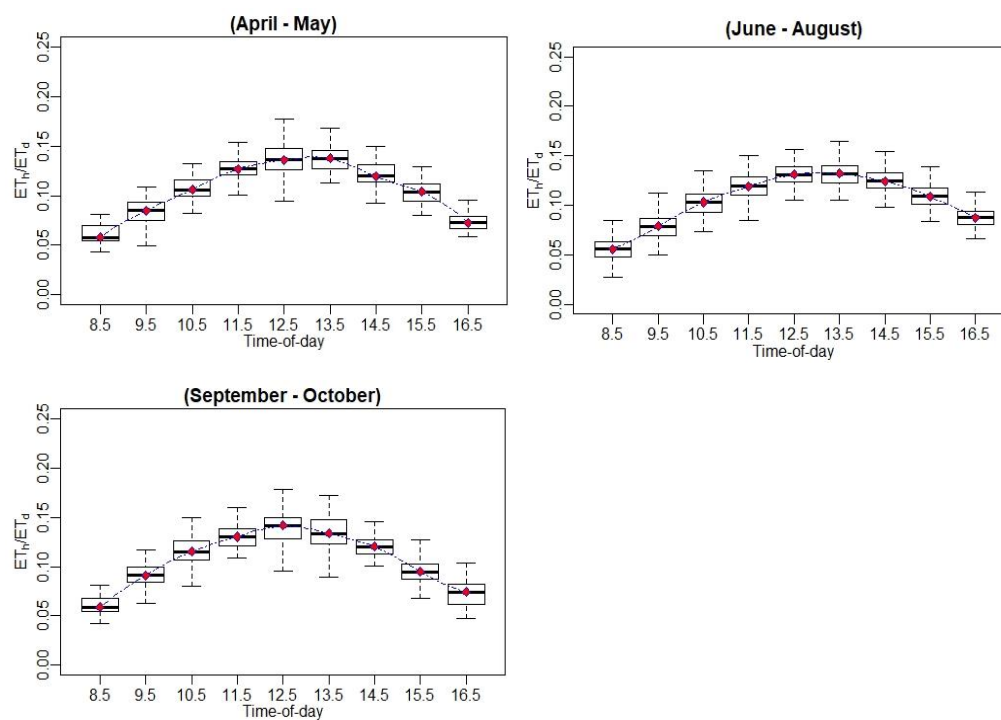


Figure B21 Hourly ET -to-daily ET ratio (ET_h/ET_d) variation using EC measurements.

Appendix B.4.4 Relative Error (E_r) at Hourly Scale for EC Measurements

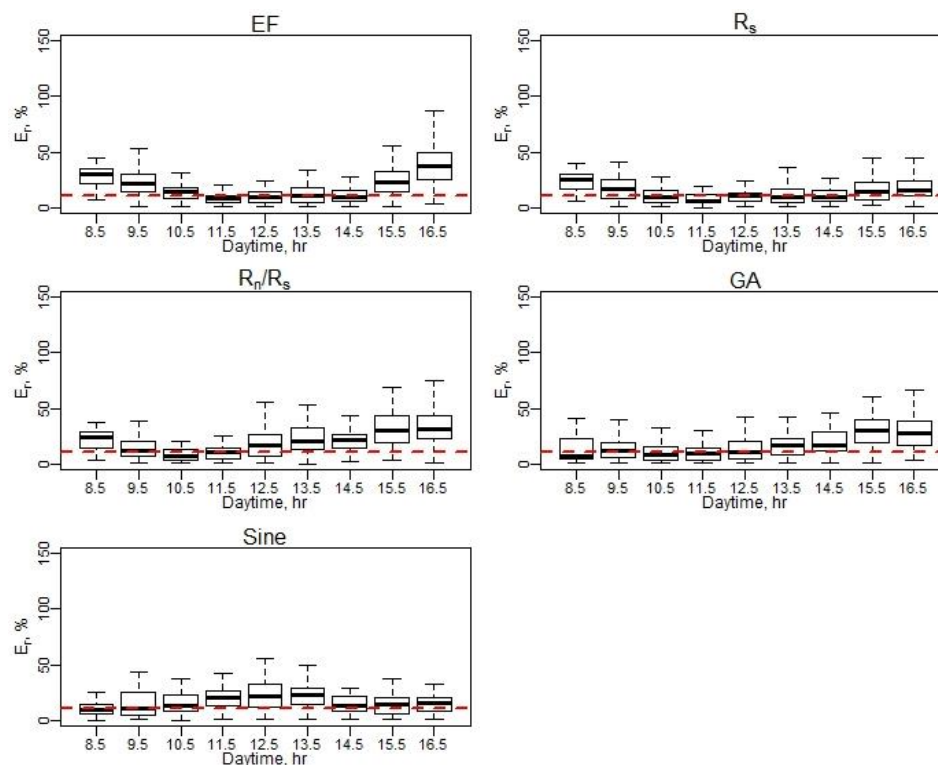


Figure B22 E_r of daily EC ET (April–May).

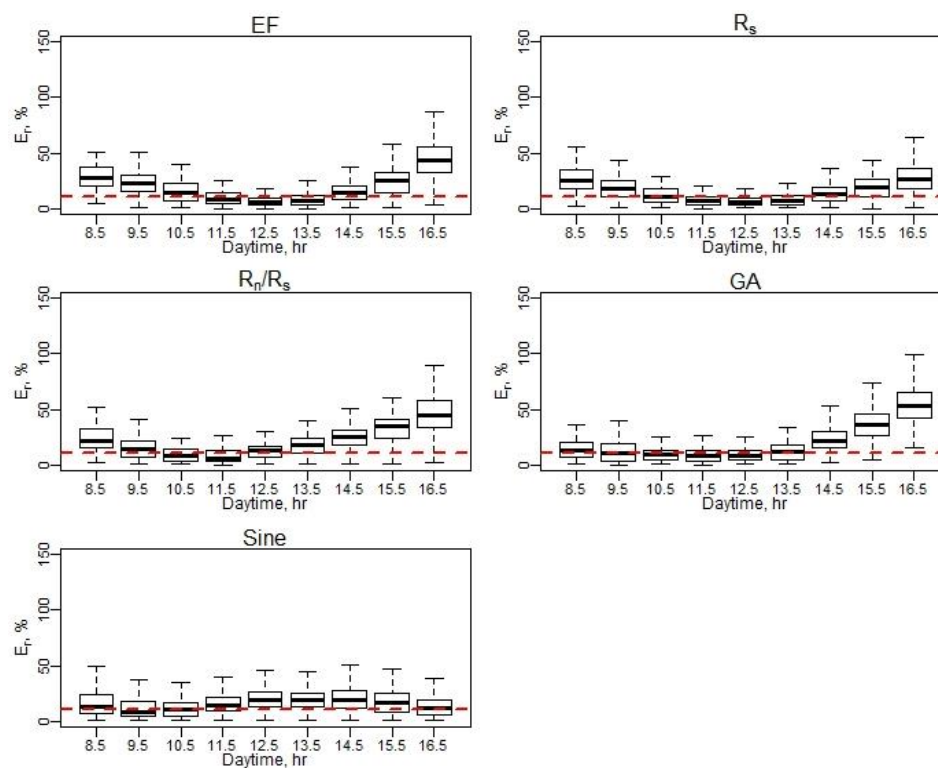


Figure B23 E_r of daily EC ET (June–August).

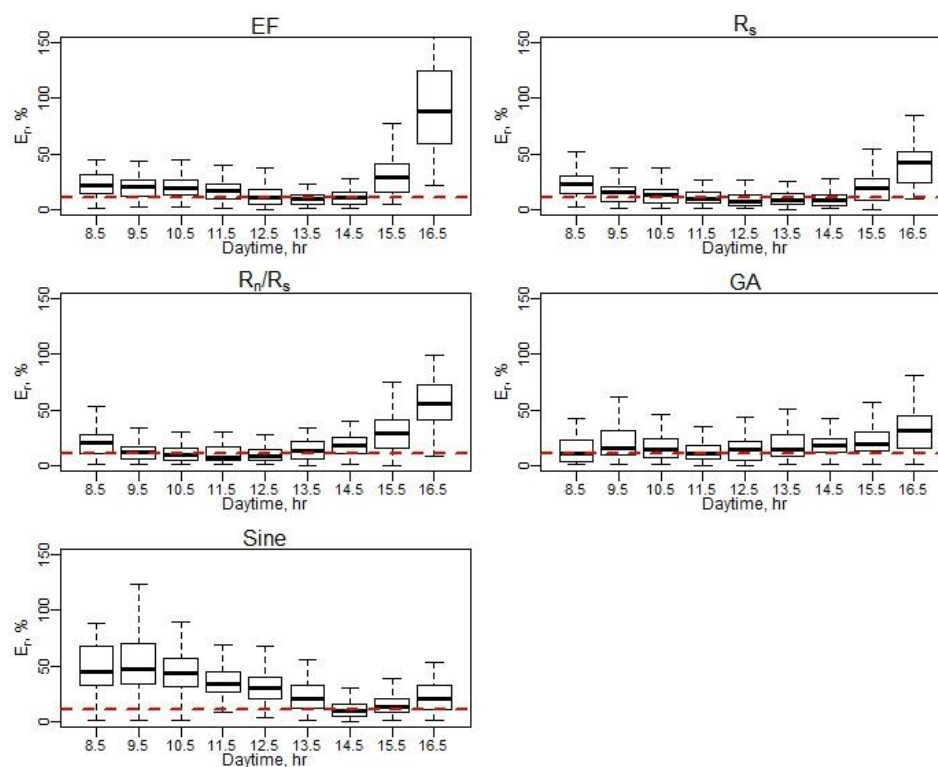


Figure B24 E_r of daily $EC ET$ (September–October). Note: Red dash line represents a 10% relative error (E_r).

Appendix B.4.5 Daily *RMSE* Performance Using Hourly *EC ET* Values

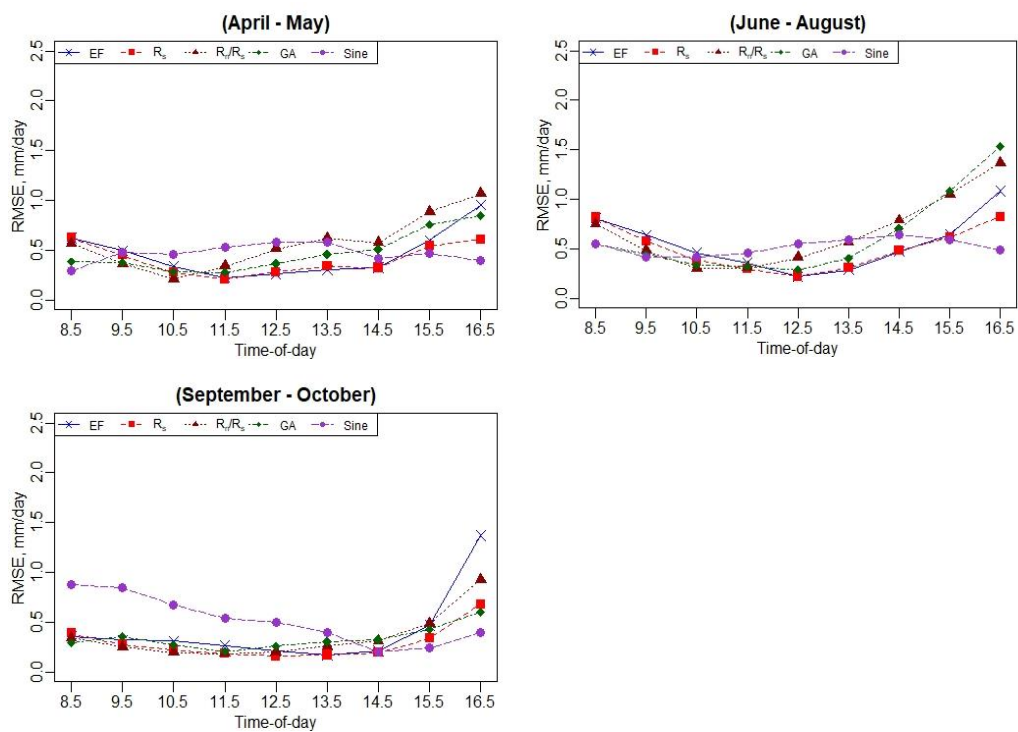


Figure B25 Daily *RMSE* performance using hourly *EC ET* values.

Appendix C: Authorship Permission

Paper I

Dear All,

I am in the process of preparing my dissertation in the Civil and Environmental Engineering Department at Utah State University.

I am requesting your permission to include the journal paper “Influence of Model Grid Size on the Estimation of Surface Fluxes Using the Two Source Energy Balance Model and sUAS Imagery in Vineyards”, of which you are a coauthor, as a chapter in my dissertation. Please indicate your approval of this request.

Thank you,
Ayman

Dr. Alfonso Torres-Rua

Ayman,

You did a great job. You have my permission.

Alfonso

Dr. William Kustas

Dear Ayman:

Congratulations! These are great papers and happy to have been invited and contribute to both papers as a co-author. I certainly approve having both the journal papers entitled “Influence of Model Grid Size on the Estimation of Surface Fluxes Using the Two Source Energy Balance Model and sUAS Imagery in Vineyards”, and “Assessing Daily Evapotranspiration Methodologies from One-Time-of-Day sUAS and EC Information in the GRAPEX Project” as chapters in your PhD dissertation.

Regards

Bill

Bill Kustas
USDA-ARS Hydrology & Remote Sensing Lab
10300 Baltimore Av.
Bldg 007 BARC-West
Beltsville, MD 20705
Tel:301-504-8498

Dr. Héctor Nieto

Dear Ayman,

First of all, congratulations for this great milestone!

I hereby give my approval for including the journal paper “Influence of Model Grid Size on the Estimation of Surface Fluxes Using the Two Source Energy Balance Model and sUAS Imagery in Vineyards”, in which I am co-author, in your PhD dissertation.

All the best,

Héctor Nieto

COMPLUTIG

hector.nieto@complutig.com

Complutum Tecnologías de la Información Geográfica S.L.

C/ Colegios 2

28801, Alcalá de Henares, Madrid

www.complutig.com

Dr. Mac McKee

Ayman:

Cool. Go for it.

M

Dr. Lawrence Hipps

Of course!

Dr. David Stevens

I approve this request.

David Stevens

Dr. Joseph Alfieri

Hi Ayman – Of course. That is your work; I am simply honored that I was include. And, since this for the university and has to be blunt: as a co-author who made only modest contributions to your research, you have my permission to include the publication named below as a part of your dissertation.

Best Regards

Joe

Dr. John Prueger

Yes. That would be fine Ayman. Good Luck.

John

Dr. Maria Mar Alsina

Good morning, Ayman:

Congratulations for your great work and for reaching this important point in your career. It has been a pleasure to work with you, and I thank you for including me in these publications.

You have my permission to include the two following peer reviewed publications as chapters in your PhD dissertation.

“Influence of Model Grid Size on the Estimation of Surface Fluxes Using the Two Source Energy Balance Model and sUAS Imagery in Vineyards”

“Assessing Daily Evapotranspiration Methodologies from One-Time-of-Day sUAS and EC Information in the GRAPEX Project”

Best of luck in your next steps

Mimar

Maria Mar Alsina

Research Scientist-viticulture

E&J Gallo Winery

530 219 7366

Mariadelmar.alsina@ejgallo.com

Dr. Lynn McKee

Fine with me

Thanks - Lynn

Lynn McKee

USDA, ARS, Hydrology & Remote Sensing Lab

10300 Baltimore Ave, Bldg 007 Rm 104

Beltsville, MD 20705

301-504-8081

301-648-6644(cell)

Dr. Calvin Coopmans

Yes, I approve!

Dr. Luis Sanchez

Nassar, I approve of course, and thank you for including me as coauthor and for all your hard work.

Dr. Nick Dokoozlian

Approved – thank you – Nick

Paper II

Dear All,

I am in the process of preparing my dissertation in the Civil and Environmental Engineering Department at Utah State University.

I am requesting your permission to include the journal paper “Assessing Daily Evapotranspiration Methodologies from One-Time-of-Day sUAS and EC Information in the GRAPEX Project”, of which you are a coauthor, as a chapter in my dissertation.

Please indicate your approval of this request.

Thank you,
Ayman

Dr. Alfonso Torres-Rua

Ayman,

Yes, I approve this too.

Alfonso

Dr. William Kustas

Dear Ayman:

Congratulations! These are great papers and happy to have been invited and contribute to both papers as a co-author. I certainly approve having both the journal papers entitled “Influence of Model Grid Size on the Estimation of Surface Fluxes Using the Two Source Energy Balance Model and sUAS Imagery in Vineyards”, and “Assessing Daily Evapotranspiration Methodologies from One-Time-of-Day sUAS and EC Information in the GRAPEX Project” as chapters in your PhD dissertation.

Regards

Bill

Bill Kustas
USDA-ARS Hydrology & Remote Sensing Lab
10300 Baltimore Av.
Bldg 007 BARC-West
Beltsville, MD 20705
Tel:301-504-8498

Dr. Joseph Alfieri

Hi Ayman – Of course. That is your work; I am simply honored that I was include. And, since this for the university and has to be blunt: as a co-author who made only modest contributions to your research, you have my permission to include the publication named below as a part of your dissertation.

Best Regards

Joe

Dr. Lawrence Hipps

Roger that!

Dr. John Prueger

Yes. That would be fine Ayman. Good Luck.

John

Dr. Héctor Nieto

Yes, I also approve the inclusion of this other paper,

Cheers!

Héctor Nieto

COMPLUTIG

hector.nieto@complutig.com

Complutum Tecnologías de la Información Geográfica S.L.

C/ Colegios 2

28801, Alcalá de Henares, Madrid

www.complutig.com

Dr. Maria Mar Alsina

Good morning, Ayman:

Congratulations for your great work and for reaching this important point in your career. It has been a pleasure to work with you, and I thank you for including me in these publications.

You have my permission to include the two following peer reviewed publications as chapters in your PhD dissertation.

“Influence of Model Grid Size on the Estimation of Surface Fluxes Using the Two Source Energy Balance Model and sUAS Imagery in Vineyards”

“Assessing Daily Evapotranspiration Methodologies from One-Time-of-Day sUAS and EC Information in the GRAPEX Project”

Best of luck in your next steps

Mimar

Maria Mar Alsina
Research Scientist-viticulture
E&J Gallo Winery
530 219 7366
Mariadelmar.alsina@ejgallo.com

Dr. William White

Hi Ayman,

That’s fine with me. Good luck with your dissertation!

-Alex

William Alexander White
Hydrology and Remote Sensing Laboratory
USDA Agricultural Research Service
Rm 104 Bldg 007 BARC-West
10300 Baltimore Ave
Beltsville, MD 20705
301-504-6542
Alex.White@usda.gov

Dr. Lynn McKee

That is fine
Thanks - Lynn

Lynn McKee
USDA, ARS, Hydrology & Remote Sensing Lab
10300 Baltimore Ave, Bldg 007 Rm 104
Beltsville, MD 20705
301-504-8081
301-648-6644(cell)

Dr. Calvin Coopmans

Yes I approve! Cheers!

—

Calvin Coopmans
Research Assistant Professor, Utah State University Electrical and Computer Engineering
Dept.
Director, USU AggieAir
<http://aggieair.usu.edu/>

Dr. Luis Sanchez

Ayman,
I approve being included as coauthor of your submission “Assessing Daily
Evapotranspiration Methodologies from One-Time-of-Day sUAS and EC Information in
the GRAPEX Project”
Thank you,
Luis Sanchez

Dr. Nick Dokoozlian

Approved – thank you – Nick

Curriculum Vitae

Ayman M. M. NassarEmails: aymnassar@gmail.com; ayman.nassar@usu.eduGoogle scholar: <https://scholar.google.com/citations?user=6flaS3YAAAAJ&hl=en>LinkedIn: <https://www.linkedin.com/in/ayman-nassar-24a92723/>**HIGHLIGHTS**

- Hydrologic modeler to advance cyberinfrastructure that supports large scale collaborative, reproducible hydrologic modeling.
- 5+ years served as a lecturer in GIS, Remote Sensing and Hydrologic Information Systems (HIS) at different universities.
- 4+ years served as water and wastewater engineer/expert at consulting engineering firms and NGOs.
- Awarded a prestigious fellowship in advanced data analytics and computational methods funded by NSF / Purdue University.
- Member of the USDA-led GRAPEX (Grape Remote sensing Atmospheric Profile and Evapotranspiration eXperiment) and HydroFrame (Computational and Data Innovation Implementing a National Community Hydrologic Modeling Framework for Scientific Discovery) projects.
- Trained visiting scholars from Brazil and Turkey on energy and water balance.

EDUCATION**Ph.D.** Civil and Environmental Engineering/Hydrology and Water Resources, Utah State University, Logan UT- 2021**Dissertation:** Estimation of High-Resolution Evapotranspiration in Heterogeneous Environments Using Drone-Based Remote Sensing.**M.Sc.** Civil Engineering/Infrastructure and Water Engineering, Islamic University of Gaza, Palestine - 2012**B.Sc.** Civil Engineering, Islamic University of Gaza, Palestine – 2008

PUBLICATIONS

Peer-Reviewed Publications

1. **Nassar, A.**; Torres-Rua, A.; Kustas, W.; et al. Assessing Methodologies for Daily Evapotranspiration Estimation from sUAS over Commercial Vineyards in California. Remote Sens. **2021**, *13*, 2887. <https://doi.org/10.3390/rs13152887>
2. **Nassar, A.**; Torres-Rua, A.; Kustas, W.; et al. Influence of Model Grid Size on the Estimation of Surface Fluxes Using the Two Source Energy Balance Model and sUAS Imagery in Vineyards. Remote Sens. 2020, 12, 342. <https://doi.org/10.3390/rs12030342>
3. Al-Juaidi, A.; **Nassar, A.**; Al-Juaidi A. 2018. Evaluation of Flood Susceptibility Mapping Using Logistic Regression and GIS Conditioning Factors. Arabian Journal of Geosciences. <https://doi.org/10.1007/s12517-018-4095-0>
4. Safre, A.; **Nassar A.**; Torres-Rua, A.; et al. Performance of Sentinel-2 SAFER ET model for Daily and Seasonal Estimation of grapevine water consumption. (Under-review- Irrigation Science journal)
5. **Nassar, A.**; Torres-Rua A.; et al. Characterizing the Spatial Heterogeneity in a River Corridor to Evaluate its Impact on the Evapotranspiration Estimates Using TSEB Model and sUAS Information. (Under-review- Remote Sensing journal)

Proceeding Conference Papers

1. **Nassar, A.**; Torres-Rua, A.; Kustas, W.; et al. Assessing Methodologies for Daily Evapotranspiration Estimation from sUAS over Commercial Vineyards in California. Remote Sens. **2021**, *13*, 2887. <https://doi.org/10.3390/rs13152887>
2. **Nassar, A.**; Torres-Rua, A.; Kustas, W.; et al. Influence of Model Grid Size on the Estimation of Surface Fluxes Using the Two Source Energy Balance Model and sUAS Imagery in Vineyards. Remote Sens. 2020, 12, 342. <https://doi.org/10.3390/rs12030342>
3. Al-Juaidi, A.; **Nassar, A.**; Al-Juaidi A. 2018. Evaluation of Flood Susceptibility Mapping Using Logistic Regression and GIS Conditioning Factors. Arabian Journal of Geosciences. <https://doi.org/10.1007/s12517-018-4095-0>
4. **Nassar, A.**; Torres-Rua, A.; et al. Development of High-Performance Computing Tools for Estimation of High-Resolution Surface Energy Balance Products Using sUAS

- Information. Proc. SPIE 11747, Autonomous Air and Ground Sensing Systems for Agricultural Optimization and Phenotyping VI, 117470K (12 April 2021); <https://doi.org/10.1117/12.2587763>
5. Gao, R.; Torres-Rua, A.; **Nassar, A.**; et al; Evapotranspiration Partitioning Assessment Using Machine Learning –Based Leaf Area Index and The Two-Source Energy Balance (TSEB) Model With sUAS Information. Proc. SPIE 11747, Autonomous Air and Ground Sensing Systems for Agricultural Optimization and Phenotyping VI, 117470N (12 April 2021); <https://doi.org/10.1117/12.2586259>
 6. Torres-Rua, A.; Aboutalebi, M.; Wright, T.; **Nassar, A.**; et al. Estimation of Surface Thermal Emissivity in a Vineyard for UAV Microbolometer Thermal Cameras Using NASA Hytes Hyperspectral Thermal, and Landsat and Aggieair Optical Data. Proc. SPIE 11008, Autonomous Air and Ground Sensing Systems for Agricultural Optimization and Phenotyping IV, 1100802 (14 May 2019); <https://doi.org/10.1117/12.2518958>
 7. McKee, M.; **Nassar, A.**; Torres-Rua, A; et al, (2018). Implications of Sensor Inconsistencies and Remote Sensing Error in the Use of Small-Unmanned Aerial Systems for Generation of Information Products for Agricultural Management. Autonomous Air and Ground Sensing Systems for Agricultural Optimization and Phenotyping III. SPIE. <https://doi.org/10.1117/12.2305826>
 8. **Nassar, A.** ; Torres-Rua, A. ; Kustas, W.; et al. Implications of Soil And Canopy Temperature Uncertainty in the Estimation of Surface Energy Fluxes Using TSEB2T and High-Resolution Imagery in Commercial Vineyards, Proc. SPIE 11414, Autonomous Air and Ground Sensing Systems for Agricultural Optimization and Phenotyping V, 114140F (26 May 2020); <https://doi.org/10.1117/12.2558715>
 9. **Nassar, A.** ; Torres-Rua, A. ; Kustas, W.; et al. To What Extend Does the Eddy Covariance Footprint Cutoff Influence the Estimation of Surface Energy Fluxes Using Two Source Energy Balance Model and High-Resolution Imagery in Commercial Vineyards?, Proc. SPIE 11414, Autonomous Air and Ground Sensing Systems for Agricultural Optimization and Phenotyping V, 114140G (26 May 2020); <https://doi.org/10.1117/12.2558777>

Conference Presentations

1. **Nassar, A.**; Torres-Rua, A.; et al. Influence of Spatial Heterogeneity in Evapotranspiration Modeling at Natural Areas Using sUAS High Resolution Data. AGU Fall Meeting 2020.
2. Gao, R.; **Nassar, A.**; et al, Grapevine Leaf Area Index Estimation With Machine Learning And Unmanned Aerial Vehicle Information. AGU Fall Meeting 2020.
3. Safre, A.; **Nassar A.**; et al, Validation of the SAFER ET model using Landsat 8 and Sentinel-2 images over commercial vineyards in California. AGU Fall Meeting 2020.
4. **Nassar, A.**; Torres-Rua, A., et al. Assessment of High-Resolution Daily Evapotranspiration Models Using Instantaneous sUAS ET in Grapevine Vineyards. 2019 AGU, San Francisco, California.
5. Torres-Rua, A.; Aboutaleb, M.; **Nassar, A.**; Nieto, H.; et al. Getting Closer to Landsat: Advances from the GRAPEX Project in the Application of UAVs for High-Resolution Evapotranspiration. 2019 AGU, San Francisco, California.
6. McKee, M.; Torres-Rua, A.; Aboutaleb, M.; **Nassar A.**; Coopmans, C.; Kustas W.; et al. Challenges that beyond-visual-line-of-sight technology will create for UAS-based remote sensing in agriculture., Proc. SPIE 11008, Autonomous Air and Ground Sensing Systems for Agricultural Optimization and Phenotyping IV, 110080J (14 May 2019); <https://doi.org/10.1117/12.2520248>
7. **Nassar, A.**; Torres-Rua, A.; McKee, M.; et al. Assessment of UAV Flight Times for Estimation of Daily High-Resolution Evapotranspiration in Complex Agricultural Canopy Environments. 2019 UCOWR /NIWR, Annual Water Resources Conference, Snowbird, Utah.
8. **Nassar, A.**; Nieto, H.; Aboutaleb, M.; Torres-Rua, A.; et al. (2018). Pixel Resolution Sensitivity Analysis for the Estimation of Evapotranspiration Using the Two Source Energy Balance Model and sUAS Imagery under Agricultural Complex Canopy Environments. AGU Fall Meeting 2018.

WORK EXPERIENCE

Teaching Experience

Jan 2020–May 2020

Teaching assistant

Utah State University, Logan UT

- Teaching assistant of remote sensing class.
- Carried out training sessions in Python programming.

Aug 2019–Dec 2019

Teacher

Utah State University, Logan UT

- Co-taught graduate level class, namely Environmental and Hydrologic Data Analysis and Experimentation.
- Conducted training sessions using R programming.

Jan 2019–May 2019

Teaching assistant

Utah State University, Logan UT

- Remote sensing class.
- Training sessions in Python programming language.
- Physical hydrology class (Terrain Modeling) – Guest lecturer.

Jan 2013–May 2017

Lecturer

University College of Applied Sciences, Palestine

- Taught undergraduate level courses (Surveying, GIS in Hydrology, Civil and Infrastructure Planning, Applied Statistics, Applied Mathematics, Advanced GIS, Remote Sensing Applications, GIS Customization and Programming)
- Followed-up the progress of students' projects.

Sep 2013–May 2017

Part-time lecturer

Islamic University of Gaza, Palestine

- Taught courses (HIS, GIS, Remote Sensing)

Sep 2008–May 2009

Lecturer

Polytechnic University, Palestine

- Taught undergraduate level courses.

Research/Professional Experience

Expected (Sep. 2021)

Postdoctoral researcher

Utah State University

- Develop hydrologic modeling use cases to address large scale questions related to flood prediction, inundation mapping, and water availability.
- Apply the modeling use cases to improve computational approaches implemented in community collaboration platforms (e.g. HydroShare, JupyterHub) in support of collaborative, reproducible hydrologic modeling.
- Explore approaches for publishing models and results where the datasets are large.
- Advance available cyberinfrastructure for supporting modeling and sharing of model forcing data and results.

Aug 2017 – August 2021

Graduate research assistant

Utah State University

- Conducted research in geospatial and remote sensing energy balance.
- Conducted research in evapotranspiration (ET) in natural environments.
- Carried out original, high-level collaborative research with other team members.
- Collected field data that serve the research and models validation.
- Participated in scientific conferences.

Nov 2015–Dec 2015

Water resources expert

Action Against Hunger (ACF), Palestine

- Reviewed the stormwater master plan of Khanunyis city, Palestine.
- Carried out stormwater drainage design.

Feb 2014–Feb 2015

Water resources expert

Action Against Hunger (ACF), Palestine

- Evaluated the existing stormwater infrastructure and identified the flooded-areas.

- Designed stormwater harvesting system.

- Conducted training sessions in hydrologic modeling and stormwater design.

Jan 2010–Jan 2013

Water and wastewater engineer

ALMADINA - ENFRA -DHV-Netherland joint venture

- Provided technical assistance on using the non-conventional water resources (treated wastewater reuse and stormwater harvesting).

Aug 2008–Dec 2009

Office manager

Engineering, Management and Infrastructure (ENFRA) Consultants, Palestine.

AWARDS / HONORS

1. 2020 - "**Outstanding Student Spotlight**" Utah Water Research Laboratory -Utah State University.
2. 2020 - "**Best Conference Paper**" Society of PhotoOptical Instrumentation Engineers Conference.
3. 2020 - "**Cyber Training Award**" National Science Foundation Findable-Accessible-Interoperable-and-Reusable Program, Purdue University.
4. 2020 - "**First Place Technical Writing Competition**" College of Engineering, Utah State University.
5. 2020 – "**Travel Award**" National Science Foundation.
6. 2019 - " **Eva Nieminski Honorary Graduate Science Engineering Scholarship** " American Water Works Association - Intermountain Section
7. 2019 - " **Graduate Student Travel Award** " - Utah State University Office of Research and Graduate Studies.
8. 2019 - " **Graduate Student Travel Award** " – College of Engineering, Dean Office, Utah State University.
9. 2019 - " **Utah Water User Association Scholarship** " Utah Water User Association.

10. 2019 - " **Graduate Student Travel Award** " – Utah State University Office of Research and Graduate Studies.
11. 2019 - " **Graduate Student Travel Award** " – College of Engineering, Dean Office, Utah State University.
12. 2018 - " **Graduate Student Travel Award** " – Utah State University Office of Research and Graduate Studies.
13. 2018 - " **Graduate Student Travel Award** " – College of Engineering, Dean Office, Utah State University.
14. 2017 - " **Scholarship for PhD Study in Civil and Environmental Engineering** " Utah Water Research Laboratory - Utah State University.
15. 2016 - " **Outstanding Teacher** " University College of Applied Sciences.
16. 2015 - " **Outstanding Teacher** " University College of Applied Sciences.
17. 2013 - " **Outstanding Teacher** " University College of Applied Sciences.
18. 2008 – " **Trustee Board Scholarship for Distinction for MSc Study in Civil Engineering** " Islamic University of Gaza.

FUNDED PROJECTS

- Contributed to proposal for California Almond Board, \$399,880 (2020).
- FAIR Cyber Training (FACT) Fellowship for Climate and Water Fellowship, Funded by NSF/Purdue University, \$2,000 (May 2020 – May 2021).
- “GIS for Community” project, University College for Applied Sciences, Funded by Quality Improvement Fund (QIF), World Bank, ~\$150,000 (2017-2020).

COMPUTER SKILLS

- Data management and modeling (Arc GIS, SQL server, Silverlight, Google Earth Engine).
- Remote sensing (ERDAS, ILWIS, IDRISI, ENVI).
- Computer programming (Python, MATLAB , GrADS).
- Statistical packages (R, SPSS).
- Hydrologic modeling systems (WRF-Hydro.NWM, ParFlow.CONUS, HEC-HMS, HEC-Geo HMS, Archydro, SWMM).
- Subsurface hydrology model (MODFLOW, Hydrus).

- Others (MS Project, Word, Excel, Power Point, AutoCAD)

MEMBERSHIPS

- American Geophysical Union (AGU).
- American Water Works Association (AWWA).
- Engineering syndicate (PA).

PROFESSIONAL ACTIVITIES

- Coordinator, University College of Applied Sciences (UCAS) Applied GIS program.
- Curriculum committee member – Applied GIS and Civil Engineering programs, University College of Applied Sciences.
- Chair, GISday, Consortium of University College of Applied Sciences, Islamic University of Gaza, and American University of Jenin

ONLINE OPEN-SCIENCE REPOSITORIES

1. Gao, R., A. F. Torres-Rua, **A. Nassar**, et al (2021). Comparison between the *TSEB* results and eddy covariance (*EC*) ground measurements, HydroShare, <https://doi.org/10.4211/hs.eb6eeccdbe546fc941f3c219cb05a34>
2. Torres-Rua, A., **Nassar A.** “USU Remote Sensing Laboratory sessions”, 2020, https://github.com/torresrua/prj_earthengine_hydroshare
3. Gao, R., **Nassar, A.** *EC* footprint model, 2021, https://github.com/RuiGao9/EC-Tower_Data_Organizing

MEDIA OUTREACH / OTHER ACTIVITIES

- I received a prestigious fellowship awarded by NSF in collaboration with Purdue university <https://mygeohub.org/cybertraining/fellowship/fellows2020>
- UWRL Outstanding Student Spotlight, Utah State University: <https://uwrl.usu.edu/news/main-feed/2020/ayman-nassar-spotlight>, Accessed May 21, 2020.

- American Water Works Association - Intermountain Section Scholarship
<https://uwrl.usu.edu/news/main-feed/2019/ayman-nassar-scholarship-2019> Accessed June 14, 2019
- Utah Water Users Association Scholarship <https://engineering.usu.edu/news/main-feed/2019/grad-student-awarded-uwua-scholarship>
- Volunteer Training Coordinator at Nassej Association for Building Capacity (2006/2007)
- Trainer for visiting scholars from Brazil and Turkey in energy balance modeling (February 2020- February 2021).
- Participated in GISday (2018) – Joint-event between University College of Applied Sciences and American University of Jenin.
- Trainer of Python programming for beginners (2019) - Civil and Environmental Engineering, Utah State University.